STUDY OF CHARGE TRANSPORT BEHAVIOR IN ORGANIC SOLAR CELLS

SHAHINO MAH BIN ABDULLAH

THESIS SUBMITTED IN FULFILLMENT OF
THE REQUIREMENT FOR THE DEGREE OF
DOCTOR OF PHILOSOPHY

FACULTY OF SCIENCE
UNIVERSITY OF MALAYA
KUALA LUMPUR

2015

UNIVERSITY OF MALAYA
ORIGINAL LITERARY WORK DECLARATION

Name of Candidate: Shahino Mah bin Abdullah (I.C/Passport No: 870717-23-5333)

Registration/Matric No: SHC130056

Name of Degree: Doctor of Philosophy

Title of Thesis ("this Work"):

STUDY OF CHARGE TRANSPORT BEHAVIOR IN ORGANIC SOLAR CELLS

Field of Study: Organic Electronics

I do solemnly and sincerely declare that:

(1) I am the sole author/writer of this Work;
(2) This Work is original;
(3) Any use of any work in which copyright exists was done by way of fair dealing and for permitted purposes and any excerpt or extract from, or reference to or reproduction of any copyright work has been disclosed expressly and sufficiently and the title of the Work and its authorship have been acknowledged in this Work;
(4) I do not have any actual knowledge nor do I ought reasonably to know that the making of this work constitutes an infringement of any copyright work;
(5) I hereby assign all and every rights in the copyright to this Work to the University of Malaya ("UM"), who henceforth shall be owner of the copyright in this Work and that any reproduction or use in any form or by any means whatsoever is prohibited without the written consent of UM having been first had and obtained;
(6) I am fully aware that if in the course of making this Work I have infringed any copyright whether intentionally or otherwise, I may be subject to legal action or any other action as may be determined by UM.

Candidate's Signature Date: 4 / 12 / 2015

Subscribed and solemnly declared before,

Witness's Signature Date: 4/12/2015

Name: Dr. Khaulah Sulaiman

Designation: Associate Professor

Associate Prof Dr Khaulah Sulaiman
Low Dimensional Materials Research Center
(LDMRC), Department of Physics
Faculty of Science, University of Malaya
50603 Kuala Lumpur, Malaysia

ABSTRACT

The energy harnessing devices like solar cells based on organic materials known as organic solar cells (OSCs) have attracted much interest in research and industrial field as they are believed to achieve promising performance for consumers needs and become very competitive in the near future. However, as compared to commercially available inorganic solar cells, the performance of OSCs, in their existing form, is relatively low and does not suit for practical use in electronic application due to poor nature of organic material. In order to face this challenge, the study of OSCs charge transport behavior by means of electrical characterization is very crucial to provide useful knowledge for the enhancement of OSCs performance. Therefore, the study of charge transport behavior in OSCs has become the main purpose in the present research work where it is done by two types of measurements; (1) current-voltage (I-V) method, and (2) electric field induced second harmonic generation (EFISHG) technique. The study of charge carrier dynamics has been carried out, individually, for materials such as vanadyl 2,9,16, 23-tetraphenoxy-29H, 31H-phthalocyanine (VOPcPhO) a phthalocyanine derivative, and poly[N-9'-heptadecanyl-2,7-carbazole-alt-5,5-(4',7'-di-2-thienyl-2',1',3'-benzothiadiazole)] (PCDTBT) a carbazole derivative, by means of I-V method and EFISHG technique, respectively. The I-V results have unveiled the fact that VOPcPhO has an ambipolar property in which the mobility of electron (8.3×10^{-5} cm^2/Vs) was found comparable with the hole mobility (3.7×10^{-4} cm^2/Vs) which makes it work not only as a donor, but also as an acceptor component when combined with other donor material such as poly(3-hexylthiophene-2,5-diyl) (P3HT) in the OSCs. The EFISHG measurement was performed for both selected donor materials (VOPcPhO and PCDTBT) which showed better compatibility for the study of charge carrier in PCDTBT based devices as the technique requires non-centro symmetrical material structure. It is found that the hole mobility of PCDTBT measured by EFISHG technique is higher (5.6×10^{-5} cm^2/Vs) than the mobilities measured by I-V method (2.4×10^{-5} cm^2/Vs), time-of-flight (0.9×10^{-5} cm^2/Vs), OTRACE (4.1×10^{-5} cm^2/Vs), and photo-CELIV (5.0×10^{-5} cm^2/Vs) methods, reported in the literature. Furthermore, study of the charge transport behavior in the OSCs, based on the blend of donor (PCDTBT) and acceptor [6,6]-phenyl C_{71} butyric acid methyl ester ($PC_{71}BM$), was carried out by EFISHG technique. The EFISHG characterization has enabled us to discover several new facts in this work, which are stated as: the individual electric fields of both PCDTBT and $PC_{71}BM$ could be measured in the PCDTBT:$PC_{71}BM$ bulk heterojunction OSCs by using selected fundamental laser wavelengths (1000 nm for PCDTBT, and 1060 nm for $PC_{71}BM$), the direction of internal electric field in PCDTBT:$PC_{71}BM$ solar cells was reversed (from ITO-blend-Al to Al-blend-PEDOT:PSS-ITO) by introducing a PEDOT:PSS layer leading to a longer electron transit time and thus increased efficiency of OSCs. The present study has provided a deeper insight and understanding on the mechanism of charge transport behavior in OSC devices which is very useful for the improvement of both efficiency and stability of the OSCs.

ABSTRAK

Peranti yang mampu menghasil tenaga terutamanya berasaskan bahan organik dikenal sebagai sel solar organik (OSCs) telah menarik minat yang tinggi di dalam bidang kajian dan industri apabila ia dilihat mampu memberi prestasi yang memberangsangkan untuk keperluan pengguna tidak lama lagi. Walau bagaimanapun, jika dibandingkan dengan sel solar bukan organik dipasaran kini, OSCs mempunyai prestasi yang lebih rendah dan masih tidak sesuai untuk kegunaan praktikal dalam bentuknya yang sekarang kerana kelemahan sifat semulajadi bahan organik itu sendiri untuk aplikasi elektronik. Bagi menanganinya, kajian angkutan cas dalam OSCs dengan menggunakan pencirian elektrikal menjadi satu kemestian untuk menyediakan pengetahuan yang berguna bagi meningkatkan prestasi OSCs ini. Oleh itu, kajian angkutan cas di dalam OSCs menjadi tujuan utama kajian ini dimana ia dilaksanakan dengan menggunakan dua teknik berbeza; (1) kaedah biasa arus-voltan (I-V), dan (2) penghasilan harmonik kedua dari medan elektrik (EFISHG). Kajian perilaku cas angkutan ini telah dilakukan terhadap bahan organik termasuk vanadyl 2,9,16, 23-tetraphenoxy-29H, 31H-phthalocyanine (VOPcPhO), dan poly[N-9'-heptadecanyl-2,7-carbazole-alt-5,5-(4',7'-di-2-thienyl-2',1',3'-benzothiadiazole)] (PCDTBT), dengan menggunakan kaedah I-V dan teknik EFISHG. Keputusan I-V telah mendedahkan bahawa VOPcPhO mempunyai sifat ambipolar dengan mobiliti elektron (8.3×10^{-5} cm^2/Vs) didapati hampir setara dengan mobiliti lohong (3.7×10^{-4} cm^2/Vs) yang membuatkannya bukan sahaja berfungsi sebagai penderma, malah sebagai penerima elektron apabila ia dicampurkan bersama komponen penderma yang lain seperti poly(3-hexylthiophene-2,5-diyl) (P3HT). Dalam masa yang sama, teknik EFISHG digunakan untuk pencirian kedua-dua bahan terpilih (VOPcPhO dan PCDTBT) dan ia menunjukkan kesesuaian yang lebih baik terutamanya untuk kajian peranti berasaskan

PCDTBT kerana ia menghendaki bahan yang tidak simetri. Mobiliti PCDTBT ditemui lebih tinggi apabila dikira dengan teknik EFISHG (5.6×10^{-5} cm^2/Vs) berbanding teknik lain seperti kaedah I-V (2.4×10^{-5} cm^2/Vs), masa-terbangan atau *time-of-fligth* (0.9×10^{-5} cm^2/Vs), *OTRACE* (4.1×10^{-5} cm^2/Vs), dan foto-*CELIV* (5.0×10^{-5} cm^2/Vs) seperti yang dilaporkan terdahulu. Kajian lanjut bagi perilaku angkutan cas dijalankan dengan menggunakan teknik yang sama terhadap OSCs berasaskan campuran PCDTBT dan komponen penerima, [6,6]-phenyl C_{71} butyric acid methyl ester ($PC_{71}BM$). Pencirian melalui teknik EFISHG membolehkan beberapa penemuan baru dicerap seperti; mendedahkan bahawa medan elektrik PCDTBT dan $PC_{71}BM$ boleh diukur secara berasingan daripada sel solar PCDTBT:$PC_{71}BM$ simpang-hetero dengan menggunakan panjang gelombang tertentu yang masing-masing adalah 1000 nm untuk PCDTBT dan 1060 nm untuk $PC_{71}BM$, penemuan pertukaran arah medan dalaman di dalam sel solar PCDTBT:$PC_{71}BM$ (dari ITO-campuran-Al) dengan kehadiran lapisan PEDOT:PSS (kepada Al-campuran-PEDOT:PSS-ITO) yang kemudiannya memanjangkan masa angkutan elektron dan sekaligus meningkatkan prestasi OSCs. Kajian ini telah memberikan kefahaman yang lebih mendalam tentang perilaku cas angkutan di dalam OSCs dan ia sangat berguna untuk penambahbaikan prestasi OSCs termasuklah peningkatan kecekapan dan kestabilannya.

ACKNOWLEDGEMENTS

First and foremost, I would like to thank God for the strength He has given to me that kept me moving on to accomplish this work. As I used to greet in Arabic *“Alhamdulillah”*, all praise be to Allah. I would like to thank my family, especially my mother, Mrs. Noriah Abu Bakar, who has continuously inspired, encouraged and supported me in every single moment of my life. It is also worth considering that I received constant moral and spiritual support from them besides their financial assistance.

My supervisor, Associate Professor Dr Khaulah @ Che Som Sulaiman, has generously provided me with a great opportunity to continue my master degree and end it up at the PhD level. She should receive most of my gratitude for what I have achieved today. She was ever ready to provide specific guidance and support for the completion of this uphill task. I also admire her co-operation and concern that she showed during the entire course of my PhD. Special thanks to my helpful group mates, especially Mr. Muhamad Saipul Fakir, Mr. Lim Lih Wei, Ms. Tong Way Yun, Ms. Fadilah Wahab, and Dr. Zurianti Abd Rahman for their support since the first day when I joined the group. At the same time, I am very grateful to Dr. Zubair Ahmad, who was always willing to guide me for being more productive and efficient in every single task that needed to be done in time. I would also wish my gratitude to Dr. Mansoor Ani Najeeb, Dr. Fakhra Aziz, Dr. Qayyum Zafar, Mr. Karwan Wasman Qadir, and Mr. Mohamad Izzat Azmer for their cooperation and support during working together. Many thanks to the Low Dimensional Materials Research Centre (LDMRC) staff, Mr. Mohamad Aruf, Mrs. Norlela Mohd Shahardin, and Mr. Mohd Arif Mohd Sarjidan, for their administrative assistance that facilitated my work in the laboratory.

It is worth noting to receive financial assistance for my research work from the Postgraduate Research Grant (PG089-2012B). I am really grateful to my supervisor for providing financial support through her grants which included RG053/09AFR, FP007/2011A, and UM.C/HIR/MOHE/SC/26. Last but not the least, thanks to everyone, who is not, mentioned here, for his/her contribution, direct or indirect during the completion of my research work.

TABLE OF CONTENTS

LIST OF FIGURES

Page

LIST OF TABLES

Page

LIST OF SYMBOLS

I_{sc}	Short circuit current
ε	Dielectric constant
λ	Wavelength
θ	Trap factor
c	Velocity of light
E	Photon energy
e	Electronic charge unit
FF	Fill factor
h	Planck's constant
I_{max}	Current at maximum power
J	Current density
J_{sc}	Short circuit current density
P_{in}	Input power
P_{max}	Maximum power
R_s	Series resistance
R_{sh}	Shunt resistance
V_{max}	Voltage at maximum power
V_{oc}	Open circuit voltage
η	Power conversion efficiency
μ	Charge carrier mobility
ν	Frequency

LIST OF ABBREVIATIONS

Al	Aluminum
Au	Gold
BHJ	Bulk heterojunction
BL	Bilayer
C_{60}	Buckminsterfullerene
CB	Conduction band
EQE	External quantum efficiency
ETL	Electrons transport layer
HCl	Hydrochloric acid
HDI	Human Development Index
HTL	Holes transport layer
HOMO	Higher occupied molecular orbital
ITO	Indium-tin-oxide
kWh	Kilowatt-hours
LiF	Lithium fluoride
LUMO	Lower unoccupied molecular orbital
OFET	Organic field effect transistor
OLED	Organic light emitting diode
P3HT	Poly(3-hexylthiophene-2,5-diyl)
$PC_{61}BM$	(6,6)-phenyl C_{61}-butyric acid methyl ester
$PC_{71}BM$	(6,6)-phenyl C71 butyric acid methyl ester
PCDTBT	Poly[N-9'-heptadecanyl-2,7-carbazole-alt-5,5-(4',7'-di-2-thienyl-2',1',3'-benzothiadiazole)]
PEDOT:PSS	Poly(3,4-ethylenedioxythiophene):poly(4-styrenesulfonic) acid
PL	Photoluminescence
PV	Photovoltaic
SMU	Source measure unit
UV-Vis-NIR	Ultraviolet- Visible- Near Infrared
VB	Valence band
VOPcPhO	Vanadyl 2,9,16,23-tetraphenoxy-29H,31H-phthalocyanine

CHAPTER 1 : INTRODUCTION

1.1 Introduction

Earth is the most suitable place for living things to stay alive, grow and reproduce. To sustain the continuity of these processes, the solar energy, which come from the sun, is very important for stabilizing the atmospheric weather and the plants to grow as food. With the passage of time, living trends have evolved and so have the inventions used for the pursuit of survival. During the past century, man has learned to use different types of energy resources besides the sun such as fossil fuel (coal, natural gas, and petroleum) that could power up heavy machinery. At the moment fossil fuels, which are non-renewable energy resources, are sufficient enough to get huge machines operated, but as they are being utilized all over the world, these reservoirs will soon run out and the world will face a serious issue of energy crisis. The seek of alternative energy that can be renewed, environmental friendly and cost effective has become a dire need of the present era. Due to these reasons, wind power, hydropower, solar power, biomass, biofuel, and geothermal technology have emerged as renewable energy to generate electric power. Amongst all these resources, solar energy is the most versatile power generator that can be harnessed by photovoltaic system which is non-polluting, lightweight, affordable, low maintenance requirement, long lasting and not necessarily localized. The amount of electricity generated from solar energy could be sufficient enough for the use of large populated areas including rural, developed, and urban regions. **Figure 1.1** shows the human development index (HDI) versus per capita kWh electricity use (*Source: Human Development Index – 2010 data United Nations; Annual Per Capita Electricity Consumption (kWh) - 2007 data World Bank*). The Human Development Index is a comparative measure of life expectancy, literacy, education and living standards. Countries fall into four broad categories based on their HDI: very high, high, medium, and low human development.

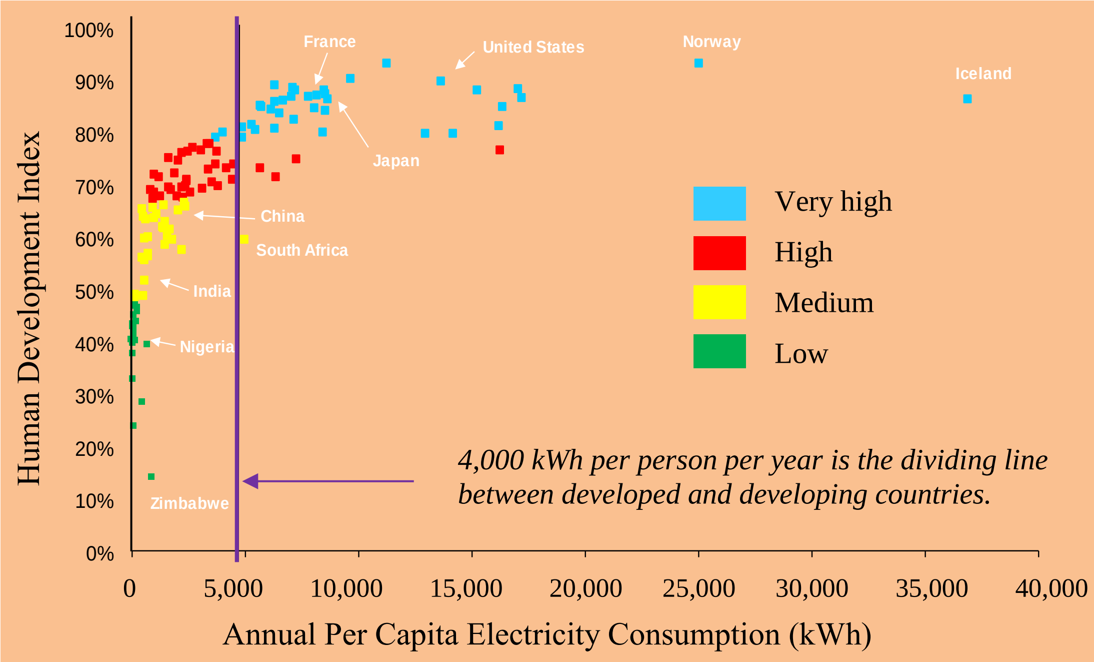

Figure 1.1 A correlation between Human Development and Per Capita Electricity Consumption.

Nowadays, human beings have turned their interest back to the nature for generating energy (i.e.from the sun) to improve the quality of life. In future, life is expected to be much more dependent on electric power.

1.2 Motivation

Photovoltaic (PV) system has been widely used to generate electric power from abundant source of solar energy. This energy has been extracted from a series of PV cells known as PV module which is normally assembled to form a PV panel. Most of the commercial PV cells that are used to power up electrical appliances are the first generation solar cells in which the cells are made up of semiconducting crytalline silicon (c-Si) wafer. This type of PV cell is suitable for installation on the rooftop since it has demonstrated a performance of 15-20 % efficiency with quite high stability. However, the fabrication of this PV cell require a lot of materials and a large amount of energy, which leads to high production cost. Moreover, in a hot sunny day, its efficiency would also drop due to high temperature resulting in the deficiency of charge transport. Later, the second generation PV or thin-film solar cells, such as amorphous silicon, cadmium telluride (CdTe), and copper indium gallium diselenide (CIGS) have been introduced in order to encounter these issues. It is lighter and physically flexible as compared to the previous types of PV cells. The cost of fabrication has been reduced since it requires less material and is capable of generating high efficiency ~20 % (as recorded in the laboratory). This type of PV system, however, becomes more difficult to be produced in mass quantity due to its high processing cost since it has to be fabricated in vacuum environment. As production cost is a prime concern, the commercialization of this PV module can only be possible for small scale production which can be found in small electronic devices such as calculator, toys, key chains etc. The obstacles for both first and second generation PVs came from the concern on how to manage silicon wafer during its preparation, device fabrication and large scale production. Moreover, it involves a lot of energy consumption, expensive materials and complex fabrication processes.

Recently, the emergence of organic electronics has captured broad attention especially those who are working in the field of research and industry as it has shown a promising potential for sensing, display and energy harvesting applications. Organic materials have shown tailoring capability in which their original properties can be tuned and made comparable to most crystalline materials. By having relatively high mobility, improved stability, and various physical colours (including high transparency as recorded in the laboratory), organic devices have appeared to be a future competitor for the previous inorganic semiconductor technology (based on Si, GaAs, InP and GaP). The third generation of solar cells has also emerged from the newly technology in which the tunable organic semiconducting materials are used as an alternate option for the expensive crystalline semiconductor wafer. It has the advantage of cheap fabrication process that can be done in ambient condition which is a promising route towards the low cost production in large scale. It also offers several more advantages including light weight, extra flexibility, ease of fabrication process, mass production, enviromental friendly and can be recycled easily. **Figure 1.2** shows a comparison of some parameters such as energy production, and payback time for three different types of PV cells (Roes et al., 2009). It can be observed that the flexible OPV has the smallest energy consumption for module manufacturing, lowest CO$_2$ emissions, and shortest energy payback time.

Technology	Energy for production (MJ.Wp^{-1})	CO$_2$ footprint (gr.CO$_2$-eq.Wp^{-1})	Energy payback time (years)
c-Si *1st generation PV*	24.9	1293	1.95
CdTe *2nd generation PV*	9.5	542	0.75
CIGS *2nd generation PV*	34.6	2231	2.71
Flexible OPV *3rd generation PV*	2.4	132	0.19

Figure 1.2 A comparison of energy production, and payback time for three different types of PV generation.

As OPV is still a new technology of harnessing solar energy, the performance efficiency is quite low due to low mobility and poor stability for practical application. Generally, PV cells operate on the principle of absorption of light, generation of charge carriers, separation of charge carriers, and the collection of charge carriers at respective electrodes to convert light into electricity. The OPV conduction mechanism is governed by carriers hopping which depends upon the energy gap between HOMO and LUMO levels, while the traditional crystalline PV conduction mechanism occurs by the principle of carrier drift due to electric fields, and charge diffusion flow due to density gradients. The mobility of charge carriers in OPV is much lower than that of crystalline PV due to the fundamental nature of transport properties, which leads to the lesser efficiency of OPV. It is believed that the performance of OPV can be improved by overcoming this constraint through the study of charge carrier behavior in a real OPV device. The aim to improve and enhance OPV performance through the fundamental understanding of charge transport mechanism has become the main motivation of this work.

1.3 Organic Solar Cells

Organic materials can be small molecules or polymers that are made of carbon atoms linked by alternating single and double bonds called π (pi) conjugation. The pi electrons from this conjugation bring unique electrical and optical properties for each organic material. Generally, organic materials have two species of charge carriers known as electrons and holes. Electron is a physical particle that carries negative charge, while hole is a theoritical concept that represent the absence of this negative-mass electron and carries positive charge. Even though both carriers are present in most organic compounds, each material has the tendency to have a specific majority carrier and can be classified as electron donor or acceptor material depending on which carrier is dominant. The combination of both materials are very important in order to ensure a balance of total carriers for the fabrication of organic solar cells (OSCs). The efficiency of OSC happens to change due to the charge transport behavior of a material used as an active light absorber. Generally, the increase in efficiency is contributed from the generation of photocurrent during the conversion of light into an electrical current. Besides, the carriers conduction mechanism, the active light absorbing layer plays an important role in controlling the OSC device performance such as the efficiency and stability. In this study, selected semiconducting organic materials are chosen on the basis of their opto-electronic properties and are characterized for charge carrier transport in organic solar cell devices. These materials are the derivatives of small molecular materials (such as phthalocyanines & fullerenes) and polymers (such as poly-thiophenes & carbazoles). **Figure 1.3** shows a structure of an OSC which consists of an active organic/polymer layer that involves generatation of photo-current in the presence of light.

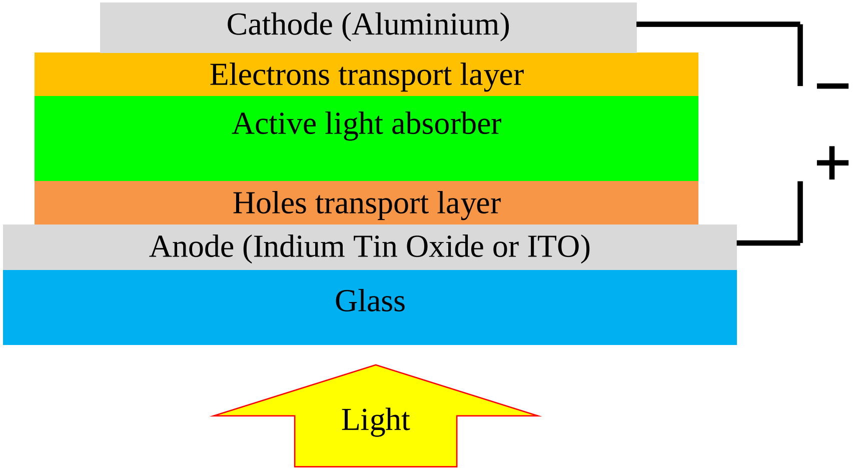

Figure 1.3 A structure of organic solar cell.

1.4 Historical Background

Solar energy is an abundant power source in which its availability is considered to be unlimited and free forever. After the sun was born around 4.57 billion years ago, it has another 6.43 billion years of its lifetime to shine the world before it turns to white dwarf at its end. It means that the Earth will receive this energy until the day it is estimated to end between 1.75 and 3.25 billion years from present (Rushby et al., 2013). However, the realization of light for the production of electricity has been made in less than 200 years ago. It was earlier observed to be utilized for photocurrent generation from the discovery of Alexandre Edmond Becquerel on photovoltaic effect in 1836. In his study, the light is shone onto the platinum electrode that is placed in aqueous solution containing silver chloride to generate voltage and current. Thereafter, in 1873 Willoughby Smith has discovered the increase in selenium conductivity upon the exposure of strong light while testing underwater cable and it explained photoconductivity phenomena as the effect of light on selenium during the passage of electric current (Smith, 1873). Through further investigation of selenium photoconductivity, W. G. Adams and R. E. Day, in 1876, have demonstrated that the electricity can be produced by illuminating the junction between selenium and platinum, which suggests that the solid material like selenium can generate electricity without heat or mechanical movements (Adams & Day, 1877). This work has led to a modern photovoltaic cell especially when the first solid state solar cell was fabricated from selenium that was coated with ultra-thin layer of gold in 1883 by Charles Fritts with the efficiency around 1 %. In 1887, Heinrich Hertz has discovered photoelectric effect when he observed a spark produced from a charged object upon the exposure of ultraviolet light. In the following years, Aleksandr Stoletov built the first cell based on the photoelectric effect, previously discovered by Hertz, but the physical mechanism behind this phenomenon was explained by Albert Einstein in 1905 in his paper in which he discussed the exchange of energy in discrete amounts of light packets called quanta which were later known as photons. Both photovoltaic and photoelectric effect sound to have a similar mechanism but actually it can be differentiated by the electrons settlement after receiving energy from the photons. In photovoltaic effect, an electron is excited to another energy state which is higher than its original state, while in photoelectric effect, an electron is ejected from the highest occupied stated to the vacuum level which is away from the material's conduction band.

The study on the photoconductivity of organic material was performed by Pochettino in 1906, and is marked as the beginnig of the field of organic electronics. Several studies were carried out on other organic materials, having different chemical groups, by many researchers such as Koenigsberger who studied the conductivity of benzene derivatives, Hoegel studied a cell with poly(N-vinyl carbazole) or PVK, while Kearns and Calvin worked on magnesium phthalocyanines. Initially, Pochettino had observed the photoconductivity in a solid organic material, anthracene, when it was exposed to the electromagnetic radiation. In 1913, the same phenomenon had been re-addressed by Volmer in his work on crystalline anthracene. There has been no further study on the same material for several decades after Pochettino and Volmer work until 1950s. Later in 1959, Kallman and Pope had made the first solar cell device from anthracene that produced a very low efficiency of about 0.1 %. Kearns had suggested that oxygen at the crystal surface of anthracene has assisted exciton dissociation which contributed to its photoconductivity. Until now, investigations on the material have been made on its derivatives or subsitutions but the efficiency is still low in the range of 1-2 %.

Afterwards, the study of solar cells based on small molecule has been carried out by Kearns and Calvin, in 1958, who built a cell containing magnesium phthalocyanines (MgPc) between two glass electrodes and obtained 200 mV photovoltage.

Phthalocyanines (Pcs) are actually macrocylic compound which are widely known as dye and pigment materials that readily form complexes with a number of metal ions. Pc compounds have bright colours depending on the metal complex they carry. In 1964, Delacote had observed a rectifying effect from copper phthalocyanines (CuPc) that was placed between two different metals electrodes. Further investigation on MgPc, made by Federov and Benderskii, demonstrated that the PV effect from MgPc was dependent on the presence of oxygen (Spanggaard & Krebs, 2004). In 1975, Tang and Albrecht studied a single layer cell based on chlorophyll-a film and the efficiency obtained from the cell only reached up to 0.01 %. Tang has made a major breakthrough in the cell performance by the fabrication of bi-layer cell containing electron donor and acceptor components. He has shown an increase in the cell efficiency by 100 order of magnitude, obtained using two different small molecules Pc and perylene derivatives (Tang, 1986).

Later on, the study on conductive polymer, which led to the use of polymeric materials in solar cells fabrication, was conducted by Hoegel, in 1956, who work on poly(vinyl carbazole) or PVK proposed its practical use as an electrophotographic agent. In the 1970s, it was discovered that the conjugated polymers such as poly(sulphur nitride) and polyacetylene could be doped by selected dopant in order to increase the conductivity. Weinberger has reported, in 1982, that polyacetylene has attained open-circuit voltage of about 0.3 V from Al/polyacetylene/graphite cell device. The studies on polythiophenes were started by Glenis who obtained open-circuit voltage around 0.4 V. Further improvement in the cell efficiency had been attempted with different electrodes but the cell suffered the same issue of low efficiency. Karg, in 1993, investigated PPV for both light emitting diode (LED) and solar cell and obtained V_{OC} of 1 V and a power consersion efficiency (PCE) of 0.1 % under white light illumination. At the same time, Sariciftci et. al demostrated the impact of fullerene (C_{60}), as an electron accepting component, in active cell layer with his study on MEH-PPV:C_{60}

heterojunction solar cell. Fullurene seemed to assist charge separation which resulted in more than 20-fold increase of the photocurrent (Sariciftci et al., 1992). In 1994, Yu made the first bulk heterojunction by combining MEH-PPV with C_{60} in 10:1 wt% ratio and obtained the photosensitivity ~5.5 mA/W which is 10 times higher than that of pure polymer. Yu's bulk heterojunction approach required soluble materials for spin coating technique but it faced a performance limitation due to low solubility of C_{60} in organic solvents. However, in 1995, Hummelen resolved this issue by synthesizing numbers of C_{60} derivatives for better solubility (Hummelen et al., 1995). Once again, Yu used soluble C_{60} derivative in polymer/fullerene solar cell fabrication and enhanced the quantum efficiency (QE) and PCE to 29 % and 2.9 %, respectively. He set a landmark in the history by fabricating polymer/polymer bulk heterojunction solar cells based on electron donor/acceptor blend system using cyno-PPV as an acceptor and MEH-PPV as a donor component (Yu & Heeger, 1995). In 2003, Brabec used a blend system, consisting of poly(3-hexylthiophene)/methanofullerenes or P3HT:PCBM, in bulk heterojunction organic solar cells and attained a QE of about 76 % (Schilinsky et al., 2004). Since then, rigorous studies on the P3HT:PCBM blend system have been performed to enhance organic solar cell performance by using PEDOT:PSS hole transport. Further improvement in the cell structure and charge transport properties enhanced the efficiency of P3HT:PCBM based solar cells up to 5 %, as reported (Ma, 2005). While in 2007, Kim achieved efficiencies of about 6 % upon controlling the nanoscale morphology of P3HT/$PC_{61}BM$ active layer (J. Y. Kim et al., 2007). The realization to use more effective materials for higher efficiency solar cells, especially polymers, has accelerated the efforts to produce new materials with better optical and electrical properties and surpass the limitations of P3HT:PCBM solar cells. In 2009, the use of another blend system based on PCDTBT:$PC_{71}BM$ has made the OSCs to achieve 6.1 % efficiency. It was claimed that the internal quantum efficiency (IQE) for such solar cell approached 100 % where every absorbed photon led to the separated pair of charge carriers and all photogenerated carriers were collected at the electrodes (S. H. Park et al., 2009). Later in 2012, Moon et al. achieved 6.9 % efficiency from the solar cells consisting of the same blend system. They discovered that the mass density variations of PCDTBT:PCBM blend are laterally oriented and could cause reduction in both fill factor (FF) and IQE as a function of layer thickness (Moon, Jo, & Heeger, 2012). In 2015, the efficiency of solar cells based on the same blend system, was further increased up to 7.12 % by another research group (Seok et al., 2015). Such efficiency was obtained by sequentially depositing bilayer (SD-bilayer) via solution processing method (Seok et al., 2015). Recently, the efficiency of the organic solar cells has been increased by improving its geometrical structure such as inverted arrangement and tandem structure. More than 10 % of efficiency has been obtained by using multiple layers of active materials which efficiently convert most of incident photons to photocurrent and generate higher open circuit voltage (C.-C. Chen et al., 2014).

Table 1.1 Organic solar cells development history

Year	Important milestone in the development of organic solar cells	References
1836	Becquerel discovered the photovoltaic effect from electrolytic cell contaning silver chloride	(Becquerel, 1839)
1873	W. Smith has discovered the increase of selenium conductivity with the expose of strong light	(Smith, 1873)
1876	W. G. Adams & R. E. Day demonstration of electricity production from illuminated selenium-platinum junction without heat or moving parts	(Adams & Day, 1877)
1883	First solar cells module was built from the selenium that has been coated with ultra-thin layer of gold by Charles Fritts	(Fritts, 1883)
1906	Pochettino studied the photoconductivity of anthracene	(Pochettino, 1906)
1910	Koenigsberger study the conductivity of benzene derivatives upon applying electric field	(Koenigsberger & Steubing, 1910)
1953	H. Mette futher study on anthracene conductivity	(Mette & Pick, 1953)
1957	H. Hoegel built polymer cell based on poly(N-vinyl carbazole) or PVK	(Hoegl, 1965)
1958	Kearns and Calvin worked on small molecule or magnesium phthalocyanines (MgPc), measuring a photovoltage of 200 mV	(Kearns & Calvin, 1958)
1959	H. Kallmann solar cells based on anthracene achieved ~0.1 % efficiency	(Kallmann & Pope, 1959)
1960	O. H. Le Blanc further investigate anthracene cell, while R. G. Kepler studied anthracene crystals	(Kepler, 1960)
1962	P. Mark investigated cell containing p-terphenyl, p-quaterphenyl, and anthracene	(Mark & Helfrich, 1962)
1964	Delacote observed a rectifying effect when copper phthalocyanines (CuPc) was placed between two different metal electrodes	(Delacote, Fillard, & Marco, 1964)
1966	N. Geacintov investigated tetracene-water cell	(Geacintov, Pope, & Kallmann, 1966)
1986	Tang fabricated the first bulk heterojunction (BHJ)-based solar cell with 1 % efficiency	(Tang, 1986)
1990	B. A. Gregg built a cell with liquid crystalline porphyrins and obtained $V_{OC} = 0.3$ V	(Gregg, Fox, & Bard, 1990)
1991	Hiramoto made the first dye/dye bulk heterojunction PV by co-sublimation	(Hiramoto, Fukusumi, & Yokoyama, 1991)
1992	N. S. Sariciftci fabricate bi-layer polymer/fullerene solar cell based on MEH-PPV:C60	(Sariciftci et al., 1992)
1994	Yu made the first bulk polymer/C60 heterojunction organic solar cell	(Yu, Pakbaz, & Heeger, 1994)
1995	Yu repeated the fabrication with soluble fullerene derivative MEH-PPV : $PC_{61}BM$ and achieved 2.9 %	(Yu et al., 1995)

2000	Peeters and Van Hal used oligomer-C60 dyads/triads as the active material in PV cells.	(Peeters et al., 2000)
2001	Schmidt-Mende made a self-organised liquid crystalline solar cell of hexabenzocoronene and perylene and Ramos used double-cable polymers in organic solar cells.	(Schmidt-Mende et al., 2001)
2001	Shaheen obtained 2.5 % conversion efficiency of organic photovoltaic	(Shaheen, Brabec, & Sariciftci, 2001)
2003	Brabec who the first used P3HT:PC$_{61}$BM blend in solar cells study	(Schilinsky, Waldauf, & Brabec, 2002)
2005	Li reported 4.4 % efficient P3HT/PC$_{61}$BM based OSC by controlling the active layer growth rate.	(G. Li et al., 2005)
2005	Ma made devices with blend of P3HT/PC$_{61}$BM with efficiencies of up to 5 %	(Ma et al., 2005)
2007	Peet et al. used PCPDTBT/PC$_{71}$BM to achieve power conversion efficiency of 5.5 %.	(Peet et al., 2007)
2007	Kim with PCPDTBT : PC$_{61}$BM, P3HT : PC$_{71}$BM (Tandem) solar cell gained 6.5 %	(J. Y. Kim et al., 2007)
2009	S. H. Park has achieved 6.1% from PCDTBT:PC$_{71}$BM solar cell	(S. H. Park et al., 2009)
2009	Liang et al. made devices based on fluorinated PTB4/PC$_{61}$BM films fabricated from mixed solvents and achieved efficiency over 6 %.	(Liang et al., 2009)
2009	Chen’s PBDTTT-CF : PC$_{71}$BM OSCs achieved 7.73 % Efficiency	(H.-Y. Chen et al., 2009)
2010	Liang’s PTB7 : PC$_{71}$BM OSCs gained 7.4 % efficiency	(Liang et al., 2010)
2011	Chu et al. used Thieno[3,4-c]pyrrole-4,6-dione and Dithieno[3,2-b:20,30-d]silole copolymer to obtain power conversion efficiency of about 7.3 %	(Chu et al., 2011)
2012	He’s PTB7 : PC$_{71}$BM (Inverted OSCs) gained 9.2 %	(He et al., 2012)
2012	Moon’s PCDTBT : PC$_{71}$BM OSCs gained 6.9 %	(Moon et al., 2012)
2012	Dou’s P3HT : ICBA, PBDTT-DPP : PC$_{71}$BM (Tandem OSCs) achieved 8.62 % efficiency	(Dou et al., 2012)
2013	W. Li fabricated DT-PDPP2T-TT : PC$_{71}$BM OSCs and achieved 6.9 % efficiency	(W. Li, K. H. Hendriks, et al., 2013)
2013	Zhang’s PBDTP-DTBT : PC$_{71}$BM OSCs achieved 8.07 % efficiency	(M. Zhang et al., 2013)
2013	Li’s PCDTBT : PC$_{71}$BM, PMDPP3T : PC$_{61}$BM, PMDPP3T : PC$_{61}$BM (Triple Junction OSCs) achieved 9.64 % efficiency	(W. Li, A. Furlan, et al., 2013)
2013	You’s P3HT : ICBA/PDTP-DFBT : PC$_{61}$BM (Tandem OSCs) gained 10.6 % efficiency	(You et al., 2013)
2014	Woo’s ZnO/PEI/PTB7 : PC$_{71}$BM (Inverted OSCs) gained 8.9 % efficiency	(Woo et al., 2014)

1.5 Objectives

The objective of the thesis is to study charge transport behavior in OSC based on organic small molecules (phthalocyanine and fullerene derivatives) and polymers (thiophene and carbazole derivatives), thereby, aiming to acquire a deep insight of the fundamental knowledge on charge carriers dynamics in order to improve existing device performance for commercial applications. Initially, the fundamental study is conducted by means of several characterization techniques related to the extraction of electrical parameters that control device performance. Secondly, detailed investigations on organic solar cell devices have been performed for their possible route towards commercialization. The objectives of this research work can be summarized as follows:

i. To characterize the physical properties which include optical, morphological, and electrical properties of organic small molecules (phthalocyanine and fullerene derivatives) and polymers (thiophene and carbazole derivatives) prior to the fabrication of OSC.

ii. To fabricate the bulk heterojunction OSCs by incorporating the blend of organic molecular and polymeric materials based on donor/acceptor system (including P3HT:VOPcPhO and PCDTBT:$PC_{71}BM$) through solution processing techniques under optimized parameters.

iii. To study of the charge carrier dynamics in OSC by means of current-voltage (I-V) characteristic, dark injection method, time-of-light (ToF), transfer & saturation characteristics, and electric field induced second harmonic generation (EFISHG).

iv. To enhance the performance of organic device in order to meet its practical usability for light sensing and solar energy harnessing applications by improving efficiency and stability of the fabricated devices.

1.6 Thesis Outline

In chapter one, a brief introduction of the importance of renewable energy is addressed by stating several drawbacks of traditional fossil fuel and focussing more on harnessing solar energy for current and future advantages. Then, several key motivations that inspired this work to be done are inscribed by comparing the improvement of solar cell development from generation-to-generation until the emergence of versatile organic solar cells. This chapter also includes an overview of organic solar cells and their historical development. It is followed by the aim and objectives of the thesis where the understanding of charge transport dymanics in OSC becomes the main concern to improve OSC performance for practical application.

In chapter two, the underlying physical concept and working principle of OSC are explained in detail. Here, the role of charge transport that is responsible for determining the efficiency of OSC, is also highlighted. Afterwards, a review has been given on the approaches towards OSC enhancement especially for practical use in sensing and energy harvesting applications.

Chapter three covers selection of materials used for the charge carriers study, experimental procedures for device fabrication, and brief explanation of thin film characterization techniques. Two types of devices were proposed to be fabricated for the electrical characterizations; photodiode and transistor, which involve both steady state and transient measurements in device physics. The study of charge carrier behaviour have been performed by the current-voltage (I-V) characteristic, OFET transfer characteristics, and electric field induced second harmonic generation (EFISHG).

Chapter four describes properties of the materials used and charge transport dynamics, while chapter five discusses the results obtained from experimental work and enhancement of organic device for practical applications. Both chapters (four and five) are divided into two main parts by different donor/acceptor blend systems used in this study. The first part consists of fabrication of OSC based on the blend of P3HT and VOPcPhO, while the second part comprises fabrication of OSC based on PCDTBT and $PC_{71}BM$. The work was originally started with the first blend system (VOPcPhO:P3HT) for the investigation of VOPcPhO (known as donor) to hold a role as an acceptor component in the blend system for OSC fabrication. The second blend system of PCDTBT and $PC_{71}BM$ was employed to further investigate the underlying physical phenomena of charge carrier transport in OSC for improved performance. Finally, chapter six highlights the achieved conclusions for the overall study in the thesis and suggests several ideas for enhancement in the performance of OSCs in the future studies.

CHAPTER 2 : LITERATURE REVIEW

2.1 Semiconductor Materials

A semiconductor is a material that has intermediate conductivity between a conductor and an insulator i.e. its electrical conduction is less than a conductor but more than that of an insulator. Normally, a semiconductor starts to conduct electrical current under certain value of applied electric field, E (or voltage, V) which is called a threshold voltage (V_{th}), or under certain value of temperature where the charge carriers receive sufficient energy for conduction. The conduction mechanism occurrs in the semiconductoras long as it receives a sufficient amount of energy and leads to the formation of free (delocalized) charge carriers (electrons and holes). These energies are not only limited to the specific forms such as temperature and external applied voltage for free charge carrier generation but they also occur in the form of light especially in photovoltaic devices. The radiation of light always brings along some amount of energy that could add sufficient energy to release charge carriers to be ‘free’ and delocalized. Most of the common semiconducting materials are made of silicon wafers doped with electrons rich dopants or holes rich dopants and are known as n-type and p-type, respectively. Both types of semiconductor are really popular for their use in commercial photovoltaic system and can be easily found on the rooftop, road, and selected areas for the energy harvesting purposes. Recently, different organic compounds and polymers have shown interesting features similar to inorganic semiconducting material but in a different manner of conduction mechanism. Extensive research has been conducted to make these materials competitive with existing silicon semiconductors. As a result, organic semiconducting materials have caught global attention as they have shown remarkable advantages, namely light weight, high flexibility, lower material cost, ease of fabrication and environmental friendly, for future technological applications. The comparison of both types of semiconductors will be discussed in the following sections.

2.1.1 Inorganic Silicon Semiconductors

Inorganic semiconductors based on silicon (Si), gallium arsenide (GaAs), indium phosphide (InP), and gallium phosphide (GaP) have been well known their usage in present applications especially in transistors, light emitting diodes (LED) and photovoltaics. These materials have very high carrier mobility. Basically, the crystalline inorganic semiconductors are made of three dimensional crystal lattice in which their lower unoccupied molecular orbitals (LUMOs) and higher occupied molecular orbitals (HOMOs) have strong intermolecular forces that allow the formation of conduction band (CB) and valence band (VB) throughout the material. Inorganic semiconductors possess free or delocalized carriers due to the contribution of extrinsic dopant. These carriers lead to the flow of current in the presence of an external applied electric field. Under such conditions, the transport mechanism of charge carriers, in the inorganic semiconductor, is simply known as carrier drift. While the carriers transport that is caused by thermal energy is known as carrier diffusion. Both drift and diffusion currents produced by these carriers contribute to the total current in the material. **Figure 2.1** shows lattice structure of inorganic semiconductor with dopant components that make n-type or p-type semiconductor (www.pveducation.org/pvcdrom/pn-junction/doping). While **Figure 2.2** shows the charge transport mechanism in junction diode (en.wikipedia.org/wiki/Depletion_region).

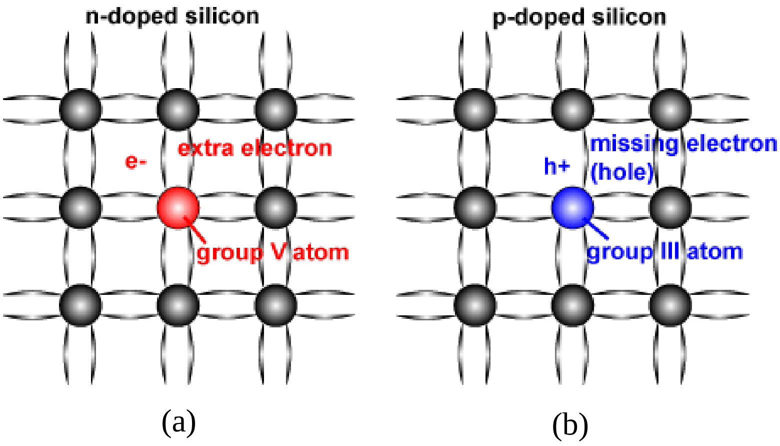

Figure 2.1 The lattice structure of inorganic semiconductor with a dopant component as (a) n-type, and (b) p-type.

The applied electric field, ε (or E), will cause the carriers to accelerate but in the presence of impurities and lattice vibrations, the inter-collisions happen to dominate the transport of carriers and result in a constant average velocity, v. The ratio of the carrier velocity to the applied field is also known as the carrier mobility.

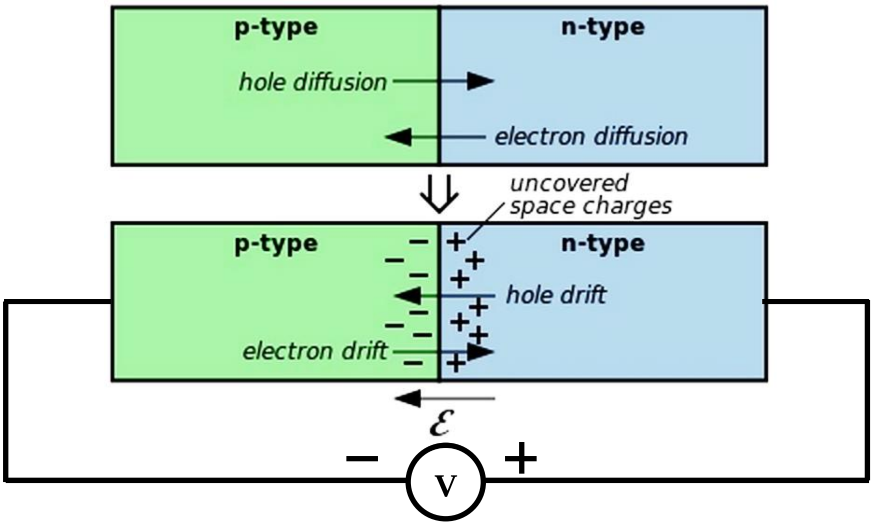

Figure 2.2 A charge transport mechanism in an inorganic semiconductor diode.

2.1.2 Solution Processable Organic Semiconductors

Solution processable devices, such as sensors and photovoltaic devices, are basically made of materials that can be conveniently dissolved in common organic solvent. These materials can either be small molecular or polymeric materials that have favorable interaction with particular solvent which ensures their degree of solubility. These organic materials are made up of carbon atoms which are linked by alternating single and double bond, known as pi (π) conjugation. A π-conjugated system gives unique optical and semiconducting properties as it has delocalized electrons transporting along its backbone structure. This system contains connected π-orbital of delocalized electrons in alternating single and multiple carbon-carbon (C-C) bond configuration.

Basically, in any molecule, a molecular orbital is a probable region for finding a wave like behavior of a single electron. The term orbital was introduced by Robert S. Mulliken as an abbreviation for one-electron orbital wave function. There are several types of interactions between these atomic orbitals that can be categorized by their symmetric labels such as σ (sigma), π (pi), δ (delta), φ (phi) and γ (gamma). But in the case of conjugation system, π-orbital interactions form covalent π-bonds to allow delocalization of electrons within the molecule. Normally, the electronic states of organic semiconductors are localized and disordered. The localization of photo-excited states and charges lead to low carrier mobility, while the molecular packing and conjugated units are disordered and vary in energy. **Figure 2.3** shows the example of π-orbital of benzene molecule and delocalized electron distribution (en.wikipedia.org/wiki/Conjugated_system). While **Figure 2.4** shows some small molecular and polymeric materials with semiconducting properties and sensitivity towards light.

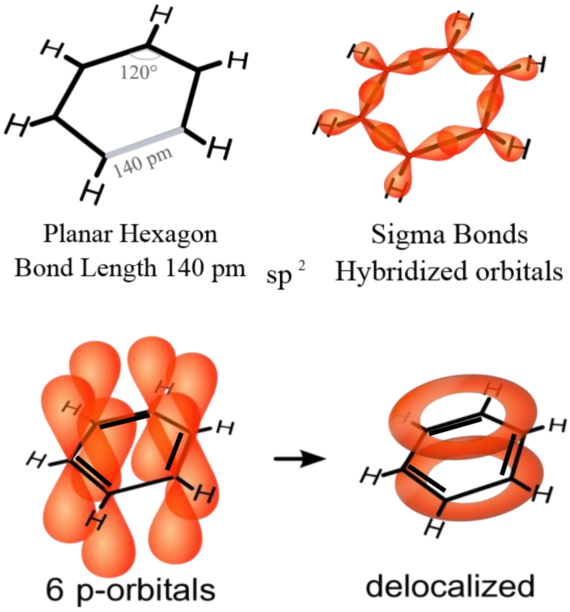

Figure 2.3 A π-orbital of conjugated system in benzene ring.

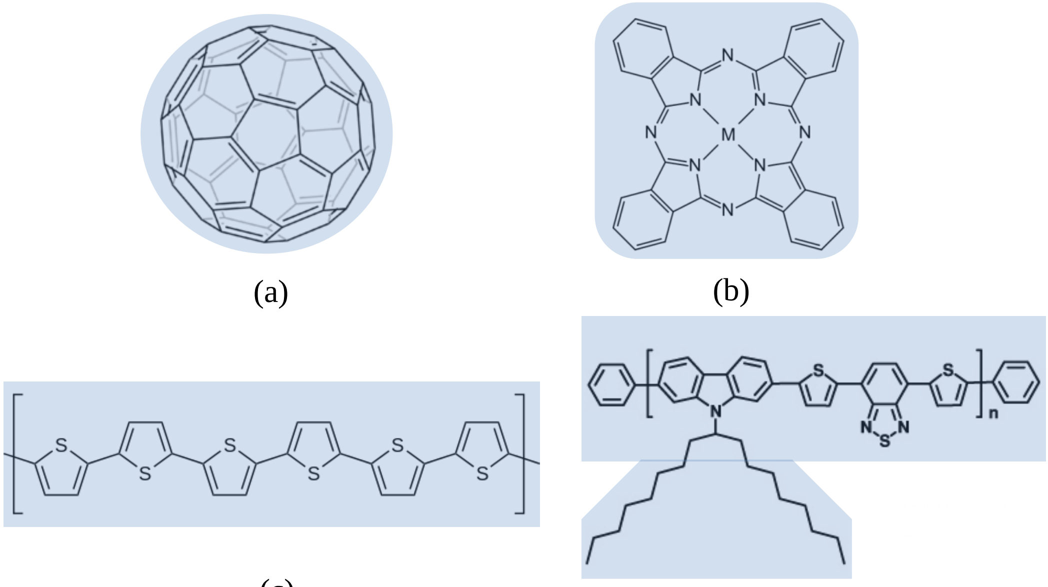

(a)

(b)

(c)

(d)

Figure 2.4 Conjugated molecule: (a) fullerene, and (b) phthalocyanine as electron acceptor, while conjugated polymer: (c) polythiophene, and (d) carbazole derivative as electron donor materials.

2.2 Physics of Organic Solar Cells

So far, OSCs exist in several types of structure i.e. bi-layer, bulk heterojunction, inverted and tandem structures. They vary from one another on the basis of improvement in terms of efficiency and stability. Bi-layer solar cells consist of donor and acceptor components which are deposited separately to form a junction similar to a p-n junction diode. The charge carrier behavior during their transport can be ascribed to this type of structure as shown in **Figure 2.5** below.

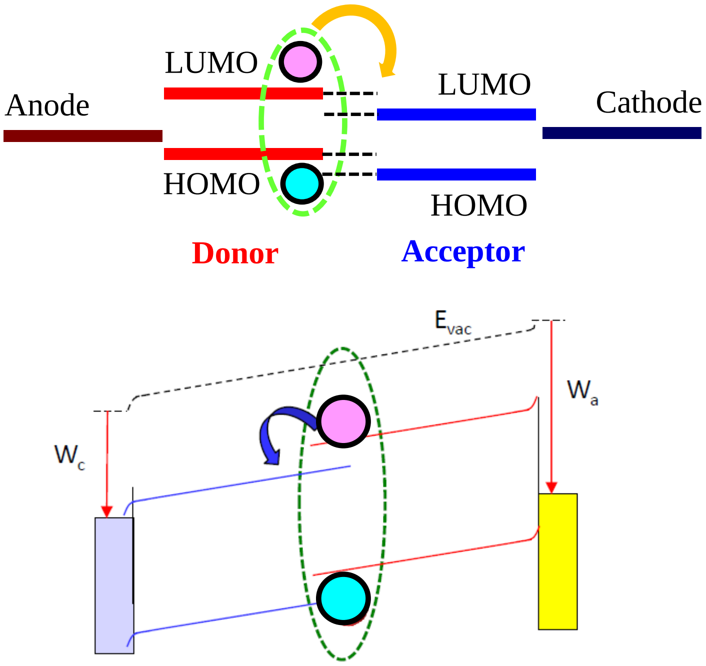

Figure 2.5 Charge transport in bi-layer organic solar cells.

Normally, donor and acceptor materials have different energy levels of LUMO and HOMO. The LUMO level is responsible for electron transport, while the HOMO level serves as a hole transport medium. For the transport of electrons, the energy levels must be aligned in such a manner that LUMO level of donor, LUMO of acceptor and the work function of cathode should appear in descending steps. As carriers in organic semiconductor are transported by hopping mechanism, the differences between theenergy levels (donor, acceptor, and electrodes) are made such that the carrier can easily hop across the junction during its transport. For more details, the working principle of OSCs will be discussed in the following sections which include photo-absorption and exciton generation, exciton diffusion, exciton dissociation, geminate charge separation, and charge transport and collection to electrodes.

2.2.1 Photo-absorption and Exciton Generation

Light illumination in the visible range consists of different wavelengths of photons at which accumulative electron-hole pairs are produced at the same time.The ability of a material to absorb photons is really important for the generation of photocurrent. Inorganic silicon-based semiconductor normally has a band gap of around 1.1 eV, which can absorb light in almost all regions, but the lowest energy that can excite charge carrier from valence band to conduction band is when the light has a wavelength equal to 1100 nm or less. In the case of organic semiconductor, the energy gap is determined by the difference between LUMO and HOMO levels. Normally, it has larger value at least 2.0 eV and requires charge carrier to have more energy in order to be excited. As the carriers receive enough energy for excitation, it will form a bound electron-hole pair known as exciton, a neutral species of charge transfer (CT) state. In this situation, the carriers are still in localized state where they are limited by the exciton diffusion length before they can be separated at the donor/acceptor interface. The photoexcitation state of charge carriers in organic semiconductor begins with the formation of localized exciton in bound state as compared to the charge carriers in silicon semiconductor which directly turn into free carriers when exposed to light. **Figure 2.6** shows the difference between inorganic and organic semiconductor photoexcitation processes.

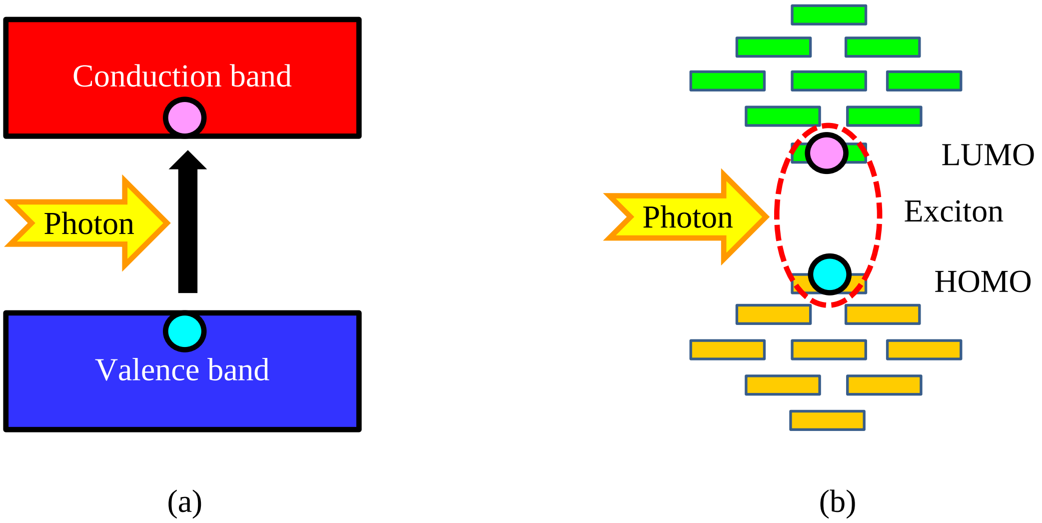

Figure 2.6 Photoexcitation in (a) inorganic, and (b) organic semiconductor.

Basically, there are two types of excitons in most of the materials which are based on their intermolecular or interatomic size; 1) Frenkel exciton, and 2) Wannier-Mott exciton. Frenkel exciton consists of an electron and a hole that are separated by a distance comparable to the atomic spacing in which the hole is localized at a position, while electron is around it within a molecular orbital. Such type of excitons normally exist in most small molecular materials and rare-gas crystals. Wannier-Mott exciton consists of an electron and a hole that are separated by the distance much larger than that of atomic spacing in which the bound electron-hole pair is not localized. This kind of excitons are normally seen in semiconductor with covalent bonding. Therefore, in organic semiconductor, the Frenkel exciton model is used to describe the photo-excitation state of electon-hole pair as the material is made of disorder molecular structures. **Figure 2.7** shows an illustration of both types of excitons.

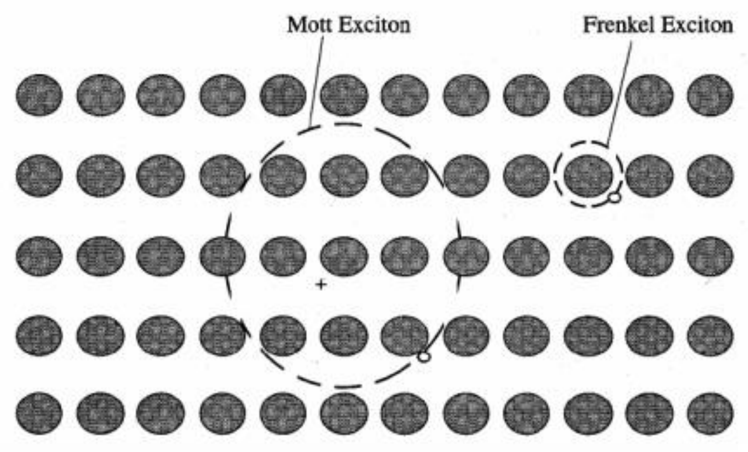

Figure 2.7 An exciton can exist in two forms as suggested by Mott and Frenkel.

In an organic solar cell, when an electron at HOMO level receives enough energy from the photon, it excites to the LUMO level and leaves behind a hole. At this stage, the electron can still not move freely within the LUMO level as the exciton is created. The process will continue to the next stage where the exciton diffused at the interface of donor/acceptor before dissociation. **Figure 2.8** shows photo-excitation in the OSCs forming a bound state of electron-hole pair.

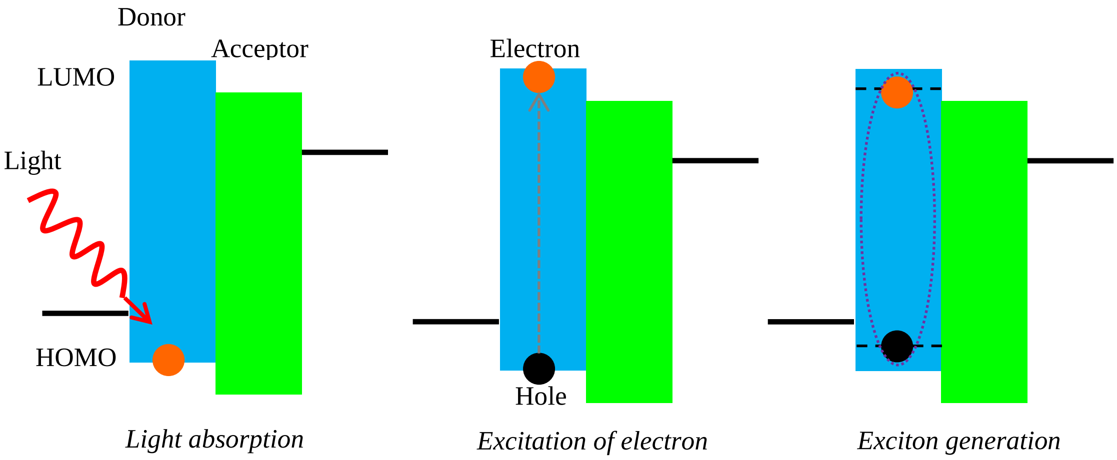

Figure 2.8 A process of photo-excitation in organic solar cells.

2.2.2 Exciton Diffusion

Once the electron-hole pairs are created, they can migrate toward donor/acceptor heterojunction interfaces over a length of approximately 5-10 nm. This migration process is called exciton diffusion process where excitation energy is transferred towards lower-energy sites. During a finite exciton lifetime, it has a limited distance of migration to the donor/acceptor interface which is known as diffusion length. It means, the exciton should be formed within the interface diffusion length in order to ensure its dissociation, otherwise, it will decay back to its ground state. **Figure 2.9** shows the diffusion of exciton towards the donor/acceptor interface after it is created by the photo-excitation process.

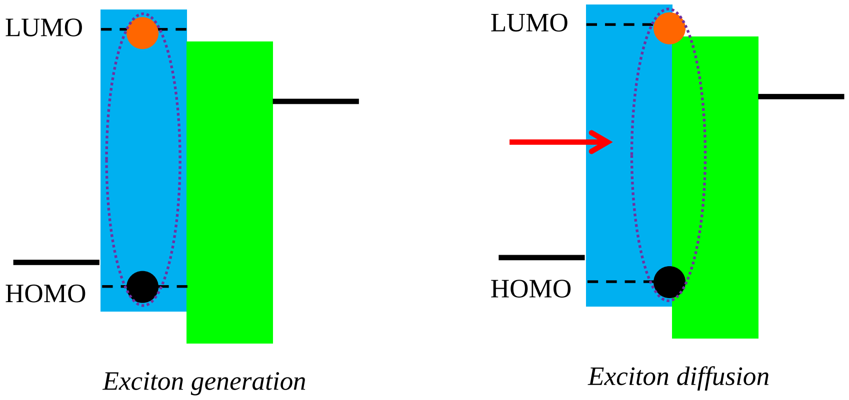

Exciton generation　　*Exciton diffusion*

Figure 2.9 Exciton diffusion process.

The above figure roughly shows the diffusion of exciton in bi-layer OSCs. In case of bulk heterojunction OSCs, the interfacial area between donor and acceptor is much bigger and the number of excitons to be potentially diffused is higher because the exciton diffusion length is reduced by composite blend systems.

2.2.3 Exciton Dissociation

Normally, photocurrent generation occurs at the junction between a donor and acceptor during the exciton dissociation process in which the charge carriers are separated and collected of at the electrodes. In silicon semiconductor, charge carrier that receives enough energy from the light, will excite and form a free carrier thus directly producing photocurrent when moving towards electrodes. In the case of organic semiconductor, the carriers that form exciton upon illumination, will dissociate into free electron and hole at donor/acceptor interface and will be collected at the respective electrodes. Thus, exciton dissociation process is really important to determine the generation of photocurrent in OSCs. However, the dissociation of exciton requires a strong acceptor component so that the electron can escape from the bound state. **Figure 2.10** shows the exciton dissociation process occuring right after the diffusion of exciton at the interface of donor/acceptor.

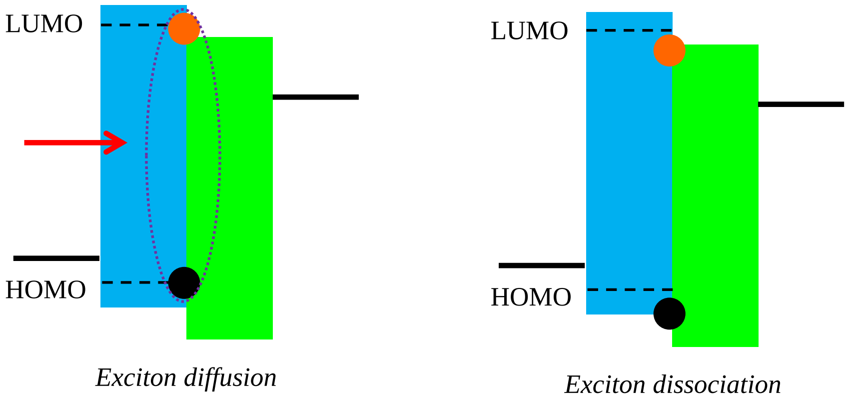

Figure 2.10 Exciton dissociation process.

2.2.4 Geminate Charge Separation

Structural properties of materials have somehow played an important role in charge separation in both crystalline inorganic semiconductor and amorphous organic semiconductor. In 3D crystalline structure of inorganic silicon semiconductor, the photon absorption produces free electrons and holes which allows delocalization of these charge carriers to have lon-range separation. For this reason, the amount of dopant (electron rich or poor element) shall be controlled to tailor semiconducting properties of a material, otherwise,a highly doped semiconductor will turn into a conductive material. In case of organic semiconductors, a disordered morphological nature of the material can be one of the reasons for the charge carrier to have a short-range separation. At the same time, organic materials normally have a small dielectric constant which make charge separation even more difficult. However, recent study has shown that organic semiconductors can also have an ultrafast long-range charge separation (Gélinas et al., 2014). It occurs atthe early time of separation when the residual Coulomb attraction between charges is at or below thermal energies to easily separate electrons and holes. The separation of charge carriers in organic materials are generally considered to occur at short-range for charge transport in continuous longer time (Peumans & Forrest, 2004). **Figure 2.11** shows the charge carrier in an inorganic semiconductor having a long-range separation within the crystal lattice, while that in organic semiconductor has a limited and short-range separation due to its disordered molecular structure.

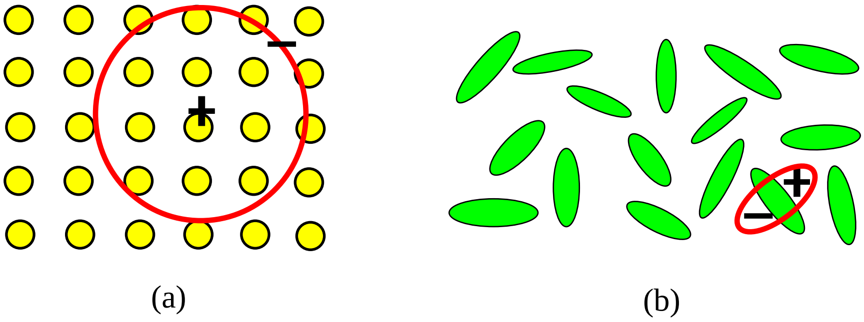

(a) (b)

Figure 2.11 Charge separation in (a) inorganic, and (b) molecular semiconductor.

In OSCs, the separation of geminate electron-hole pair occurs once it is dissociated at the interface of donor/acceptor after the diffusion process. Then, the separated charge carrier will be collected at the respective electrodes by means of the charge transport mechanism. However, there is an electrostatic attraction between the electrons and holes during the stage of exciton diffusion. In just a few nanosecond (ns) to hundreds of ns, if the charge separation distance (or mean-free-path) is not sufficient to overcome this attraction, then a geminate (or initial pair) recombination will occur before it can be separated (Pal et al., 2010). **Figure 2.12** shows charge separation process of dissociated electron and hole in OSCs.

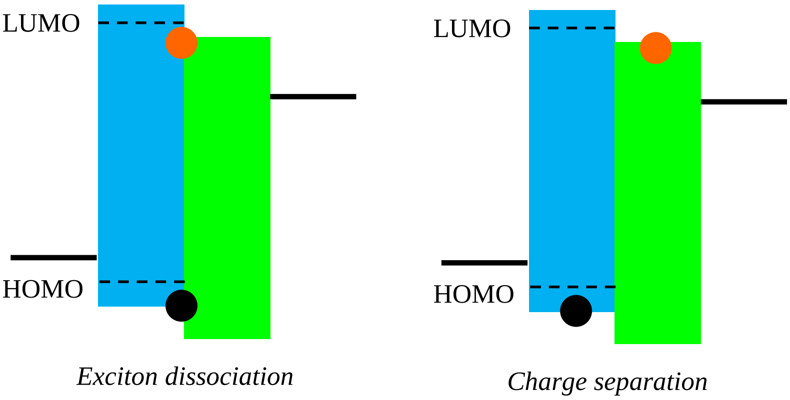

Figure 2.12 Charge separation in OSCs.

2.2.5 Charge Transport and Collection at Electrodes

Generally, crystalline inorganic semiconductor has a 3D crystal lattice and has individual LUMO and HOMO levels that are capable of forming a conduction band (CB) and a valence band (VB) throughout the material. As CB and VB are formed, the transport of charge carriers within the band is known as carrier drift, also called band transport, occurs in highly crytalline ordered materials at low temperature. While in organic semiconducting materials, 3D crystal lattices could not be formed due to weak intermolecular forces. As a mater of fact, most of the organic molecules are bound by weak Vander Waal forces which cause the material to have disordered structure. Consequently, the CB and VB cannot be formed because the molecular LUMOs and HOMOs do not have enough strong interaction. Therefore, the charge transport in organic semiconductor material will be achieved by hopping between localized molecular states (amorphous state that require high temperature). As a result, the charge carrier mobility of organic semiconducting materials is generally lowerthan that of crystalline inorganic semiconductors. **Figure 2.13** shows the transport of charge carriers in inorganic and organic semiconductors.

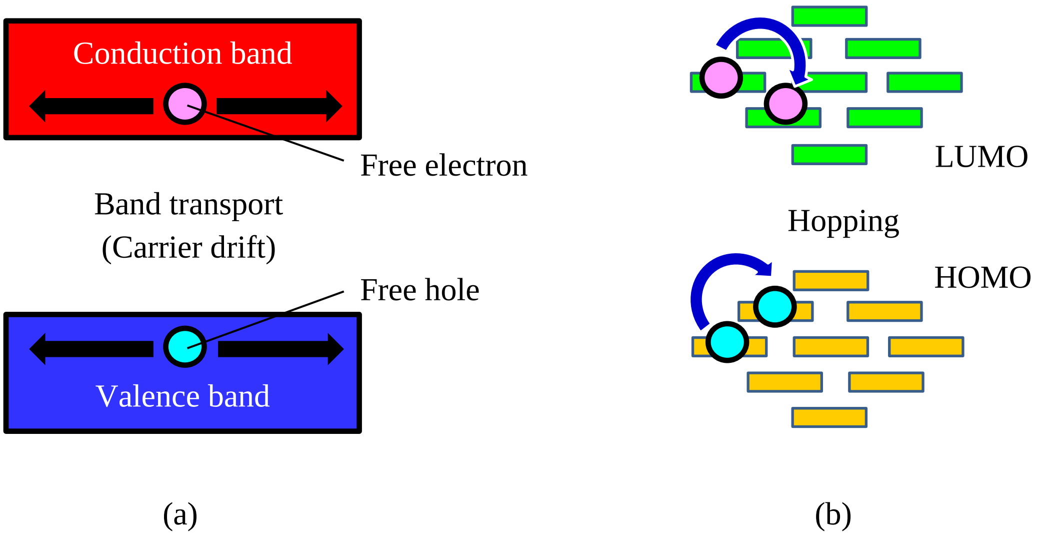

Figure 2.13 Transport mechanism in (a) inorganic, and (b) organic materials.

Figure 2.14 shows charge separation process and the transport of free charge carriers toward the electrodes. The collection of these carriers at the electrodes can be described as the final step of photo-current generation in the OSCs active layer. The separated electron-hole pair (free charge carrier) does not always continue with its collection at respective electrode. The presence of traps in disordered amorphous materials, including organic small molecular and polymeric materials, can lead to non-geminate recombination of free charge carrier even after the exciton dissociation process. The non-geminate recombination can be a serious issue for OSCs performance because the active layer, that contains donor and acceptor components, is morphologically amorphous and always provides traps for the generated free charge carrier. This recombination will reduce the amount of photocurrent generated thus lowering the efficiency of OSCs.

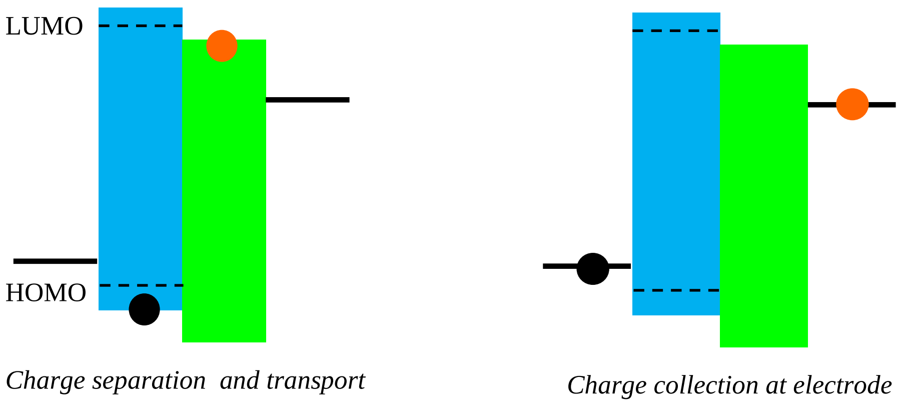

Figure 2.14 Charge collection in electrode.

2.3 Characterization of OSCs

The performance of OSC is determined by its ability to produce output power upon application of input power received from the light. The power conversion efficiency (PCE or η) of the OSC is the ratio of output power to input power . The evaluation of OSCs performance can be done by measuring its photo-current from the current density-voltage (*J*-*V*) characteristics in order to calculate the PCE of solar cell. **Figure 2.15** shows a diagram of *J*-*V* curve for OSC that is characterized in the dark and under light illumination. The photo-current generation can be seen from the *J*-*V* curve obtained under light illumination where the value of modulus current density is increased by the downwards change of the curve. Generally, the efficiency of OSCs is controlled by several parameters that can be extracted from the *J*-*V* curve such as short circuit current density (J_{sc}), open circuit voltage (V_{oc}), maximum output current density (J_{max}), maximum output voltage (V_{max}), maximum ouput power (P_{max}), and the fill factor (*FF*).

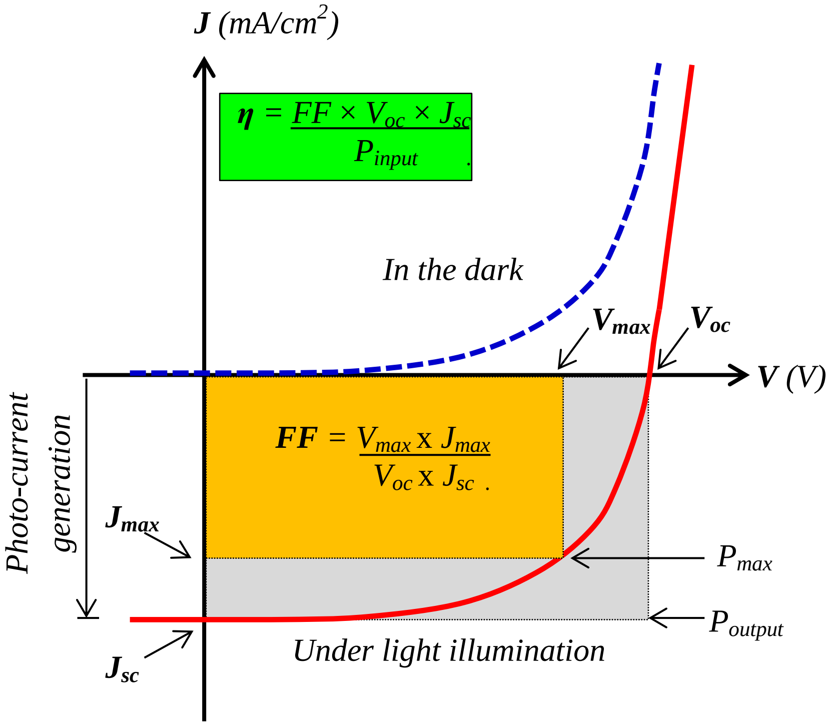

Figure 2.15 The current density-voltage (*J*-*V*) curve of OSCs.

For the measurement of OSCs performance, the cell is placed in open circuit arrangement in standard illumination conditions. Usually, the separated electrons and holes start to flow towards the low and high work function electrodes, respectively, as explained in section 2.2. The free charge carriers are collected at respective electrodes until a maximum value of potential difference is reached, which is known as open circuit voltage (V_{oc}). This value is limited by the difference of HOMO energy level of the donor and LUMO energy level of the acceptor. Once the connection is made to both the electrodes, the free charge carriers flow through the circuit which result in the current. For every material, there is a specific value of maximum current that can flow throughout the cell and is known as short circuit current density (J_{sc}) which is determined during zero potential in illuminated conditions. The I_{sc} normally demonstrates a successive charge separation that contributes to the generation of photo-current and its transport in the cell. The maximum power produced by the OSCs can be obtained by the product of J_{max} and V_{max} as shown in the previous figure. The fill factor is given by (J_{max}×V_{max}) / (V_{oc}×J_{sc}) or the ratio of maximum output power to the maximum square-area of illuminated J-V curve and is typically around 0.4 – 0.9 V. Finally, the power conversion efficiency (η) of the OSC device is defined as the ratio of the maximum generated electrical power (P_{max}) and the incident optical power (P_{input}), P_{max} / P_{input} or (FF ×V_{oc}×J_{sc}) / P_{input}.

The characterization of OCS performance has to be done by using a standard illumination condition as suggested by the Committee Internationale d'Eclairage (CIE) or International Commission on Illumination and American Society for Testing and Materials (ASTM). A standard condition of illumination is defined as 100 mW/cm^2 (CIE 904-3) and 96.38 mW/cm^2 (ASTM E-892) of total incident power density which is referred as a 1 sun value in the ambient temperature of 25 °C. Normally, the standard test condition (STC) used for this characterization is the Air Mass 1.5 spectrum (AM

1.5G) which represent the Sun at an oblique zenith angle 48° whith a tilted surface at 37° facing due south above the earth’s atmosphere. **Figure 2.16** shows the solar irradiance spectrum (https://en.wikipedia.org/wiki/Solar_irradiance) and air masses at different sun zenith angle (http://www.greenrhinoenergy.com/solar/radiation/spectra.php).

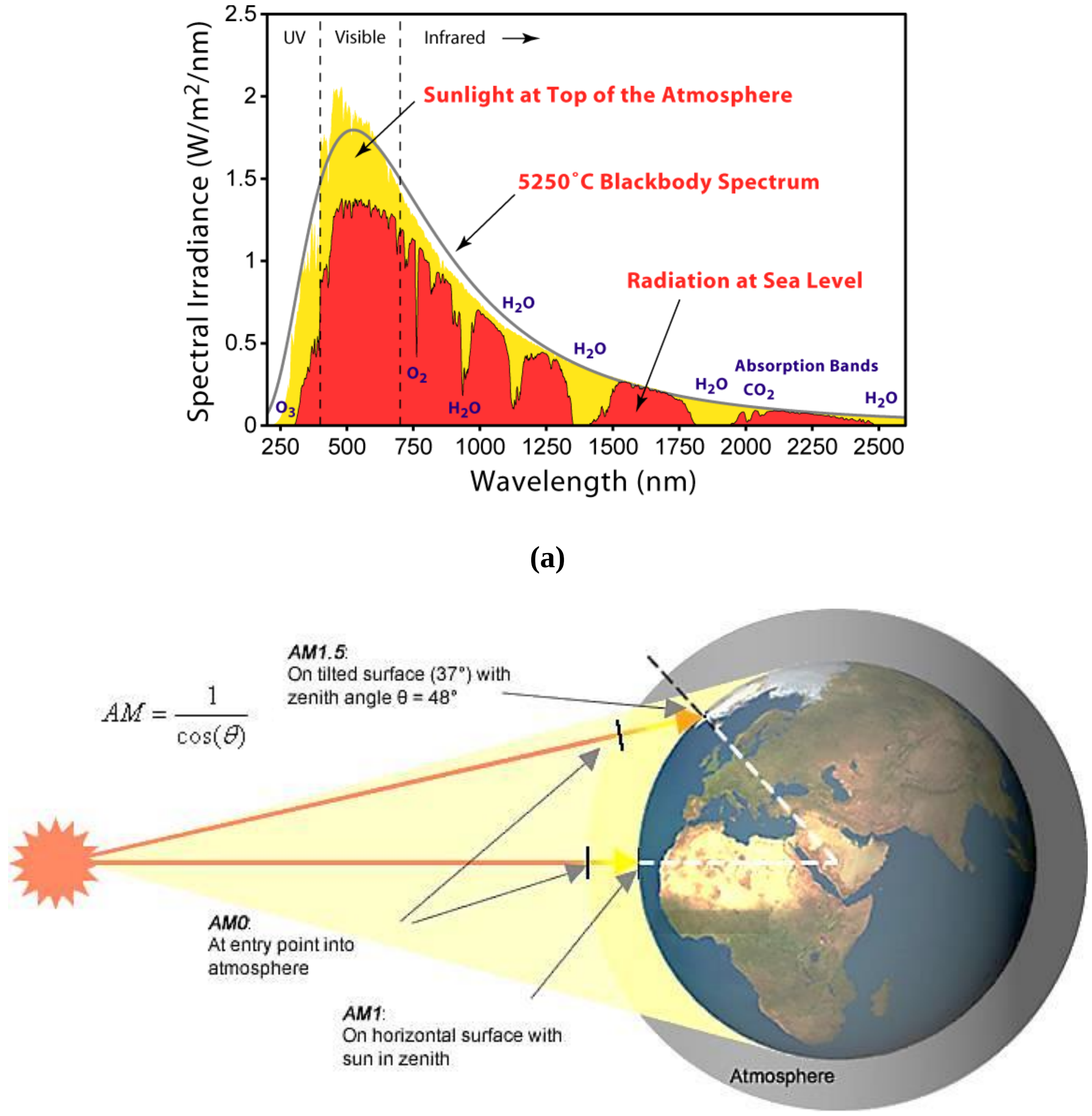

(a)

(b)

Figure 2.16 (a) The solar irradiance spectrum, and (b) air masses at different sun zenith angle.

2.4 Approaches for Practical Applications

The approaches towards OSC improvement will be discussed in the following three sub-section; (1) selection of materials, (2) device characterization for fundamental study of carrier transport, and (3) device enhancement for practical applications. The selection of organic material, which plays a key role in the performance of an OSC, is required prior to the fabrication of any device. Secondly, the fundamental knowledge of OSC device physics has to be investigated to give exact domain where the device can be applied. Moreover, further work for enhancement in the performance of OSC needs to be carried out on previously fabricated devices to meet practical application requirements. The enhancement in the device performance can be well-understood by the following flow-chart as illustrated in **Figure 2.17**.

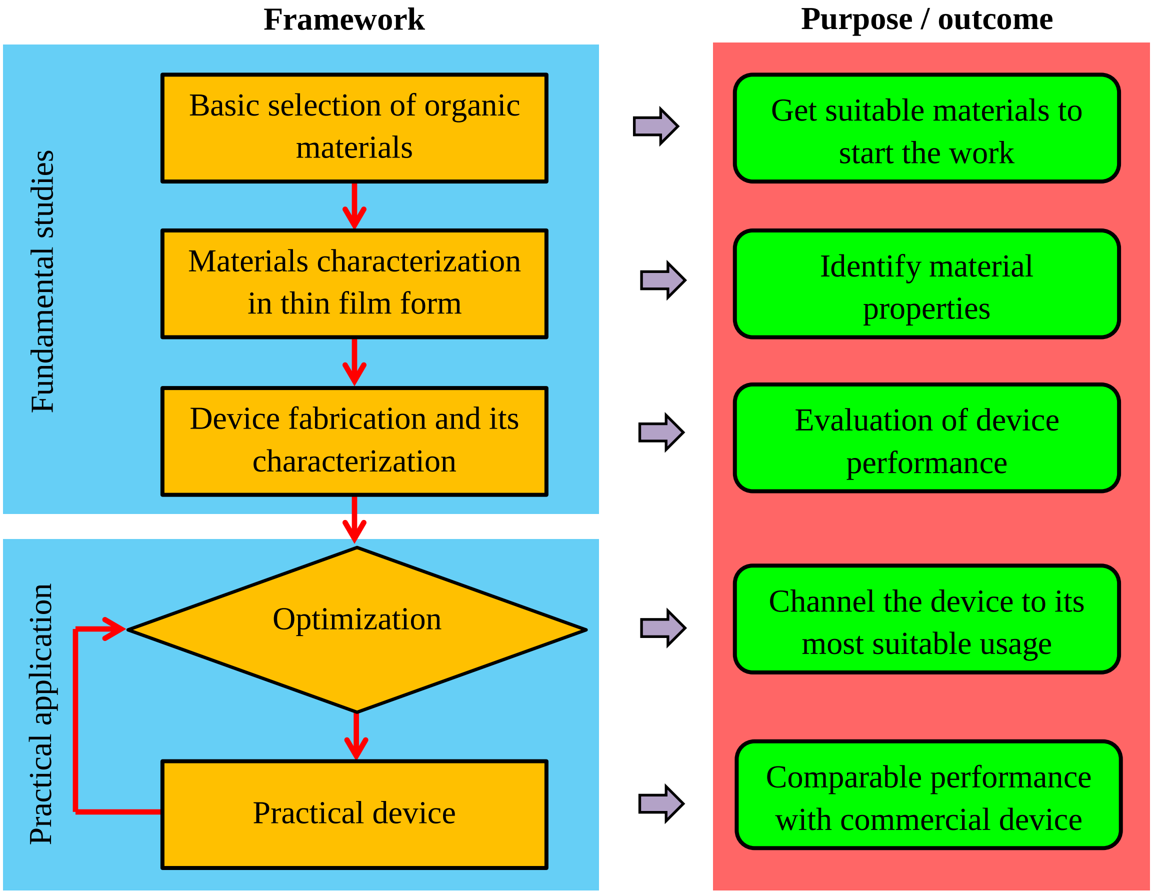

Figure 2.17 The flowchart illustrates the steps taken for organic device enhancement.

The main part of the work is related to the fundamental investigations, especially on the carrier transport behavior. Prior to the charge transport characterization, the selection of materials should be made so that the device could be fabricated with the most suitable materials for better performance. Polymers and organic small molecular materials have to be prepared in thin film form and then characterized by ultraviolet-visible (UV-Vis) spectroscopy, photoluminescence (PL), and Raman spectroscopy. The UV-Vis measurement is necessary as it determines the material absorption capability in specific wavelength range which is really important for photo-absorption of OSC. The PL measurement is used to estimate the amount of charge recombination in a material which is helpful in choosing materials with high potential photo-current generation. The Raman spectroscopy is used to identify the species present in specific volume of the sample, and provide the information of material's properties such as vibrational, rotational, and other low-frequency modes in a system of organic material. Then the study of charge transport can be done accordingly with several characterization techniques such as current-voltage (I-V) characteristics, time-of-light (ToF), dark injection method, transfer characteristic of OFET and electric field induced second harmonic generation (EFISHG). These characterization methods will be briefly explained in the sub-sections to follow. In this work, only three methods have been used to study the charge transport which includes diode I-V method, OFET transfer characteristic, and EFISHG. The enhancement in the OSC device performance is presented in the next sub-section. The donor/acceptor blend system, known as bulk heterojunction (BHJ), has been used for which optimization of materials concentration for balanced charge carriers, optimization of optical absorption of material for better sensing capability, and the effect of thermal annealing on device performance and stability have been investigated.

2.4.1 Selection of Materials

1. **Phthalocyanine derivative (VOPcPhO)**

Organic solar cells have acquired great interest as they are considered a source of energy, which is completely clean and renewable (Brabec, 2004; Brabec, Sariciftci, & Hummelen, 2001; Coakley & McGehee, 2004; Padinger, Rittberger, & Sariciftci, 2003). Numerous low molecular weight organic semiconductors have been investigated for photovoltaic and photoconductive applications (Peumans, Yakimov, & Forrest, 2003; Sayyad, 2009). Among these organic semiconductors, copper phthalocyanine has been widely studied as a potential material for single-heterojunction solar cell due to its better photovoltaic and photoconductive properties (Peumans et al., 2003; Yakimov & Forrest, 2002). The open circuit voltage, under “one-sun” illumination for CuPc-based devices were obtained in the range of 450 mV to 1.2 V by varying thickness of the active layer (Rajaputra, Vallurupalli, & Singh, 2007), device structure and top electrodes (Peumans et al., 2003; Yakimov & Forrest, 2002).

It has become very important to explore new materials which could be conveniently used in the fabrication of the solar devices to meet the growing needs of energy. Metal-phthalocyanines (MPcs) and their soluble derivatives have attracted great interest for electronic and optoelectronic applications because they are thermally and chemically stable (Ahmad, Sayyad, & Karimov, 2010; Leznoff & Lever, 1996) and possess large absorption coefficient in the Q-band (visible spectral) region (Rosenthal, 1991). Among many other phthalocyanine complexes, vanadyl phthalocyanine derivative (VOPcPhO) can be conveniently dissolved in a variety of organic solvents due to its high solubility as compared to other phthalocyanines (Aziz, 2012). The use of VOPcPhO for photovoltaic applications is important because of its high solubility.

Figure 2.18 shows the molecular structure of vanadyl 2,9,16,23-tetraphenoxy-29H,31H-phthalocyanine (VOPcPhO). The photovoltaic response of the VOPcPhO based single-junction organic solar cell has shown the potential of this material to play an important role in fabricating simple, easy and inexpensive devices.

Over the past decade, research has been focused on P3HT as a donor material with high-performance bulk heterojunction solar cells fabricated from the blend of P3HT and [6,6]-phenyl C61 butyric acid methyl ester (PCBM) (Y. Kim et al., 2006; G. Li et al., 2005; Ma et al., 2005; Y. Wang et al., 2012). Even though P3HT has shown a wide absorption range towards sunlight, yet there is some portion of solar spectrum, which needs to be covered. Several attempts have been made to overcome this limitation, which includes modification of the chemical structure of electron-donor and electron-acceptor materials (MacNeill et al., 2011), the plasmonic effect within organic tandem solar cells (Duche et al., 2009; Kulkarni et al., 2010) and the introduction of ternary systems, in which a third component of organic compound is added to a binary bulk heterojunction (Honda et al., 2011; Ruderer, Hinterstocker, & Müller-Buschbaum, 2011). All these methods, used for enhancing solar absorption spectrum, have been known to improve the performance of solar cells.

As materials from the phthalocyanine family have been reported to improve absorption of solar spectrum (Honda et al., 2011; Shen et al., 2008) and exhibit very intense absorption in the UV-Vis spectral region (El-Nahass, Abd-El-Rahman, & Darwish, 2005; El-Nahass & Yaghmour, 2008), which intrigued us to use vanadyl 2,9,16,23-tetraphenoxy-29H,31H-phthalocyanine (VOPcPhO) in the fabrication of OSC device. Moreover, recent reported literature has shown that electron mobility in phthalocyanines can be as high as hole mobility (Kraus et al., 2011). As a matter of fact, among phthalocyanines, VOPcPhO has a dominant absorption in the Q-band region i.e. from 600 nm to 750 nm, where the P3HT absorbs very little. The use of VOPcPhO for photovoltaic applications is particularly attractive due to its high solubility in a variety of organic solvents. Moreover, this low molecular weight organic semiconductor is reported to have low series resistance and a relatively high mobility for single component films (Khan, Sayyad, & Karimov, 2010). Due to the above mentioned interesting properties of VOPcPhO, the blend of P3HT and VOPcPhO becomes attractive for this study. This composite structure is expected to yield broader absorption range of solar spectrum that could induce remarkable increase in charge generation.

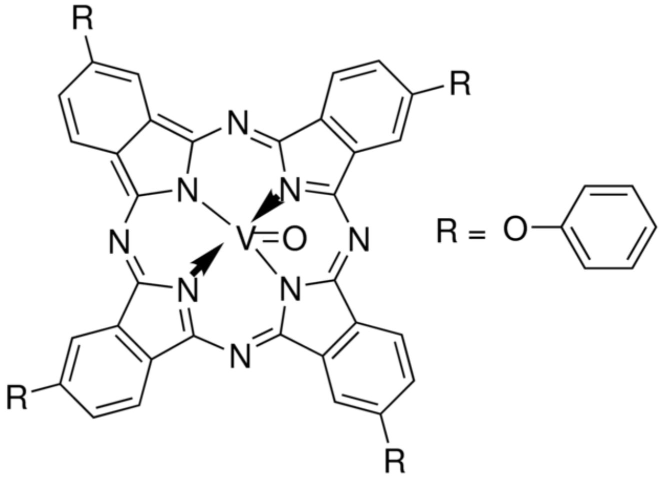

Figure 2.18 The molecular structure of vanadyl 2,9,16,23-tetraphenoxy-29H,31H-phthalocyanine (VOPcPhO).

2. Carbazole derivative (PCDTBT)

Over the past few years, high-performance bulk heterojunction solar cells have been reported using the blend of P3HT and PCBM. Even though P3HT based solar cells have shown good efficiency, but it has several limitations (S. H. Park et al., 2009). Alternatively, polymer materials consisting of poly (2,7-carbazole) derivatives are particularly of interest for photovoltaic applications. These compounds allow to have a better charge transfer from an electron rich unit to an electron deficient moiety within the repeated unit (S. H. Park et al., 2009) and also the deeper HOMO level of carbazole gives larger value of V_{OC} (Blouin et al., 2008). In this study, poly(2,7-carbazole) derivative, poly[N-9'-heptadecanyl-2,7-carbazole-alt-5,5-(4',7'-di-2-thienyl-2',1',3'-benzothiadiazole)] (PCDTBT) has been chosen as an electron donor component, due to its remarkable potential and performance, in the fabrication of OSC (D. H. Wang et al., 2012). Moreover, the V_{OC} value for PCDTBT up to 0.9 V (Blouin, Michaud, & Leclerc, 2007) and the internal quantum efficiency of the PCDTBT:$PC_{71}BM$ bulk heterojunction solar cell approaching 100 % (S. H. Park et al., 2009), has been reported. It is also reported that the blend of PCDTBT and $PC_{71}BM$ shows more efficiency and better stability than a standard P3HT:$PC_{71}BM$ blend. The PCDTBT:PCBM composite carrier mobility calculated using ToF and photo-CELIV methods are found in the range of 4-6 x 10^{-5} cm^2/Vs (Clarke et al., 2012).

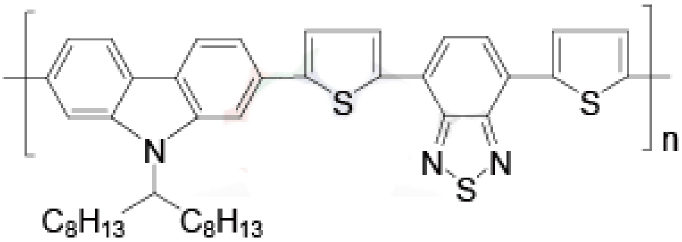

Figure 2.19 The molecular structure of poly[N-9'-heptadecanyl-2,7-carbazole-alt-5,5-(4',7'-di-2-thienyl-2',1',3'-benzothiadiazole)] (PCDTBT)

2.4.2 Charge Transport Characterization

The charge carriers transport in organic semiconductors is one of the key factors that determine the efficiency of OSC devices. Recently, through the advances in characterization of charge carrier motion, several significant differences of carrier transport behaviours, that lead to the change in its performance, have been observed. One of the important parameters of semiconducting materials is the mobility of free charge carriers that flow in OSC devices. The variation in the mobility is not only limited to different type of materials but it also varies for the same material. There might be several reasons that contribute to the variation of transport mechanism in OSC devices. One reason can be the nature of material such as high dielectric constant, amorphous structure, interaction with environment, low stability, and poor electronic conduction, that plays an important role in transport mechanism. Secondly, there may be extrinsic elements or traps in the active region which might develop during the preparation and fabrication process of organic devices. And thirdly, there are underlying phenomena in OSC device physics, such as changes in optical and electrical properties that might be due to internal or external interactions, which are not yet fully understood. In order to provide a fundamental explanation about charge behaviour in OSC for improved performance, there are several techniques including current-voltage (I-V) characteristic, dark injection method, time-of-light (ToF), OFET transfer & saturation characteristics, and EFISHG, that can be adopted for better insight of charge transport mechanism.

2.4.2.1 Current-Voltage (I-V)

This technique is considered as a conventional method because it is used not only for the calculation of OSCs efficiency when measured under light illumination, but also used for the study of charge carrier transport when measured in the dark. This technique is very useful to characterize thin-film-devices. The fundamental interpretation of charge transport mechanism under this technique is explained under space-charge-limited current (SCLC) transport regime where the flow of maximum current is limited through the OSC device. Normally, when the electrode supplies unlimited number of carriers, the excess electric charge will build up in the space of the bulk material and distribute over this region (so-called space-charge). The change from ohmic to SCLC region is indicated by the threshold voltage (V_{th}) in the I-V curve, where the slope of two regimes change from 1 (ohmic) to 2 (SCLC).

According to Mott-Gurney square law, the constant mobility of charge carrier can be calculated straight away from this SCLC regime provided the device has no defect or localized-state in the band gap (so-called traps). The traps regime always shows a slope more than 2. If the trap is present during the charge transport, a trap factor should be added to the calculated mobility by taking a ratio of mobile charge density to the total (mobile and immobile) charge density. The presence of traps requires charges to fill vacancies up to certain level of voltage (so-called trap-filled limited or TFL regime) and proceed until the slope of I-V equals 2 or the I-V enters SCLC region again. **Figure 2.20** shows several transport regimes of charge carrier in OSC devices for nearly an ideal case (www.stallinga.org/ElectricalCharacterization/2terminal/index.html). It shows that the carrier transport begins with an ohmic regime, and follows SCLC region. Then the traps tend to change the carrier transport to TFL and finally enters a regime with a value similar to SCLC which is known as trap-free SCLC regime.

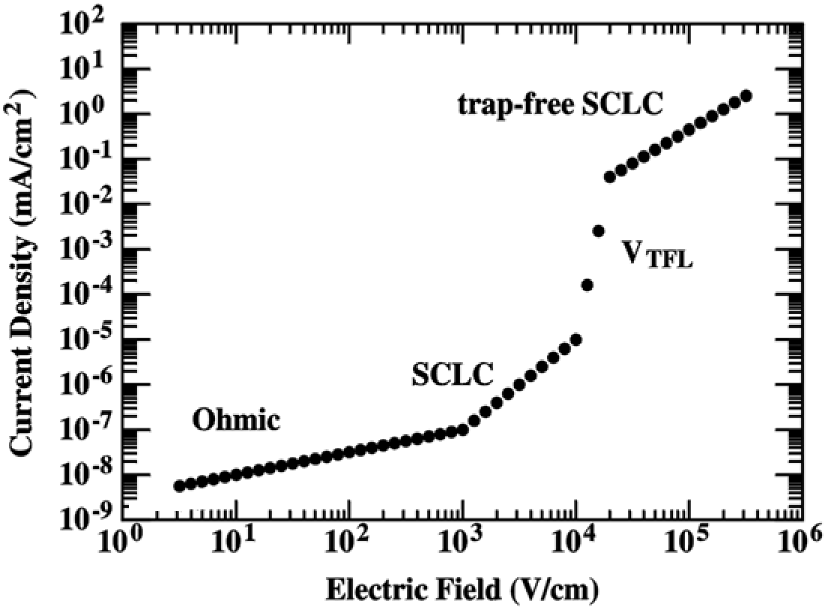

Figure 2.20 The transport of charge carriers in several regimes including space-charge-limited current (SCLC) region as defined by conventional I-V method.

Some other models, such as Cheung's method and Norde's function, are used to describe the charge carrier transport and concurrently used to extract several semiconductor parameters.

2.4.2.2 Time-of-Flight

The time-of-flight (ToF) method is a very popular technique used to calculate carrier mobility of organic semiconductors, and also describes the behavior of the charge transport. The laser pulses are applied directly on the active layer of the device to create a moving photogenerated charge under the influence of bias electric field. The polarity of bias voltage is very important to selectively measure the charge carrier species either electrons or holes. Upon application of laser pulses, the photogenerated charges will be created at transparent side of electrode which posses sufficient energy to travel to the electrode on the other side. The transit time taken by photogenerated charges to migrate (or flight) between two electrodes under the influence of electic field, can be used for the calculation of charge carrier mobility, $\mu = d^2/(\tau.V)$. This method focuses on material characterization as the measurement is only done for thick active layer (5-10 µm) not on the real device. **Figure 2.21** illustrates the migration of charges during ToF measurement.

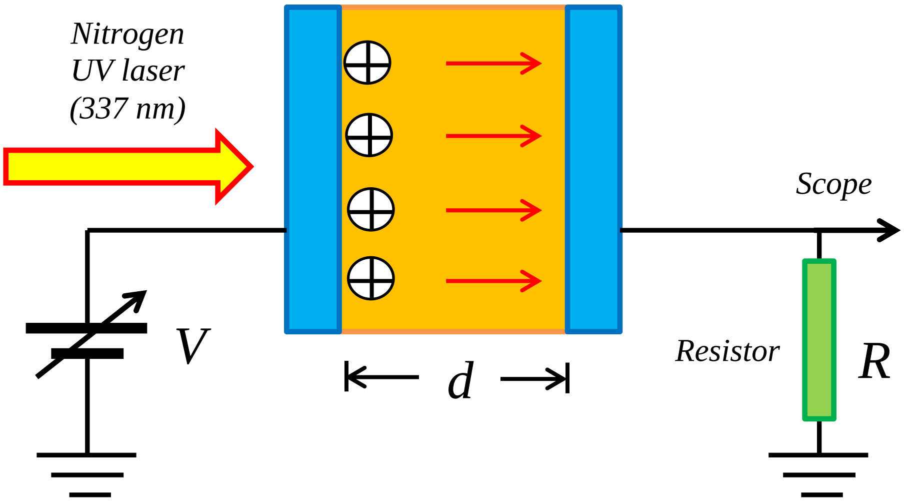

Figure 2.21 The migration of charges during ToF measurement.

2.4.2.3 Dark Injection

Dark injection space-charge-limited transient current (DI SCLC), also referred as time resolved dark injection, is another technique used to calculate the mobility of charge carrier like ToF but it involves the measurement of transient current stimulated by the electrical voltage pulse. The characterization is done in the dark during the injection of charge through the ohmic contact. Both the voltage step and transient current are compared by using an oscilloscope. **Figure 2.22** shows the ideal DI SCLC transient current. The transient signal will reach its maximum at a well-defined dark injection time and decay to a steady-state value after a long time when the anode/material contact is ohmic and material/cathode contact is electron blocking (Cheung et al., 2008). Both the DI-SCLC and TOF measurements are widely used for calculating the charge mobilities of organic materials, but these techniques require thick samples as the observed transient signal is produced by the superposition of the charging current and transient current (H. Li et al., 2014).

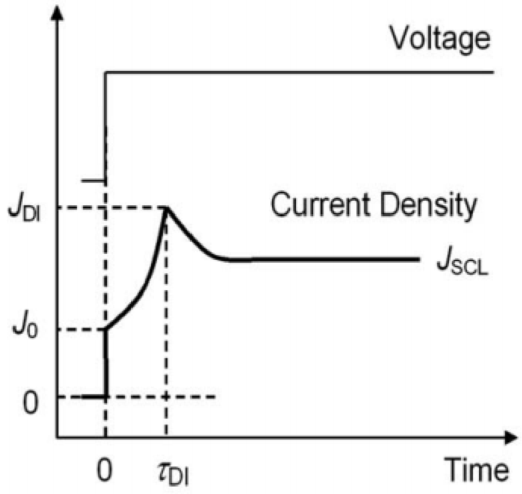

Figure 2.22 An ideal DI SCLC transient.

2.4.2.4 Transfer and Saturation Characteristics

The mobility of organic semiconductor materials can also be determined by means of field effect in organic field effect transistor (OFET). Usually, the mobility obtained from the OFET characterization technique is higher than that of ToF and DI SCLC mobility. Such variations are mostly due to the differences in device geometrical structure that result in the charge carrier travelling in different paths and directions. The devices, fabricated for ToF and DI SCLC characterizations, are made in such a way that the thick active material is sandwiched between the two electrodes. On the other hand, in OFET, the (source and drain) electrodes are prepared on a very thin layer (~100nm) in the planar form, so that the motion of charge carrier from source drain electrode create a surface mobility which has a value higher (several orders of magnitude) as compared to the bulk mobility obtained by ToF and DI SCLC. The field effect at the gate electrode comes is capable enough to control the flow of current and selectively choose carrier species during the OFET characterization. There are two common types of measurement in OFET characterizations; transfer and saturation characteristics. The transfer curve is really helpful to identify which species of charge carrier is dominant in a material either it can be holes, electron or both. The saturation curve is normally used to determine the field effect mobility of a material. **Figure 2.23** shows the standard OFET structure used for OFETcharacterization.

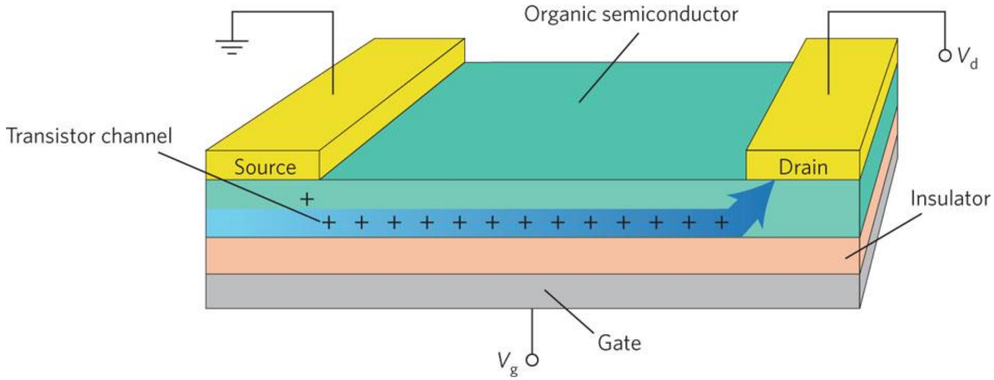

Figure 2.23 A standard OFET structure.

2.4.2.5 Electric Field Induced Second Harmonic Generation

Electric field induced second harmonic generation or EFISHG is the characterization method that is used to probe and visualize the generated second harmonic wave from the material in which the generated signal corresponds to the motion of charge carriers of a material in the OFET structure. Continuous pulses from infrared (IR) laser are applied to the channel, between source and drain, during the charge carrier transport under an induced field condition. This technique can manipulate non-linear optical properties of any material by breaking the optical centro-symmetrical properties through induced electric field, and concurrently probe the corresponding charge transport signal in visible motion via its second harmonic generation (SHG) wave. By using this technique, a mobility of charge carriers, higher than that achieved from the OFET technique, can be obtained by elimination of charge injection effect. This elimination can be done when the carrier motion is directly examined by CCD camera which continuously records the time taken by charge to be injected, transported and arrived at the other electrode. Several more characterizations can be performed by manipulating the EFISHG technique to get deeper understanding of OSC device physics. **Figure 2.24** shows the EFISHG setup for probing the charge carrier motion.

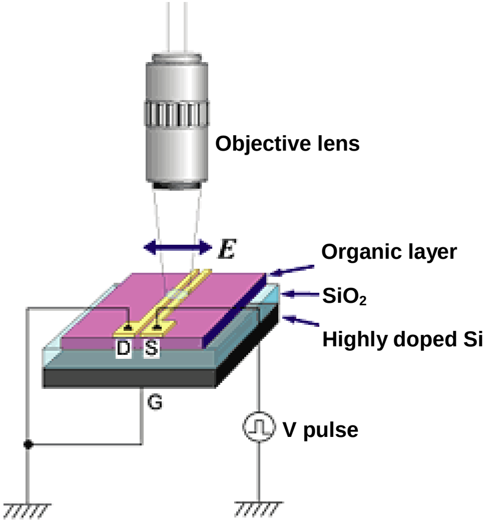

Figure 2.24 The EFISHG measurement.

2.4.3 Improving Device Performance for Practical Application

1. Bulk Heterojunction of Donor/Acceptor Blend System

Organic solar cells (OSCs) exhibit very interesting properties including light weight, physical flexibility and low fabrication cost (Hoppe & Sariciftci, 2004). Much effort has been devoted to increase their efficiency to a value sufficient enough for commercial needs. Currently, several types of organic solar cell structures are under investigation worldwide. In particular, donor/acceptor blend based bulk heterojunction (BHJ) solar cells have undergone comprehensive study. The establishment of the interpenetrating donor/acceptor (D/A) networks improves the charge transfer and allows the efficient transport of the generated charges to their respective electrodes. Under illumination, the transport of delocalized charge carriers plays a major role in the photocurrent generation. It happens to be generated from the dissociation of excitons into free electrons and holes at the interface of donor and acceptor layer. However, short lifetime and low carrier mobility in organic material has restricted the excitons diffusion length to only about 10 nm for the generation of effective charge carrier (Menke & Holmes, 2014). These drawbacks have led the researchers to eradicate the limitation of charge separation by improving the morphology (Z. Li et al., 2013) and nanostructure (DeLongchamp, Klinea, & Herzing, 2012) of the materials in the bulk heterojunction (BHJ) solar cell.

2. Used of Ambipolar Material as New Acceptor Component

A long-standing speculation pertaining to the conduction phenomenon in organic semiconductors is that π-conjugated semiconductors are intrinsically p-type semiconductors. Based on few studies, it was believed earlier, that polymeric materials like Poly(*p*-phenylenevinylene) (Spanggaard & Krebs, 2004), polythiophenes (Tsumura, Koezuka, & Ando, 1988), polyacetylene(Ozaki et al., 1980) and macromolecules (Dimitrakopoulos & Malenfant, 2002) e.g., metal phthalocyanine, pentacene and merocyanine exhibit high hole mobility, and thus are p-type organic semiconductors. However, recently, several research and development (R&D) efforts (Blom, De Jong, & Vleggaar, 1996; Cornil et al., 2007; Opitz et al., 2012) have been made to measure the mobility of the charge carriers which led to a significant advancement in understanding both positive (+ve) and negative (-ve) transports in organic semiconductors. It has now become clear that π-conjugated semiconductors e.g., fullerene (Anthopoulos et al., 2006), copper phthalocyanine (Kraus et al., 2011) and pentacene (Singh et al., 2005) exhibit ambipolar charge transport. Nevertheless by so far, electron mobility has never been found greater than the holes mobility (Cornil et al., 2007).

The predominant factors by virtue of which ambipolar transport has been so much elusive in the past are; an impurity of material, improper processing and device characterization conditions (Bao, 2000), electronic traps (Lenes et al., 2009), disordered thin film morphology and mismatched electrode material for charge injection. These factors have now been extensively studied and properly addressed (Chua et al., 2005; Katz et al., 2000; Reese et al., 2008) to enhance n-type conductivity in organic molecules. Mobilities as high as 0.1 cm^2/V s have been achieved for both electrons and holes. Particularly in solar cells, balanced electrons and holes mobility are stringently required to reduce the recombination. Therefore, it is interesting to seek out solution processable materials having generic ambipolar transport properties. The phthalocyanine derivative, VOPcPhO, has become the most suitable candidate in this study especially for the fabrication of OSC. The blend of popular donor material, P3HT and ambipolar material VOPcPhO becomes attractive for the present study as the later was previously known as a donor component. The composite structure is expected to yield broader absorption range of solar spectrum that could induce remarkable increase in charge generation. It is suggested in this present work that the P3HT:VOPcPhO blend will be used as an active layer to fabricate the ITO/PEDOT:PSS/P3HT:VOPcPhO/Al solar cell. The ITO/PEDOT:PSS/P3HT:VOPcPhO/Al configuration leads to such a stacking order, according to the electron affinity and ionization potential, that the generated charge can efficiently flow inappropriate direction within the cell structure.

3. Optimization of Light Absorption for Sensing Application

For the past few years, the bulk heterojunction, effective concept from the processing cost point of view, has been considered a dominant design for organic photodiodes and solar cells (Abdullah et al., 2012; Guvenc, Ozkan, & Ozkan, 2012; Ichikawa et al., 2012; Lilliu et al., 2011). It has been reported by Sayhan et al. that the use of polymers together with organic dye content enhances the harvesting of photons from light (Sayhan et al., 2008). The study of a polymer-dye device in the form of a thin film by Honda et al. (Honda et al., 2011) has revealed proficient light harvesting by both dye and polymer components. This device consists of a donor–acceptor blend structure with a dye component selectively localized between the heterojunction interface. The photocurrent has been increased by the addition of dye material which is capable of collecting more photons in the spectrum where the donor and acceptor blend is unable to efficiently harvest. These investigation show that the introduction of a dye material is to achieve a high photo-conversion as the photocurrent of the device increases due to direct photo-excitation (Honda et al., 2009).

Among the organic dyes, phthalocyanines are the heterocyclic macrocyclic organic compounds. Phthalocyanines molecules are fully conjugated, containing a p-electron system (Natale et al., 1998). This conjugated system is responsible for their high sensitivity (Ahmad et al., 2011). The new combination of donor-blended system is introduced in this work, consisting of P3HT and VOPcPhO. The introduction of VOPcPhO, in P3HT matrix, is to encounter the limitation of a big fraction of the solar spectrum absorption. The best composition of this blend system has not been reported yet. In this study, the contribution of VOPcPhO content and the influence of different P3HT:VOPcPhO compositions of the blended system will be investigated. The aim of this work is to introduce a novel blend system that can open the doors to the development of a highly sensitive photo-sensor which can cover the whole visible range.

4. Thermal Treatment Effect on OSC Device Stability

Organic solar cells (OSCs) are thought to be one of the most promising energy harvesting devices that could be fabricated by easier means at a large scale and require low production cost (Krebs, Gevorgyan, & Alstrup, 2009). The stability of the OSCs is very crucial for their practical applications and it should be taken into account not only for medium term but also for long term applications (Jørgensen, Norrman, & Krebs, 2008). However, most of organic materials cannot withstand the ambient conditions due to the presence of oxygen that can cause carrier traps and accelerate degradation (Cao et al., 2014; Kawano et al., 2006). Besides, light illumination can also be a factor for OSCs degradation due to the morphological changes in the polymer materials (Rivaton et al., 2010). There are many reports in the literature describing several methods that are used to overcome the issue of degradation of the OSCs such as temperature annealing and device encapsulation (Brinkmann & Wittmann, 2006; Yang & Uddin, 2014). The thermal annealing process on OSC device has been reported to give a better efficiency and longer stability in OSCs based on P3HT/PCBM blend (Wu et al., 2014). It is believed that the thermal annealing encourages crystallite growth and increases structural order in P3HT. However, for the case of OSC based on PCDTBT/PCBM blend system, it has been reported that higher power conversion efficiency could be achieved without post annealing process (Gusain et al., 2013; Wakim et al., 2009; Zhao et al., 2014) which is contrary to the previous work on P3HT/PCBM based OSCs. It is believed that, thermal annealing of PCDTBT reduces the coherent length of the π–π stacking, and increases disorder in the polymer electronic structure (Beiley et al., 2011). Anyway, solar cell based on PCDTBT/PCBM has better morphological stability under thermal treatment as compared to P3HT/PCBM blend system, which was confirmed by X-ray photoelectron spectroscopy (XPS) and energy dispersive X-ray spectroscopy (EDS) results reported by Wang et al. (D. H. Wang et al., 2012). In most of the reported work on PCDTBT/PCBM based OSCs, only the active layer has undergone thermal annealing at ~70 ºC.

CHAPTER 3 : METHODOLOGY

3.1 Chemicals and Materials

The study of transport and behaviour of charge carriers has been carried using diode and transistor which require a very thin layer of photoactive material. Prior to the fabrication of any device, thin film samples of selected photoactive materials were prepared by dissolving the organic materials in their appropriate solvents. The solution processable materials were then spin-coated on substrates to form homogeneous thin films for identification of their electrical, optical, and morphological properties. The choice of suitable substrates, e.g. cleaned glass and indium tin oxide (ITO) coated glass for the thin film characterization, is also important for investigating material's natural properties. Useful information on materials properties can be used to optimize material composition for the fabrication of electrical devices.

In the present study, the organic materials have been used in blend composition and have been divided into two groups according to their potential applications. The electrical characterizations techniques used here are I-V method, OFET characteristic and EFISHG technique. All of these characterizations use a thin layer of active component and are suitable for dielectric materials, but the last technique (EFISHG) requires additional non-linear optical properties for the generation of second-harmonic wave. The binary blends used in this study are P3HT:VOPcPhO and PCDTBT:PCBM based on donor/acceptor blend system. The combination of such materials are based on their electron and hole mobilities under selected volumetric ratios. The proposed potential applications for the fabricated devices by these blend materials are light sensor and solar cell. The procedures used for preparing the blend solutions, substrates patterning, cleaning processes, and electrodes preparationare explained in the following sections.

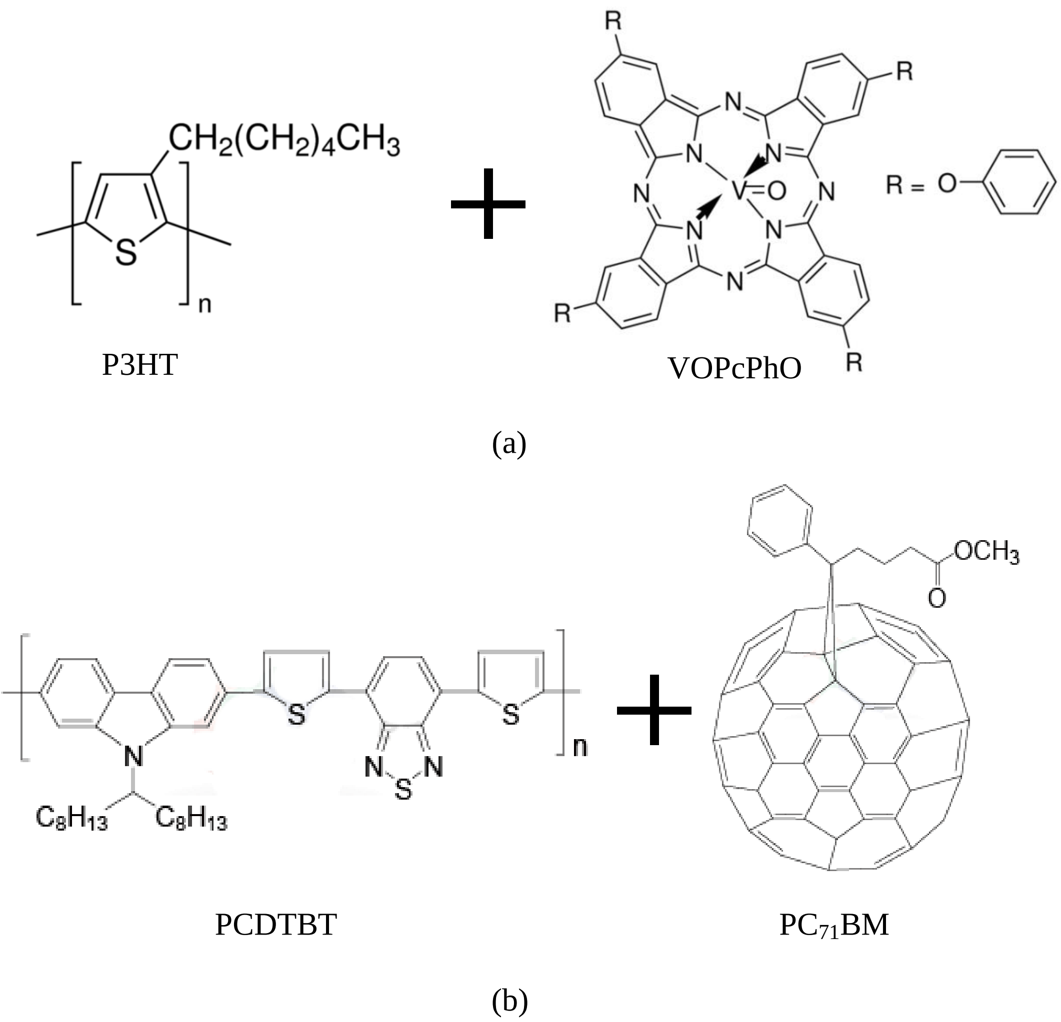

Figure 3.1 Molecular structure of selected organic materials for preparation of blends: (a) P3HT and VOPcPhO, and (b) PCDTBT and $PC_{71}BM$.

3.1.1 Solution Preparation

I. P3HT:VOPcPhO

P3HT (regioregular poly(3-hexylthiophene-2,5-diyl)) and VOPcPhO (vanadyl 2,9,16,23-tetraphenoxy-29H,31H-phthalocyanine, with dye content 98 %) are photo-sensitive organic materials. For the present work, these materials have been obtained, from Sigma-Aldrich (product of Rieke Metal®, Inc.). P3HT is a π-conjugated polymer that has regioregularity greater than 90 %. Its molecular formula is $(C_{10}H_{14}S)_n$ and it possess high solubility in most of the organic solvents (Machui et al., 2012). While VOPcPhO ($C_{56}H_{32}N_8O_5V$) is one of the phthalocyanine (Pc) derivatives, that also has good solubility in organic solvents. By virtue of high solubility of P3HT and VOPCPhO in organic solvents, these materials find their extensive utilization in the fabrication of solution processable devices. Both materials P3HT and Pc derivative, are well known electron donor materials which are normally used in the fabrication of OSCs. Both materials have been dissolved in a selected control solvent; chloroform (with 99.99 % purity) in 20 mg/ml concentration separately. To ensure the materials are dissolved completely, the solutions have been stirred at 200 rpm stirring speed at room temperature using magnetic strirring bar for at least an hour. Before the active thin film deposition, the solutions have been filtered using disposable PTFE filter (filtration membranes size ~0.25μm). Several volumetric ratios of blend solutions have been prepared from individual solutions of P3HT and VOPcPhO (20 mg/ml concentration each). The details are listed in the following table:

Table 3.1 The blend ratio of P3HT:VOPcPhO.

Blend system	Volume ratio (P3HT : VOPcPhO)
P3HT : VOPcPhO (20 mg/mL in chloroform)	1.0 : 1.0
	1.0 : 1.5
	1.0 : 2.0

II. PCDTBT:$PC_{71}BM$

PCDTBT (poly[N-9'-heptadecanyl-2,7-carbazole-alt-5,5-(4',7'-di-2-thienyl-2',1',3'-benzothiadiazole)]) and $PC_{71}BM$ ((6,6)-Phenyl C71 butyric acid methyl ester, mixture of isomers) have been purchased from Lumtec and used without further purification. These organic materials have a major difference in their charge carrier categories; PCDTBT (molecular formula: $C_{43}H_{47}N_3S_3$)n is an electron donor material, while $PC_{71}BM$ (molecular formula: $C_{82}H_{14}O_2$)is an electron acceptor material. Both the materials have good solubility in organic solvents especially in chloroform, therefore they have been dissolved in chloroform separately in 10 mg/ml concentration.

The initial photophysical study related to the PCDTBT:$PC_{71}BM$ binary blend system has been extensively performed and the optimized volume ratio has been deduced to be 1:4. Once the volumetric ratio is optimized, various other volumetric ratios of the binary blend are not really required to be prepared and tested. The optimized volumetric composition of the binary blend as revealed by photophysical study is widely accepted in the literature for improved performance of the fabricated devices. Therefore, following this information, a thin film of PCDTBT:$PC_{71}BM$ with a composition of 1:4 volume ratio, is formed on the conductive substrate for device fabrication. The blend active layer should have a thickness of about 70 nm instead of 100 – 150 nm, which is usually observed for common organic bulk heterojunction layer. It is believed that, the thinner the film, the lesser the traps. But a very thin film shows low absorption of light especially for OSCs application, thus the optimized film thickness has to be between 70 – 80 nm. The same steps of thin films preparation are adopted for the fabrication of P3HT:VOPcPhO based solar cells except for the annealing process. The details on annealing treatment will be discussed in section 3.3.1 (II).

3.1.2 Substrate Patterning and Cleaning

Two types of substrates have been utilized in the present study in order to characterize OSC devices; glass and indium-tin oxide (ITO)-coated glass substrates. Glass substrate is normally used for materials characterization and initial optimization of active binary blend composition. ITO-coated glass substrate however, is mainly used for OSCs fabrication since it is a transparent conductive electrode that allows the light to pass through. Substrate cleaning process is very crucial in order to form a smooth and homogeneous active thin film on the substrates. A normal cleaning process can be done by sequential rinsing method using soap water, de-ionized (DI) water, isopropanol, and again DI water. It can also be done by putting the substrates in these solutions sequentially in an ultrasonic bath for 10 min. Later, the substrate are dried up with a stream of inert nitrogen gas and properly kept in air-tight container (dust free environment).

Normally, the OSC devices are fabricated on a substrate with specific dimension of active area. For the ease of optical and electrical measurements, the ITO coated part is modified according to a desired pattern. The commercially available pre-patterned ITO-coated glass substrate, obtained from Ossila, allows six OSC devices to be fabricated on each substrate, simultaneously. The substrate pattern forms 0.045 cm^2 active area for each OSC as depicted in **Figure 3.2**. For the characterization of OSC, legs are mounted at the edge of the substrate in order to create a stable contact between all the electrodes and the device.

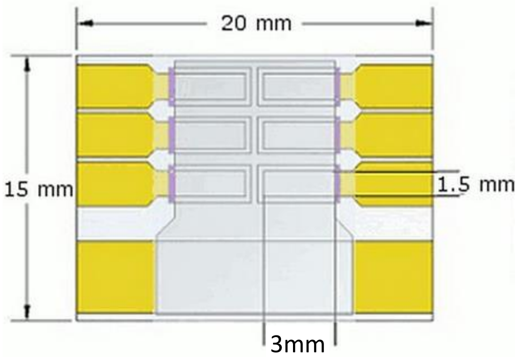

Figure 3.2 Geometrical design of pre-patterned ITO-coated glass substrate.

Pre-patterned ITO can also be made in the laboratory by photolithography process. Photolithography is the process that enables microfabrication of specific geometrical patterns of thin film, such as ITO on the substrate. The film is, primarily, coated with a photo-resist layer and exposed to the ultra-violet (UV) light through a shadow mask of a specific pattern. After UV exposure, the exposed part of photoresist gets hardened and the unexposed part of photo-resist is removed by a developor solution leave a negative pattern on the film, ITO for instance. The patterning process occurs when a diluted acid is used to etch uncovered part of the film. Once the etching process is done, the photo-resist layer is striped off by diluted sodium hydroxide and followed by a normal cleaning process using de-ionized water.

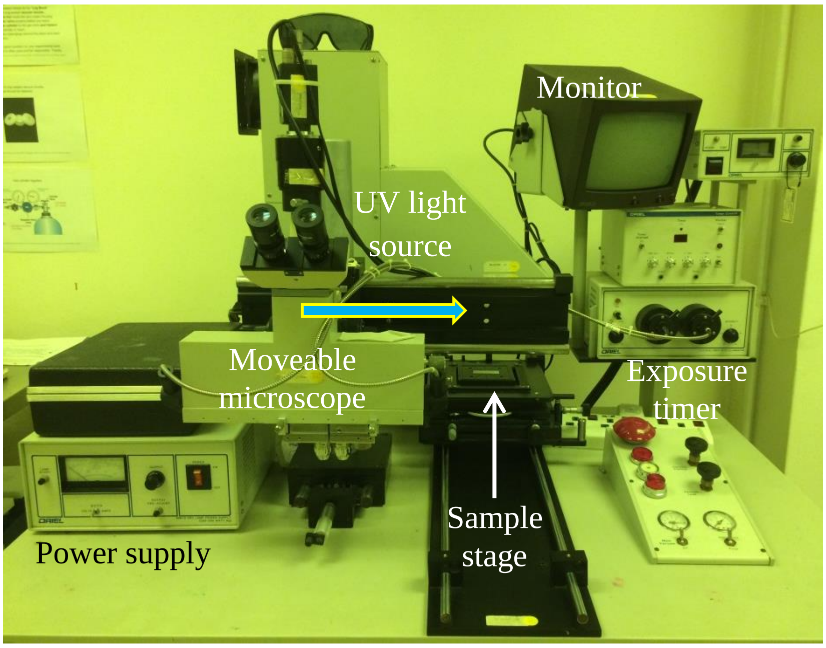

Figure 3.3 The photolithography system consisting of UV light source.

The steps of substrate patterning process is illustrated in the following figure:

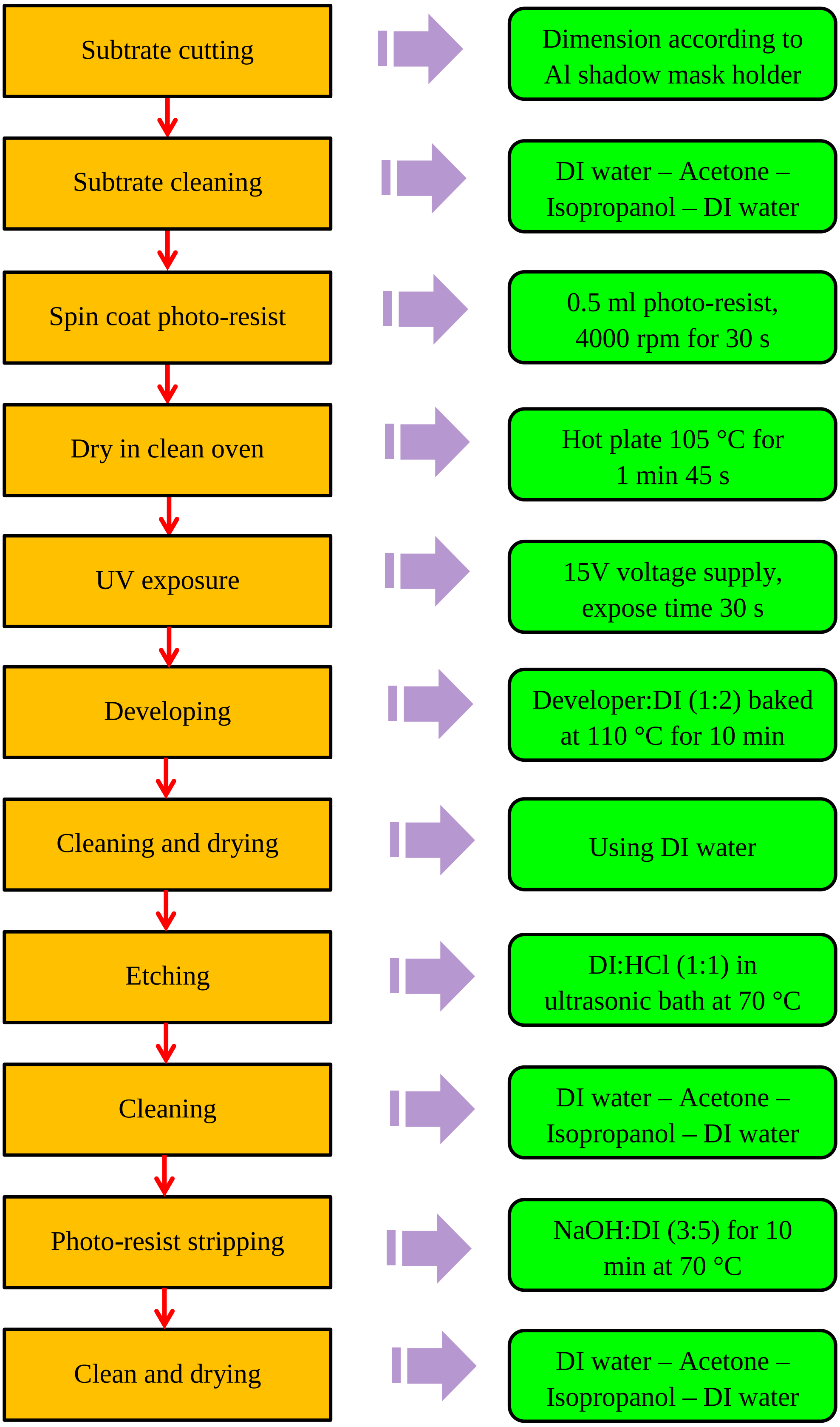

Figure 3.4 Substrate patterning process via photolithography technique.

3.1.3 Thin Film Preparation

Generally, there are several techniques that can be used for thin film formation from the solution such as drop casting, dip-coating, and spin coating. Solution drop casting produces a thick film above nanoscale and its thickness cannot be controlled easily. Dip-coating method requires large amount of solution for depositing a thin film and involves unnecessary deposition at the back of substrate during film formation. That is why, spin-coating tehcnique has been used in this study to deposit desired thin films. The process provides ease of control over thickness and requires only small amount of solution. Spin-coated film is generally thin (mostly in nanoscale range). In the present study, the spin-coating process has been carried out using a spin coater from Laurell (model WS-650MZ-23NPP) as shown in **Figure 3.5**.

Figure 3.5 Spin coater Laurell model WS-650MZ-23NPP.

A small amount of solution is dispensed on the top surface of a cleaned substrate just before spinning at the desired spin rate. Since, thickness of the film depends on spin rate, hence, the film thickness decreases as the spin rate increases, and vice versa. **Figure 3.6** shows a spin-coating process for thin film formation.

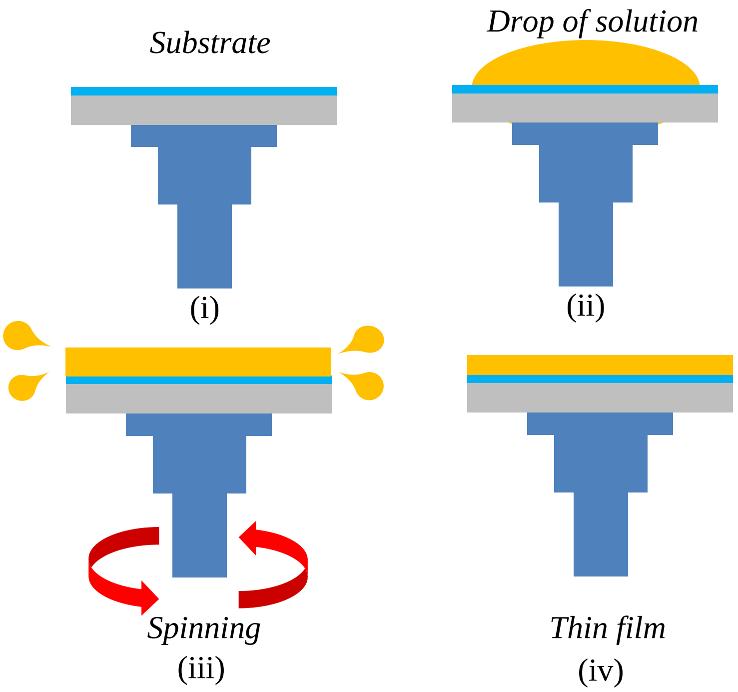

Figure 3.6 Spin coating process.

Several sets of individual films (with different concentrations) have been prepared at several spin rates for optimization of the thin film. These sample films were used for material characterization prior to the device fabrication. Then, both blend systems (P3HT:VOPcPhO and PCDTBT:$PC_{71}BM$) were prepared in optimized ratios. The first blend system is made to investigate VOPcPhO as an electron acceptor and P3HT as an electron donor (as the hole mobility of P3HT is far greater than its electron mobility) compenents in OSCs fabrication. Moreover, the charge carrier transport mechanism of VOPcPhO has also been investigated. It is noteworthy, that the blend system comprising P3HT and VOPcPhO has never been reported so far. The second blend system (PCDTBT:$PC_{71}BM$) is made to further elucidate fundamental dynamics of charge carrier transport and improve the performance of OSCs for practical applications. In this study, a buffer layer from holes injection group such as poly(3,4-

ethylenedioxythiophene) polystyrene sulfonate (PEDOT:PSS) is deposited between the ITO-coated glass substrate and photoactive materials as a buffer layer. The use of buffer layer is mainly to improve charge transport by providing suffucient number of holes and controlling electron transport direction, thereby creating balanced charge transport from both the species. The PEDOT:PSS buffer layer is normally used as a very thin layer ~ 40 nm before the deposition of an active absorber layer. The buffer layer needs to be annealed for 30 min at 120 °C to completely evaporate the solvent and to increase its conductivity. Then, the composite blend solutions of P3HT:VOPcPhO and PCDTBT:$PC_{71}BM$ are deposited onto this layer (with thicknesses ~100–150 nm and 70 nm, respectively).

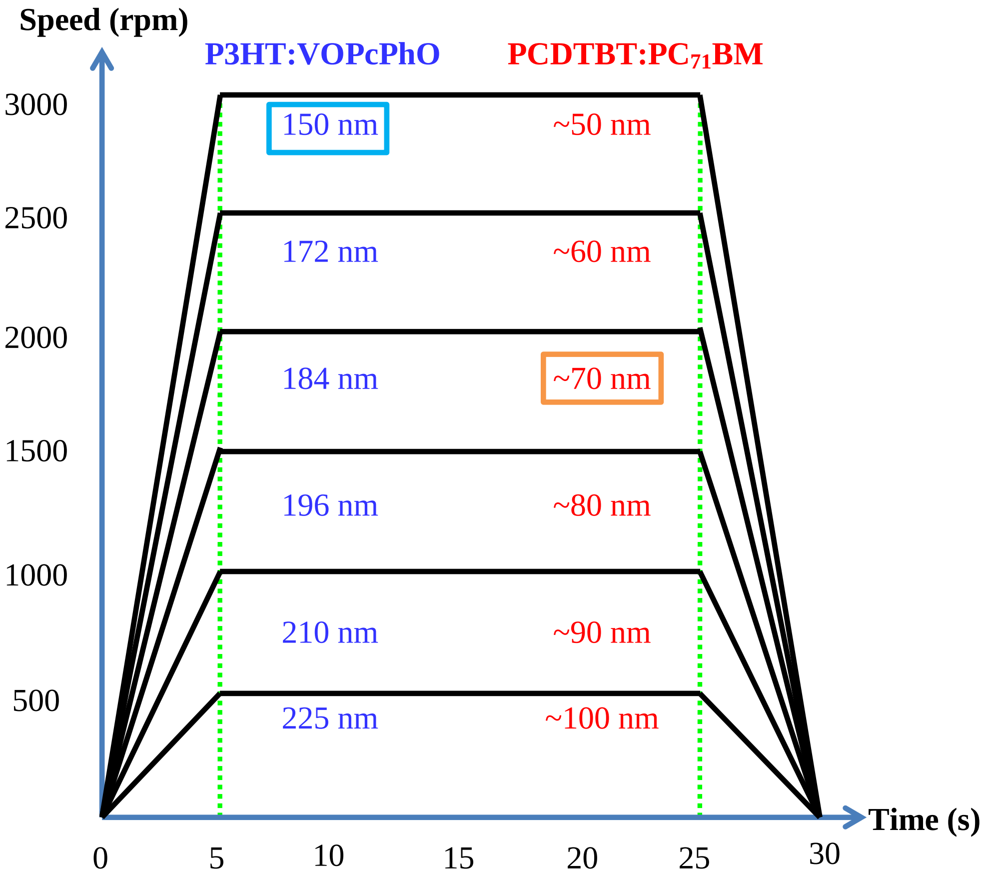

Figure 3.7 Films thicknesses produced by different spin rates for blend films made of P3HT:VOPcPhO and PCDTBT:$PC_{71}BM$. Thicknesses in the boxes are the chosen ones.

3.1.4 Thermal Evaporation

In some cases, a buffer layer can also be introduced on the top of a photoactive layer as electron transport layer such as lithium fluoride (LiF). The deposition of LiF is done by thermal evaporation technique through the sublimation process. The thickness of LiF is controlled to be < 1 nm, otherwise a thicker layer turns into an insulator that only contributes to deficiency of the device performance.

The top Aluminium (Al) contact is deposited on the photoactive layer by means of thermal evaporation using Edward AUTO 306 thermal evaporator as shown in **Figure 3.8**. The deposition of Al should be done in high vacuum condition under a controlled evaporation rate in order to deposit < 100 nm top contact. The Al electrodes can be deposited by shadow mask either in square or round shape, according to the device pattern, as shown in **Figure 3.9**. A square shape shadow mask is normally used during the Al deposition for devices using pre-patterned ITO-coated glass substrate which produces as active area of 4.50 mm^2 (3.0 mm x 1.5 mm). Whereas, a round shape shadow mask is used when the device is fabricated with plain ITO substrate (without any pattern) which results in an active area around 3.15 mm^2 (radius 1 mm). A schematic structure of thermal evaporator is as shown in **Figure 3.10**. A complete fabricated device is recommended to be annealed to improve the contact between organic active layer and metallic electrode. The devices are encapsulated in order to prolong their performance and stability for extended period of time. The encapsulation process is very useful to prevent penetration of external element such as oxygen which causes oxidation process. Such processes can cause a degradation of active material and thus reduce the device performance exponentially.

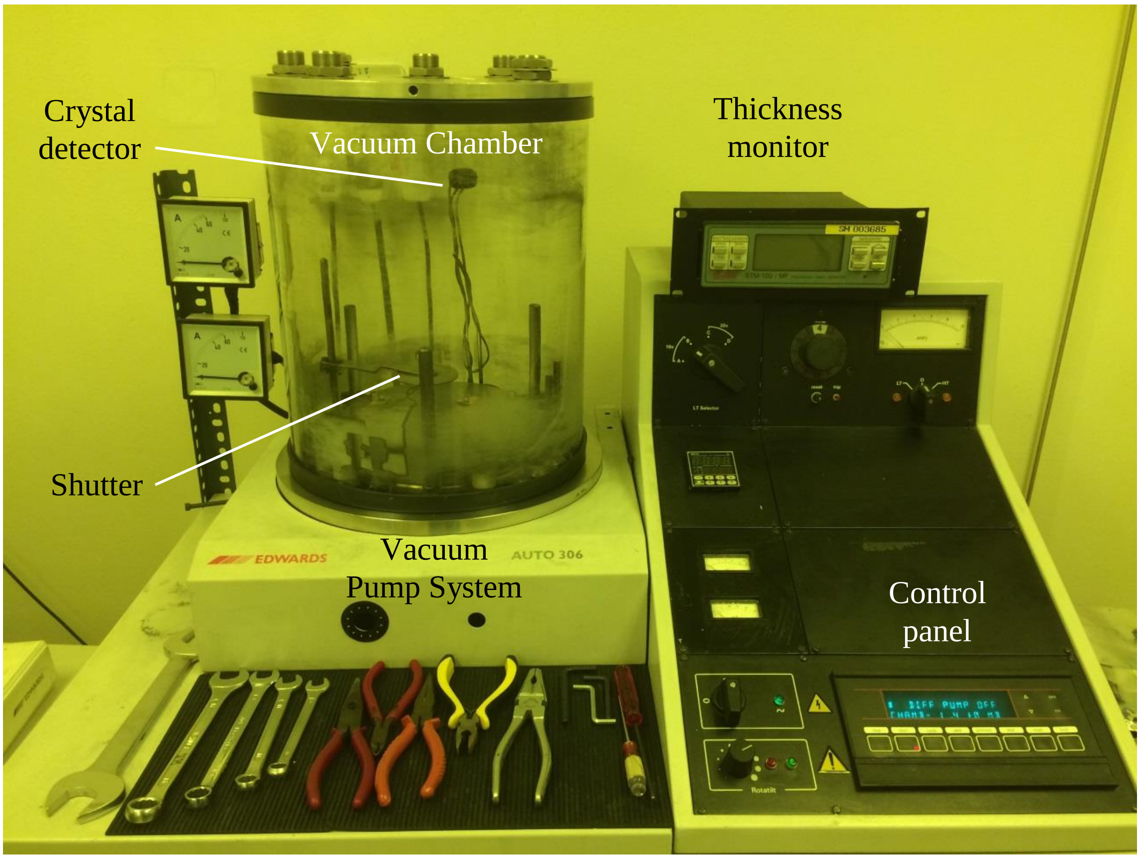

Figure 3.8 Thermal evaporator system (Edwards Auto 306).

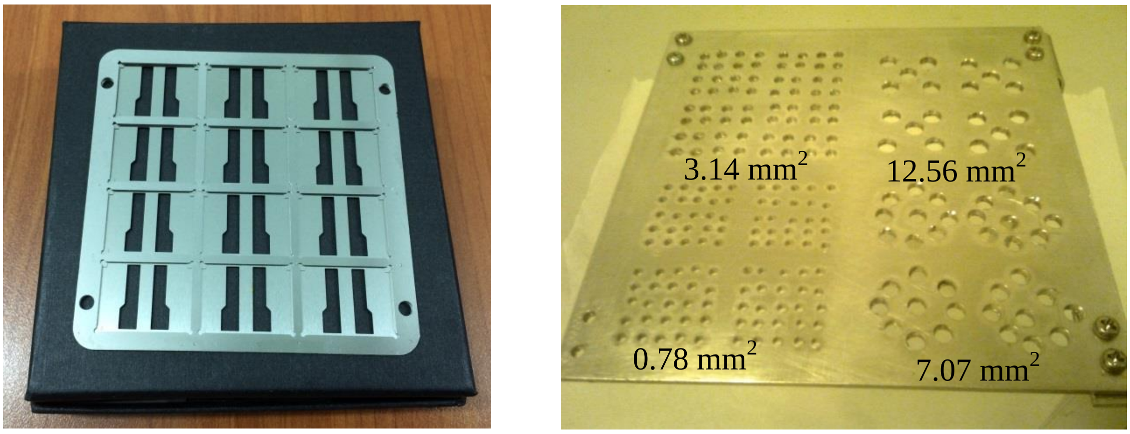

Figure 3.9 A picture of shadow mask for (a) pre-patterned Ossila ITO-coated glass substrate, and (b) plain ITO-coated glass substrate (without pattern).

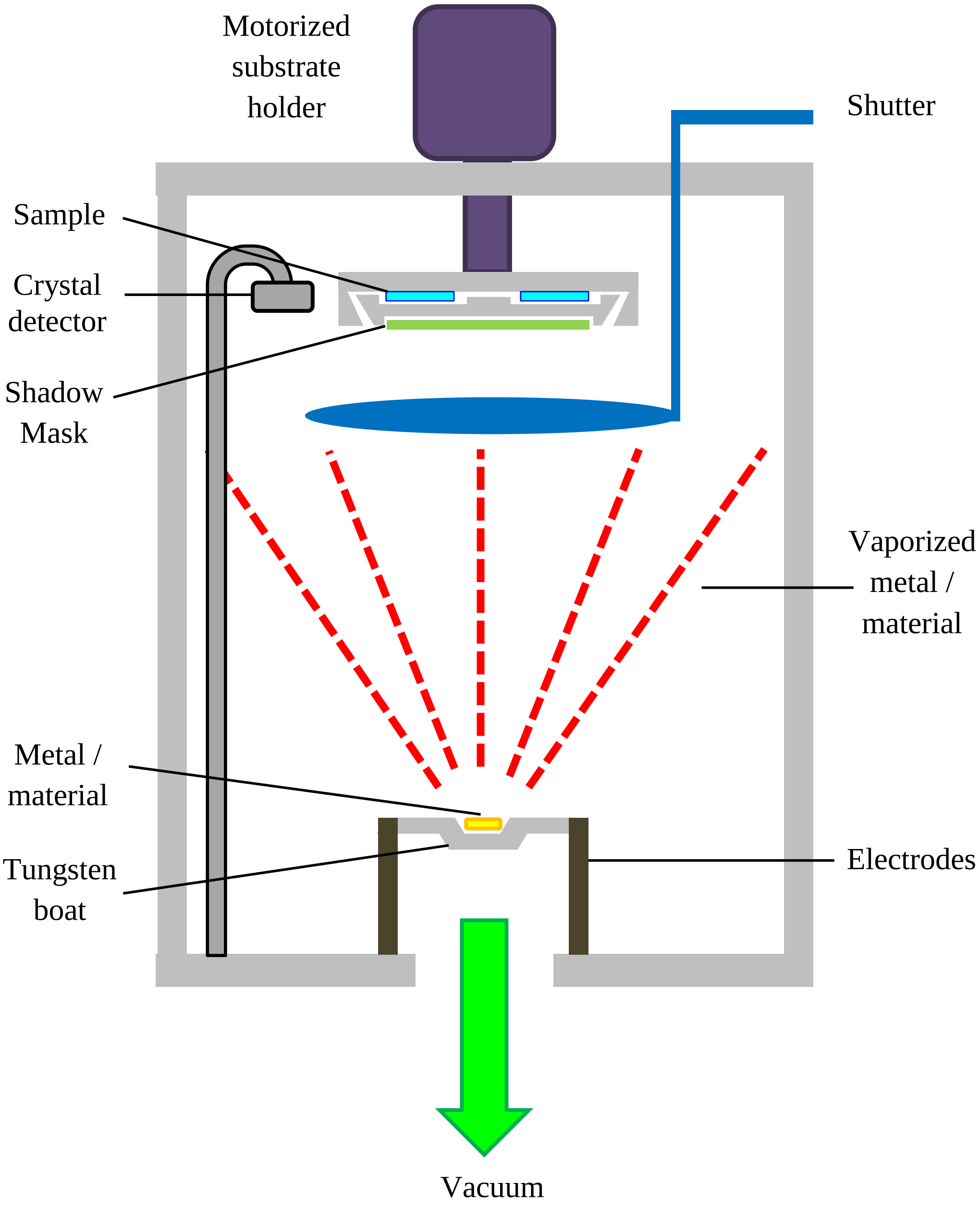

Figure 3.10 Schematic structure of physical vapor deposition (PVD) system for thermal evaporation process in the glove box.

3.2 Thin Film Characterizations

The characterizations of thin films in this study have been carried out by using surface profilometer, UV/visible/NIR, photoluminescene(PL) spectrophotometer and Raman microscope as discussed in the following sections.

3.2.1 Surface profilometer

KLA Tencor Surface profilometer (model P-6 Stylus Profiler), whose photograph is shown in **Figure 3.11**, has been used to probe the surface profile and topography of the material in order to quantify the roughness up to a resolution of 0.5 Å. This type of profiler works by a contact method in which the stylus (probe) tip moves vertically across the sample surface and measures small surface variations as a function of position with a maximum scan length of 150 mm, stylus force of 0.3 – 5.0 mg, and vertical (height) range of 327 µm. The profiler stylus tip is made of diamond with 2.0 µm 60° radius which uses a mass cantilever system to keep the tip at a constant force during the scanning process.

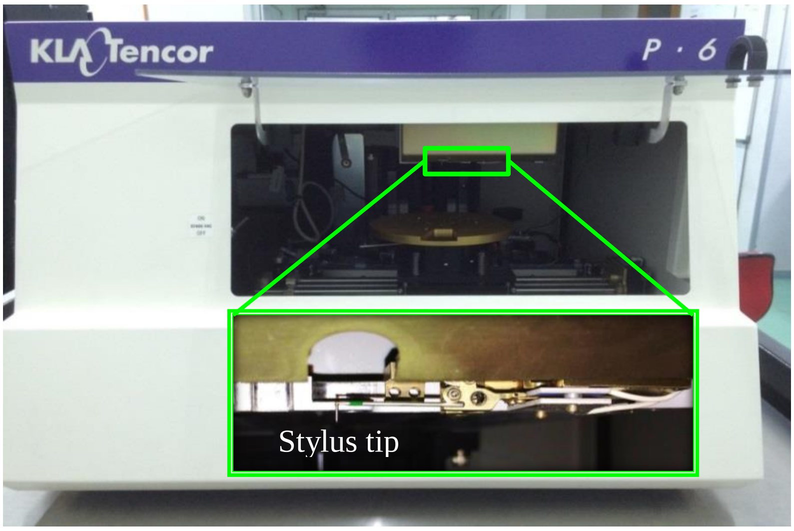

Figure 3.11 Surface profiler meter KLA Tencor (P-6).

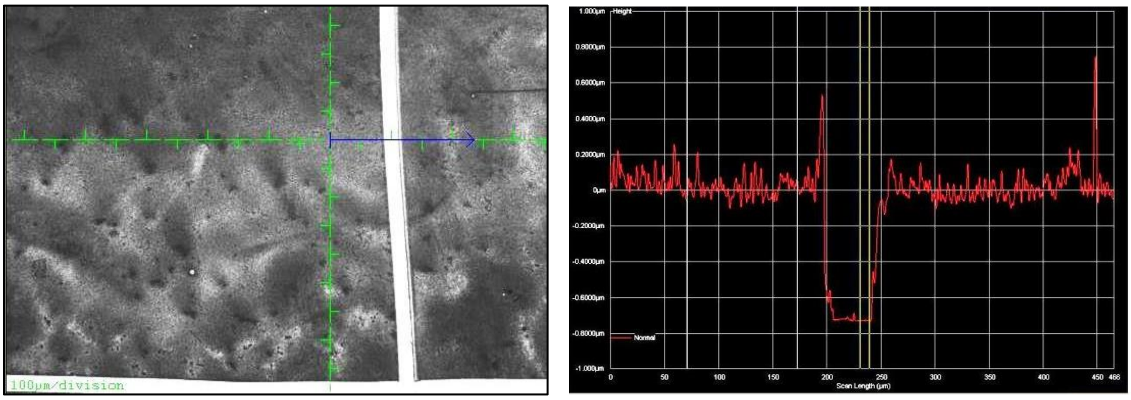

(a) (b)

Figure 3.12 Surface analysis to determine surface roughness and film thickness.

Surface profilometer is not only used to measure the surface roughness at a finest scale, but it can also be used to measure thickness of a thin film. The thickness measurement is done by preparing the thin film with a linear (see **Figure 3.12**) to form a trace of step between film and the substrate surface. The stylus tip is dragged perpendicularly across the scratched trace which detects a difference between the film and the substrate levels. The thickness of the thin film can thus be measured by comparing the distance between these two surface levels. **Figure 3.13** shows the thickness determination by moving profiler stylus on a scratched thin film surface.

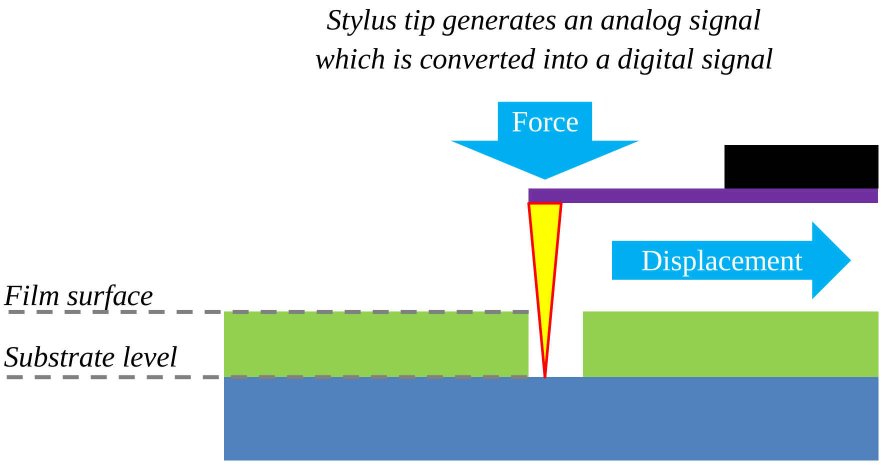

Figure 3.13 Thickness measurement by a profiler stylus.

3.2.2 Ultraviolet/Visible/Infrared (UV/Vis/NIR) Spectrophotometer

The study of interaction between electromagnetic radiations (UV/Vis/NIR) and a matter is known as spectroscopy. The spectrophotometer is an instrument which measures the amount of lightin a specific wavelength range that passes through a medium. Generally, the light that propagates through a material will have an interaction with the molecules of the respective material causing several phenomena to occur such as absorption, transmission and reflection of light by the material. These interactions occur when the energy from electromagnetic (light) photons is absorbed by the electrons in the HOMO level, thereby creating transition of electrons to the LUMO level of the material. There are several possible energy transitions involving bonded pi (π), sigma (σ), and unbonded neutral (n) electrons, namely; pi to pi star transition (π- π*), n to pi star transition (n - π*), sigma to sigma star transition (σ - σ *), and n to sigma star transition (n - σ *), where star is representing the antibonding of respective transition electrons. Normally, n - π* and π- π* transitions occur in longer wavelength range between 200 – 700 nm and noticeable in UV-visible region, while n - σ * and σ - σ * transition occur in shorter wavelength range less than 200 nm. **Figure 3.14** shows the electron transitions with respect to a wavelength range of the absorbed light.

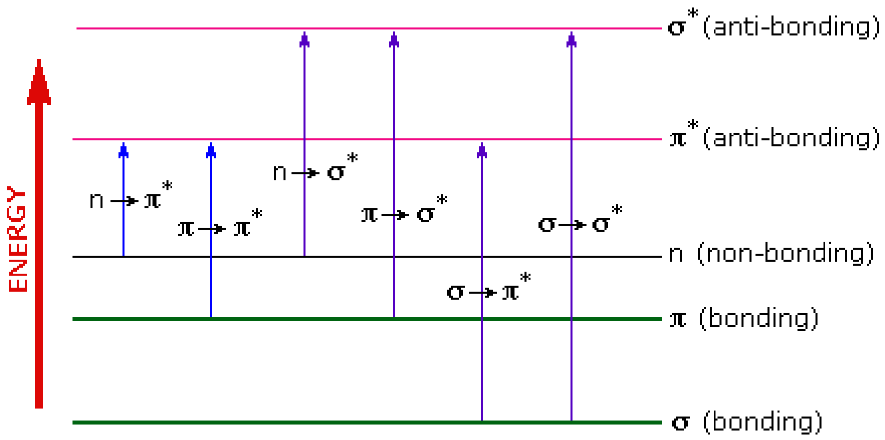

Figure 3.14 Possible transition of electrons.

Organic molecules generally consist of pi-conjugated structure with alternating single and double carbon-carbon bonds. Normally, a double bond will contribute to the pi star electron transitions either from pi or n electrons. Such transitions can be detected from the absorption of light by organic molecule using UV/Vis/NIR spectrophotometer. The characterization of thin film absorption has been done by Perkin Elmer Lambda 750UV/Vis/NIR spectrophotometer (see **Figure 3.15**) that can measure absorbance of light in the wavelength ranging from 190 to 3300 nm. It has UV-Vis resolution from 0.17 to 5.00 nm and NIR resolution from 0.20 to 20.00 nm.

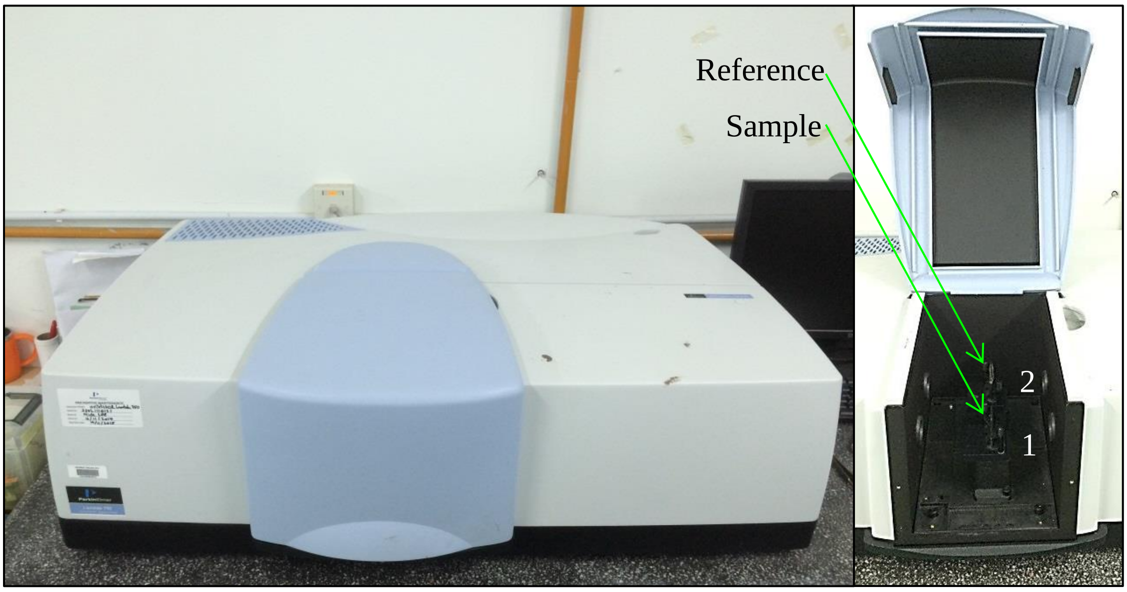

Figure 3.15 UV/visible/NIR spectrophotometer Perkin Elmer model Lambda 750.

Spectrophotometer is provided with two substrate holders; one used for the baseline calibration and other for optical characterization of organic thin film. The baseline measurement is performed by placing two identical un-coated substrates on the holders. When the baseline measurement is done, one of the substrates, placed at the first holder (labelled as 1), is replaced with a thin film coated substrate, while the other un-coated substrate remains at holder 2. The measurement of light absorption capability of the thin film is then performed with reference to uncoated substrate. The spectrophotometer uses both deutrium and tungsten lamps as light sources to provide light from the UV and NIR ranges. The light source automatically changes from deutrium to tungsten lamp at 319.20 nm wavelength, providing a continuous source of light over the whole UV/visible/NIR wavelength range. During light illumination, the built-in double holographic grating monochromators selectively narrow theincident light (band of wavelengths) to a single wavelength (colour) output. Monochromatic light then propagates to a chopper that directs the output light into two directions as; (1) sample beam and (2) reference beam, alternately. Both of the monochromatic light beams traverse through the thin film coated substrate and the reference substrate and continue to propagate to the last part of spectrophotometer which consists of highly-sensitive photomultiplier and peltier cooled detector. **Figure 3.16** shows the path of light from its source to the monochromator, chopper, sample, photomultiplier and peltier cooled detector including the programmable parameter setting during UV/vis/NIR absorption measurement.

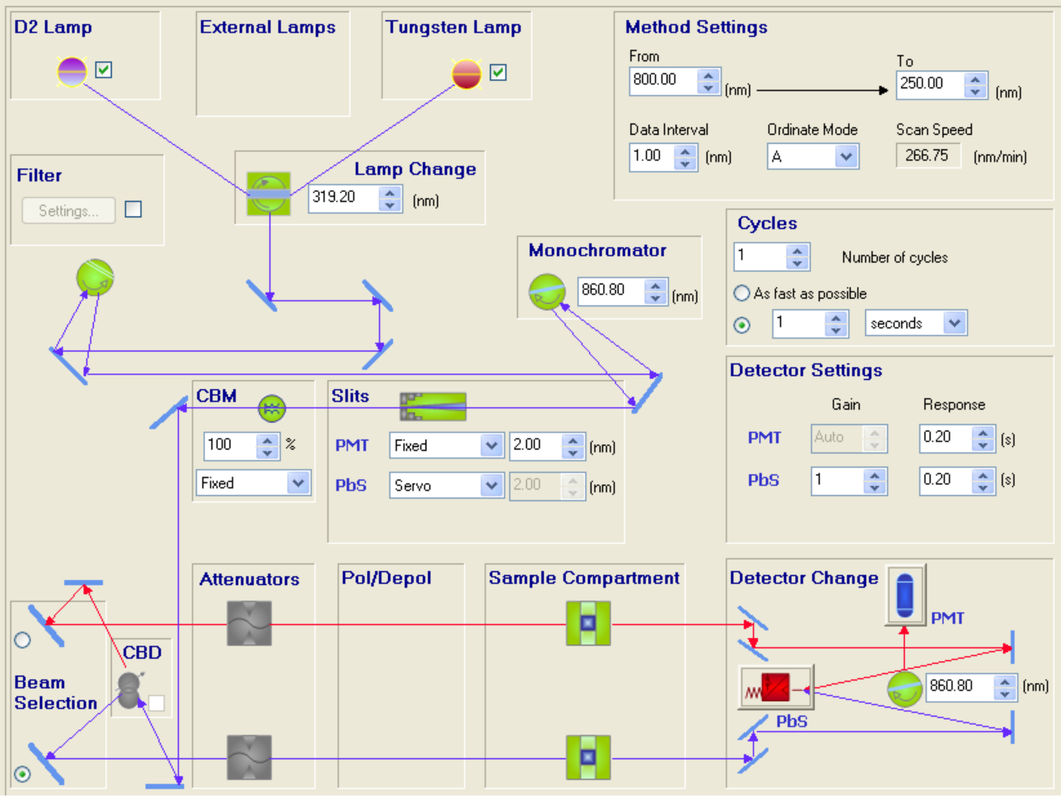

D2 Lamp ☑

Tungsten Lamp ☑

Method Settings

From 800.00 (nm) → To 250.00 (nm)

Data Interval 1.00 (nm)

Ordinate Mode A

Scan Speed 266.75 (nm/min)

Filter Settings... ☐

Lamp Change 319.20 (nm)

Monochromator 860.80 (nm)

Cycles

1 Number of cycles

○ As fast as possible

● 1 seconds

CBM 100 %

Fixed

Slits

PMT Fixed 2.00 (nm)

PbS Servo 2.00 (nm)

Detector Settings

	Gain	Response
PMT	Auto	0.20 (s)
PbS	1	0.20 (s)

Detector Change 860.80 (nm)

Figure 3.16 Method setting for UV/visible/NIR absorption measurement.

3.2.3 Photoluminescence (PL) Spectroscopy

Luminescence is the process in which the radiations or other forms of energy are converted to visible light. Photoluminescence process occurs in a material when an electron in lower energy state (valence band or HOMO energy level) excites to a higher energy state (conduction band or LUMO energy level) by incident radiations of sufficient external energy and then falls back to a lower energy state by emitting photon with a lower energy. There are several other types of luminescence such as chemiluminescence, crystalloluminescence, electroluminescence, mechanoluminescence, radioluminescence, and thermoluminescence which result from a chemical reaction, during crystallization, electric current through a substance, a mechanical action on a solid, bombardment by ionizing radiation, and the re-emission of absorbed energy when a substance is heated, respectively.

Photoluminescene (PL) gives very helpful information in both OLED and OSC studies regarding the optoelectronic properties of the photoactive materials. In the OLED application, the higher the PL, the better the material for the production of light due to large number of recombination units. Whereas for OSC application, lower magnitude of PL is desired for the production of photocurrent due to less recombination process. PL results might give initial understanding on electron-hole pair interaction, i.e., either they tend to recombine back or furhter dissociate under circumstances where energy is emitted in the form of photonic energy. **Figure 3.17** shows a photo-excitation and emission process that occurs when an electron receives sufficient energy to excite and then return back to the valence band by releasing energy.

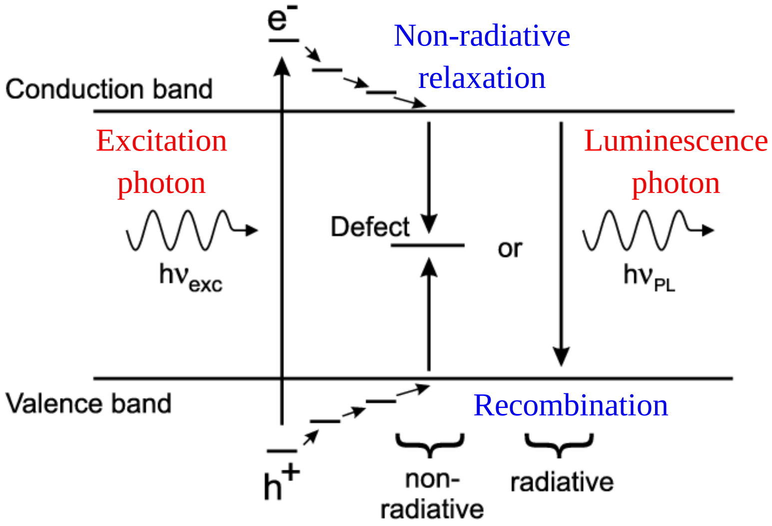

Figure 3.17 Photo-excitation and emission process.

In this study, a luminescence spectrometer from Perkin Elmer (model LS-50B) was used to measure the PL intensity of thin film sample. It is a computer controlled ratio luminescence spectrometer that is capable of measuring fluorescence, phosphorescence, chemiluminescence and bioluminescence. **Figure 3.18** shows the PL spectrometer which consists of a compartment especially designed for mounting solution sample in a cuvette or thin film on a solid substrate. The operational illustration of PL measurement is as shown in **Figure 3.19**.

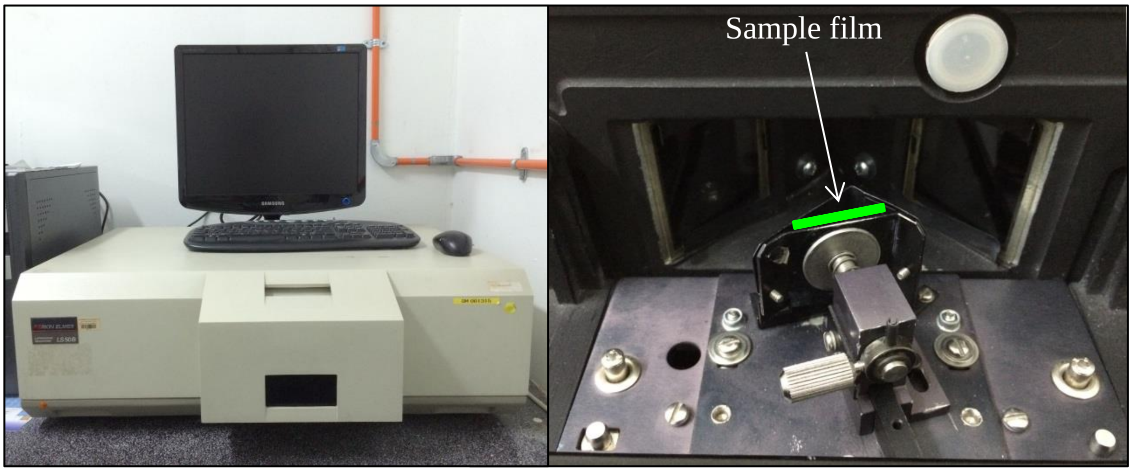

Figure 3.18 Luminescene spectrometer Perkin Elmer LS-50B for PL measurement.

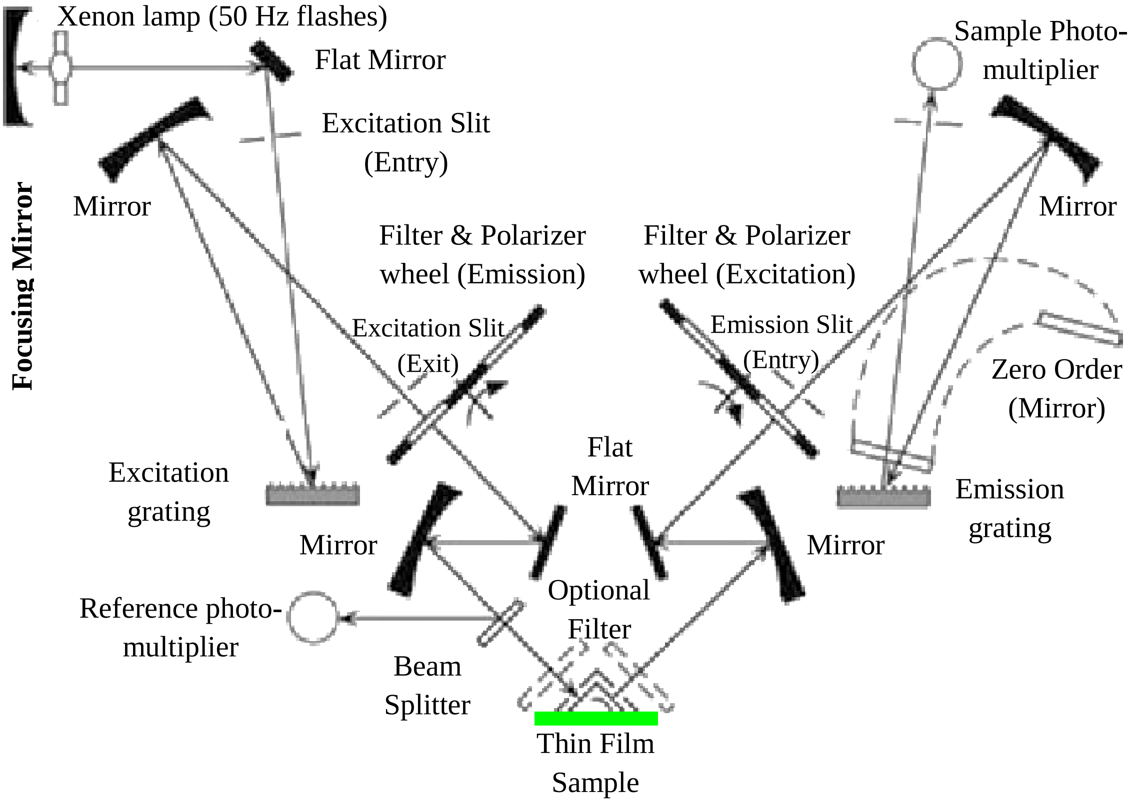

Figure 3.19 Mechanical operation of PL measurement.

This spectrometer has a Xenon discharge lamp as a light source, equivalent to 20 kW for 8 μs duration with the pulse width at half height <10 μs. The sample and reference detector are gated photomultiplier that can operate up to around 650 nm. The monochromators cover the excitation from 200 to 800 nm with zero order selectable, and emission from 200 to 650 nm with standard photomultiplier with zero order selectable. Both monochromators can be driven to any valid wavelength (200-800 nm for excitation and 200-900 nm for emission) and can scan either individually or synchronously. The PL intensity can also be measured by Renishaw inVia Raman microscope which will be discussed in the next section.

3.2.4 Raman Microscopy

When the incident light (photon) propagates into a material, it will be dispersed in two different ways; elastically (Rayleigh scattering) and inelastically (Raman scattering). In Rayleigh scattering, the incident photon that passes through a material will be emitted with the same energy and frequency but with the change in its direction of propagation. During this scattering, the material's electronic state does not change at all. While in Raman scattering, the energy of incident photon is absorbed by a material (molecule) exciting it to a virtual electronic level. The molecule then relaxes back to a lower energy level (Stokes) or higher energy level (Anti-Stokes) relative to its original state by emitting another photon. In most of the cases, the emitted photon has lesser energy than the incident photon. In Raman spectroscopy, a monochromatic light from a laser (in the UV/visible/NIR range) is used to make interaction with molecular vibration system, in which the shifting in laser photon gives information about vibrational modes in the system. **Figure 3.20** shows Jablonski diagram for the Rayleigh and Raman scattering with respect to change of molecular energy states due to sufficient amount of energy from incident laser photon.

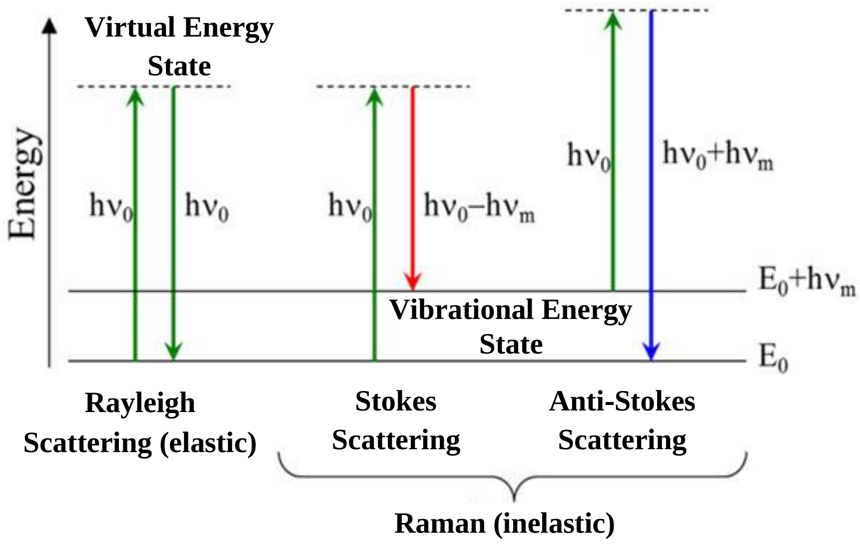

Figure 3.20 Jablonski diagram representing quantum energy transition for Rayleigh and Raman scattering.

In this study, Raman spectroscopy is done by Renishaw inVia Raman microscope. A photograph of the instrument and mechanical structure are as shown in **Figure 3.21**. For measurement, a 512 nm wavelength laser source has been used to observe Raman spectrum of organic thin films. This microscope can also carry out PL spectrophotometry by swicthing the light source to a 325 nm UV laser.

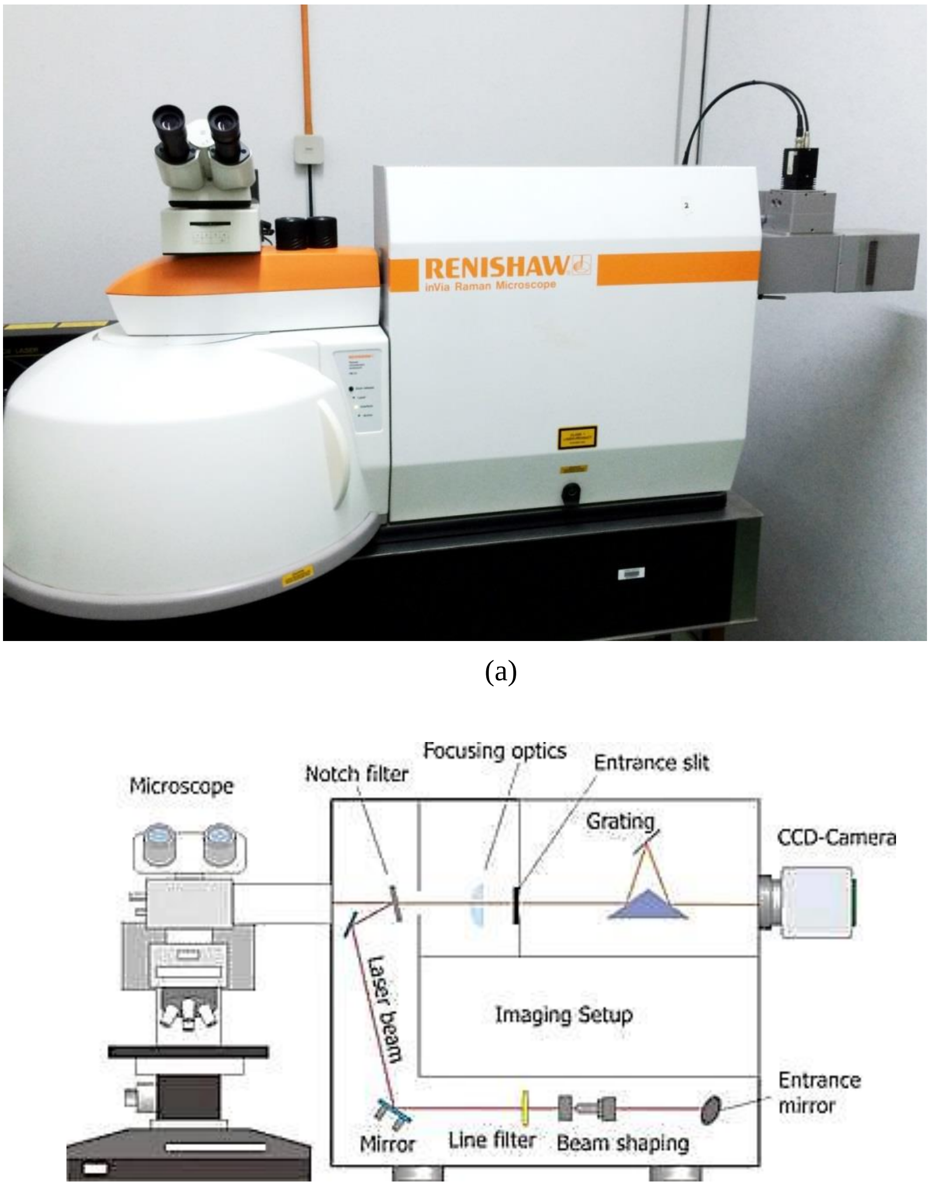

(a)

(b)

Figure 3.21 Renishaw inVia Raman microscope (a) photograph, and (b) structure.

3.3 Device Fabrication and Measurement

There are two types of devices that have been fabricated in this study; (1) practical devices for both P3HT:VOPcPhO and PCDTBT:PC$_{71}$BM blend systems, and (2) transport devices including three types of transport diodes, SHG detection diode, and transistors. The fabricated devices have been characterized with diode and transistor characterization techniques in dark and under illumination at a specific wavelength range. The fabrication of all the devices and their measurement techniques are discussed below.

3.3.1 Practical Devices

I. P3HT:VOPcPhO Photodiodes

The first phase of this study is the fabrication of OSCs by using blend of P3HT:VOPcPhO as an active layer. The two materials (P3HT and VOPcPhO) are dissolved in chloroform separately. The blend of these two materials is prepared in several compositions according to the volume ratios; 1.0:1.0, 1.0:1.5, and 1.0:2.0. Both stand-alone and blended thin films including P3HT, VOPcPhO, and P3HT:VOPcPhO films, are characterized by UV/visible/NIR spectroscopy, inVia Raman microscope and photoluminescene (PL) in order to study optical properties of the stand-alone thin films and to identify the best blended composition for OSC device fabrication. Once the most promising blend composition is selected, the OSC device are fabricated accordingly.

For OSC device fabrication, a buffer layer of PEDOT:PSS is deposited on ITO-coated glass substrate which needs to be subsequently thermally treated at 100 °C for 30 min. Then, the blend spin-coated to form a 100-150 nm thick active layer. It is recommended that the active thin film layer should be thermal annealed to improve crystallinity of P3HT moeity in the blend. Normally, annealing process takes around 30 min at 100-120 °C. The possible advantages of thermal annealing are an increase in material crystallinity, absorption intensity and range, device stability and enhancement in photo-current generation. Finally, the formation of 100 nm Al top contact on the active layer is performed in vacuum condition by means of thermal evaporation. **Figure 3.22** shows the energy band diagram for ITO/PEDOT:PSS/P3HT:VOPcPhO/Al solar cell and hopping mechanism for transport of charge carriers during photo-current generation.

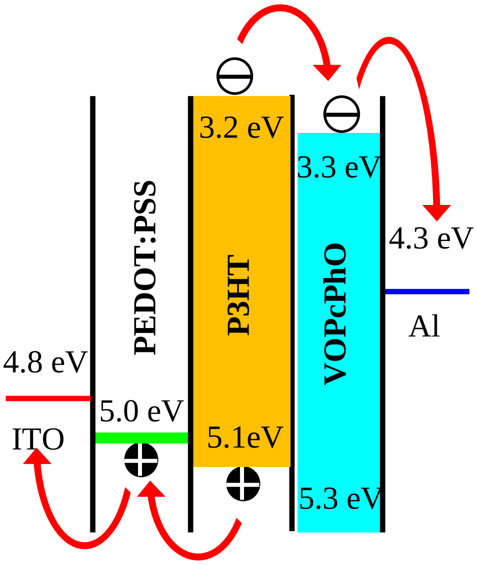

Figure 3.22 The energy diagram for ITO/PEDOT:PSS/P3HT:VOPcPhO/Al solar cell.

II. PCDTBT:$PC_{71}BM$ Solar Cells

In the second phase, the annealing process becomes a control condition and plays an important role in improved device peformance. In this second phase of the study, a well-known blend system PCDTBT:$PC_{71}BM$ is used to obtain a fundamental understanding on the charge transport behaviour in OSC devices and the effect of thermal annealing on device performance. There are three difference annealing protocols that have been followed in order to study the thermal effect especially related to device efficiency and stability. The OSC devices have been divided into three categories based on the annealing steps they undergo. All of the devices are subjected to thermal annealing process only after the deposition of PEDOT:PSS buffer layer. In the first type of OSCs, marked as OSC-1, the photoactive layer has not undergone any thermal treatment even after the aluminium contact deposition. The OSC-1 has been encapsulated right after the completion of device fabrication before it is characterized by computer interfaced I-V measurement set-up. The second type of OSC marked as OSC-2, has been annealed once after the deposition of active layer followed by the formation of Al top contact and encapsulation process. The third type of OSC marked as OSC-3, has been annealed twice; after the deposition of active layer and also after the Al top contact formation. All devices have been encapsulated by a piece of thin glass slide using an exopy resin and then cured under UV light. The I-V characterization has been carried out for all devices in fresh condition and repeated every 24 h for seven days in order to observe the stability of OSCs performance. A fundamental study on carrier transport behaviour has been performed for the most stable OSC device using EFISHG technique.

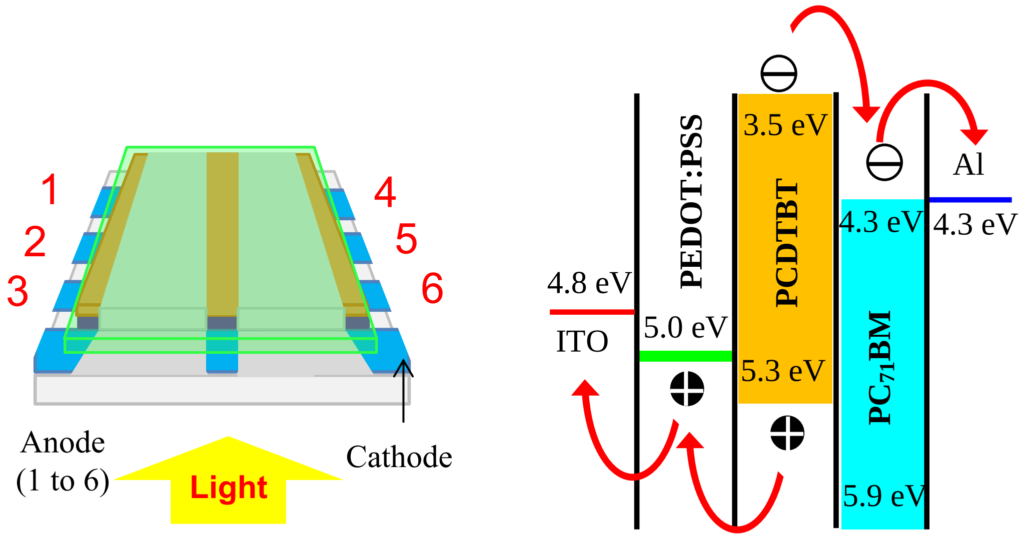

(a) (b)

Figure 3.23 (a) Encapsulated OSC device, and (b) energy diagram for ITO/PEDOT:PSS/PCDTBT:$PC_{71}BM$/Al solar cell.

Figure 3.23 (a) shows OSC structure when it is fabricated using a pre-patterned ITO-coated glass substrate and subjected to encapsulation process using a glass slide and epoxy glue. Six working OSC devices are fabricated at a time. **Figure 3.23** (b) shows the energy band diagram of the solar cell (ITO/PEDOT:PSS/PCDTBT:$PC_{71}BM$/Al) device and a possible path of electron and hole transport during photo-current generation.

3.3.2 Transport Devices

I. Transport Diode

Transport diode devices have been fabricated in order to study the selected charge carrier transport by using Keithley 236 source measuring unit (SMU). There are three types of transport diodes that are fabricated according to the selected species of charge carrier; (1) holes only, (2) electrons only, and (3) ambipolar transport diode. The construction of transport diodes is carried out by using selected charge injection layers and proper types of electrodes for anode and cathode. A basic structure of transport diode is as shown in **Figure 3.24**.

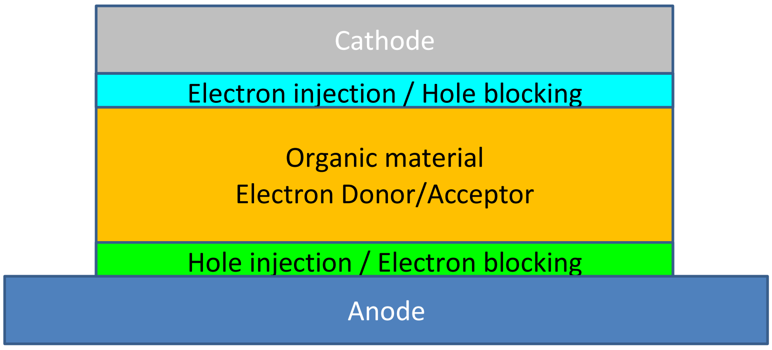

Figure 3.24 A schematic diagram for a basic structure of transport diode.

For holes only transport diode, the anode and cathode are made of ITO and gold (Au) layer, respectively. While buffer layers used in this diode are PEDOT:PSS (on ITO) and N,N′-bis (3-methylphenyl)-N,N′-diphenyl-benzidine (or TPD) layer before Au top contact. The active layer is sandwiched between these buffer layers in such a way that the ITO/PEDOT:PSS is located on the bottom while TPD/Au is on the top forming ITO/PEDOT:PSS/active layer/TPD/Au holes only transport diode. For electron only transport diode, the anode and cathode are made of aluminium (Al). Whereas, the buffer layer use in this type of diode is lithium fluoride (LiF) located between active layer and the top contact. The structure of electrons only diode is Al/active layer/LiF/Al. For the ambipolar transport diode, the anode and cathode are made of ITO and Al, respectively. The buffer layers used in this diode are PEDOT:PSS (on ITO) and LiF (before Al top contact). The structure for all the three types of transport diodes are as depicted in **Figure 3.25**.

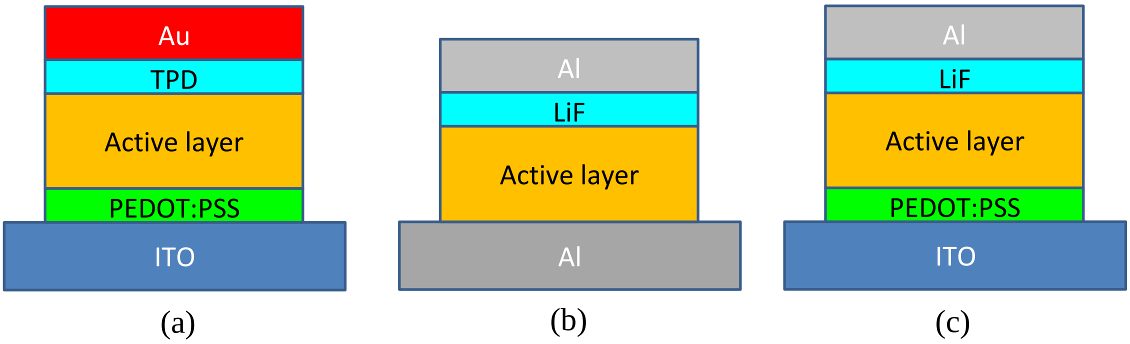

(a) (b) (c)

Figure 3.25 The schematic diagram of (a) holes, (b) electrons, and (c) ambipolar transport diodes.

PEDOT:PSS is used as holes injection layer as it is really useful to assist the transport of holes to the ITO anode (restricting the flow of electrons). Further the solubility of PEDOT:PSS in water allows a solution of active material (dissolved in chloroform) to be spin-coated on the top of PEDOT:PSS buffer layer. The PEDOT:PSS layer on ITO has been used for both holes and ambipolar transport diodes. TPD, deposited by means of thermal evaporation, has only been used in holes transport diode to allow dominant transport of holes rather than electrons. In the present study, TPD which is also a solution processable material, has been deposited by sublimation process in order to avoid two successive layers having same solvent. LiF is inorganic component that is used as electron injection layer for electrons transport diode. It can only be deposited via thermal evaporation technique in vacuum condition. The LiF layer should be around 1 nm or less, otherwise it functions as an insulator layer. The arrangement of electrodes and buffers layers has been made by considering their work function and energy levels of LUMO and HOMO of the materials as depicted in **Figure 3.26**.

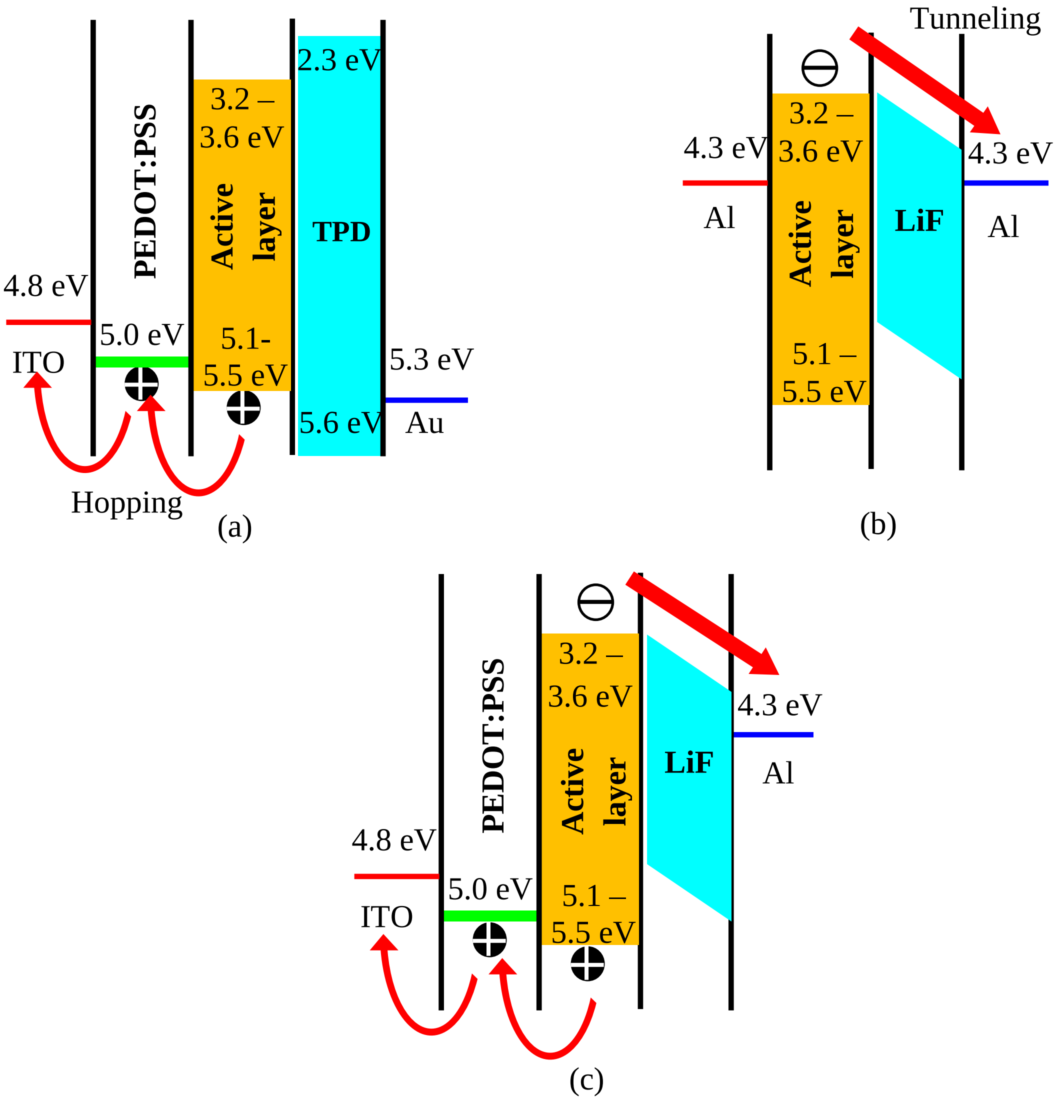

Figure 3.26 The energy diagram for (a) holes, (b) electrons, and (c) ambipolar transport diodes.

The holes transport diode allows easy hopping of holes from active layer to ITO by providing an assisting step of energy level from PEDOT:PSS work function. At the same time, a huge difference between TPD LUMO level and Au work function indirectly blocks transport of electrons from active layer to cathode. Therefore, in holes transport diode, only holes are allowed to transport throughout the device and the flow of electrons is restricted. In the electrons transport diode, the Al electrodes are used to ensure large energy difference between electrode work function and the HOMO level of active layer so as to restrict the holes transport. Besides, LiF layer is placed between photo active layer and cathode to assist electron transport from active layer to cathode by tunneling mechanism, while blocking the holes to flow in the device. An ambipolar transport device consist of both holes injection layer (PEDOT:PSS) and electrons injection layer (LiF) that allows both charge species to flow throughout the device easily. PEDOT:PSS is placed between the active layer and anode to allow holes and block electrons transport, while LiF layer is placed between active layer and cathode to allow electrons flow and block hole transport. In this way, the transport of both charge carriers (holes and electrons) is controlled to respective electrodes (anode and cathode) for efficient electric current flow. The characterization of transport devices is done by conventional I-V method in dark condition using Keithley 236 source measuring unit (SMU). The diode parameters have been extracted by analyzing the I-V curve in dark condition, when measured at higher degree of applied voltage. The charge transport behavior has been interpreted by the I-V curve in ohmic, SCLC, traps, TF-SCLC regimes as discussed in section 2.4.2.1. The SCLC regime is identified and the mobility of charge carriers has been calculated accordingly.

Other than the transport diode, there is another type of diode used to detect production of second harmonic (SH) wave, also known as second harmonic generation (SHG). This diode device is characterized under infrared (IR) light in order to observe SHG signal produced for each wavelength unit in visible region. Actually, SHG is the process in which the electromagnetic (EM) wave in the form of photons interact with a nonlinear material, forming a wave which has twice the frequency and half the wavelength, thus twice the energy of the original wave. The new wave produced, is called second harmonic wave that occurs in SHG process. For SHG, a material should be a nonlinear optical material, i.e., a material in which the dielectric polarization (P) responds nonlinearly to the electric field (E) of the light. A high intensity light source with wavelength in the infrared (IR) region is used for the production of SHG. It is believed that, only electric field E from the light source is interacting with the subject material and the relation of P and E during the SHG can be described by its polarization: $P(2\omega) = \varepsilon_o\chi^{(2)}: E(\omega)\, E(\omega)$, where ε_o is the dielectric permittivity of vacuum, $\chi^{(2)}$ is the second-order non-linear susceptibility, $E(\omega)$ is the electric field of incident laser light, and ω is the angular frequency of the incident laser. The setup of SHG spectrum detection is illustrated in **Figure 3.27**.

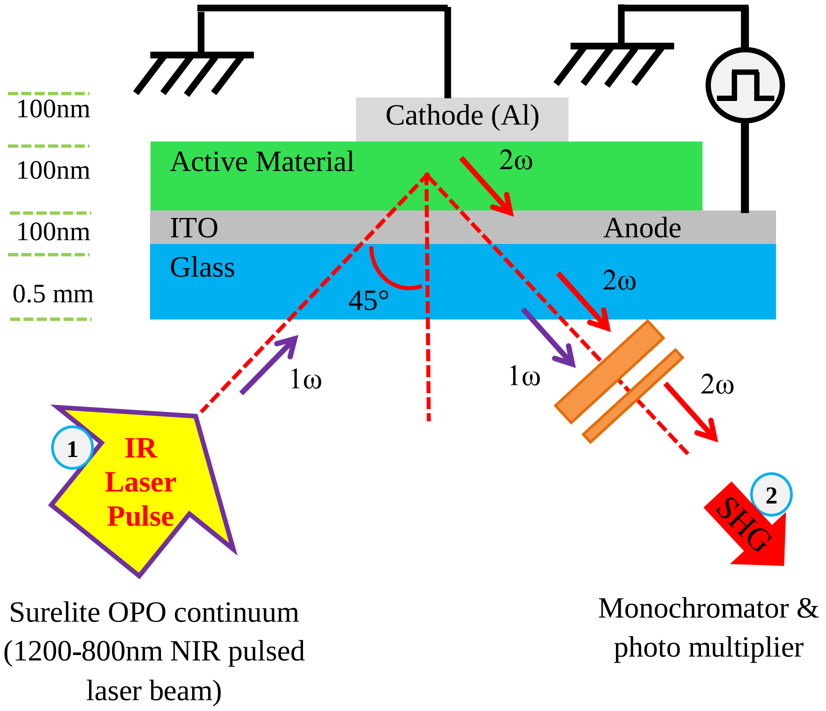

Figure 3.27 A setup of SHG spectrum detection measurement.

During this measurement, bias voltage is applied in the form of square wave (Vex = 0, +10 and -10 V) with 10 Hz frequency and a delay time of applied IR laser pulse equals 1 μs. The purpose of mentioned applied bias-voltages; 0 V (no potential), -10 V, and +10 V, is mainly to generate an electric field between the two electrodes only. In this measurement, the observation was focused on the effect of electric field towards generation of SHG but the charge carriers (holes or electrons) injection might possibly occur and affect the output results. Since the main focus of the present work is to observe the SHG generation in the presence of electric fields; zero potential (0 V), negative potential (-10 V), and positive potential (+10 V), therefore, the SHG signal is selectively probed by two different filters; (1) fundamental cut to remove NIR light and (2) band pass filter to allow only a certain range of SHG to pass through. The electrical settings, related to the laser pulse and the applied bias electric field are depicted in the following figure:

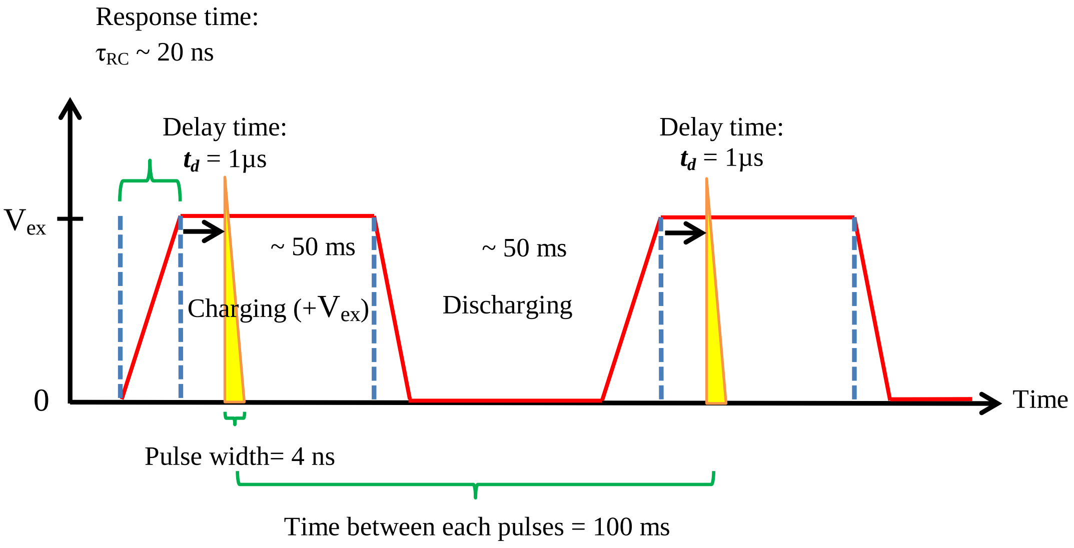

Figure 3.28 An applied IR laser pulse, and biased electric field SHG signal detection.

II. Field effect transistor

Organic field effect transistor (OFET) is fabricated using the organic materials mentioned in section 3.1.1, as its active layer. As briefly explained in section 2.4.2.4, an OFET device should consist of dielectric-coated substrate which is normally made of highly doped silicon semiconductor, a thin organic layer, and the electrodes (source, drain, and gate). Two types of OFET substrates are commercially available; (1) highly doped p-type silicon and (2) highly doped n-type silicon substrates. Both types of substrates can be used in OFET characterization and the selection is based on material transport type; holes or electrons transport. Commonly, a dopant for p-type silicon is boron, while for n-type is phosphorus. P-type silicon has higher holes concentration than electrons, while n-type silicon has opposite charge concentration. A dielectric layer is really important for OFET fabrication as it separates highly doped-silicon substrate from the organic layer. Thickness of the dielectric layer is normally in the range of 300-500 nm to avoid leakage current either from the organic layer or silicon substrate and allow the organic layer to undergo the desired electric field. Normally, a commercially available dielectric-coated layer is made of silicon oxide (SiO_2) on highly doped silicon substrate with a shiny smooth surface where the active layer is to be deposited. The substrate should be cleaned before the fabrication of the OFET. The bottom part of substrate has a rough surface and has an oxidized thin layer that should be removed by either scratching method or using a diluted hydrochloric acid (HCl) in order to provide a gate contact. Once the oxide layer is removed, a thin chromium (Cr) layer is deposited (~15 nm) as a metallizing agent before the deposition of 50 nm gold (Au) contact for gate electrode.

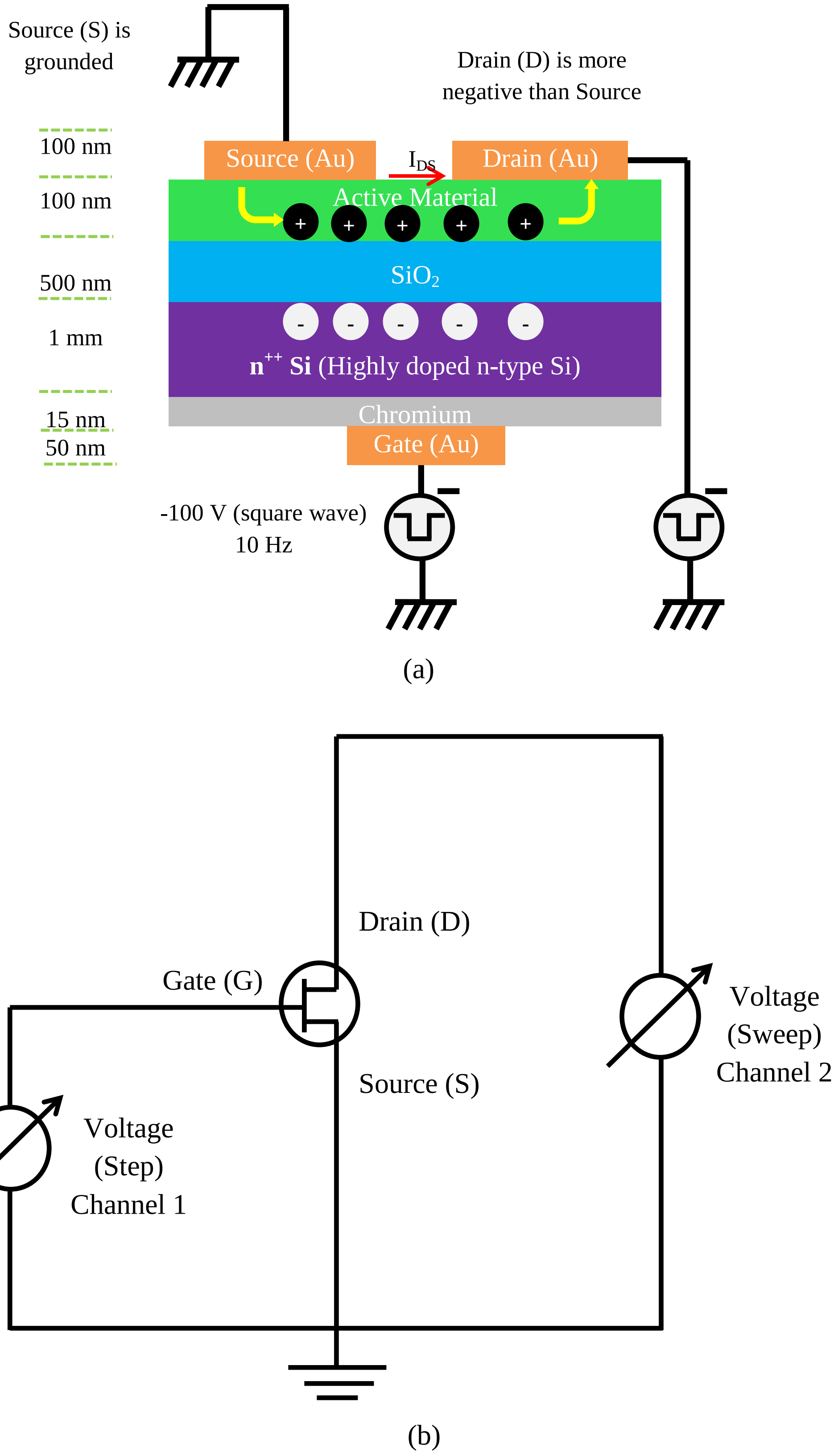

Figure 3.29 (a) Construction of OFET, and (b) electrical connection of OFET to a two-channel SMU.

The organic layer (~100 nm) is deposited on the shiny smooth surface of dielectric layer via spin coating technique. The layer should be annealed for 30 min at 100 °C. The top contacts of source (S) and drain (D) are deposited by means of thermal evaporation in a vacuum condition with a pure gold wire in a tungsten basket. The formation of source-drain (S-D) channel is performed by a micro-patterned shadow mask that gives different gaps between the electrodes normally around 30, 40, 50, 60, 70, and 80 μm.

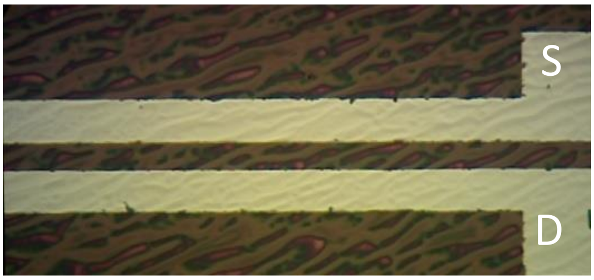

(a)

(b)

Figure 3.30 An image of (a) deposited source (S) and drain (D) electrodes with a 60 nm gap and 3 mm channel, and (b) electrical connection to the source and drain electrodes during OFET characterization.

For the OFET device characterization, the transfer and saturation characteristic for respective organic materials are obtained. Transfer curve can directly give the charge carrier species existing in a material. The exponential curves towards positive and negative applied voltages indicate a predominance of negatively charged carrier (electrons) and positively charged carrier (holes), respectively. The transfer curve is obtained from the I-V measurements of $-I_{ds}$ vs. $-V_{gs}$ for the OFET. The bias voltage that is applied to the device is taken from -100 to 100 V. Through the transfer characteristics, the materials can be identified as donor, acceptor or ambipolar. At the same time, the saturation curve shows transport of charge carriers under the influence of electric field and provides information about the field effect mobility of charge carriers. In fact both types of characterizations are important to provide a clear picture of the charge transport behavior in organic materials. However, in this study, only the transfer curve is employed to investigate the charge carrier species. The OFET device structure has thus been used in the electric field induced second harmonic generation (EFISHG) characterization for the study of charge carrier behavior.

Time-resolved EFISHG experiment requires some information from UV-Vis-NIR absorption and photoluminescence (PL) spectra in order to identify the regions where SHG may possibly be generated. High intensity NIR laser source has been used on the OFET device to generate SHG. During the experiment, the pulse source must be filtered so that only the real NIR light is applied. The electric field has also been polarized by using few polarizer's to produce parallel (p-) polarized E_o. The laser is pointed directly over the active material deposited in the S-D (channel). The SHG generation thus appears and can be observed by a CCD camera. The CCD camera can also detect NIR light from the source along with SHG generation. The fundamental cut and band pass filters are used to discard the NIR light and allow only the SHG.

Before the characterization of TR-EFISHG, several measurement parameters are needed to be fixed according to the polarity of electric field induced which are listed in the following table:

Table 3.2 The injection of holes is made by application of negative electric field induced at 100 V with 10 Hz square wave.

	Biasing voltage	Charges flow
i.	Bias voltage (V_{ex}<0 negative voltage) to the gate (G) and drain (D) , with source (S) grounded	Holes are injected which flow from Source to Drain (Carrier transport)
ii.	Bias voltage (V_{ex}<0 or negative voltage) to the gate (G), with both source (S) and drain (D) grounded	Holes are injected which flow from both Source and Drain to the middle of the channel (Carrier accumulation)

Table 3.3 The injection of electron is made by application of positive electric field induced at 100 V with 10 Hz square wave.

	Biasing voltage	Charges flow
i.	Bias voltage (V_{ex}<0 negative voltage) to the gate (G) and drain (D) , with source (S) grounded	Electrons are injected which flow from Source to Drain (Carrier transport)
ii.	Bias voltage (V_{ex}<0 or negative voltage) to the gate (G), with both source (S) and drain (D) grounded	Electrons are injected which flow from both Source and Drain to the middle of the channel (Carrier accumulation)

Table 3.2 and **3.3** explain the flow of hole and electrons during their transport and accumulation processes and also mention the required voltage polarity applied at the source (S), drain (D), and gate (G) of the OFET device.

A nonlinear or non centro-symmetric material is the requirement to produce SHG. When the material is centro-symmetric, its susceptibility $\chi^{(2)}$ is equal to zero. Therefore, it has to be broken, using static electric field from the UV laser, so that a nonzero timeaveraged polarization field (or non-zero $\chi^{(2)}$) can be produced. In this case, the second-order polarization P(2ω) by incident laser light is given by, $P(2\omega) = \varepsilon_o\chi^{(3)}:E(0)\,E(\omega)\,E(\omega)$, where $\chi^{(2)}$ is the third-order non-linear susceptibility and E(0) is the static local electric field. By detecting the EFISHG from centro-symmetric material, static electric field can be observed in the material. The static electric field E(0) is the sum of external electric field E_{ext} and space charge field E_{sc}, where $E(0) = E_{ext} + E_{sc}$. Accordingly, the injection of charge carriers and their transport behavior can be directly observed by probing E_{sc}.

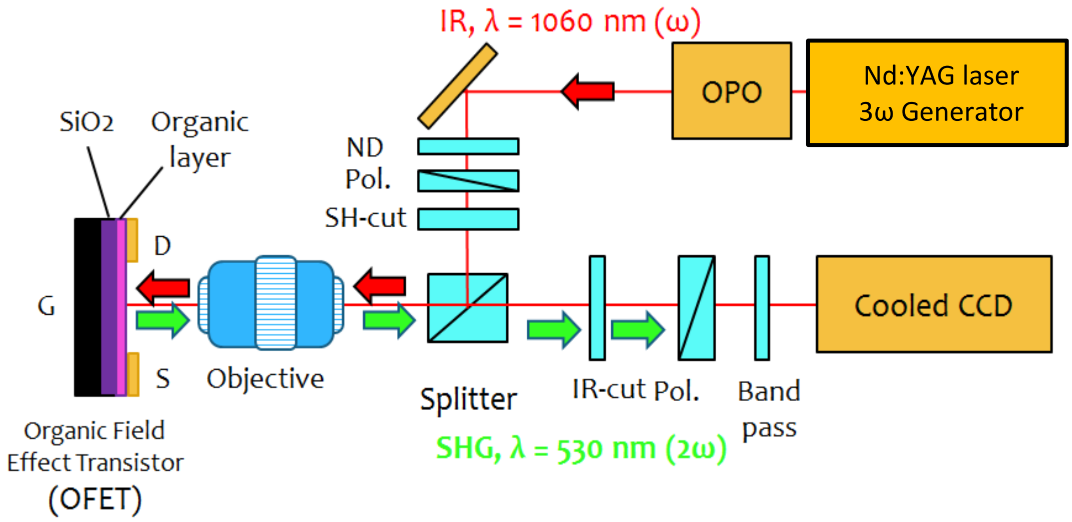

Figure 3.31 An EFISHG setup used to probe the charge carrier motion.

From the manipulation of the induced electric field, the species of charge carriers can be selectively chosen and tuned to flow either as carrier transport or carrier accumulation. From the recorded charge carriers flow, the second harmonic mobility can be calculated independent of the time consumed during the charge injection. Program settings for both transport and accumulation of charge carriers are shown in **Figure 3.32**. **Figure 3.33** shows the charge carriers transport while **Figure 3.34** shows the charge carrier accumulation for two different applied voltage polarities.

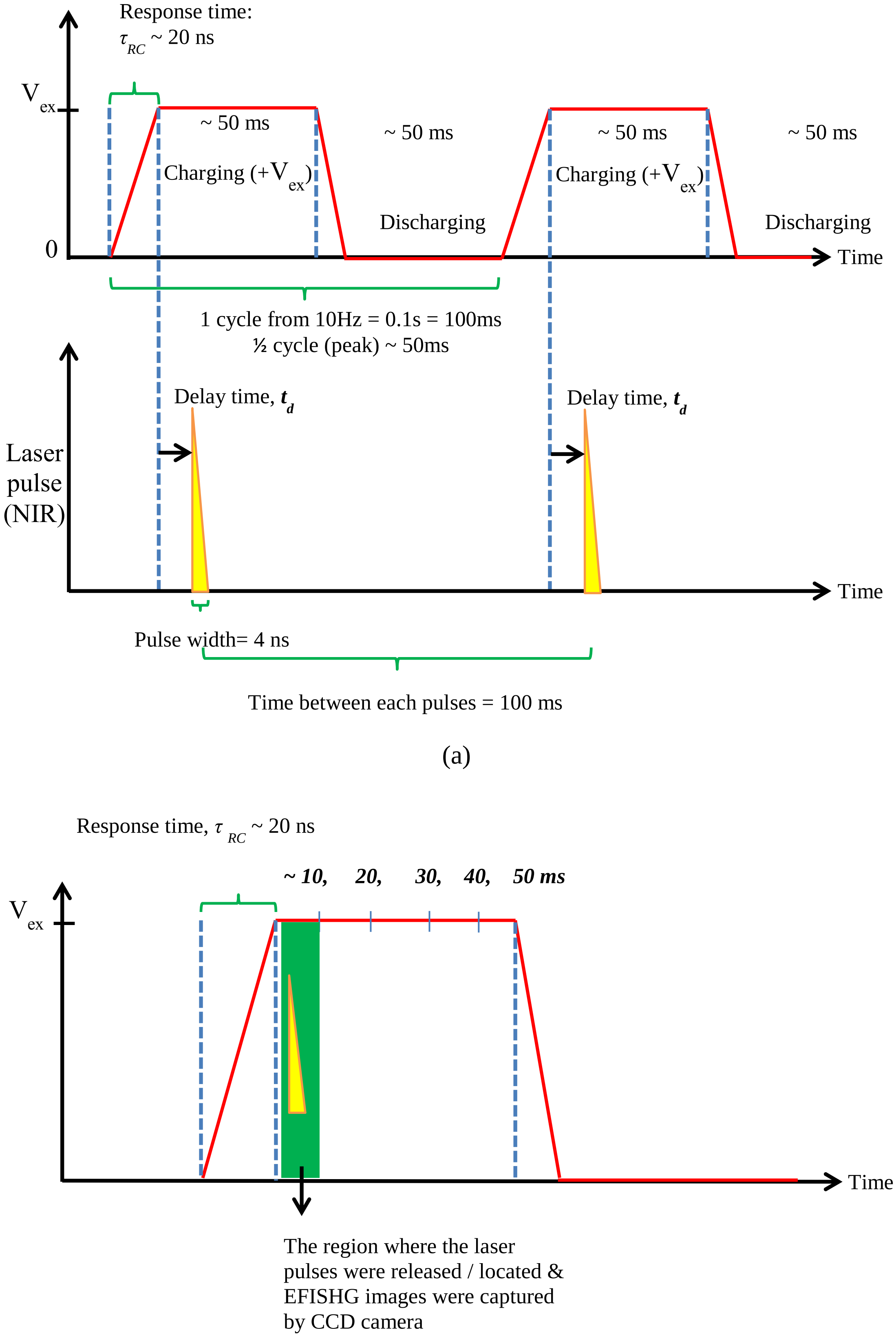

(a)

(b)

Figure 3.32 Program settings for both transport and accumulation of charge carriers measurements.

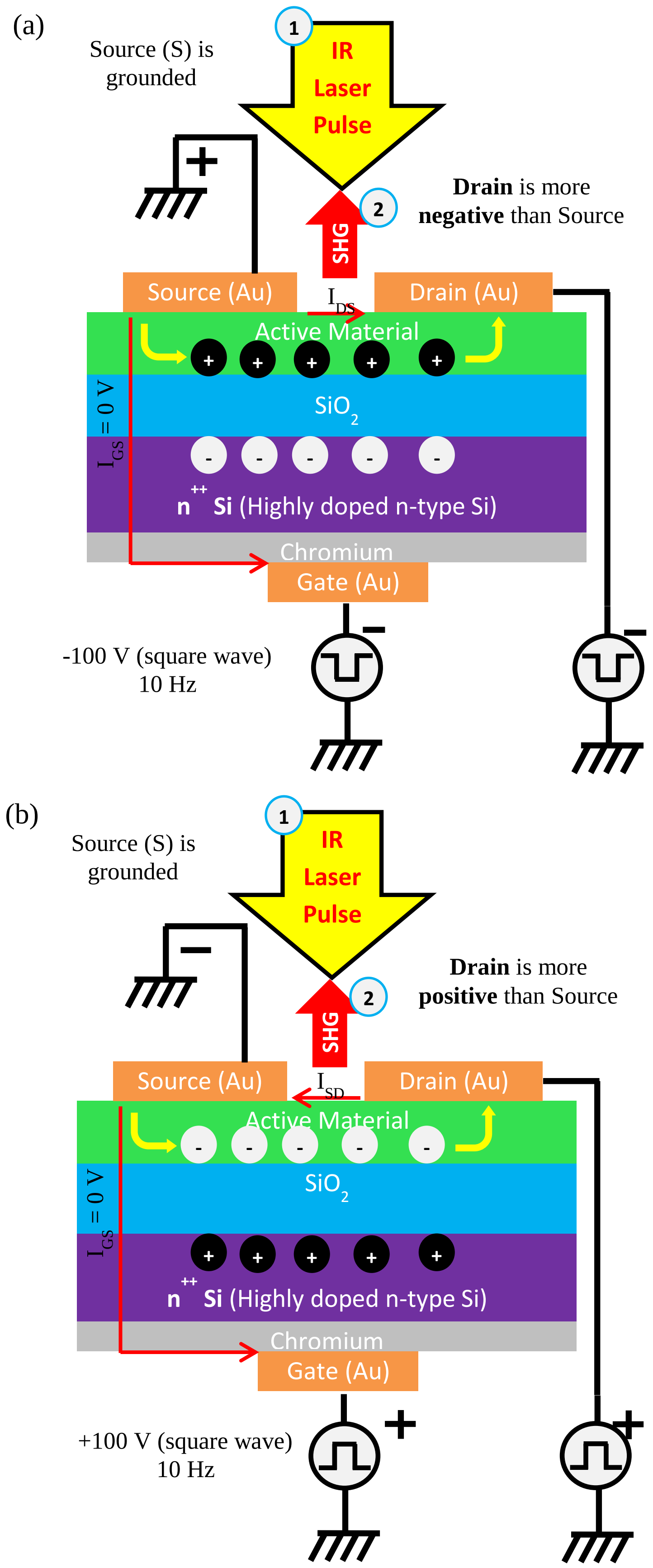

Figure 3.33 Transport of charge carriers with (a) negative bias voltage, and (b) positive bias voltage at gate.

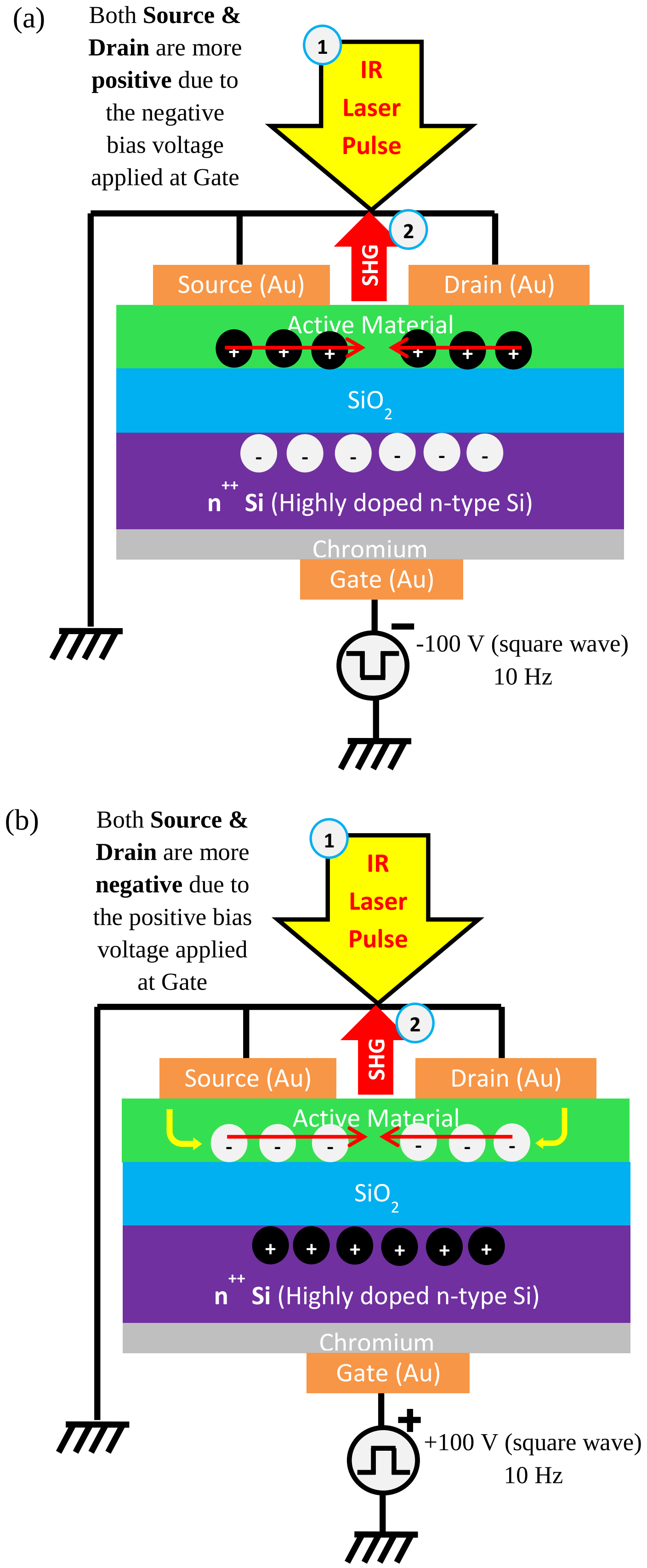

(a) Both **Source &** **Drain** are more **positive** due to the negative bias voltage applied at Gate

(b) Both **Source &** **Drain** are more **negative** due to the positive bias voltage applied at Gate

Figure 3.34 Accumulation of charge carriers with (a) negative bias voltage, and (b) positive bais voltage at gate.

3.3.3 Measurements

I. Diodes

A diode is an electronic device that has two terminals (positive and negative) which allows the current to flow in one direction and blocking it from flowing in the opposite direction. The current flows from the positive to the negative terminal in forward bias condition while in the reverse biased state it flows in the reverse direction (negative to positive terminal). Actually, there are many types of diodes but in this study, only two types of diodes (transport and photo-ssitive diodes) have been fabricated for measurements in dark and under illumination at selected wavelengths. Each diode can be distinguished by its current-voltage (I-V) characteristics. The measurement of I-V characteristics requires a sensitive ammeter, voltmeter, voltage source, and current source. Normally in diodes I-V test, a voltage source is provided to the device in a wide range and then the generated current is measured accordingly. The measurement is usually performed in sweep voltage mode in the dark condition, which is suitable for the characterization of transport diode. For photo-sensitive diodes, a higher current will be generated in the presence of light and the modulus value of short-circuit current is increased upon the exposure of light, which has been discussed in section 2.3. In this study, a computer interfaced Keithley SMU unit (see **Figure 3.35**) has been used to carry out I-V characterization for all the devices.

Figure 3.35 A single channel Keithley 236 source measure unit (SMU).

For the case of photo-sensitive diodes such as OSCs and ligth sensors, the devices were placed under the Oriel 67005 solar simulator. **Figure 3.36** shows a measurement setup for the characterization of both transport and photo-sensitive diodes in a close dark compartment. **Figure 3.37** shows the electrical connections between the device and Keithley 236 SMU system for I-V characterization.

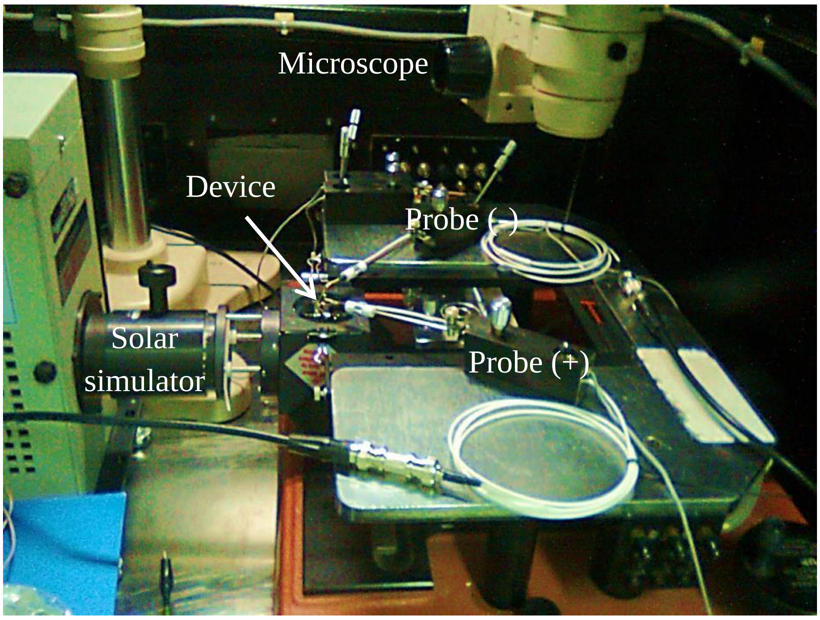

Figure 3.36 A probe station providing electrical connection between device electrodes to the computer interfaced I-V measurement system.

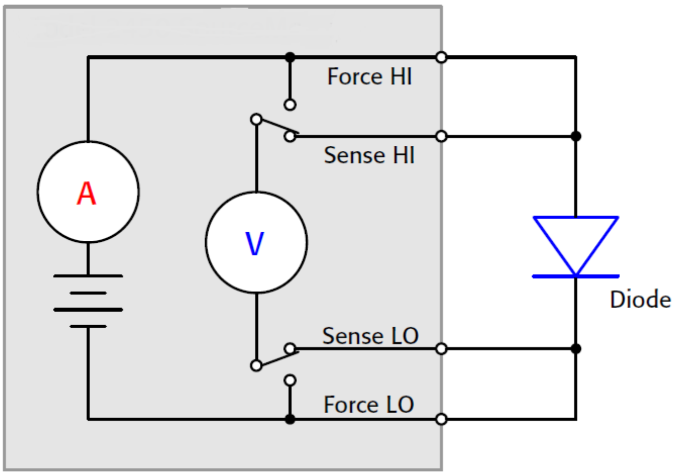

Figure 3.37 Electrical connections of diode for I-V characterization.

II. Transistor

Transistor is a three-terminal device that consist of a source (S), drain (D), gate (G), for controlling the S-D current by generated electric field, and channel through which the current flows. Normally, the source is grounded while the drain is biased with positive or negative applied voltage. The gate terminal is also biased with the same polarity of applied voltage but the value of applied electric field can be varied especially during the saturation characteristic measurements. Since transistors have more than two terminals, they require more than one SMU in order to carry out I-V measurements. However, a two-channel SMU can perform most characterizations on a single field effect transistor (FET). **Figure 3.38** shows a photograph of a two-channel SMU unit Keitley 2612B that can evaluate transistor characteristics simultaneously. **Figure 3.39** shows electrical connections made to the source and drain terminals. **Figure 3.40** shows a circuit diagram illustrating a two-channel SMU for I-V characterization of an OFET device.

Figure 3.38 A two-channel Keithley SMU model 2612B for characterization of a transistor.

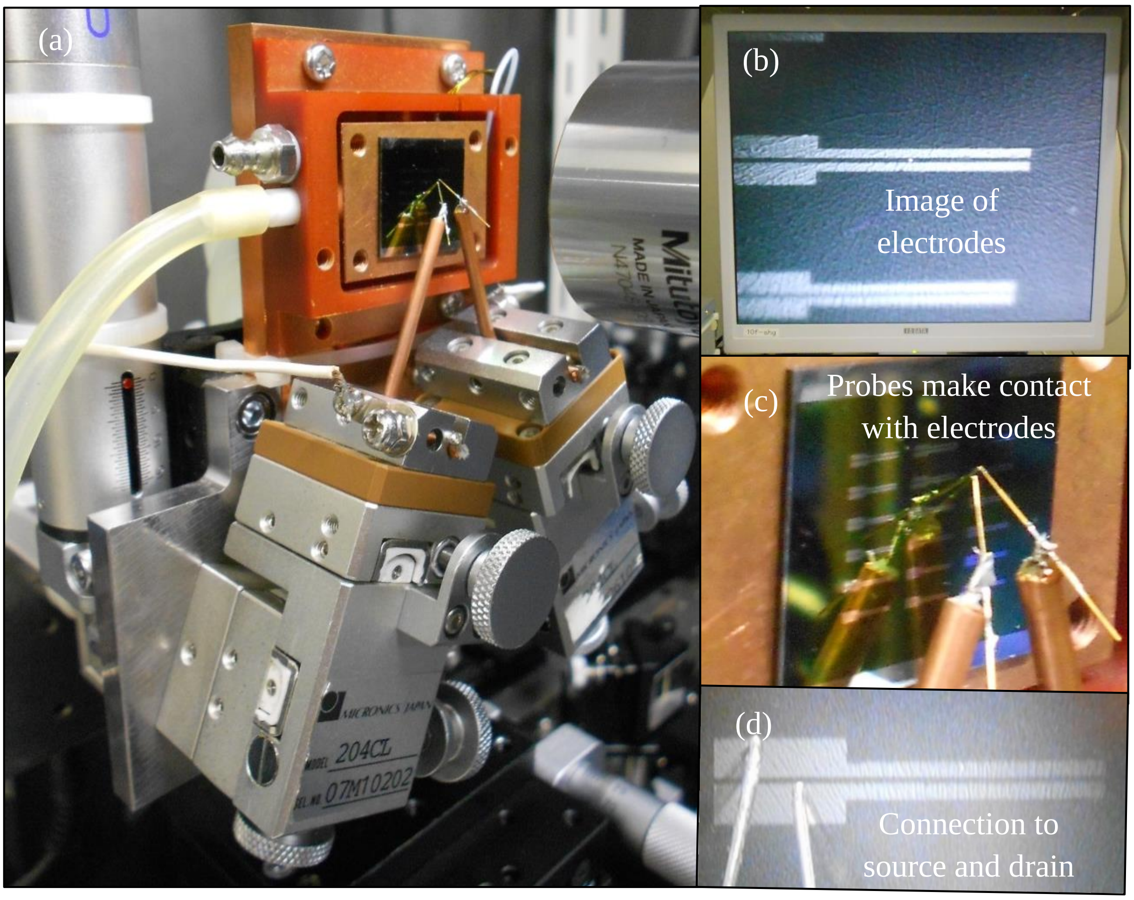

Figure 3.39 Electrical connections to the source and drain terminals and an OFET holder for gate connection.

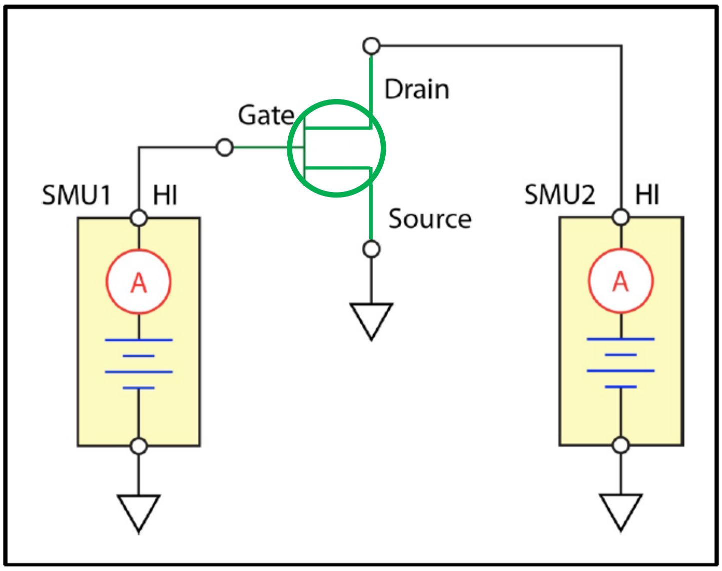

Figure 3.40 A circuit diagram showing a two-channel SMU (Keithley 2612B) for I-V characterization of an OFET.

CHAPTER 4 : CHARACTERIZATION OF ORGANIC MATERIALS

In this chapter, two types of characterizations are presented; one for the study of organic thin films and second for the study of charge transport in electronic devices. Optical characterization of organic thin films was carried out by using UV/vis/NIR spectrophotometer, PL spectrometer, and Raman microscope in order to investigate the absorption ability, the change in PL, and vibrational modes for each material, respectively. While for the charge transport investigations, the measurements were performed using I-V conventional method, FET transfer characterization, and EFISHG technique. These characterization are further divided into two parts according to the blend system used for device fabrication; part 1, P3HT:VOPcPhO, and part 2, PCDTBT:PC$_{71}$BM.

The transport study of P3HT:VOPcPhO blend system was performed entirely by I-V conventional method in order to highlight its charge carrier transport behavior as it is most suitable for photodiode application. The OFET device has also been fabricated with this blend system for further characterization especially EFISHG measurement. However, the blend did not show any significant change in SHG signals with variation of induced electric fields, therefore, this method was considered not suitable for charge transport characterization method of this kind of mixture materials. Thus, further characterization of P3HT:VOPcPhO in the form of OFET was skipped and only by diode I-V analysis was used for explaining charge transport behavior of P3HT:VOPcPhO blend system. Due to such limitation, PCDTBT:PC$_{71}$BM blend was then taken up and studied for charge carrier transport in the form of OFET. The second blend system has been successfully characterized using I-V transfer characteristic in OFET form and EFISHG due to its compatibility with such techniques.

4.1 Part 1: Investigation of P3HT:VOPcPhO Bulk Heterojunction as a New Blend System for Optoelectronic Applications

4.1.1 Characterization of VOPcPhO and P3HT films

I. UV-Vis-NIR Spectroscopy

The wavelength dependent absorption spectra of P3HT, VOPcPhO and binary blend P3HT:VOPcPhO (1:1) thin films are shown in **Figure 4.1**. Both the P3HT and VOPcPhO components lie in the range 450-750 nm of the visible spectral region. However, the spectral range of absorption for each single component is limited, but when combined together, these materials are well suited for photovoltaic applications. In the P3HT spectrum, the highest peak exists at 518 nm. The P3HT also indicates two shoulders at 550 nm and 600 nm which represent vibrational excitations due to crystalline P3HT. It can be seen from **Figure 4.1** that no absorption takes place beyond 650 nm in P3HT. Therefore, it seems feasible to add a candidate from the metal-phthalocyanine group, VOPcPhO in this case, to extend the absorption to larger wavelengths in the red region. The absorption spectrum of VOPcPhO shows the main absorption at 665 nm and 715 nm (Q-band) besides the characteristic Soret absorption bands in the region of 300-500 nm. The VOPcPhO is perfectly suited to extend the absorption spectrum of donor-acceptor blend P3HT:VOPcPhO to a larger wavelength. The blend film exhibits the absorption spectrum, which includes features of the two components P3HT and VOPcPhO. The visible spectrum of P3HT:VOPcPhO blend film reveals a prominent increase in the absorption of the P3HT shoulder at 550 nm, which is almost equal to the peak of pristine P3HT film.

This results in the broadening of the absorption band. The increase in the absorption may be associated with better ordering structure. The appearance of shoulder in P3HT in the blend P3HT:VOPcPhO indicates that the crystallization of P3HT is not hindered by the presence of VOPcPhO, rather both the materials merge well. The broad spectrum contributes to greater light harvesting and is capable of absorbing at longer wavelengths without diminishing the shorter wavelength absorption. The absorption feature of the blend film would help to improve absorption efficiency of the photovoltaic devices allowing for high photocurrent throughput. However, this spectral broadening is useful only if the donor (P3HT) is ultimately able to inject an electron to acceptor (VOPcPhO) layer upon photoexcitation (C. P. Chen et al., 2008; Sun et al., 2006; Thompson, Kim, & Reynolds, 2005).

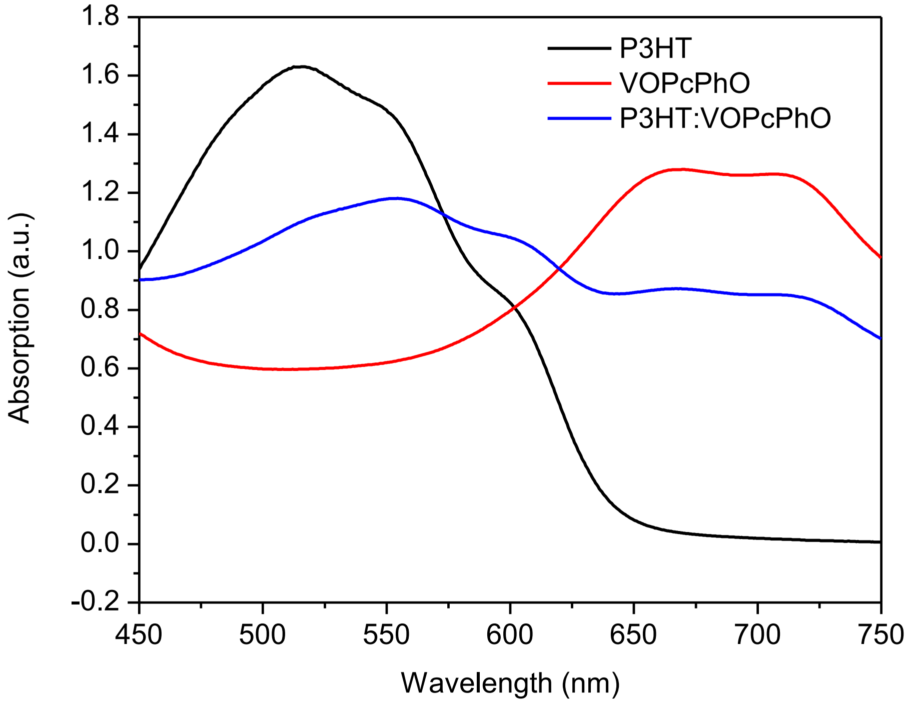

Figure 4.1 UV-Vis absorption spectrum of P3HT, VOPcPhO, and P3HT:VOPcPhO (1:1) films on glass substrates.

II. Photoluminescence (PL)

The photoluminescence (PL) of P3HT, VOPcPhO and their blend are studied for quenching phenomena in order to compare their photo-induced charge transfer efficiencies. **Figure 4.2** shows the PL spectra of VOPcPhO, P3HT, and the blend of P3HT:VOPcPhO (1:1) thin films, measured at room temperature. The PL spectra in the range from 400 to 1000 nm, of the thin films and their blends were obtained by an excitation wavelength of 325 nm.

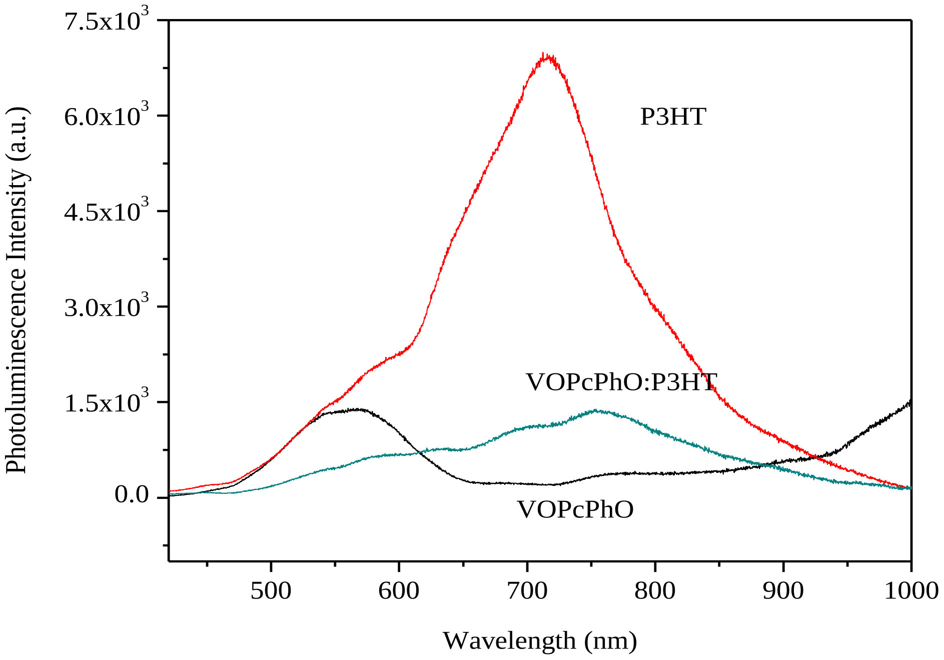

Figure 4.2 Photoluminescence spectra of P3HT, VOPcPhO, and the blend of P3HT:VOPcPhO (1:1) thin films.

The PL of the P3HT, with strong emission peak at 717 nm and a shoulder at 605 nm, lie near the red region. These PL results of P3HT are consistent with the findings reported in the literature (C. P. Chen et al., 2008). The strong PL signal can be ascribed to the first vibronic band, whereas the shoulder may result due to the pure electronic transition. The PL emission peak at the longer wavelength indicates ordering in P3HT (D.E. Motaung, Malgas, & Arendse, 2010; David E. Motaung et al., 2009). The PL spectrum of VOPcPhO shows the emission in the green region (530-600 nm) with its broad peak at around 555 nm. The main luminescence of the VOPcPhO seems to be red shifted as it is obvious from the onset of this peak around 945 nm. It is evident from **Figure 4.2** that when VOPcPhO is introduced in the P3HT matrix, the intense PL of the blend is significantly quenched and red shifted. The highly efficient photoluminescence quenching suggests a profound photo-induced charge transfer in the blended film. The excitons produced during the PL have a limited lifetime and they decay or dissociate during charge transfer process. A photo-induced charge transfer process is generally considered the most common way to dissociate excitons into free electrons and holes (David E. Motaung et al., 2009). The PL measurements show that one of the materials acts as acceptor as it is expected from the energy diagrams that VoPcPhO would be an acceptor material.

Table 4.1 The peaks of PL emission (λ_{max}) and their corresponding emission intensities (In Em) for P3HT, VOPcPhO, and VOPcPhO:P3HT thin films.

Entity	**Peak**		**Shoulder**	
	λ_{max} (nm) Em	**In Em**	**λ_{max} (nm) Em**	**In Em**
VOPcPhO	555	1399	--	--
P3HT	717	6951	605	2291
VOPcPhO:P3HT	757	1338	697	1077

III. Raman Scattering

During Raman measurements, laser source of 514 nm wavelength was used. The micro-Raman spectra of VOPcPhO, P3HT and the blend VOPcPhO:P3HT are shown in **Figure 4.3**.

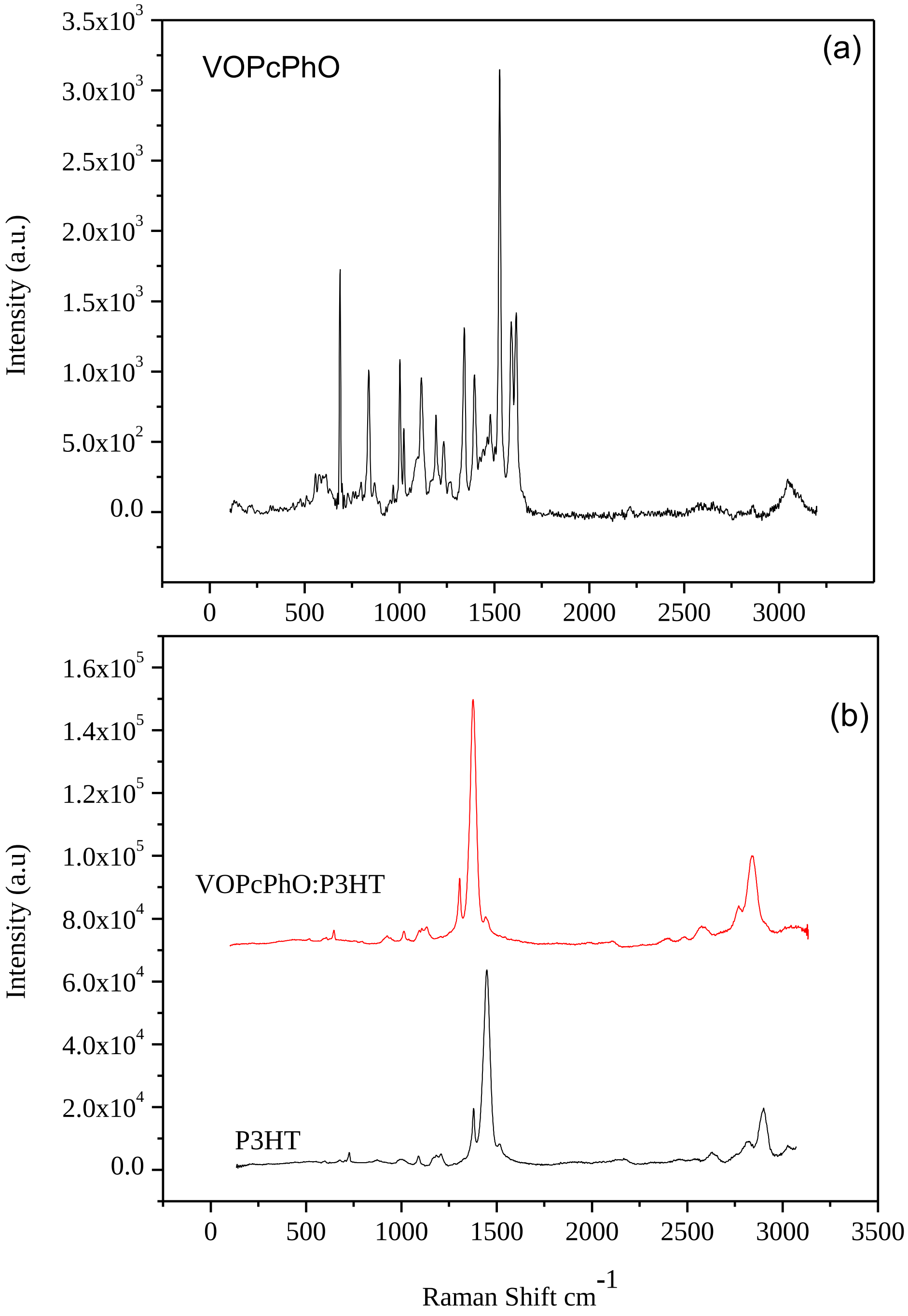

Figure 4.3 Raman spectra of (a) VOPcPhO and (b) P3HT, and P3HT:VOPcPhO blend films.

Table 4.2 Raman shifts of VOPcPhO, P3HT, and VOPcPhO:P3HT blend films.

Observed Raman shifts (cm^{-1}) and band intensities with assignment of the principal bands.ν: stretching vibration; δ: in-plane deformation vibration; γ: out-of-plane deformation vibration;

VOPcPhO	P3HT	P3HT:VOPcPhO	Approximate description of vibrations
		3109w	ν_{CH}
3049w	3052w		ν_{CH}
	2903s	2908s	ν_{CH}
	2814m,sh	2830m,sh	ν_{CH}
1610s			ν_{CC}
1530vs	1509m,sh	1520m,sh	ν_{CC}
1474m,sh	1451vs	1450vs	ν_{CC}
1396m	1373s,sh	1375s,sh	ν_{CC}
1340s			ν_{CC}
1229w			δ_{CH}
			δ_{CH}
1195m	1194w	1196w	δ_{CH}
1117s			δ_{CH}
	1094w	1084w	δ_{CH}
1028m,sh			δ_{CH}
1005s		1006w	δ_{CH}
834s			γ_{CH}
	727w	727w	γ_{CH}
682vs			γ_{CH}

***Key:** vs, very strong; s, strong; m, medium; w, weak; sh, shoulder*

The observed Raman shifts are presented in **Table 4.2**, along with tentative assignments of Raman active bands. It is observed that the stretching vibrations of C-H bonds at 3049-3109 cm^{-1} have low intensities. The bands in the range 2780-2903 cm^{-1} exhibit relatively intense C-H stretching vibrations. There are several bands lying between 1340 cm^{-1} to 1610 cm^{-1} in the C=C stretching region, which contain much detail of the materials and their composites. In-plane bending C-H vibrations occur at 1229 cm^{-1}, 1117-1195 cm^{-1} and 1005-1084 cm^{-1} (Coppedè et al., 2010; Jiang et al., 2006; Louarn et al., 1996; Matsuura & Shimoyama, 2002; X. Zhang, Zhang, & Jiang, 2004; Ziminov et al., 2006). Their intensities vary from high to low values. The bands occurring at 834 cm^{-1}, 727 cm^{-1}, 660 cm^{-1} and 682 cm^{-1} correspond to C-H out-of plane deformation including ring deformation (Louarn et al., 1996).

For P3HT the strong band appearing at 2903 cm^{-1} along with a moderate shoulder at 2831 cm^{-1} corresponds to C-H stretching vibrations. The feature with medium-intensity shoulder at 1520 cm^{-1} can be assigned to asymmetric C=C vibrations in the aromatic thiophene ring. The symmetric C=C stretching deformation manifest themselves at a very strong Raman line near 1445 cm^{-1}. The strong shoulder at 1375 cm^{-1} is due to C=C stretching deformations in the thiophene ring (Garreau et al., 1999; Louarn et al., 1996). In case of VOPcPhO, the strong band at 1610 cm^{-1} is related to skeletal C=C stretching vibrations. A very strong-intensity band at 1530 cm^{-1} corresponds to vibration of nitrogen bridging atoms. The isoindole stretching vibrations are associated with the medium-intensity shoulder band occurring at 1474 cm^{-1}. The coupled C=C pyrrole and benzene stretching vibrations are observed for strong to moderate intensities at 1340-1396 cm^{-1} (Coppedè et al., 2010; Jiang et al., 2006; Ziminov et al., 2006).

The spectrum of the VOPcPhO:P3HT blend is very similar to the corresponding spectrum of pure P3HT except that the bands are shifted to the lower wavenumber. The C-H stretching vibrations band region of the Raman spectrum of the VOPcPhO:P3HT blend (**Figure 4.3b**) shows bands at 3109 cm^{-1}, 2855 cm^{-1} and 2780 cm^{-1}. The band at 3109 seems to broaden besides the frequency shift. The main stretching vibration of C-H bonds exists at 2855 cm^{-1} whereas a shoulder lies at 2780 cm^{-1} with the intensities varying from high to moderate. Bands assigned to VOPcPhO are not observed clearly in the stretching vibrations region in Raman spectrum of VOPcPhO:P3HT blend. The VOPcPhO:P3HT blend yields bands at 1475 cm^{-1}, 1400 cm^{-1} and 1320 cm^{-1} in the C=C stretching region of the spectrum, which are close to that of pure P3HT but with a down-shift in the wavenumber. The band at 1475 cm^{-1} with medium intensity can be ascribed to C=C asymmetric vibrations in the aromatic ring. The bands at 1400 cm^{-1} and 1320 cm^{-1} with intensities varying from very strong to strong, can be attributed to C=C stretching deformations. In bending vibrations region, the Raman spectra of VOPcPhO:P3HT shows that the band observed at 1006 cm^{-1} occurs due to VOPcPhO. However, the band is attenuated in the intensity. The bands assignable to P3HT appear at 1020 cm^{-1} and 660 cm^{-1} with shifted wavenumber. The contribution of both VOPcPhO and P3HT yields a band at 1196 cm^{-1} in the lower frequency region of the spectrum.

From the micro-Raman spectroscopy it is revealed that the P3HT is a dominant material in the VoPcPhO:P3HT blend and the influence of VOPcPhO on the Raman modes of P3HT is almost negligible. A downward shift in the wavenumber indicates that the crystallinity of P3HT is enhanced and the effective conjugation length of the polymer is extended (Heller et al., 1995). Accordingly, it can be stated that the VOPcPhO:P3HT blend possesses molecular morphologies which are favorable for the transport of charge carriers and improved cell efficiencies. Generally, the intensity of the absorption and the edge of absorption wavelength contribute to the amount of light absorbed by the solar cells. In case of VOPcPhO:P3HT bulk heterojunction solar cell the improved efficiency may also be attributed to high absorption coefficient of P3HT (C. P. Chen et al., 2008).

4.1.2 Transport Study of VOPcPhO and P3HT

I. I-V characteristics

The current–voltage (I-V) characteristics play a key role in investigating the junction properties. Some of the valuable quantities, which include ideality factor (n), reverse saturation current (I_o), rectification ratio (RR) and shunt (R_{sh}) resistance, could be obtained from these measurements. The semi-logarithmic plot of I-V curves of the device (ITO/PEDOT:PSS/VOPcPhO/Al) in dark are illustrated in **Figure 4.4**. The experimental I-V characteristics, taken at room temperature, are non-linear and asymmetric, exhibiting a diode like behavior. The rectification ratio, RR (ratio of the forward current to the reverse current at a certain applied voltage for the device) was determined at ±0.5 V and was found 3.12. Since the VOPcPhO serves as a bipolar material, the rectifying phenomenon can be ascribed to charge carriers injected to the PEDOT:PSS and VOPcPhO active layer from both the electrodes i.e. the top electrode (Al) and bottom electrode (ITO).

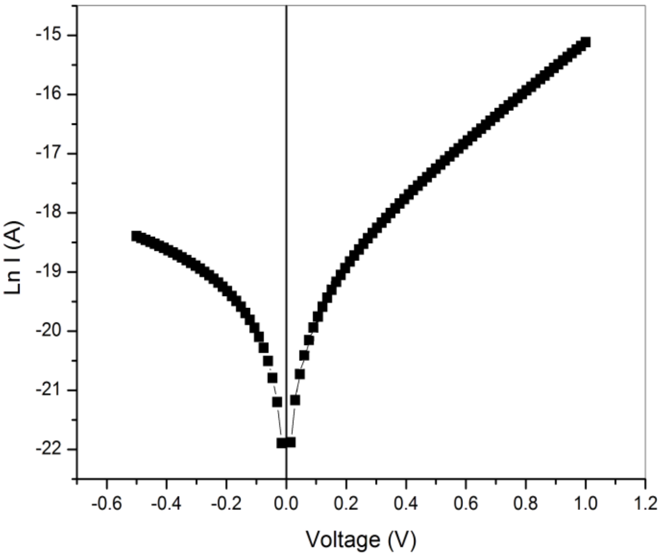

Figure 4.4 Current-Voltage characteristics of VOPcPhO–based solar cell in semi-logarithmic scale.

Generally, it is presumed that when a contact between metal and semiconductor is developed, forward bias current results due to thermionic emission current, which is given as follows (Rhoderick, 1978; Sze, 1981):

$$I = I_o exp\left(\frac{qV}{nkT}\right)\left[1 - exp\left(\frac{-qV}{kT}\right)\right] \tag{4.1}$$

The expression for reverse saturation current I_o is given below:

$$I_o = AA^{*}T^{2}exp\left(\frac{-q\emptyset_{bo}}{kT}\right) \tag{4.2}$$

where $Ø_{b0}$ is the zero-bias barrier height, V is the forward-bias voltage, k is the Boltzmann constant, T is the temperature in Kelvin, A^{*} represents the effective Richardson constant which can be obtained from Richardson-Dushman relation ($A = 4\pi emk^{2} / h^{3}$) and it was ideally found to be 10^{-2} A/cm^{2} K^{2} for most of organic semiconductor materials (Scott & Malliaras, 1999). A is the active area of the diode and n is the ideality factor. The I-V plot was exercised to determine saturation current, which was found equal to 0.3 nA. The ideality factor (diode quality factor) 'n' is defined as:

$$n = \frac{q}{kT}\left(\frac{dV}{dln\, I}\right) \tag{4.3}$$

The barrier height $Ø_{b0}$ can be determined by the following expression:

$$q\emptyset_{bo} = kT\, ln\left(\frac{AA^{*}T^{2}}{I_o}\right) \tag{4.4}$$

The current–voltage characteristics are extremely useful to provide important information about the junction properties such as ideality factor, reverse saturation current, zero bias barrier height and specially transport mechanism responsible for conduction. The semi-log I-V plot give information about the ideality factor 'n', while the extrapolated saturation current determines the zero-bias barrier height, '$Ø_{b0}$'. The values of *n* and $Ø_{b0}$ are obtained as 2.69 and 0.416 eV, respectively. In our case, the ideality factor, which should be closer to unity, deviates from the ideal value. The *n* value beyond '2' is highly suggestive of the fact that the prevalent current in single layer photovoltaic device is due to recombination (Yakuphanoglu, 2007) including the abnormal decrease of barrier height due to the effect of thermionic emission that could be another reason for the increased ideality factor. In similar case, it is well understood that, the ideality factor of phthalocyanine derivatives such as CuPc, could have large value from 7.7 to 18.2 due to the same recombination issue (Rajaputra et al., 2007).

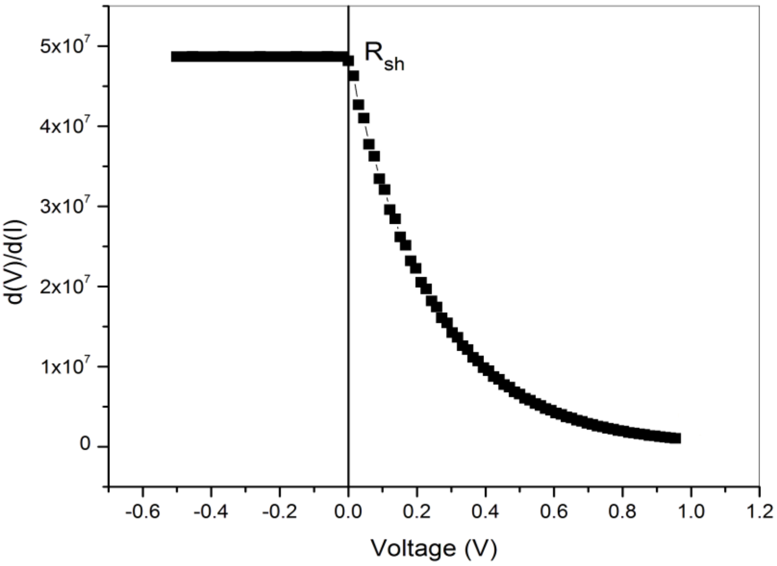

Figure 4.5 The junction resistance versus applied voltage for single layer solar cell.

The R_{sh} (shunt resistance) is determined from the graph of the junction resistance (R) versus voltage (V) shown in **Figure 4.5**. The obtained value of R_{sh} is 49 MΩ. Another method to determine the barrier height is the Norde's method. The Norde's function (Norde, 1979) can be expressed as:

$$F(V) = \frac{V}{\gamma} - \frac{kT}{q}\ln\left(\frac{I}{AA^{*}T^{2}}\right) \tag{4.5}$$

where γ is a dimensionless quantity having a first integral value greater than 'n'. The value of γ in this case is '3'. A graph of $F(V)$ and V, shown in **Figure 4.6**, is plotted to obtain the minima on x and y axes. The barrier height can be calculated by the following expression:

$$\text{Ø}_{b0} = F(V_o) + \frac{V_o}{\gamma} - \frac{kT}{q} \tag{4.6}$$

where V_o is the voltage value that corresponds to the minima of V and $F(V_o)$ represents the minima of $F(V)$. The barrier height calculated by Norde's method is 0.39 eV, which is in agreement with the value obtained by conventional I-V method.

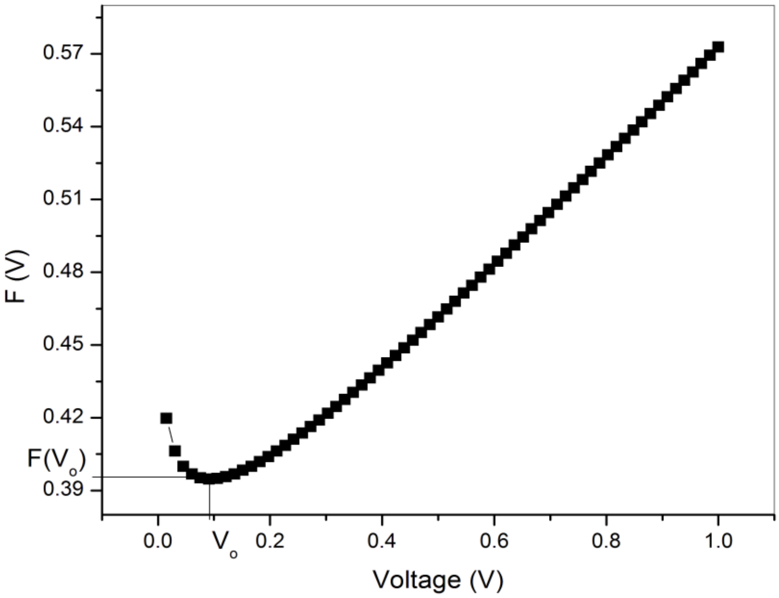

Figure 4.6 F(V) versus voltage plot of VOPcPhO based cell.

The I-V characteristics of the ITO/PEDOT:PSS/VOPcPhO/Al organic photodiode in dark and under illumination are shown in **Figure 4.7**. The device characterization was carried out under simulated 100 mW/cm^2 AM 1.5 white light illumination. **Figure 4.7** clearly shows that current value under light is greater than the value obtained in the dark. This shows that when the photons are absorbed, the electron-hole pairs are produced which result in the carrier-contributing photocurrent. A great deal of useful information about the generated electron-hole pairs at the junction can be achieved from this phenomenon. As a result of photo-excitation, the charges generated in the active region of the device under illumination are subsequently swept to the corresponding electrodes due to the electric field.

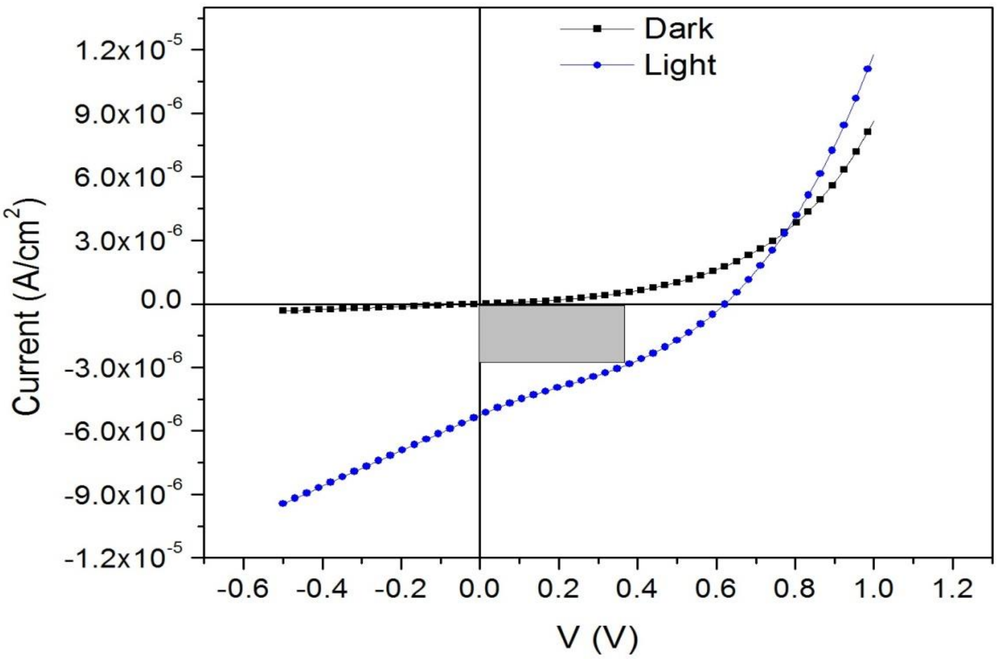

Figure 4.7 Current-voltage characteristics of VOPcPhO-based single-junction device in dark and under illumination.

The performance parameters for the cell have been extracted. The short circuit current (J_{SC}) and open circuit voltage (V_{OC}) for the single layer VOPcPhO-based solar cell are measured as 5.26 x 10^{-6} A/cm^2 and 0.621 V, respectively. The fill factor FF is obtained as 0.33. The power conversion efficiency of the organic photodiode is calculated as 1.07 x 10^{-3} %. The measured photocurrent in the active layer can be attributed mainly to the ability of charge carrier to travel to the external electrodes without being recombined (Nogueira et al., 2003). However, the active layers of greater thickness become more susceptible to the recombination of holes and electrons. Although, the efficiency shown here is very low, but this is common in single-junction photodiode structure. The lower efficiency can be attributed to the fact that the single layer VOPcPhO is a material which has low mobility of the order of 10^{-5} cm^2 V^{-1} S^{-1}. A comparison of the device operation parameters for single-junction organic solar cells, made with CuPc and VOPcPhO, is presented in **Table 4.3**. It can be concluded that the short circuit current and open circuit voltage obtained for the solution-processed VOPcPhO single-junction cell are comparable to that of the CuPc single junction device.

The electrical properties of ITO/PEDOT:PSS/VOPcPhO/Al photodiode device were investigated in dark and under illumination. The rectification behavior has been observed for the device in dark. The electronic parameters of the cell from I-V characteristics in dark have been extracted by using conventional I–V method and verified by Norde's method. The calculated values of the ideality factor and barrier height are 2.69 and 0.416 eV, respectively. The values of the photovoltaic parameters such as short circuit current density, open circuit voltage and fill factor are as 5.26 x 10^{-6} A/cm^2, 0.621 V and 0.33, respectively. The photovoltaic response of VOPcPhO-based organic solar cell has shown the potential of the material to play an important role in generating clean and inexpensive power from the abundant solar energy.

Table 4.3 Comparison of various solar cell performance parameters for different organic active layers used for the fabrication of single-junction organic solar cells.

Active layer for single-junction organic solar cell	**J_{sc} (μ A cm^{-2})**	**V_{oc} (V)**	**Reference**
CuPc (Thermally Evaporated)	9	0.7	(Parthasarathy, 2005)
VOPcPhO (Spin Coated)	5.26	0.621	Present work

To analyze the charge transport properties in VoPcPhO, unipolar and ambipolar diodes have been fabricated. For the hole-only diode ITO/PEDOT:PSS coated glass substrates were used. The active organic layer was deposited on the PEDOT:PSS and after that a 40 nm thick N,N'-bis(3-methylphenyl)- (1,1'-biphenyl)-4,4'-diamine (TPD) film was deposited to prevent electron injection from the top Au electrode. Meanwhile, the electron-only diodes contain Al films as bottom and top electrodes. In this case, a 0.5 nm thick interface doping layer of lithium fluoride (LiF) was placed between the organic film and top electrodes. For ambipolar transport the ITO/PEDOT:PSS/active layer/LiF/Al structures have been considered. The thickness of active organic layer was around 150 nm in all devices. The mobility of the unipolar and ambipolar diodes calculated in SCLC regions is given in **Table 4.4**. The results show that the VOPcPhO has bipolar transport and can act as electron as well as hole transporting material. The finding indicates that the electron mobility is comparable with holes mobility. Normally, it is found that the mobility of electron and hole are not similar, where in most organic materials, hole mobility is greater than that of electron. It is found that a strong trapping of electron in organic semiconductor device has led the hole mobility to be higher than electron mobility

Table 4.4 Extracted mobility (cm^2/Vs) values for VOPcPhO from the unipolar and ambipolar diode measurements.

Entity	Electron	Hole	Ambipolar
VOPcPhO	8.3×10^{-5}	3.7×10^{-4}	2.5×10^{-5}

A new system of donor-accepter blend for bulk heterojunction solar cell of poly(3-hexylthiophene) (P3HT) by using vanadyl 2,9,16,23-tetraphenoxy-29H,31H-phthalocyanine (VOPcPhO) as acceptor material has been fabricated and characterized for its electrical and optical properties. It is concluded that P3HT:VOPcPhO blend system has the potential to be applied in the bulk heterojunction solar cells, due to its high absorption solar spectrum in the visible region and considerably good electrical behavior. This study was performed in open air to show the potential of VoPcPhO for bulk heterojunction solar cell and further investigations were performed in the controlled environment to enhance the performance of the solar cell.

II. EFISHG

The OFET device has been fabricated by using VOPcPhO. The purpose of this OFET fabrication is to identify whether the blend system of P3HT:VOPcPhO is compatible to be characterized using a newly EFISHG technique. The technique requires a significant change of SHG signal after the active layer is induced with an electric field. **Figure 4.9** shows the SHG signal produced by the blend in different applied fields of 0, +1, and -1 V.

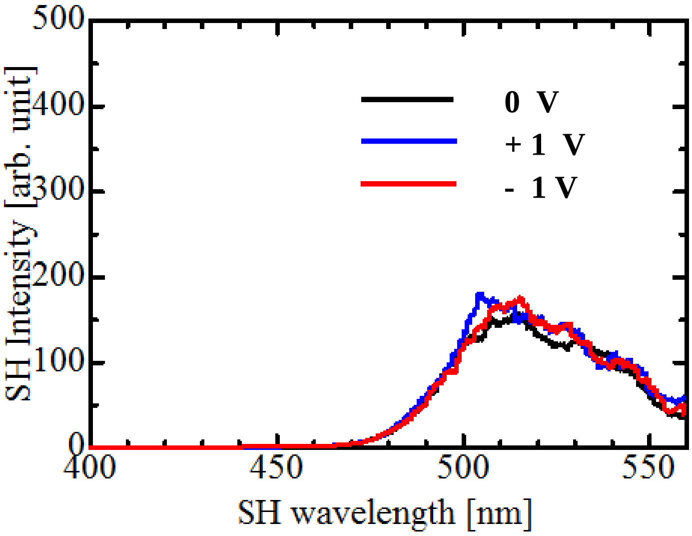

Figure 4.8 Second harmonic generation (SHG) signal for VOPcPhO thin film.

From the figure above, a significant change in SHG signal is hardly observed even after the application of induced electric field of +1 V and -1V. Such results become the evidence for incompatibility of the VOPcPhO for EFISHG characterization since the material non-linear optical property could not be manipulated. This is believed that, the centro-symmetrical structure of VOPcPhO is unbreakable and has a specific electronic field distribution at a time. Thus, further study on charge carrier transport behavior, related with OFET structure, using EFISHG technique is skipped.

4.2 Part 2: Towards an Efficient Organic Solar Cells by Utilizing PCDTBT/PC$_{71}$BM Blend System

4.2.1 Characterization of PCDTBT and PC$_{71}$BM films

I. UV-Vis-NIR Spectroscopy

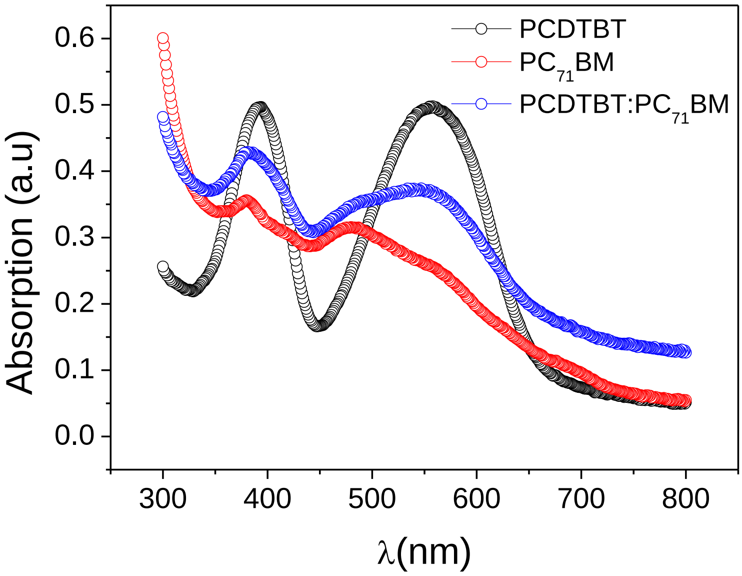

Figure 4.9 Absorbance of PCDTBT, PC$_{71}$BM, and PCDTBT:PC$_{71}$BM thin films.

The wavelength absorption spectra of PCDTBT, PC$_{71}$BM and binary blend PCDTBT:PC$_{71}$BM (1:4) thin films are shown in **Figure 4.9**. In the PCDTBT spectrum, the highest absorption peaks are observed to exist at 392 and 557 nm. Two regions with the lowest absorption are observed at 328 nm, and 450 nm. While in PC$_{71}$BM, there are two small absorption peaks at 380 nm and 477 nm with a shoulder at 570 nm. The absorption range of PC$_{71}$BM is very dominant at UV region in which the absorption is observed to keep increasing from 720 nm towards higher energy region in lower wavelength range. The absorption of PC$_{71}$BM is very high at the wavelength range lower than 340 nm in UV absorption region. The blend of both materials (PCDTBT:PC$_{71}$BM) has combined these absorptions by showing two peaks at 380 nm and 550 nm with a shoulder at 484 nm. The blend system has an improved absorption range from the UV region to about 640 nm wavelength range.

II. Photoluminescence (PL)

The photoluminescence (PL) of PCDTBT, $PC_{71}BM$ and PCDTBT:$PC_{71}BM$ blend are also studied for quenching phenomena in order to compare their photo-induced charge transfer efficiencies. **Figure 4.10** shows the PL spectra of PCDTBT, $PC_{71}BM$ and PCDTBT:$PC_{71}BM$ (1:4) measured at room temperature. The PL spectra of the thin films and their blends were obtained by an excitation wavelength of 325 nm in the range from 400 to 1000 nm.

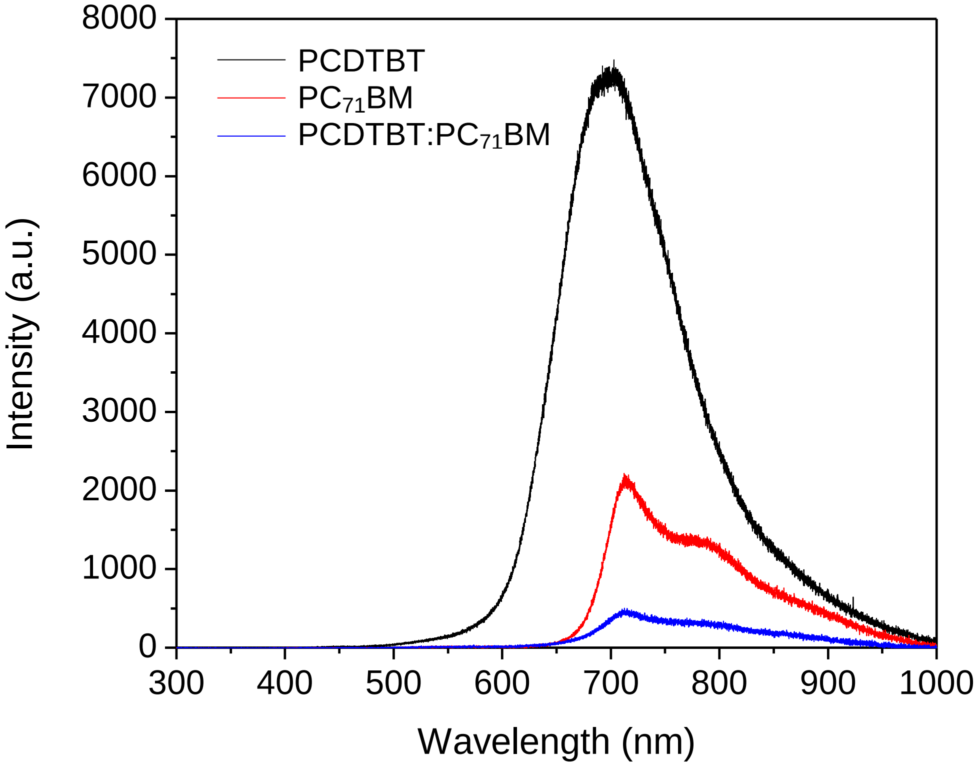

Figure 4.10 PL of PCDTBT, $PC_{71}BM$, and PCDTBT:$PC_{71}BM$ thin films.

A strong peak of the PCDTBT photoluminescence emission is observed at 698 nm which is lying near the red region. The results of PCDTBT are consistent with the results reported in the literature. The PL spectrum of $PC_{71}BM$ shows the emission at nearly the same region (713 nm) with a shoulder at longer wavelength region around

795 nm. It is evident from **Figure 4.10** that when $PC_{71}BM$ is introduced in the PCDTBT, the intense PL of the blend is significantly quenched and appears to be the lowest amongst all. The PL of PCDTBT:$PC_{71}BM$ shows a small peak and shoulder at a similar region (712 and 793 nm, respectively) to $PC_{71}BM$ but with a slight (blue) shifted due to strong influence of quenched PCDTBT PL emission region. As observed in the previous blend system (P3HT:VOPcPhO), the highly efficient photoluminescence quenching in the current blend system also suggests a profound photo-induced charge transfer in the blended film.

Table 4.5 Peaks of PL emission (λ_{max}) and their corresponding emission intensities (In Em) for $PC_{71}BM$, PCDTBT, and PCDTBT:$PC_{71}BM$ in PL thin films.

Entity	**Peak**		**Shoulder**	
	λ_{max} (nm) Em	**In Em**	**λ_{max} (nm) Em**	**In Em**
$PC_{71}BM$	713.24	2196.76	794.66	1262.60
PCDTBT	698.66	7383.41	--	--
PCDTBT:$PC_{71}BM$	712.31	477.95	792.90	332.56

III. Raman Scattering

The Raman spectra of $PC_{71}BM$, PCDTBT and PCDTBT:$PC_{71}BM$ blend are as shown in **Figure 4.11**.

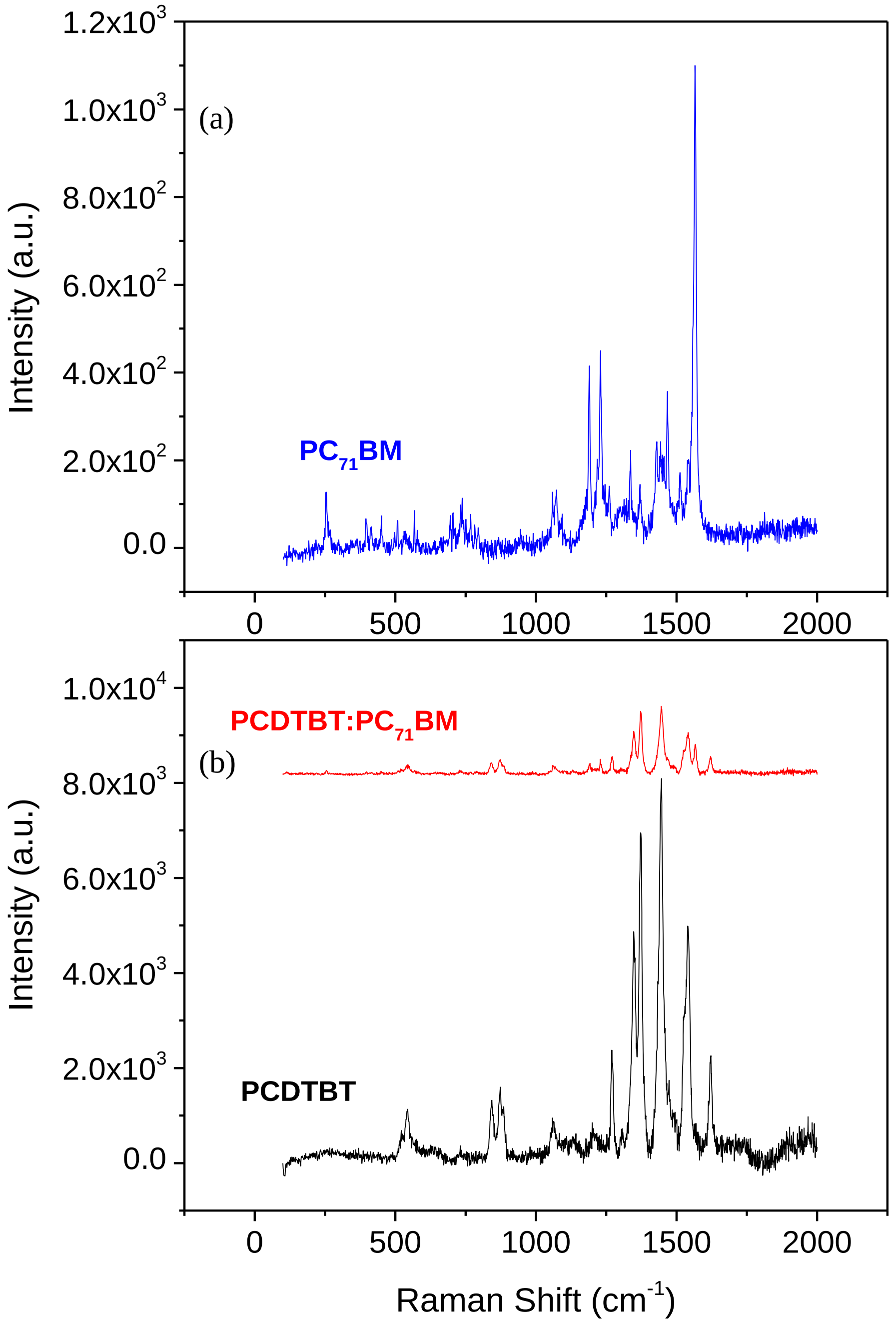

Figure 4.11 Raman spectra of (a) $PC_{71}BM$, and (b) PCDTBT and PCDTBT:$PC_{71}BM$ blend thin films.

Table 4.6 Raman shifts of $PC_{71}BM$, PCDTBT, and PCDTBT:$PC_{71}BM$ blend thin films.

Observed Raman shifts (cm^{-1}) and band intensities with assignment of the principal bands.v: stretching vibration; δ: in-plane deformation vibration; γ: out-of-plane deformation vibration;

$PC_{71}BM$	**PCDTBT**	**PCDTBT:$PC_{71}BM$**	**Approximate description of vibrations**
	1620s	1620w	ν_{CC}
1568s		1568w	ν_{CC}
1514w	1542vs	1542w	ν_{CC}
1467m	1445vs	1445s	ν_{CC}
1430w			ν_{CC}
	1374vs	1374m	ν_{CC}
1336w	1348vs	1348m	ν_{CC}
	1270s	1270w	γ_{CH}
1230m		1230w	ν_{CC}
1189m			δ_{CH}
	1201m		δ_{CH}
1070w		1195sh	δ_{CH}
	1061w	1061sh	δ_{CS}
	873m	873w	γ_{CH}
	841m	841w	γ_{CH}
735sh		732sh	γ_{CH}
	542m	545sh	γ_{CH}
254w		254sh	γ_{CH}

Key:*vs, very strong; s, strong; m, medium; w, weak; sh, shoulder*

The observed Raman shifts for $PC_{71}BM$, PCDTBT and PCDTBT:$PC_{71}BM$ blend are presented in **Table 4.6**, along with their tentative assignments of Raman active bands. For PCDTBT, the peaks at 841, 873, 1061, and 1270 cm^{-1} are assigned for C-H in plane bending modes. Two peaks at 1201 and 1270 cm^{-1} are assigned as C-H deformation and bending, respectively. There are several strong peaks at 1348, 1374, 1445, 1542, and 1620 cm^{-1} assigned to C-C stretching vibrational mode. In $PC_{71}BM$, there are small peaks at 254 and 735 cm^{-1} which correspond to the C-H bending mode, and few others at 1070 and 1189cm^{-1} corresponding to the C-H deformation mode. Peaks at 1230, 1430, 1467, 1541, and 1568 cm^{-1} are assigned to C-C stretching vibrational modes. In the blend PCDTBT:$PC_{71}BM$ system, all of C-H bending modes in both PCDTBT and $PC_{71}BM$ appear with low intensities. There are several peaks that remain high such as peaks in PC71BM at 1230 and 1568 cm^{-1} and in PCDBT at 1270, 1348, 1374, 1445, 1542, and 1620 cm^{-1}. All of the peaks correspond to the C-C stretching mode. However, some of the peaks disappear in the blend system i.e. at 1201cm^{-1} (PCDTBT) and 1189, 1430, 1467, and 1514 cm^{-1} ($PC_{71}BM$).

4.2.2 Transport Study of PCDTBT and $PC_{71}BM$

I. Transfer Characteristics

To study the charge transport behavior of PCDTBT, OFETs were fabricated using PCDTBT as active layer. In order to prepare the devices, the n^{++} - Si substrates, with pre-deposited 500 nm thick SiO_2 films, have been cleaned. The Cr/Au back contacts on the substrates were deposited by evaporating the Cr (15 nm) and Au (50 nm). In order to deposit PCDTBT thin films, 10 mg/ml solution of the PCDTBT was prepared in chloroform. PCDTBT thin films (~100 nm) were deposited at 2000 rpm. The Au contacts (source and drain) were thermally deposited on the PCDTBT films. The fabricated devices were electrically characterized under standard steady state conditions using Keithley 2400 source meter. The TRM-SHG technique was used to investigate electric field profiles across the channels of the OFETs.

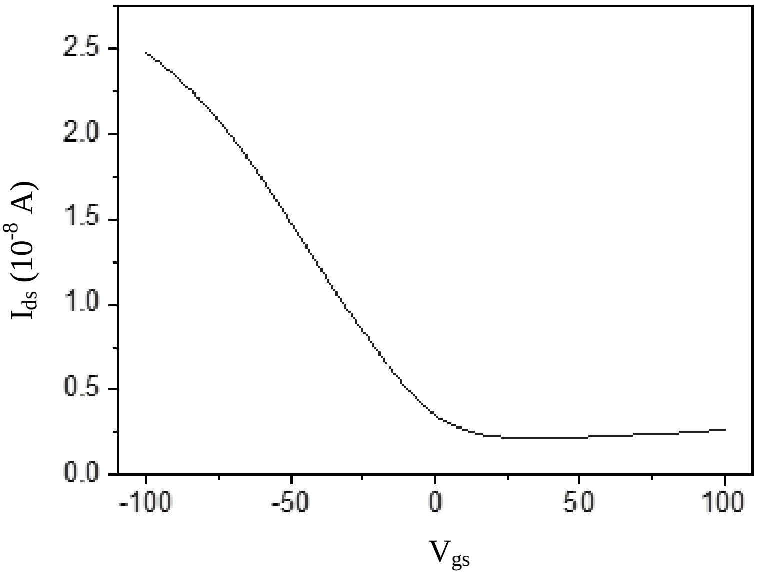

Figure 4.12 A transfer curve of PCDTBT-OFET.

The transfer characteristics of the PCDTBT based OFETs with SiO_2 as a gate-insulator are shown in **Figure 4.12**. The transfer curve shows hole transport behavior of PCDTBT. The hole mobility calculated from the transfer curve was 2.4×10^{-5} cm^2/Vs. The I_{ds}–V_{gs} characteristics followed the relation given in (Taguchi et al., 2012).

$$I_{ds} = \frac{W}{2L} C_g \mu (V_{gs} - V_{th})^2 \tag{4.7}$$

where, C_g is the gate capacitance, $C_g = 5.6 \times 10^{-5}$ F/cm^2, μ is the drift mobility of charge carriers and V_{th} is the threshold voltage. The length and width of the channel were 60 µm and 3 mm, respectively. The equation 4.7 can be derived using the Maxwell–Wagner model, assuming that the active PCDTBT layer in OFETs has the dielectric nature (Weis et al., 2010) and if the slope of potential distribution is constant under the steady state condition, the current (I_{ds}) flows along the gate-insulator interface.

II. EFISHG

The PCDTBT:PCBM composite charge carriers mobilities calculated using ToF and photo-CELIV methods are found in the range of 4-6 x 10^{-5} cm^2/Vs (Clarke et al., 2012), but there is no literature that shows dynamic behaviour of PCDTBT charge carriers transport in a single device. The basic mechanism of charge carriers transport in the material should be investigated in order to address the possibility of enhancement in the device performance. In this work, a PCDTBT single layer OFET was studied by time resolved microscopic second harmonic generation (TRM-SHG) technique to analyze the charge carriers motion in PCDTBT. A comparison of the charge carriers mobilities obtained from both transfer-characteristics and TRM-SHG methods are also presented. The studies on holes transport and their accumulation motion in the OFET channel have been carried out. It is expected that the knowledge of charge transport behavior in PCDTBT thin films will help in designing and fabricating PCDTBT based solar cells with improved efficiency. The aim of this work is to understand the carrier mechanism in the thin films of a potential organic photovolatic material, PCDTBT, using TRM-SHG. This could be a gateway to investigate the carrier lifetime in PCDTBT based OSCs by TRM-SHG measurement, to further improve the efficiency of PCDTBT based solar cells.

Keeping in view the photoluminescence (PL) and absorption spectra of the PCDTBT, the fundamental laser wavelength used was 1060 nm. The light source used for the SHG measurement was a Q-switched Nd: YAG laser equipped with an optical parametric oscillator (OPO). Laser light spot size was ~70 µm. The laser pulse width was 4 ns, whereas the laser pulse frequency was 10 Hz and polarization direction was along the channel. Finally, SH light was recorded by a cooled CCD camera. The exposure time of the CCD camera was 1200 s. To distinguish SH light from the PL, an appropriate optical bandpass filter was used. PCDTBT has a PL peak at the wavelength of ~702 nm. The absorption and PL spectra of the PCDTBT thin films have been previously shown in section 4.2.1. For the TRM-SHG experiment, a -150 V square wave voltage signal was applied at the gate for observing transient-state electric field profile. Details on the TRM-SHG system setup can be found in section 4.1.2 (II).

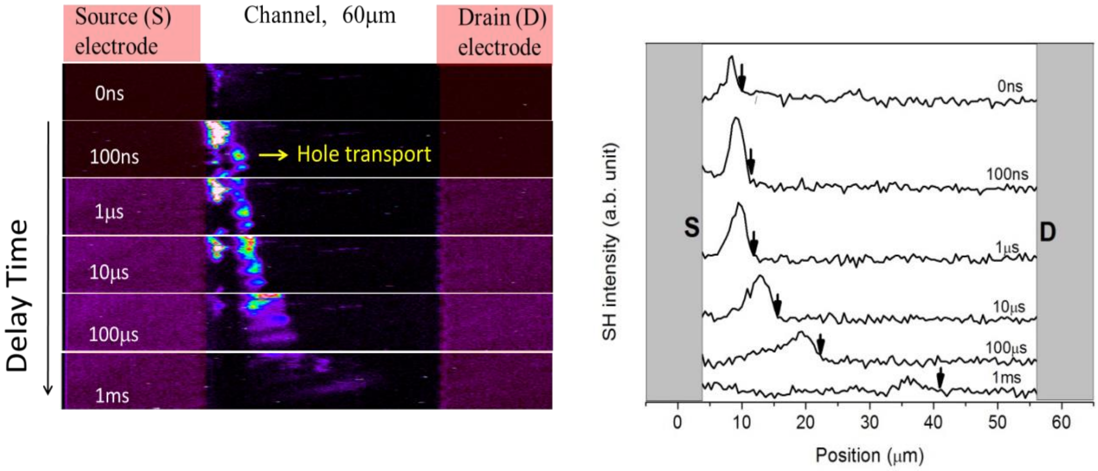

Figure 4.13 The observed carrier behavior in the PCDTBT-OFET by using the TRM-SHG measurement in the time span 0-1 ms, (a) TRM-SHG images, and (b) the cross section of SHG density distribution.

The spacial position of the SHG signal from the source electrode with elapsed time is shown in **Figure 4.13**. The optical second harmonic wave, SHG, is generated due to second-order-nonlinear polarization $P(2\omega)$ that is induced in the active layer by impinging laser light. $P(2\omega)$ can be expressed mathematically by the following equation (4.8) (Ohshima et al., 2011):

$$P(2\omega) \propto \varepsilon_o \chi^{(2)}\colon \vec{E}(\omega)\vec{E}(\omega). \tag{4.8}$$

Here ε_o is the dielectric permittivy constant for vacuum whereas $\chi^{(2)}$ is the second order nonlinear susceptibility. $\chi^{(2)}$ is strongly depends on structure of the materials. If the material has centro-symmetric structure then the square of susceptibility becomes zero ($\chi^{(2)} = 0$) and the SHG cannot be activated, $\vec{E}(\omega)$ is the electric field, and ω is the angular frequency of the source light. On the other hand the central-symmetry of a material can be changed by applying a electro-static field and the SHG induced due to the presence of the static field is known as EFISHG. EFISHG, $P(2\omega)$, can be explained by the equation 4.9 given below:

$$P(2\omega) \propto \varepsilon_o \chi^{(3)} \vdots \vec{E}(0)\vec{E}(\omega)\vec{E}(\omega) \tag{4.9}$$

where$\chi^{(3)}$ is a third-order-nonlinear susceptibility and $\vec{E}(0)$ is a local electro-static field. The $\vec{E}(0)$ is assumed as a sum of E_{ext} (external electric field) and a E_{sc} (space charge field) as shown in the equation 4.10 below:

$$\vec{E}(0) = \vec{E}_{ext} + \vec{E}_{sc}. \tag{4.10}$$

The time resolved SHG images in the channel region of OFETs are shown in **Figure 4.13** (a). The TRM-SHG images were recorded at t_d= 0, 0.1, 1, 100 and 1000 µs. **Figure 4.13** (b) shows the cross section of SHG profile distribution along the channel (between drain and source). A -150 V square wave signal with 50 ms pulse width was applied to the source-gate (V_{gs}) electrodes whereas the source electrode was grounded. It is obvious from this figure that there is a weak SHG signal at t_d = 0s at the source, however, it moved towards the drain with time, showing that the holes are injected from the source electrode have moved along the OFET channel. According to the equation given above, a Poisson electric field originating from injected holes is formed in the PCDTBT film, which is given by the second term in the above equation 4.10. The visualization of the hole transport across the channel has enabled us to analyze the details of the charge transport mechanism in the PCDTBT thin films. The transit-time of the hole can be given by the following equation (4.11) (Manaka et al., 2008).

$$t_r = \frac{x^2}{2\mu V_{gs}}, \tag{4.11}$$

where x is the position of injection electrode, μ is the mobility of the charge carriers and V_{gs} is the voltage applied at the gate-source electrodes. Using equation (4.11), the hole mobility was estimated as 5.6 × 10^{-5} cm^2/Vs. The mobility value found by TRM-SHG is ~2.33 times higher than that calculated from the I-V characteristics. The TRM-SHG measurement is a transient experiment, whereas the I-V measurement is a steady-state experiment. During the I-V measurements carrier motion through the channel starts from the charge injection at the contacts while in TRM-SHG measurements, only the carrier motion is recorded along the channel and the contacts injection process has not been taken into account. Therefore, the TRM-SHG technique allows us to measure the intrinsic carriers mobility which is needed to study the carriers transport mechanism in the thin films.

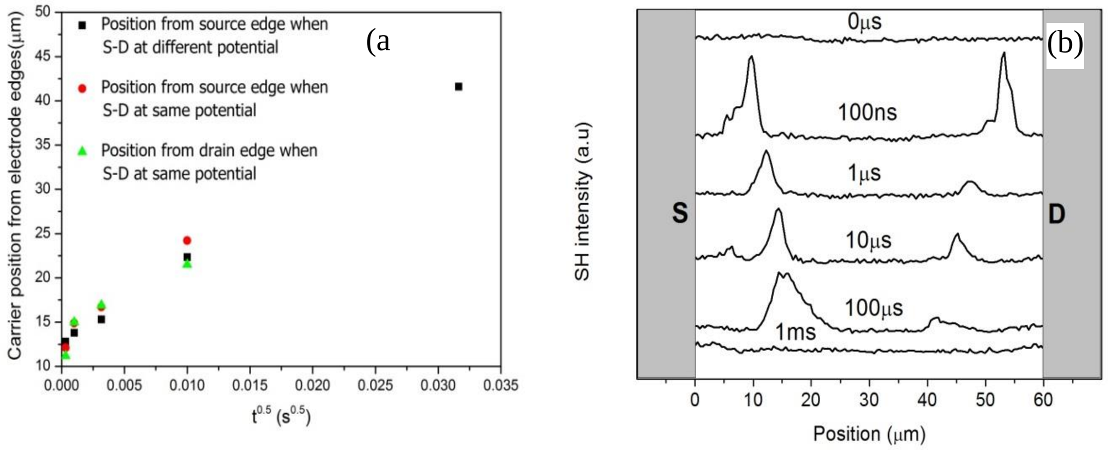

Figure 4.14 Carrier position from the electrode edges. (a) carrier transport process showing linear relation between x and $\sqrt{t}$, (b) cross section of SHG density distribution during hole accumulation process in the channel of PCDTBT-OFET, where the source and drain are grounded and gate biasing is -150 V.

Figure 4.14 shows that motion of the carriers through OFET according to $x \propto \sqrt{t}$. By assuming interface charge propagation, described by the Maxwell-Wagner model and the ladder RC-circuit model, square root dependence of the carrier transit time can be easily explained (Weis et al., 2010). In the present study, the carriers migrate from the source to the drain either by carrier drift between the source and drain electrodes (proportional to V_{ds}) or by the field between the gate and source electrodes (proportional to V_{gs}). This is in accordance with the SHG experiment, where the injected carriers keep moving even though the source and drain are electrically shorted as shown in **Figure 4.14** (b). The TRM-SHG images also show that the charge motion is almost symmetric from both electrodes when the source and drain electrodes are at the same potential. Since no drift field between source and drain exists under the drain source short circuit conditions, therefore, the carrier propagation is due to interface charging but not because of the diffusion of carriers (Burgi, Friend, & Sirringhaus, 2003).

Even though the IQE for PCDTBT based photovoltaic devices is 100 % (S. H. Park et al., 2009), the best reported PCE for a bulk heterojunction solar cell based on a PCDTBT:$PC_{70}BM$ blend (as single junction polymer solar cell) is 6.1 % until now (Helgesen, Søndergaard, & Krebs, 2010). However, the solar cell conversion efficiency is still not too high to meet the requirements of the practical application. This might be due to its relatively low charge mobility which is normally observed in organic semiconductors due to their disordered structures. Moreover, due to low mobility, an increase in thickness results in the increase of internal resistance of the active layer and consequently, the fill factor drops with increase in the thickness. Therefore, all the highest attained efficiencies for the case of organic solar cells were recorded in the active layers of less than 100 nm thickness, which is not ideal in order to get the maximum performance and commercial development. The measured hole mobility for

PCDTBT in this study was found to be in the order of 10^{-5} cm^2/Vs (using OFET structure) which is higher than that of the pristine PCDTBT film calculated by ToF method (9 x 10^{-6} cm^2/Vs) (Clarke et al., 2012) that can be attributed to the charge carrier density dependence of mobility in OFETs (Tanase et al., 2003). The mobility value for PCDTBT might be enough to get the ~6 % efficiency when it is mixed with PCBM material, but there is a need to investigate deeply the charge carrier motion in the PCDTBT, in order to improve the efficiency. Therefore, in this study, the carrier motion behavior of PCDTBT thin films become the main focus, which might assist in designing the PCDTBT based solar cells with improved efficiency.

The TRM-SHG images of the OFET devices with an active layer of PCDTBT material have been recorded in order to study the carrier motion in the PCDTBT thin films. The holes motion has also been visualized by using this technique. Furthermore, the visualized carriers’ motion has been used for the calculation of intrinsic mobility of holes in the PCDTBT based OFET devices, which is 2.33 times higher than that measured from the transfer curve of the PCDTBT based OFET. It is expected that the TRM-SHG technique could be a gateway to investigate the carrier lifetime in PCDTBT in order to improve the efficiency of the PCDTBT based solar cells.

4.2.3 Study of Charge Transport Behavior in PCDTBT/PC$_{71}$BM Blend Device: Further Characterization by EFISHG Technique.

The study on PCDTBT based organic field effect transistors (OFETs), in the previous section, has shown that the time-resolved microscopic electric-field-induced optical second-harmonic-generation (TRM-EFISHG) technique can be used to visualize carrier transport in the PCDTBT layer by directly measuring the electric field arising from the moving carriers. These measurements had already been employed to probe the internal electric field in pentacene:C$_{60}$ bulk heterojunction (BHJ) solar cells (X. Chen et al., 2014) by selectively probing pentacene and C$_{60}$ layers, individually. The results showed that crystalline pentacene and C$_{60}$ are phase-separated and internal electric field is formed oppositely in the pentacene and C$_{60}$ domains where each domain develops contact with both anode and cathode. It was also suggested that the potential distribution is allowed on the surface of Al electrodes owing to the surface property (X. Chen et al., 2014). On the other hand, in the present study, the main focus is on the polymer-type BHJ OSCs (PCDTBT:PCBM). In the polymer-type BHJ layer, small domains rarely make contact with anode and cathode electrodes simultaneously. Nevertheless, using buffer layers such as PEDOT:PSS significantly improves photodiode performances. That is why, the impact of PEDOT:PSS buffer layer on the internal electric field in the BHJ layer and the carrier transport in the PCDTBT:PC$_{71}$BM bulk heterojunction (BHJ) organic photodiode have been investigated. Finally, it is found that TR-EFISHG is a novel way of probing the carrier transport in bulk-hetero structure photodiode device, and thus can be used for studying the impact of interfacial layer on electrons and holes transport in the bulk-heterojunction photodiode.

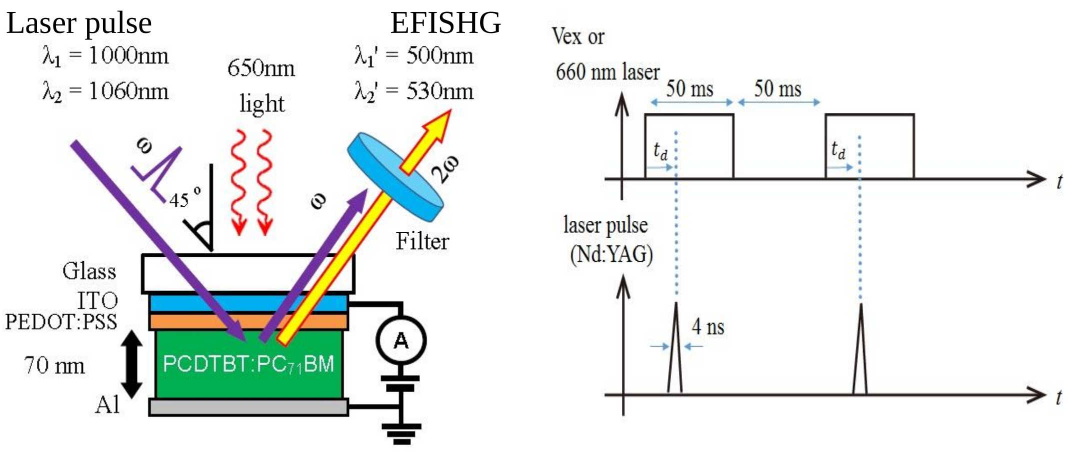

(a) **(b)**

Figure 4.15 Across-sectional view of fabricated devices and schematics of experimental setup: (a) ITO/PEDOT:PSS/ PCDTBT:PC$_{71}$BM/Al solar cell, (b) pulse width and frequency of the fundamental laser lights.

Figure 4.15 (a) and (b) show the structure of the fabricated PCDTBT:PC$_{71}$BM based bulk heterojunction photodiode, and the properties of fundamental laser pulse, respectively. Photodiode laser was used to provide a red light (660 nm) to OSC device in order to allow photo-current generation, and the selected fundamental IR laser (1000 or 1060 nm) with 4 ns pulse width impinged at an angle of 45° has been applied on the OSC to create SHG signal. **Figure 4.16** shows the J-V characteristics of the fabricated OSCs in dark and under solar simulator (100mW/cm^2). By introducing the PEDOT:PSS layer, the J_{SC} was ~2.9 times increased. The V_{OC} was enhanced from 0.40 V to 0.75 V. Consequently, the efficiency was improved ~4.07 times. It is noteworthy that the J-V characteristics gradually decayed with time.

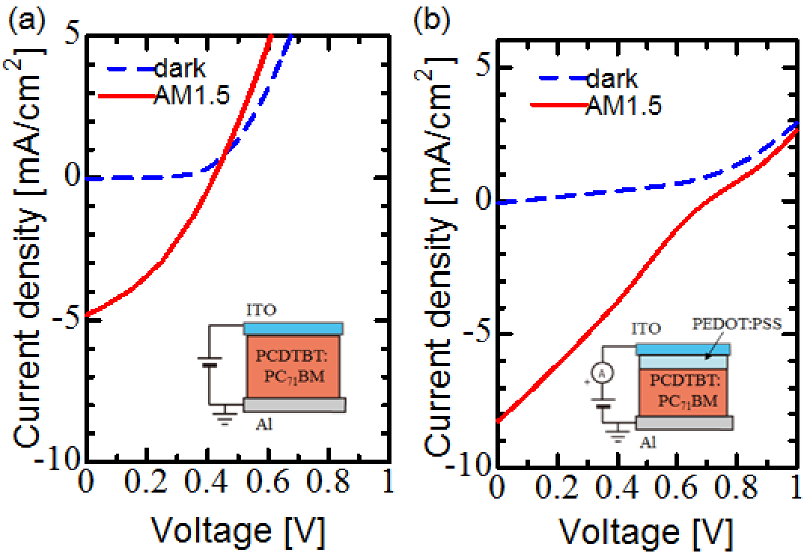

Figure 4.16 J-V characteristics of BHJ solar cells in dark and under solar simulator. (a) ITO/PCDTBT:PC$_{71}$BM/Al solar cells. (b) ITO/PEDOT:PSS/PCDTBT:PC$_{71}$BM/Al solar cells.

In this characterization, the SHG signal produced by OSC was detected using a monochromator synchronized with the laser source, in the same manner as reported in the previous literature (L. Zhang et al., 2010). By impinging the selective laser wavelengths on the BHJ layer, the EFISHG signals in PCDTBT and PC$_{71}$BM are generated due to coupling of electrons in the molecules and electro-magnetic waves $\vec{E}(\omega)$. In the case of EFISHG, the second-order polarization is induced as $\vec{P}(2\omega) \propto \varepsilon_o \chi^{(3)} : \vec{E}(0)\vec{E}(\omega)\vec{E}(\omega)$. Here, $\vec{E}(0)$ is the local electroststic field, $\vec{E}(\omega)$ is the electric field of the selective laser wavelength, ω is its angular frequency, $\chi^{(3)}$ is the third-order nonlinear susceptibility and ε_o is the dielectric permittivity constant. The $\vec{E}(0)$ is given by the equation $\vec{E}(0) = \vec{E}_b + \vec{E}_{ext} + \vec{E}_{sc}$, where $\vec{E}_b$ is the internal electric field caused by work function different etc., $\vec{E}_{ext}$ is the external electric field, and $\vec{E}_{sc}$ is the space charge field. Here, $\vec{E}_b$ is formed due to work function difference of the electrodes, whereas $\vec{E}_{ext}$ and $\vec{E}_{sc}$ are mainly formed under voltage application (Cui et al., 2013;

Taguchi et al., 2011; L. Zhang et al., 2011). In the presence of local electric field $\vec{E}(0)$, the EFISHG is activated. During the EFISHG measurements, the red light (660 nm wavelength, 10 Hz repetition, and 50 ms duration) emitted from a laser diode was used to induce photo current. The red light intensity (275 mW/cm^2 for ITO/PCDTBT:PCBM/Al and 300 mW/cm^2 for ITO/PEDOT:PSS/PCDTBT:PCBM/Al) was selected in such a way that it generates the same short-circuit current as produced under 100 mW/cm^2 solar simulator illumination.

It is worth noting, here, that the EFISHG is material dependent and generated in proportion to the $\chi^{(3)}$, where $\chi^{(3)}$ is a function of angular frequency ω of the laser light. As a result, EFISHG signals are enhanced at different laser beam wavelengths depending on the material properties. That is, the potential of selective probing is an advantage of this method for analyzing electric field in a complex BHJ layer. In order to choose appropriate laser beam wavelength, single-layer devices with structures ITO/PCDTBT/Al and ITO/PC$_{71}$BM/Al were prepared. **Figure 4.17** shows the SHG spectra of these devices under various applied voltages where the SHG intensities vary proportionally with the applied voltages, suggesting that the generated SHG is due to the EFISHG. From the EFISHG spectra of **Figure 4.71**, two laser beam wavelengths, 1000 nm and 1060 nm have been selected in order to probe the electric fields in PCDTBT and PC$_{71}$BM, respectively. It is noteworthy that the wavelength of the laser beam is larger than the BHJ layer thickness. Consequently, the average electric field formed in PCDTBT (PC$_{71}$BM) domain can be selectively probed at the laser wavelength of 1000 nm (1060 nm).

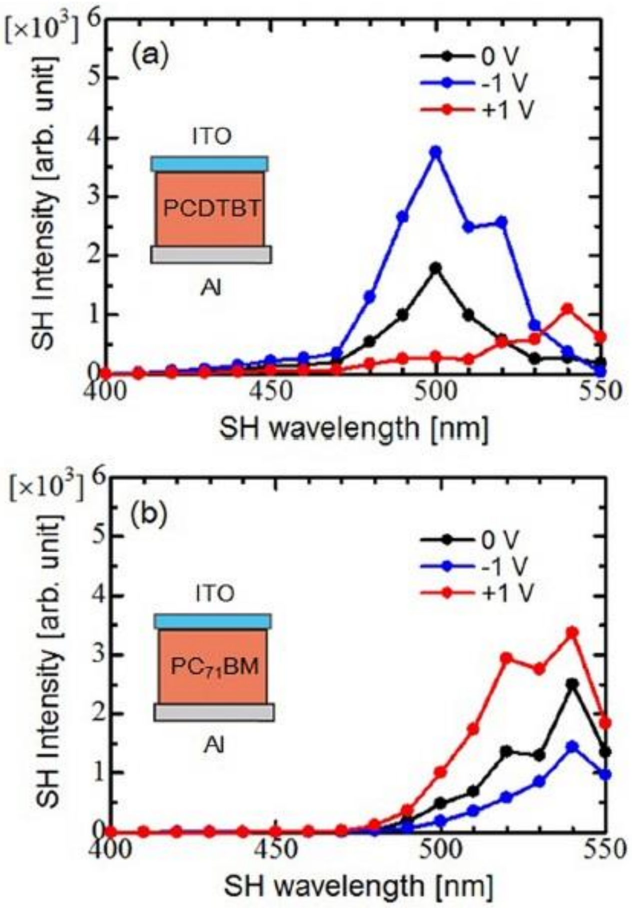

Figure 4.17 EFISHG spectra of fabricated devices, (a) ITO/PCDTBT/Al, and (b) ITO/$PC_{71}BM$/Al.

Figure 4.18 shows results of the time-resolved EFISHG measurements for ITO/PCDTBT:$PC_{71}BM$/Al photodiode under applied *d.c.* step voltages in dark. In the experiment, two different laser wavelengths, 1000 nm from PCDTBT and 1060 nm from $PC_{71}BM$, are chosen to probe SH waves generated at 500 nm and 530 nm, respectively.

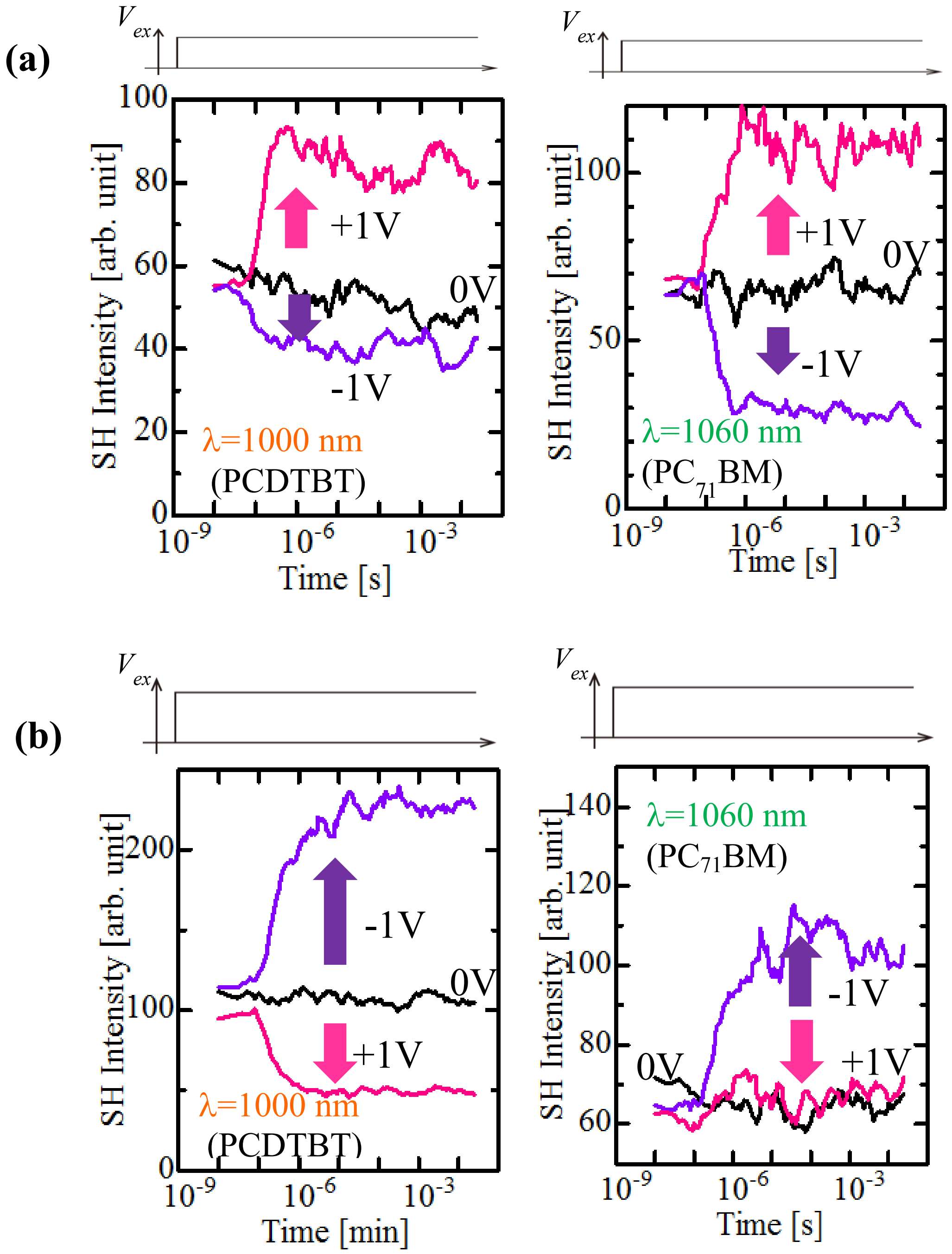

Figure 4.18 A time-resolved EFISHG for PCDTBT:$PC_{71}BM$ OSCs under applied d.c. step voltages in dark condition. Second harmonic intensity vs. time plots for PCDTBT and $PC_{71}BM$: (a) ITO/ PCDTBT:$PC_{71}BM$/Al and (b) ITO/ PEDOT:PSS/PCDTBT:$PC_{71}BM$/Al samples at laser wavelengths of λ = 1000 nm (left) and λ = 1060 nm (right).

By applying a positive *d.c.* step voltage (V_{ex} = +1 V), the SH intensity generated at 500 nm increases when the fundamental laser with 1000 nm wavelength is used. Similarly, the SH intensity generated at 530 nm is increased by the application of 1060 nm laser wavelength. On the other hand, the SH intensity decreases by using a negative step voltage (V_{ex} = -1 V). It is noteworthy that a non-zero electric field is developed in the ITO/PCDTBT:PC_{71}BM/Al device due to the work function difference of electrodes, i.e. ITO and Al. Accordingly, electric field "E_{b1} (E_{b2})" is non-zero built-in field in PCDTBT (PC_{71}BM). Application of the external voltage, additionally, forms electric field "$E_e(t)$" in the PCDTBT and the PC_{71}BM. As a result, the SH intensity in the BHJ layer is generated in proportion to $|E_b + E_e(t)|^2$, where $E_e(t)=(V_{ex}/d)(1-exp(-t/t_{RC}))$ (Cui et al., 2013; Taguchi et al., 2010; Taguchi et al., 2011; L. Zhang et al., 2011). Here, d is the thickness of BHJ layer, and t_{RC} is the circuit response time that can be given by $t_{RC}=RC$ (R is the series resistance of the circuit; C is the capacitance of the OSC). The decrease or increase in the electric field of BHJ layer depends on the polarity of "E_b". Results given in **Figure 4.18** (a) show that the electric fields "E_{b1}" in PCDTBT and "E_{b2}" in PC_{71}BM are pointing from ITO to Al electrode. It is notable that the electric field in OSCs, caused by the work function difference should be in the direction from Al (ϕ =3.4 eV) to ITO (ϕ =4.5 eV) electrode. Therefore, it is believed that there are other sources of internal electric field such as charge transfer at the electrode/organic interface (X. Chen et al., 2014) which can be described by E_{sc}, but their presence does not affect our generic discussion, here.

Figure 4.18 (b) shows the time-resolved EFISHG for the OSCs with PEDOT:PSS layer (ITO/PEDOT:PSS/PCDTBT:PC_{71}BM/Al). Under the positive and negative applied voltages, the SH intensity decreases and increases, respectively, at the SH wavelengths of 500 and 530 nm. The results indicate that the electric field decreases under positive applied voltage while increases under negative applied voltage in

PCDTBT and PC$_{71}$BM. Therefore, it is believed that internal electric field in PCDTBT (E_{b1}) and PC$_{71}$BM (E_{b2}) is pointing from Al electrode to the ITO. After comparing the results of **Figure 4.18** (a) and (b), it can be concluded that the direction of the internal field in photodiode changes by the introduction of PEDOT:PSS layer. This is one of the most important findings, which has been discovered by the use of EFISHG measurements. In the OSCs, excitons are dissociated into free holes and electrons at the molecular interface between PCDTBT and PC$_{71}$BM which are, then, transferred along the internal electric field. Accordingly, the internal field pointing from Al and ITO helps to transport free holes to the ITO and free electrons to Al electrode. This supports the efficient flow of short-circuit current in an appropriate direction across the OSCs incorporating PEDOT: PSS layer. It is noteworthy, that the internal field formed in single component based devices (**Figure 4.17**) differs from that in the BHJ devices, possibly due to the difference in the contact condition between polymer and electrodes.

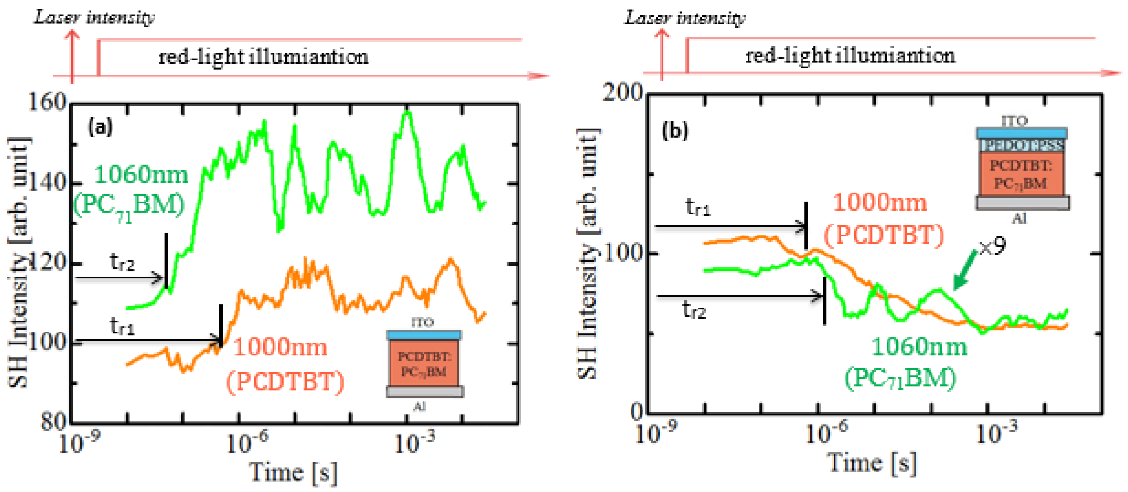

Figure 4.19 Transit time response for ITO/PCDTBT:PC$_{71}$BM/Al (a) and ITO/PEDOT:PSS/PCDTBT:PC$_{71}$BM/Al (b) devices.

Figure 4.19 (a) shows the EFISHG measurement of the ITO/PCDTBT:PC$_{71}$BM/Al samples under illumination. The SH intensity increases in

PCDTBT and $PC_{71}BM$, suggesting that open-circuit voltage of photodiode will increase. Under illumination, excitons are created in PCDTBT and $PC_{71}BM$ which are then dissociated into free holes and electrons at the molecular interfaces. Subsequently, the free holes transfer via PCDTBT molecules and arrive at ITO electrode with a transit time "t_{r1}". On the other hand, the free electrons transfer $PC_{71}BM$ molecules and are collected at the Al electrode with a transit time "t_{r2}". These transported electrons and holes accumulate at the electrodes and results in an open-circuit voltage (V_{OC}). The transit time of carriers is determined directly from the transient EFISHG, by assuming that the SH intensity begins to increase at the time corresponding to the transit time. The results of EFISHG in **Figure 4.19** (a), show that electrons and holes are collected at Al electrode at $t_{r2} = 3\times10^{-8}$ s and at ITO electrode at $t_{r1} = 4\times10^{-7}$ s, respectively. **Figure 4.19** (b) illustrates the EFISHG measurements of ITO/PEDOT:PSS/PCDTBT:$PC_{71}BM$/Al device for investigating the influence of PEDOT:PSS layer on the charge transport behavior in the organic solar cell. The SH intensity decreases in the same way at both the wavelengths 500 and 530 nm, under illumination, as shown in **Figure 4.19** (b). The generated holes and electrons move towards the ITO and Al electrode, respectively, and generate an open-circuit voltage ($V_{OC} > 0$) at ITO electrode with reference to the grounded Al electrode. The transit times for holes and electrons are measured as $t_{r1}=5\times10^{-7}$ s and $t_{r2} = 1\times10^{-6}$ s, indicating that the electron transport time is longer for OSCs having PEDOT:PSS layer. This is also one of the novel findings achieved by the transient EFISHG measurement.

On the basis of the Maxwell-Wagner effect model analysis (Maxwell, 1954; Wagner, 1914), the enhancement of the open-circuit voltage is discussed. For the ITO/PCDTBT:$PC_{71}BM$/Al device, photo generated excitons diffuse to the PCDTBT:$PC_{71}BM$ interface and dissociate into free electrons and holes. After the carrier separation, holes transport in PCDTBT with time "t_{r1}", electrons move in

$PC_{71}BM$ with time "t_{r2}" and generate the open-circuit voltage. Therefore, excess charges will be accumulated at the interface according to $Q_s=J_{SC}(t_{r2}-t_{r1})$. This is a well-known Maxwell-Wagner effect that accounts for the carrier accumulation at the two material interfaces. In other words, excess carriers accumulate at the interface when carrier spreading times of the adjacent two materials are different. The EFISHG measurement showed that transit times of PCDTBT and $PC_{71}BM$ differ in ITO/PCDTBT:$PC_{71}BM$/Al and ITO/PEDOT:PSS/PCDTBT:$PC_{71}BM$/Al BHJ devices. Accordingly, the excess of holes accumulates at PCDTBT:$PC_{71}BM$ molecular interface in ITO/PCDTBT:$PC_{71}BM$/Al device ($t_{\mathrm{r1}} \gg t_{\mathrm{r2}}$ and $J_{\mathrm{sc}} \ll 0$), whereas electrons accumulate in the ITO/PEDOT:PSS/PCDTBT:PCBM/Al device ($t_{\mathrm{r1}} \ll t_{\mathrm{r2}}$ and $J_{\mathrm{sc}} \ll 0$). These are the results of the Maxwell-Wagner effect. The accumulated excess holes form an electrostatic potential at the molecular interface lead to a decrease in the open-circuit voltage. In the photodiode device without PEDOT:PSS layer, holes $Q_s = 1.8\times10^{-9}$ C/cm^2 accumulate at the molecular interface with short-circuit current $J_{sc} = -4.8\times10^{-3}$ A/cm^2. As a result, charge-separated electrons additionally lose electrostatic energy $e\Delta V = enQ_s/(C_1 + C_2)$ to move to an Al electrode (e: elementary charge, ΔV: voltage loss, n: ratio of molecular interface area to electrode area, C_1 and C_2: capacitance of PCDTBT and PCBM layer). This energy loss is calculated as $e\Delta V = 0.2$ eV with values $n = 17$, $C_1 = C_2 = 7.6\times10^{-8}$ F/cm^2. On the other hand, in ITO/PEDOT:PSS/PCDTBT:$PC_{71}BM$/Al device, electrostatic energy loss is small, i.e., $e\Delta V = 0.02$ eV ($Q_s = 4.1\times10^{-9}$ C/cm^2 and $n = 1$). Consequently, the open-circuit voltage of photodiode with PEDOT:PSS layer is 0.2 V higher than that of photodiode with no PEDOT:PSS layer. Actually, the PEDOT:PSS layer blocks a short electron transport path in BHJ layer, which results in the enhancement of open-circuit voltage. As mentioned above, the carrier transport in photodiode can be traced by using the EFISHG measurement. Finally, it is accomplished that TR-EFISHG can be used for studying the impact of interfacial layer on the electron and hole transport in bulk-heterojunction OSCs.

In this study, the EFISHG technique has been applied to investigate the BHJ photodiode. It is concluded that, the selectively probed SHG measurement is useful to study electron and hole behaviors in BHJ OSCs and provide a direct way to investigate the transit time of the electrons and holes in BHJ OSCs. This study has also led to some novel findings that the internal field direction is changed when a PEDOT:PSS layer is introduced. Furthermore, the transit time for electron is longer in the PCDTBT:$PC_{71}BM$ OSCs with the PEDOT: PSS layer. Finally, it is worth stating that TR-EFISHG can be used as a novel way for studying the impact of interfacial layer on the transport of carriers in bulk-heterojunction photodiode and solar cells.

CHAPTER 5 : ORGANIC PHOTODIODE

Overview

This chapter is divided into two parts; the first part is about the investigation of P3HT:VOPcPhO blend as a new blend system for optoelectronics applications, while the second part is about the enhancement of PCDTBT:$PC_{71}BM$ blend for the fabrication of efficient organic solar cells. In particular, the first part involves the study of VOPcPhO charge transport including the calculation of its electron and hole mobility by I-V conventional method. VOPcPhO is actually a donor material but in this study it has been blended together with another donor material, P3HT. P3HT has a dominant holes transport so it behaves as a donor while VOPcPhO acts as an acceptor in the P3HT:VOPcPhO blend system due to its comparable electron and hole mobility. The OSC fabricated from this blend (ITO/PEDOT:PSS/P3HT:VOPcPhO/Al) has yielded an efficiency of around 1.09 %. Due to its slow power conversion efficiency, this device has been used for light sensing application by broadening its absorption range through the optimization of blend composition between the two components. The light sensor has shown very fast response time and high sensitivity in the broad visible range. While in the second part, another blend system has been used by combination of PCDTBT and $PC_{71}BM$ for the fabrication of OSCs. The optimization of OSCs based on this blend has already been taken up, rigorously, by other researchers but in the present work, the interest has been focused on the study of its charge transport properties (as discussed in Chapter 4 section 4.2.3) and the stability study of PCDTBT:$PC_{71}BM$ based OSCs fabricated in three different procedures involving layer-by-layer fabrication and thermal treatment. Further discussion on the stability of these OSCs is also discussed at the end of this chapter.

5.1 Part 1: Investigation of P3HT:VOPcPhO Bulk Heterojunction as a New Blend System for Optoelectronic Applications

5.1.1 Fabrication of Organic Solar Cells based on VOPcPhO/P3HT Blend

The materials; regioregular poly(3-hexylthiophene-2,5-diyl) (P3HT), vanadyl 2,9,16,23-tetraphenoxy-29H,31H-phthalocyanine (VOPcPhO) and poly(3,4-ethylenedioxythiophene):poly(styrene sulfonate) (PEDOT:PSS) were used as received without further purification. The conductivity of PEDOT:PSS was 900-1000 Scm^{-1}. Indium tin oxide (ITO) coated glass substrates (~10 Ω/sq. sheet resistance) were cleaned by sonication in acetone, isopropyl alcohol and de-ionized water followed by nitrogen blowing for drying. 20 mg/mL solutions in chloroform were prepared for both P3HT and VOPcPhO. All the solutions were filtered using nylon 0.45 µm filters. The blend was prepared by mixing P3HTand VOPcPhO in the ratio of 1:1. For the device fabrication, PEDOT:PSS aqueous solution was spin coated on the pre-cleaned substrates at 4000 rpm for 1 min resulting in the thickness of 45 nm and was annealed at 120 ºC for 30 min. The active layers were spin coated on the ITO/PEDOT:PSS coated glass substrates. The samples were, then, thermally annealed at 120 ºC for 30 min. The thickness of the active layers was 150 nm. Finally, thermal evaporation was carried out for the deposition of top aluminum (Al) electrode to complete the device fabrication process. The top Al electrodes were deposited in round shape using shadow mask. The diameter of each device was 2 mm. The post deposition annealing was performed at 120 ºC for 30 min. All the fabrication process was conducted in the clean room environment. Molecular structure of VOPcPhO and P3HT and the cross-sectional view of the fabricated ITO/PEDOT:PSS/P3HT:VOPcPhO/Al device is shown in **Figure 5.1**.

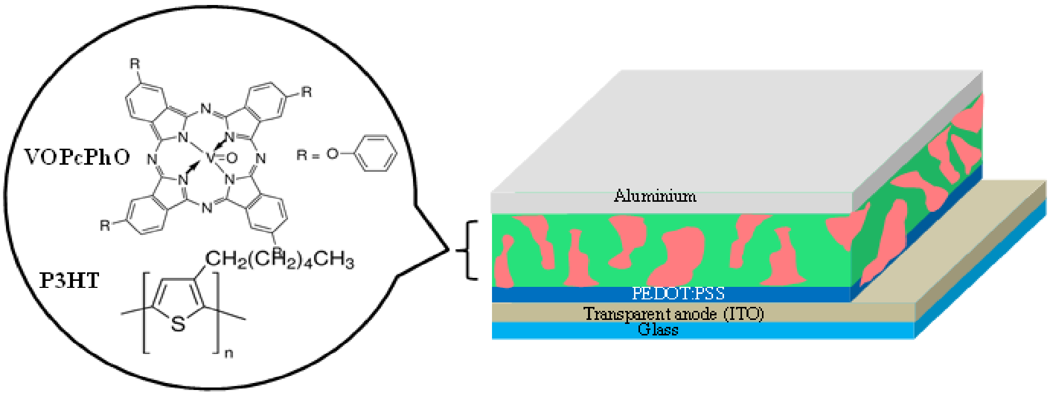

(a) **(b)**

Figure 5.1 (a) Molecular structure of VOPcPhO and P3HT. (b) Cross-sectional view of the ITO/PEDOT:PSS/P3HT:VOPcPhO/Al solar cell.

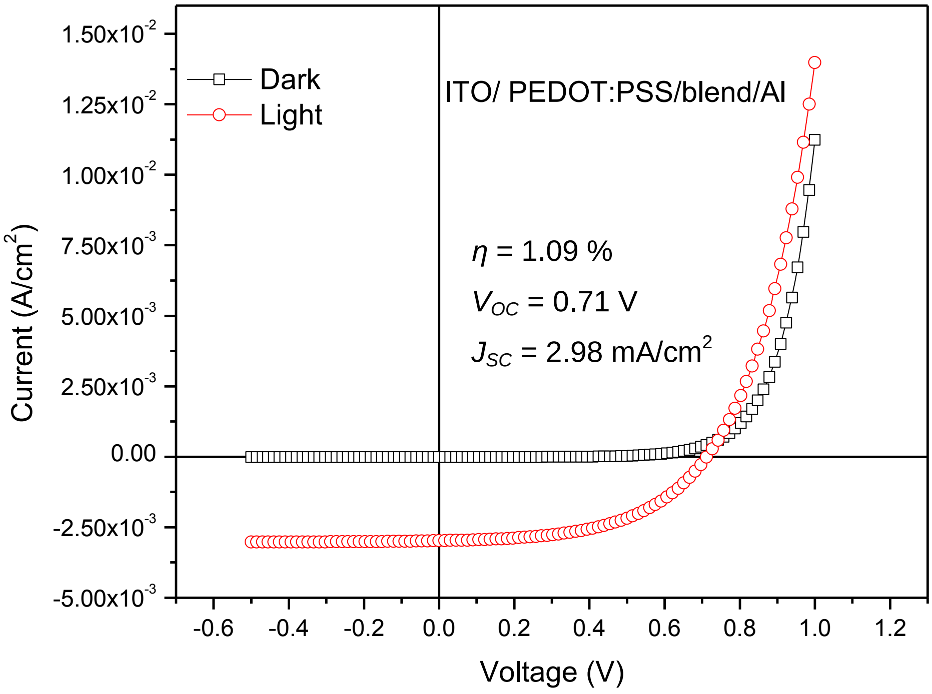

Figure 5.2 Current-voltage (J-V) characteristics of ITO/ PEDOT:PSS/blend/Al photovoltaic device under 100 mWcm^{-2} solar simulator illumination.

The J-V characteristics in dark and under illumination for the ITO/ PEDOT:PSS/P3HT:VOPcPhO/Al photovoltaic device, are plotted in **Figure 5.2**. The photovoltaic parameters such as open-circuit voltage (V_{OC}), short-circuit current density (J_{SC}), fill factor (FF) and power conversion efficiency (η), and are also given in **Figure 5.2**. The efficiency depends on two factors. One, broader absorption range of solar spectrum which is necessary for increased charge generation. Second, dissociation of excitons generated in VOPcPhO and P3HT under illumination due to the bulk heterojunction which is restricted in the single layer and bilayer solar cells because a typical travel path of carriers is less than 20 nm before recombination (Cai, Gong, & Cao, 2010). The OSC made by this blend system yields the best efficiency of about 1.09 %, which is considered relatively quite low for practical use in solar energy harnessing application. Therefore, it is suggested to be employed into the light sensor application by optimizing the absorption range in the visible region. The optimization steps for the fabrication of photodiode are discussed in the following sections.

5.1.2 VOPcPhO/P3HT Blend for Light Sensing Application

For the fabrication of light sensor in the form of organic photodiode, a new solution has been prepared in three different ratios for optimization purpose. P3HT and VOPcPhO were dissolved in chloroform to make 20 mg/mL solution separately and then mixed in three volume ratios (1.0:1.0, 1.0:1.5, 1.0:2.0). A ~40 nm thick PEDOT:PSS film was deposited on the cleaned ITO-coated glass substrate using a spin coater. The PEDOT:PSS film was annealed at 120 °C for 30 min. The P3HT:VOPcPhO blend solution was spin coated on PEDOT:PSS layer to deposit 150 nm thick film followed by annealing at 120 °C for 30 min. Finally, the top contact of Al electrode was deposited by means of thermal evaporation under vacuum conditions. The fabricated

ITO/PEDOT:PSS/P3HT:VOPcPhO/Al device were post annealed at 120 °C for 30 min. Electrical characteristics of the sensor were measured using a computer interfaced (Keithley) source measuring unit (SMU) and the Oriel 67005 solar simulator. The intensity of light irradiant was varied from 40 mW/cm^2 to 140 mW/cm^2 and the calibration was done by using a power meter (Newport model 1815-C). The characterization was carried out in ambient conditions at room temperature. The electrical measurements of the light sensor after the aging effect of three weeks, showed good stability.

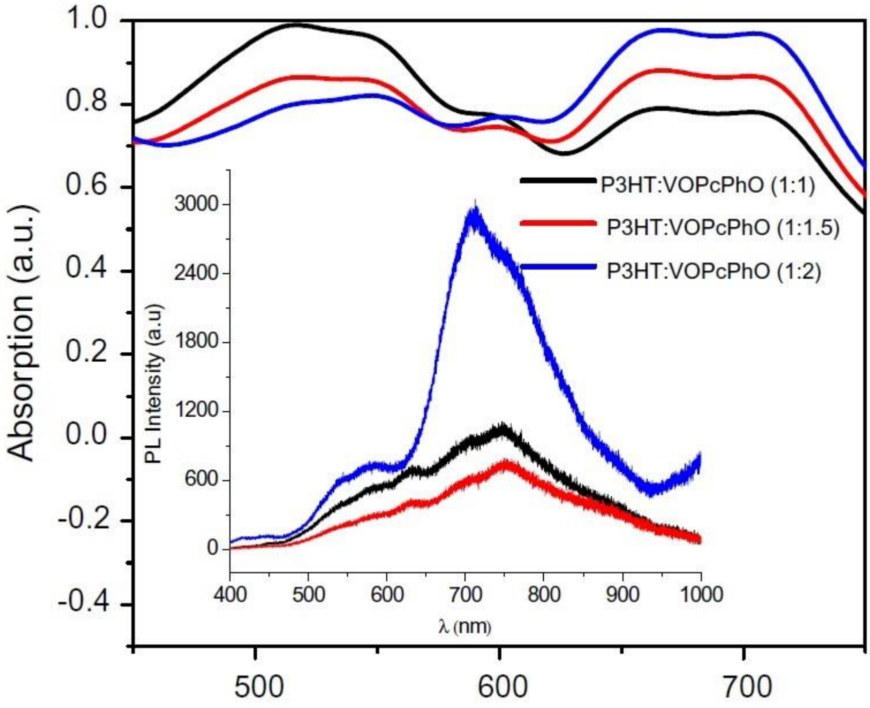

Figure 5.3 UV-Vis absorption spectra of P3HT:VOPcPhO composite films. Inset shows the photoluminescence spectra of P3HT:VOPcPhO composite films.

The absorption spectra of the P3HT:VOPcPhO composite thin films with different volumetric ratios are shown in **Figure 5.3**. Both the P3HT and VOPcPhO components lie in the range 450-750 nm of the visible spectral region. However, the spectral range of absorption for each component is limited but when combined together, these materials are well suited for light applications. The high absorption peak for P3HT exists at 518 nm with two shoulders at 550 nm and 600 nm. No light absorption can take place beyond 650 nm in the pristine P3HT film. Therefore, it seems feasible to add VOPcPhO so as to extend the absorption to longer wavelength in the red region. The VOPcPhO is perfectly suited to extend spectrum to a longer wavelength as shown in **Figure 5.3.** The blended film exhibits the absorption spectrum which includes features of the component P3HT and VOPcPhO. The broad absorption spectrum may contribute to greater light harvesting and is capable of absorbing at longer wavelength without diminishing the shorter wavelength absorption. The PL of P3HT and VOPcPhO blend have been studied to optimize the ratio of P3HT and VOPcPhO for further investigation for photo sensors. The inset in **Figure 5.3** shows the PL spectra of the blend of P3HT:VOPcPhO measured at room temperature. It is evident from same figure that when P3HT and VOPcPhO are mixed in the volumetric ratio 1.0:1.5, the intense PL of the blend is significantly quenched. The photoluminescence quenching indicates that the photo-induced charge transfer in P3HT:VOPcPhO (1.0:1.5) blended film is much better than the rest of the ratios and this ratio is selected for the fabrication of the photo sensor.

The electrical characteristics of the ITO/PEDOT:PSS/P3HT:VOPcPhO/Al light sensors were measured under different illuminations intensities. **Figure 5.4** shows the effect of variation of applied biasing on the photocurrent of P3HT:VOPcPhO-based light sensor. The results show that the photocurrent rises by increasing the applied voltage on the sensor. Besides, as the biasing increases, the sensitivity of the sensor also increases. The reverse biased current has increased in the negative (-ve) direction along y-axis (current axis), thereby, giving an increase in the short circuit current under illumination.

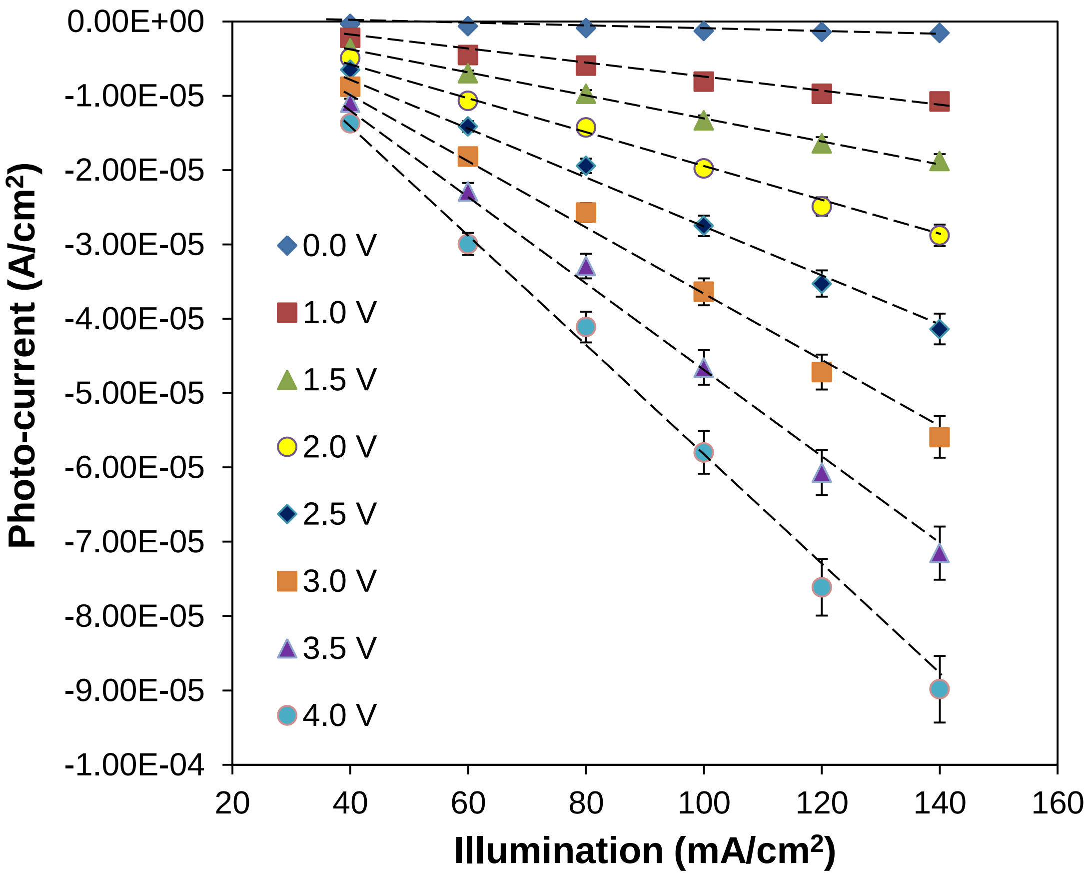

Figure 5.4 Photocurrent-illumination intensity characteristics of the sensor under different applied voltages.

The light intensity dependent change in the photocurrent can be expressed by the following equation (Yakuphanoglu, 2008):

$$I_{light} = AF^{\alpha} \tag{5.1}$$

where I_{light} is the current under illumination, F is the light intensity; A is a constant and α is an exponent. The value of α can be determined by the slope of I_{light} vs. F (light intensity) graph. The photovoltaic effect in the P3HT:VOPcPhO composite based photodiode is based on the formation of exciton (bound electron-hole pair) and subsequent dissociation due to the bulk heterojunction and charge collection at the electrodes (the photovoltaic mechanism has been clearly stated in section 2.2). The photocurrent is due to the charge carriers formed at the P3HT:VOPcPhO interface as a result of the electron-hole pair separation. The separated photo-carriers are transported toward the electrodes. The current at a certain voltage increases as the illumination intensity increases. The device fabrication was done in an open environment as the light sensor fabrication does not really require nitrogen conditions like OSCs and characterization was performed after aging in order to observe sensing stability for a long term use. The photovoltaic parameters of the device are good for solar cell applications, but are sufficient for photodiode applications. As a matter of fact, the solar cells are designed to minimize energy loss, whereas photodiodes are designed to achieve a rapid time response and spectral response (Pierret, 1996).

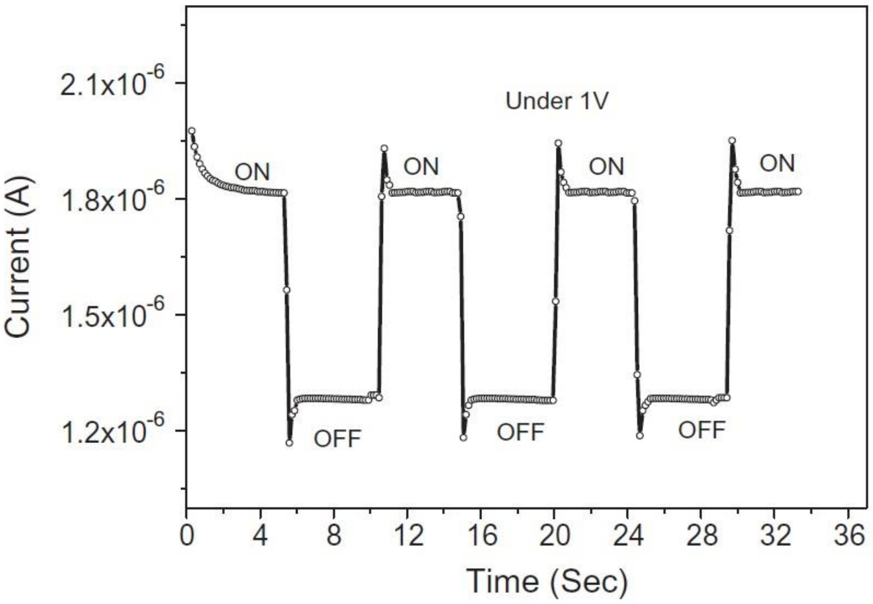

Figure 5.5 Photocurrent of the sensor, measured at +1.0 V under 100 mW/cm^2 (ON) and under dark (OFF) states.

Figure 5.5 illustrates the change in photocurrent after switching the light between ON and OFF states. The sensor exhibits photoresponsivity, photoconductivity, and rapid change of states with photocurrent showing a stable plateau value. The photoconductivity sensitivity of the device can be determined by the following relation (S.-H. Park, Ogino, & Sato, 2000):

$$S = I_{light}\, d / PAV \tag{5.2}$$

where I_{light} is the current under illumination, P is the power of incident light, d is the film thickness, A is the area of the device and V is the applied potential. The photoconductivity sensitivity value of the sensor is found as 5.65 x 10^{2} Sm/W. The responsivity of the sensor was determined as 2.1 x 10^{-4} A/W. These values of photoconductivity and responsivity are mentioned in the aged sample. The responsivity value of the fresh sample was 2.98 x 10^{-2} A/W, which is ~10^{2} times higher than the aged sample.

In conclusion, a bulk heterojunction photo sensor using a new donor-acceptor blend of P3HT and VOPcPhO has been successfully fabricated and characterized for its optical and electrical properties. It has been found that the P3HT:VOPcPhO blend has a great potential to be applied for photovoltaic and photoconductive devices due to its high absorption, considerably good light harvesting in the visible range of the solar spectrum and better charge transfer.

5.2 Part 2: Towards an Efficient Organic Solar Cells by Utilizing PCDTBT/PC$_{71}$BM Blend System

As the study on P3HT:VOPcPhO charge transport, in the previous sections, showed that this blend having incompatibility with EFISHG characterization techniques, a second blend system has been introduced which is PCDTBT:PC$_{71}$BM. The characterizations of the second blend system from the previous chapter have shown interesting results on the study of charge transport and thus, it is used for enhancement of OSCs via thermal study. The aim to produce OSCs with high efficiency has led to the fabrication of solar cells in three different protocols involving thermal annealing effect. The stability of OSCs under this study is also discussed at the end of this chapter.

5.2.1 The Fabrication of Organic Solar Cells based on PCDTBT/PC$_{71}$BM Blend

Both the active materials, poly[N-9'-heptadecanyl-2,7-carbazole-alt-5,5-(4',7'-di-2-thienyl-2',1',3'-benzothiadiazole)] (PCDTBT) and (6,6)-Phenyl C$_{71}$ butyric acid methyl ester (PC$_{71}$BM) without any further purification. The 10 mg/ml solutions for each material have been prepared in chloroform. Solutions of PCDTBT and PC$_{71}$BM have been mixed in 1:4 volumetric ratio and stirred for an hour. Prior to the fabrication process, the pre-patterned ITO-coated glass substrates (from Ossila) have been cleaned by sonication in acetone, isopropanol, and de-ionized water, consequently. Poly(3,4-ethylenedioxythiophene) polystyrene sulfonate solution or PEDOT:PSS (H.C. Starck PH1000) has been deposited onto the cleaned substrates by spin coater (Laurell WS-650-8B) at 4000 rpm for 60 s in order to get ~40 nm thick films followed by annealing at 120 ^{o}C for 30 min. Then, the PCDTBT and PC$_{71}$BM blend (1:4) solution has been spin coated on the PEDOT:PSS films at 2000 rpm for 20 s to form 70 nm thick blend layer. The detail of fabrication procedure is illustrated in **Figure 5.6**. Sample 1 (OSC-1) was fabricated without any thermal treatment whereas for sample 2 (OSC-2) the PCDTBT:PC$_{71}$BM film was annealed at 70 ºC for 30 min prior to the deposition of top Al electrode. Sample 3 (OSC-3) was annealed two times at the same conditions, once before top electrode deposition and once after the fabrication.

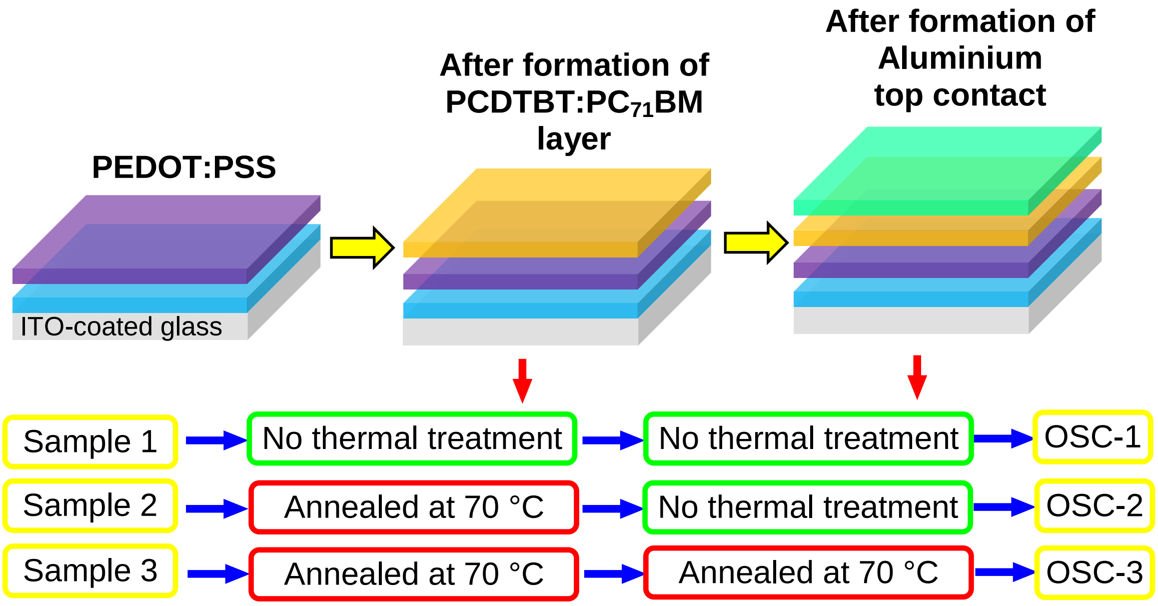

Figure 5.6 The OSC devices fabrication in three different protocols.

Table 5.1 A comparison of efficiencies of three different devices (OSC-1, OSC-2, and OSC-3) prepared in three different conditions.

Device types	Annealing (Active layer)	Post-Annealing (After Al top electrode deposition)	Jsc (mV/cm^2)	Voc (V)	Efficiency (%)
OSC-1	No	No	33.2	0.85	9.03
OSC-2	Yes	No	17.2	0.82	4.80
OSC-3	Yes	Yes	12.1	0.75	2.36

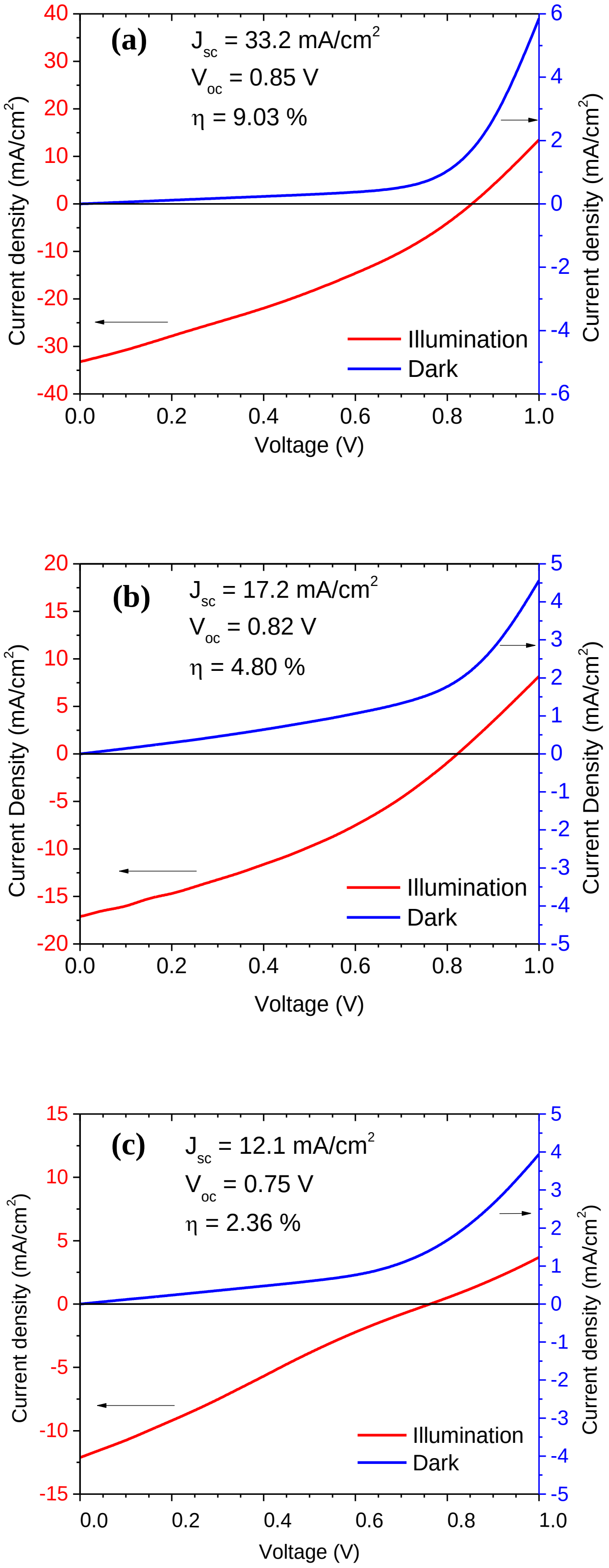

Figure 5.7 I-V characteristics for (a) OSC-1, (b) OSC-2, and (c) OSC-3 in dark and under light illumination.

Table 5.1 shows photovoltaic parameters of the three devices (OSC-1, OSC-2, and OSC-3) fabricated under different protocols as shown above in **Figure 5.6**. Though the efficiency of OSCs in **Figure 5.6** is still low, we can conclude from the statistical experimental data that the efficiency is dependent on preparation process. Also, we can discuss the degradation process by using the sample data in **Figure 5.7** and **5.8**. Noteworthy that experimental error bars obtained from numbers of fabricated OSCs (6 to 24) devices in a sample that were repeated for more than nine fabrication batches. A standard deviation based on the calculation and graph fitting is in the range of 5-7 %. The efficiency of the first type of OSC device (OSC-1) is as high as 9.03 % but it decreases with the passage of time and finally the efficiency drops to 0.11 % within 24 hr. It is observed that a very high short circuit current (33.2 mA/cm^2) of OSC-1 has led to a very high efficiency as shown in **Figure 5.7**. During the I-V characterization, it is observed that the OSC devices have experienced a change in the temperature once exposed to a bright light (100 mW/cm^2) of solar simulator. In most cases, a longer light exposure is needed in order to perform the I-V characterization over a particular range of electric field (V) with some repetitions for the sake of stable I-V results. As a result, heat from the simulator lamp is transferred to the OSC device via the light irradiation. As a matter of fact, heat from light source (simulator) may cause increase in OSC performance or in contrast, it may lead to OSC multi-step degradation. It is important to take the effect of temperature into account as photovoltaic parameters that control OSCs performance such as J_{SC} and V_{OC} are temperature dependent. For the second type of OSC device (OSC-2), 4.80 % efficiency is achieved and its efficiency is considerably good but lower than the OSC-1. The stability of the OSC under such annealing treatment can be far better than the OSC-1 as discussed in reference (Gusain et al., 2013). The third type of device (OSC-3) has been thermally treated two times which exhibits 2.36 % efficiency as shown in **Figure 5.7**. The stability of this type of OSC devices is relatively better than the other two devices. In the case of OSC-1, the disordered nature of untreated PCDTBT:PC$_{71}$BM blend system may be the cause that leads to the charge trapping in this active layer, which in turn causes higher carrier concentration (Etzold et al., 2011; Kaake, Barbara, & Zhu, 2010). In the case of OSC-2, the active layer has been thermally treated and the obtained efficiency is relatively lower but the device is stable over longer period of time. It has been reported for the PCDTBT:PC$_{71}$BM solar cell that when annealing is done at the temperature less than 100 ºC, the glass transition temperature for the active layer remains unchanged (T. Wang et al., 2012). The best annealing temperature is around 70-80 ºC for achieving optimum efficiency. Here, it is important to mention that the thermal annealing of the PCDTBT:PC$_{71}$BM layer is very crucial for stable efficiency of OSCs in order to ensure its morphological stability (D. H. Wang et al., 2012). The OSCs with such thermal treatment have been widely discussed in literature directly and indirectly (Gusain et al., 2013; Roesch et al., 2013). While in the case of OSC-3, the device has undergone annealing treatment twice, and as a result the efficiency has further reduced but the stability is improved. The S-shaped I-V characteristics has been observed in this case which might be attributed to the restricted charge transport at the metal-organic interface where space charge accumulates and form a non-ohmic contact (Wagenpfahl et al., 2010). Such transport barriers are formed after the post fabrication annealing which cause an unbalanced charge carrier mobility at metal-organic interfaces (Tress et al., 2011). The space charge is built up at the interfaces because the electrons and holes cannot be extracted rapidly, thereby, increasing the recombination and reducing the fill factor (FF). In addition, the post annealing process is also reported to cause a coarse phase-separation in amorphous PCDTBT polymer structure which could also be a reason for lower efficiency (Schindler, Wollgarten, & Fostiropoulos, 2012).

5.2.2 The Stability of OSCs based on PCDTBT:PC$_{71}$BM Blend System

Figure 5.8 shows the normalized efficiency of all devices over a period of seven days. Here, the reduced efficiency represents the stability issue of each of the three OSC devices after some period of time. The efficiency of OSC-1 (fabricated without thermal annealing) ~9.03 % dropped dramatically to ~0.11 % on the second day. OSC-2, which has undergone thermal annealing after the deposition of organic active layer, has shown improved stability where as its efficiency has dropped ~47 % of the initial value. It seems that the thermal annealing process is capable of improving the stability of the PCDTBT based OSC device. Finally, the OSC-3 shows an improvement in stability with ~72.2 % reduction in its efficiency from the initial value.

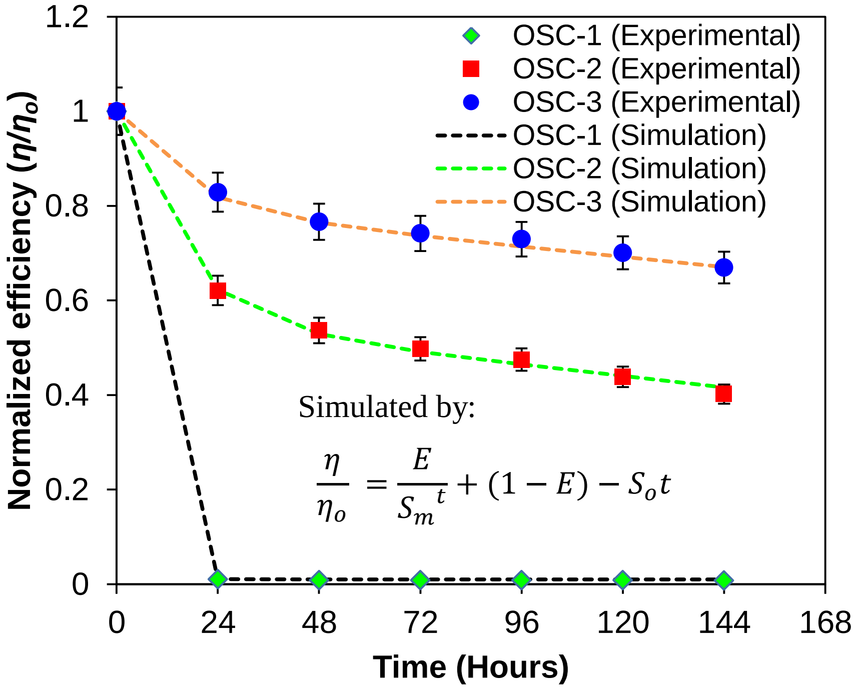

Figure 5.8 Normalized efficiency vs. time.

It is instructive, here, to mathematically express the degradation trend. The degradation effect exhibits an exponentially decaying behaviour which can be mathematically represented by the following equation (5.3):

$$\frac{\eta}{\eta_o} = \frac{1}{S^t} \tag{5.3}$$

where, η/η_o and t are the normalized degradation and time of degradation in hours, respectively, while the S^t represents the rate of degradation. For t=0, η/η_o = 1 and if t approaches ∞ then η/η_o becomes 0. For any device that experiences degradation, the value of S should be slightly greater than unity. This value increases if the rate of degradation is increased. Under these circumstances, the final value of η/η_o approaches zero. Ideally, the degradation starts just after the completing device fabrication process but there is a time difference between the time when the degradation starts and the time when the I-V measurements are carried out. Thus, by taking into account the presence of this time difference as t_d in equation (5.3), the expression takes the form as follows:

$$\frac{\eta}{\eta_o}' = \frac{S^{-t_d}}{S^t} \tag{5.4}$$

On the other hand, if there is no time difference as discussed above, then (t_d = 0) the equation (5.4) takes exactly the form of equation (5.3). It is suggested that, the degradation behaviour (for a given final normalized degradation) with $\eta/\eta_o = 1-E$ against time of degradation can be written as follows:

$$\frac{\eta}{\eta_o} = \frac{E}{S^t} + (1 - E) \tag{5.5}$$

where E is the percentage of average efficiency loss. In equation (5.5), the first term on the right hand side represents the trend of degradation rate until the normalized degradation (η/η_o) becomes constant, while the second term shows the limit of degradation over a period of time. By considering the time difference (t_d) as mentioned previously, equation (5.5) can be written as follow:

$$\frac{\eta}{\eta_o}' = \frac{ES^{-t_d}}{S^t} + (1 - ES^{-t_d}) \tag{5.6}$$

From this expression, the limit of degradation at a particular time can also be termed as degradation-limited time or t_s which means that η/η_o approaches $1 / S^t$ when $t \leq t_s$ while η/η_o tends to $1 - E$ when $t > t_s$. The t_s can be determined from the point where the efficiency becomes constant. At the same time, the value of t_s can determine the factor S by plotting the following equation (5.7):

$$\log\left(\frac{1}{\eta/\eta_o}\right) = t \log(S) \tag{5.7}$$

The value of S can be calculated by taking the antilog of the slope of the plot log 1/ (η/η_o) vs t, at t_s. In some cases, much more degradation happens to continue due to the presence of oxygen which results in further reduction in the OSCs efficiency. Such trend in degradation has been observed in this work where the normalized degradation of OSCs shows further decrease in a linear manner. A similar behaviour for OSC, characterized in ambient condition, has also been observed elsewhere as reported in ref (Gevorgyan, Jørgensen, & Krebs, 2008; Norrman, Gevorgyan, & Krebs, 2009). In our case, the oxidation in OSCs, especially OSC-2 and OSC-3, further decreased the efficiency. This effect must be taken into account and thus, the previous equation (5.5) and (5.6) should contain the third term for additional degradation effect which is probably caused by oxidation:

$$\frac{\eta}{\eta_o} = \frac{E}{{S_m}^t} + (1 - E) - S_o t \tag{5.8}$$

From equation (5.8), there are two similar factors that seem to control the rate of total degradation that exactly describe the stability of OSCs in this work. Since the parameter *S* plays an important role in controlling the degradation rate, two other fitting parameters have been introduced, here, as S_m and S_o. The rate of degradation, that might be due to deformation of the material, is controlled by a fitting parameter S_m, which shows a reverse exponential trend. On the other hand, the rate of degradation, that might be due to oxidation, is controlled by a fitting parameter S_o which shows further decrease in a linear way. From the present work, it can be concluded that the degradation of OSCs has two parts; one with reverse exponential trend due to material properties that might be deformed with time and the other with linear trend due to oxidation. Again, if we take time difference into account, equation (5.8) can be written as below:

$$\frac{\eta}{\eta_o}{}' = \frac{E{S_m}^{-t_d}}{{S_m}^{t}} + \left(1 - E{S_m}^{-t_d}\right) - S_o(t + t_d) \tag{5.9}$$

On the other hand, if there is no time difference, then ($t_d = 0$) the equation (5.9) will be take the form of equation (5.8). A simulated graph of a similar behaviour for each type of device has been plotted by using Desmos application with *E* values equal to 0.99, 0.44, and 0.20, and S_m values 1.35, 1.07, and 1.07 for OSC-1, OSC-2 and OSC-3, respectively. From the results of all devices, OSC-1 has shown a dominant effect of material degradation causing the efficiency to drops to a minimum level within 24 hours. Therefore, for this case, equation (5.3) and (5.4) are most suitable to simulate its degradation trend without involving oxidation effect. Since, OSC-2 and OSC-3 have shown both degradation trends i.e. material deformation and extended oxidation effects, therefore, equation (5.8) and (5.9) seem appropriate to simulate their degradation behaviour. The fitting parameter S_o that controls is 1×10^{-3} for both OSC-2 and OSC-3.

The suggested simulated equations have fitted each data point of normalized efficiency (η/η_o) very well as shown in **Figure 5.8.**

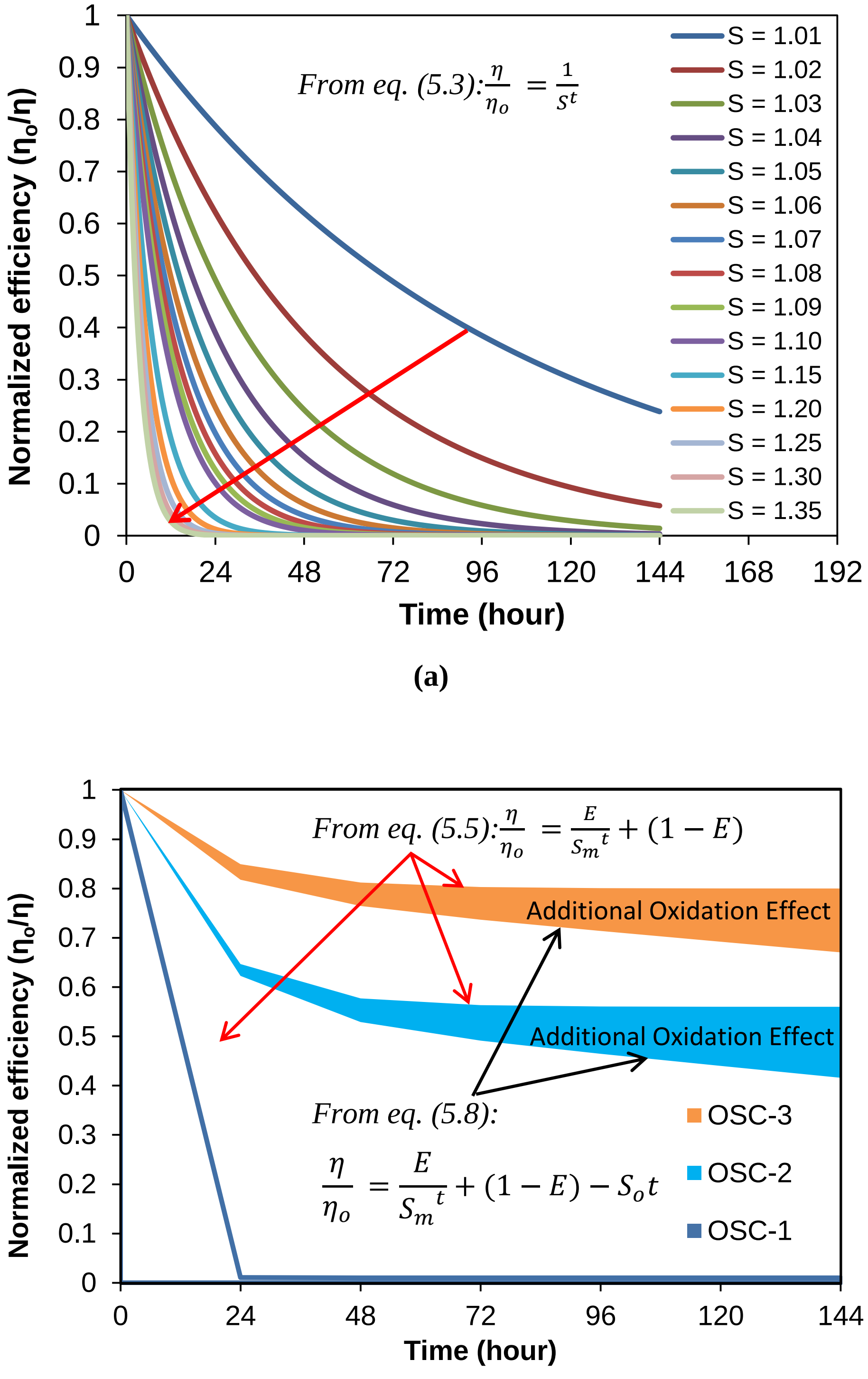

(a)

(b)

Figure 5.9 A simulated degradation model according to (a) equation 5.3, and (b) equation 5.4 and 5.6.

In details, **Figure 5.9** (a) and (b) show the simulated degradation models for OSCs with different values *S*, and degradation with additional effect caused by the oxidation of BHJ, respectively. **Figure 5.9** (a) shows the changes in the decay function by the variation of *S*, as proposed in equation (5.3), leading to a reduced OSCs performance. As the value of *S* is increased, the rate of degradation is observed to be increased as well. Such a decay trend is consistent with the degradation curve shown by OSC-l for the value of *S* or S_m given as 1.35,which can be seen in the next figure. **Figure 5.9** (b) shows simulated degradation models, as proposed by equation (5.5), and equation (5.8), in which the trend explains the degradation of both OSC-2 and OSC-3 very well. The shaded (coloured) areas represent extended degradation due to oxidation of BHJ layer. These shaded regions are actually emerged due to the different between the areas under the curve from equation (5.5) and (5.8) for OSC-2 and OSC-3, respectively. However, the OSC-1 does not show any difference in these areas since the decay trend is fully dominated by degradation of the material (BHJ layer) that leads to the total loss of device performance before extended oxidation could take place. It can be observed from the figure that the effect of oxidation on OSC performance increases and thus the stability of both OSC-2 and OSC-3 are further reduced as a function of time. The simulated degradation model of eq. (5.8) best describes the degradation trend in OSC-2 and OSC-3 while the model of equation (5.5) is the best way to describe OSC-1 degradation. However, if the extended oxidation effect is eliminated then equation (5.5) can be used to describe the degradation of all the OSCs.

There might be several other reasons that lead to the degradation of OSC such as the inflection phenomena or S-shape I-V characteristic due to photo-annealing (Lilliedal et al., 2010), long illumination time under elevated temperature (Carle et al., 2014; Norrman et al., 2010), photochemical degradation of donor monomer side chain upon illumination (Manceau et al., 2011), formation of metal oxide layer that erodes the fill factor (FF) due to oxidation (Gupta, Bag, & Narayan, 2008), and quite recently reported ultrafast electron-hole pair (or exciton) dissociation followed by non-geminate recombination (Etzold et al., 2011). Ultrafast exciton dissociation followed by non-geminate recombination can be one of the important reasons for degradation in the OSCs materials which possess disordered morphology in the thin film form. Previously, it has been observed that the pristine PCDTBT:$PC_{71}BM$ blend which shows disordered morphology could experience an ultrafast exciton dissociation in less than 100 fs after the photon absorption (Beiley et al., 2011). Therefore, here, it would be interesting to explain how the ultrafast exciton dissociation can affect both efficiency and stability at the same time. The theoretical explanation of this phenomenon can also be found in the literature (Gao & Inganas, 2014). **Figure 5.10** illustrates the mechanism of carriers transport in the OSC-1 with untreated organic blend. Normally, a bound hole-electron pair (singlet exciton) will form a charge transfer (CT) state at the heterojunction interfaces before its dissociation into free hole and electron carriers as shown in **Figure 5.10** (a). However, it has been reported that these free charge carriers can be created without passing through CT states as intermediates in the case of ultrafast exciton dissociation in less than 100 fs (Etzold et al., 2011), as shown in **Figure 5.10** (b). It is believed that delocalize free charge carriers have contributed to the generation of high photocurrent with high efficiency in OSC-1 device. There are still bound carriers that create CT exciton before dissociation takes place as shown in **Figure 5.10** (c). The geminate recombination can be possibly formed by the failure of exciton dissociation due to strong Columbic attraction of the charges (**Figure 5.10** (d)). The dissociation of exciton continues during micro-miliseconds time of photon absorption which contributes to the photocurrent, as shown in **Figure 5.10** (e). In the meantime, the concentration of charge carriers increase in a short time as a consequence of free carrier collection from the previous ultrafast exciton dissociation. Unfortunately, a disordered structure of untreated PCDTBT:PC$_{71}$BM blend provides traps for these carriers and leads to the formation of non-geminate recombination (Beiley et al., 2011) as shown in **Figure 5.10** (f). The increase in non-geminate recombination restricts the photocurrent generation and as a result, the efficiency of OSC decreases which causes to limit the stability of the device. The instability issue in the disordered PCDTBT:PC$_{71}$BM blend can be overcome by the enhancement of charge carrier dissociation without non-geminate recombination, and thus a stable OSC with high efficiency could possibly be attained. Further steps to overcome the degradation and improve the stability of OSC involve; i) implementation of water/oxygen blocking layer such as Alq3 and BCP in order to prevent cathode atoms from diffusing to organic layer and preventing oxygen molecules from permeating into the active organic films (Song et al., 2005), ii) use of less reactive cathode such as silver instead of aluminium in inverted OSC as it is not prone to degradation by oxygen or water (Krebs, Tromholt, & Jorgensen, 2010), iii) use of UV filter for OSC to avoid photo-degradation from the loss of V_{OC} (Schäfer et al., 2011), and iv) use of electron or hole transport layer (ETL and HTL) between organic/electrode interlayer because it provides more carriers for balance charge transport of electrons and holes within the OSC (Jin et al., 2009; Lo et al., 2011).

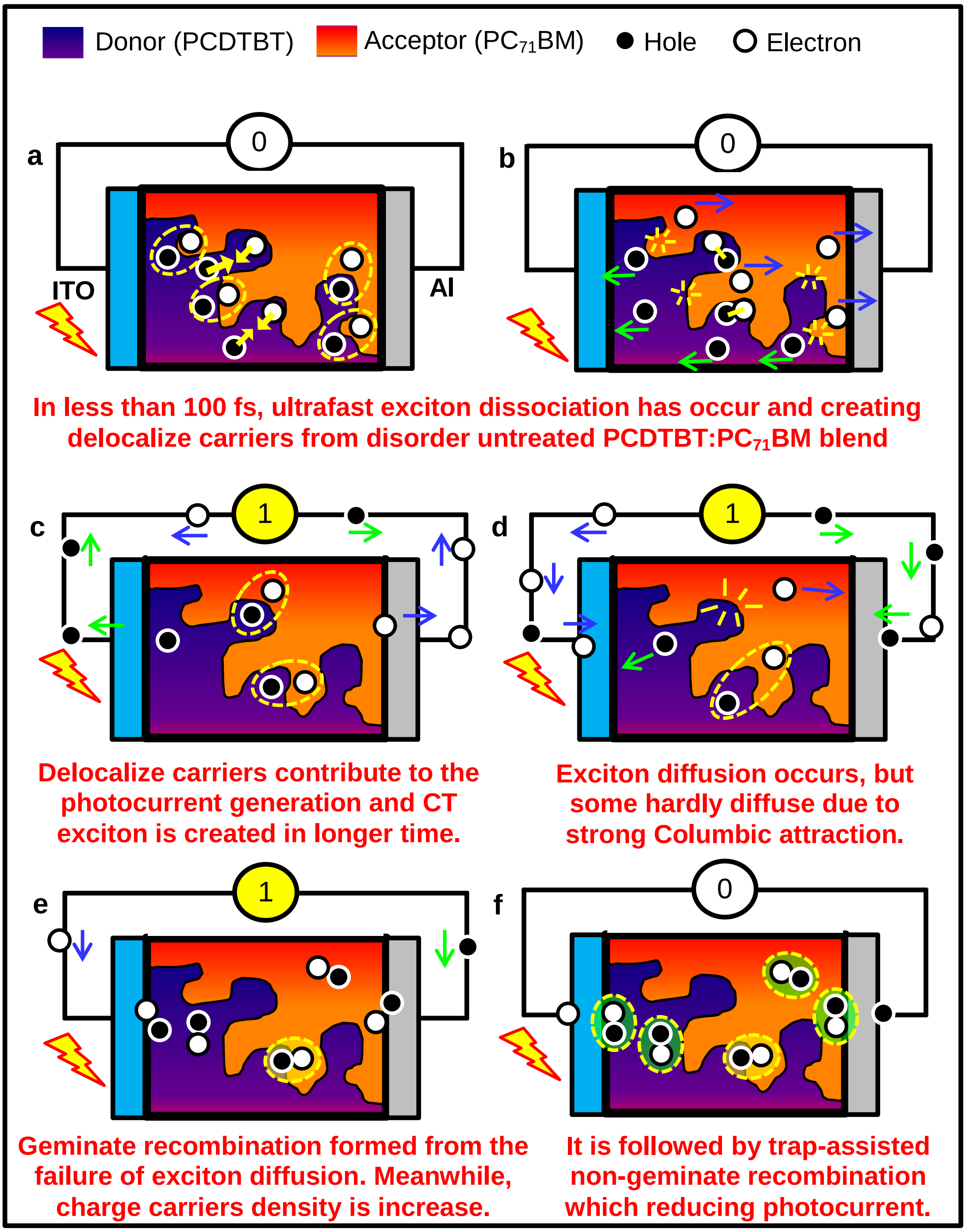

Figure 5.10 Charge carriers transport mechanism for OSC-1.

The OSCs composed of PCDTBT:PC$_{71}$BM blend system have been successfully fabricated with three different procedures of thermal treatment. From the experimental work, it was shown that OSC with untreated PCDTBT:PC$_{71}$BM active layer has the highest efficiency of around 9.03 % but it experienced a rapid drop in its efficiency with the passage of time. The ultra-fast exciton dissociation is suggested to be one of the factors that contribute to high efficiency obtained in OSC-1, but due to the non-geminate recombination, the charge carriers are unable to produce photo-current, and thus, lead to reduction in OSC performance and its stability. In the case of thermally treated BHJ layer, the PCDTBT:PC$_{71}$BM based OSCs have relatively better stability but lower efficiency. It may be attributed to the formation of more stable BHJ morphological structure upon the thermal treatment, but having less amount ultra-fast charge carrier for photo-current generation. We found that, in the case of PCDTBT:PC$_{71}$BM based OSCs, the thermal annealing only prolonged the stability of OSCs but the efficiency of OSCs was affected in return. As the OSCs showed decay in their performance, simulated decay functions have been proposed for all the OSC devices that suffered degradation due to material instability and potential oxidation effect in BHJ layer. Based on the simulated functions, the degradation behaviors that contribute to the material (BHJ) instability and oxidation effect can be distinguished clearly and can be used to fit the real OSC degradation trend as well. It is believed that, if the charge transport issue in disordered PCDTBT:PC$_{71}$BM blend can be overcome by the enhancement of charge carrier dissociation without involving non-geminate recombination, a stable OSC with high efficiency could possibly be attained.

CHAPTER 6 : CONCLUSION AND FUTURE WORKS

6.1 Conclusion

Solution processable organic thin film devices have been successfully fabricated which include organic semiconductor diode, light sensor, and solar cells. In the beginning, the selected (VOPcPhO) material has been used for a single component semiconductor diode fabrication to the extract several electronic parameters for investigating VOPcPhO charge transport nature in the real device. The diode parameters comparable to other well-known organic materials have been obtained including ideality factor, barrier height, series and shunt resistances, and mobility. VOPcPhO has shown a promising potential to be used in optoelectronic applications. The binary blend comprising VOPcPhO and P3HT has revealed improvement in the light absorption range within visible region and good balance in the transport of both charge carrier species. A solar cell based on VOPcPhO:P3HT blend has shown an efficiency of 1.09 % under white light illumination. Through this study, it is realized that most of the donor materials can play a role as an acceptor component as it exhibits electrons transport mobility comparable to hole mobility. It is, however, considered that such efficiency (~1.09 %) does not meet the sufficient power conversion amount for the real energy harvesting application as a commercial solar cell. Thus, the application of such device has been switched to light sensing by optimizing its absorption property. While in the form of light sensor, the blend of VOPcPhO:P3HT has shown very good responsivity towards changes in the light intensity. The very fast response and recovery mechanisms, even for the aged sensor device, make the sensor a promising candidate for commercial application. An attempt was made to investigate VOPcPhO charge transport via EFISHG technique but, unfortunately, the non-linear optical property of VOPcPhO could not be manipulated by this technique as the EFISHG is material dependent method of characterization. Due to these two reasons; (1) P3HT:VOPcPhO blend as active layer in OSCs achieved low efficiency, and (2) VOPcPhO is not compatible for EFISHG technique, a second blend system (PCDTBT:$PC_{71}BM$) has been introduced for further study on charge transport behavior in photodiode devices.

In the second PCDTBT:$PC_{71}BM$ blend system, the OSC devices have been fabricated for the enhancement of efficiency through thermal annealing. In this study, the efficiency of OSCs, as high as 9.03 %, has been achieved. An effort has been made to provide a deeper insight of the charge carrier transport behaviour in the blend through the EFISHG measurement technique by fabricating OFET devices. The TRM-SHG images of the OFETs, with an active layer of PCDTBT material, have been recorded to study the carrier motion in the PCDTBT thin films. The holes motion has been visualized by using this technique. Furthermore, the visualized carriers' motion has been used for the calculation of intrinsic mobility of holes in the PCDTBT based OFET device. The mobility measured by EFISHG technique (5.6×10^{-5} cm^2/Vs) is higher than that measured using I-V method (2.4×10^{-5} cm^2/Vs), time-of-flight (0.9×10^{-5} cm^2/Vs), OTRACE (4.1×10^{-5} cm^2/Vs), and photo-CELIV (5.0×10^{-5} cm^2/Vs) methods as reported in the literature. It is expected that the TRM-SHG technique could be a gateway to investigate carrier lifetime in PCDTBT in order to improve the efficiency of the PCDTBT based solar cells. TRM-SHG technique has also been found helpful to probe SHG signal selectively in bulk heterojunction (BHJ) OSCs and provide a direct way to investigate the transit time of the electrons and holes at the same device. Even though donor/acceptor components are blended together in BHJ OSCs, the EFISHG technique can still detect the SHG signals produced by donor or acceptor components individually. Furthermore, this study has also led to some novel findings that the injection barrier is increased and the internal field direction is changed when a PEDOT:PSS layer is introduced. Besides, the transit time for electrons and holes gets balanced in the PCDTBT:$PC_{71}BM$ based OSCs after the introduction of the PEDOT: PSS layer which results in the higher efficiency.

6.2 Future Works

The remarkable optoelectronics properties of PCDTBT polymer material and its successful application in solution-processed organic solar cells based on ITO/PEDOT:PSS/PCDTBT:$PC_{71}BM$/Al bulk heterojunction suggest the following research studies that should be undertaken as future work:

- The fabrication of solution-processed organic solar cells based on PCDTBT:$PC_{71}BM$ shall be carried out in a nitrogen (N_2) controlled condition to avoid oxidation and achieve the better efficiency and prolong lifetime.
- Growing silver (Ag) nanoparticles (~10 nm in average) on ITO surface prior to the fabrication process to improve a light trapping mechanism in OSCs active layer for increased efficiency. At the same time, the Ag nanoparticles might improve the stability of OSCs.
- The use of electron injection layer in the OSC to improve electron transport by depositing LiF ultrathin layer by means of thermal evaporation before the deposition of Al forming ITO/PEDOT:PSS/ PCDTBT:$PC_{71}BM$/LiF/Al device. By this way, the efficiency of OSCs might be increased even more than the current efficiency (9.03 %).

REFERENCES

Abdullah, S. M., Ahmad, Z., Aziz, F., & Sulaiman, K. (2012). Investigation of VOPcPhO as an acceptor material for bulk heterojunction solar cells. *Organic Electronics, 13,* 2532–2537.

Adams, W. G., & Day, R. E. (1877). The Action of Light on Selenium. *Philosophical Transactions of the Royal Society London, 167,* 313-349.

Ahmad, Z., Sayyad, M. H., & Karimov, K. S. (2010). CuPc based organic-inorganic hetero-junction with Au electrodes. *Journal of Semiconductors, 31*, 074002.

Ahmad, Z., Sayyad, M. H., Yaseen, M., Aw, K. C., M-Tahir, M., & Ali, M. (2011). Potential of 5,10,15,20-Tetrakis(3',5'-di-tertbutylphenyl)porphyrinatocopper(II) for a multifunctional sensor. *Sensors and Actuators B: Chemical, 155,* 81-85.

Anthopoulos, T. D., Kooistra, F. B., Wondergem, H. J., Kronholm, D., Hummelen, J. C., & de Leeuw, D. M. (2006). Air-Stable n-Channel Organic Transistors Based on a Soluble C84 Fullerene Derivative. *Advanced Materials, 18*(13), 1679-1684.

Aziz, F. (2012). *Investigation of Electrical and Optoelectronic Properties of Vanadyl Phthalocyanine for Organic Electronic Devices.* PhD dissertation, Ghulam Ishaq Khan Institute of Engineering Sciences & Technology.

Bao, Z. (2000). Materials and fabrication needs for low-cost organic transistor circuits. *Advanced Materials, 12*(3), 227-230.

Becquerel, A. E. (1839). *Comptes Rendus de l'Académie des Sciences, 9,* 145.

Beiley, Z. M., Hoke, E. T., Noriega, R., Dacuña, J., Burkhard, G. F., Bartelt, J. A., Salleo, A., Toney, M. F., & McGehee, M. D. (2011). Morphology-Dependent Trap Formation in High Performance Polymer Bulk Heterojunction Solar Cells. *Advanced Energy Materials, 1*(5), 954-962.

Blom, P. W. M., De Jong, M., & Vleggaar, J. (1996). Electron and hole transport in poly (p-phenylene vinylene) devices. *Applied Physics Letters, 68*(23), 3308-3310.

Blouin, N., Michaud, A., Gendron, D., Wakim, S., Blair, E., Neagu-Plesu, R., Belletête, M., Durocher, G., Tao, Y., & Leclerc, M. (2008). Toward a rational design of poly (2, 7-carbazole) derivatives for solar cells. *Journal of The American Chemical Society, 130*(2), 732-742.

Blouin, N., Michaud, A., & Leclerc, M. (2007). A low-bandgap poly (2, 7-carbazole) derivative for use in high-performance solar cells. *Advanced Materials, 19*(17), 2295-2300.

Brabec, C. J. (2004). Organic photovoltaics: technology and market. *Solar Energy Materials and Solar Cells, 83*(2), 273-292.

Brabec, C. J., Sariciftci, N. S., & Hummelen, J. C. (2001). Plastic solar cells. *Advanced Functional Materials, 11*(1), 15-26.

Brinkmann, M., & Wittmann, J. C. (2006). Orientation of Regioregular Poly(3-hexylthiophene) by Directional Solidification: A Simple Method to Reveal the Semicrystalline Structure of a Conjugated Polymer. *Advanced Materials, 18,* 860–863.

Burgi, L., Friend, R. H., & Sirringhaus, H. (2003). Formation of the accumulation layer in polymer field-effect transistors. *Applied Physics Letters, 82*(9), 1482-1484.

Cai, W., Gong, X., & Cao, Y. (2010). Polymer solar cells: Recent development and possible routes for improvement in the performance. *Solar Energy Materials and Solar Cells, 94*(2), 114-127.

Cao, H., He, W., Mao, Y., Lin, X., Ishikawa, K., Dickerson, J. H., & Hess, W. P. (2014). Recent progress in degradation and stabilization of organic solar cells. *Journal of Power Sources, 264*(0), 168-183.

Carle, J. E., Helgesen, M., Madsen, M. V., Bundgaard, E., & Krebs, F. C. (2014). Upscaling from single cells to modules - fabrication of vacuum- and ITO-free polymer solar cells on flexible substrates with long lifetime. *Journal of Materials Chemistry C, 2*(7), 1290-1297.

Chen, C.-C., Chang, W.-H., Yoshimura, K., Ohya, K., You, J., Gao, J., Hong, Z., & Yang, Y. (2014). An Efficient Triple-Junction Polymer Solar Cell Having a Power Conversion Efficiency Exceeding 11%. *Advanced Materials, 26*(32), 5670-5677.

Chen, C. P., Chan, S. H., Chao, T. C., Ting, C., & Ko, B. T. (2008). Low-bandgap poly (thiophene-phenylene-thiophene) derivatives with broaden absorption spectra for use in high-performance bulk-heterojunction polymer solar cells. *Journal of The American Chemical Society, 130*(38), 12828-12833.

Chen, H.-Y., Hou, J., Zhang, S., Liang, Y., Yang, G., Yang, Y., Yu, L., Wu, Y., & Li, G. (2009). Polymer solar cells with enhanced open-circuit voltage and efficiency. *Nature Photonics, 3,* 649-653.

Chen, X., Taguchi, D., Manaka, T., & Iwamoto, M. (2014). Selective observation of photo-induced electric fields inside different material components in bulk-heterojunction organic solar cell. *Applied Physics Letters, 104*(1), 013306.

Cheung, C. H., Kwok, K. C., Tse, S. C., & So, S. K. (2008). Determination of carrier mobility in phenylamine by time-of-flight, dark-injection, and thin film transistor techniques. *Journal of Applied Physics, 103*(9), 093705.

Chu, T.-Y., Lu, J., Beaupré, S., Zhang, Y., Pouliot, J.-R., Wakim, S., Zhou, J., Leclerc, M., Li, Z., Ding, J., & Tao, Y. (2011). Bulk Heterojunction Solar Cells Using Thieno[3,4-c]pyrrole-4,6-dione and Dithieno[3,2-b:2′,3′-d]silole Copolymer with a Power Conversion Efficiency of 7.3%. *Journal of the American Chemical Society, 133*(12), 4250-4253.

Chua, L. L., Zaumseil, J., Chang, J. F., Ou, E. C. W., Ho, P. K. H., Sirringhaus, H., & Friend, R. H. (2005). General observation of n-type field-effect behaviour in organic semiconductors. *Nature, 434*(7030), 194-199.

Clarke, T. M., Peet, J., Nattestad, A., Drolet, N., Dennler, G., Lungenschmied, C., Leclerc, M., & Mozer, A. J. (2012). Charge carrier mobility, bimolecular recombination and trapping in polycarbazole copolymer: fullerene (PCDTBT: PCBM) bulk heterojunction solar cells. *Organic Electronics, 13*(11), 2639-2646.

Coakley, K. M., & McGehee, M. D. (2004). Conjugated polymer photovoltaic cells. *Chemistry of Materials, 16*(23), 4533-4542.

Coppedè, N., Castriota, M., Cazzanelli, E., Forti, S., Tarabella, G., Toccoli, T., Walzer, K., & Iannotta, S. (2010). Controlled Polymorphism in Titanyl Phthalocyanine on Mica by Hyperthermal Beams: A Micro-Raman Analysis. *The Journal of Physical Chemistry C, 114*(15), 7038-7044.

Cornil, J., Brédas, J. L., Zaumseil, J., & Sirringhaus, H. (2007). Ambipolar transport in organic conjugated materials. *Advanced Materials, 19*(14), 1791-1799.

Cui, X., Taguchi, D., Manaka, T., & Iwamoto, M. (2013). Analysis of carrier behavior in C60/P(VDF-TrFE) double-layer capacitor by using electric-field-induced optical second-harmonic generation measurement. *Journal of Applied Physics, 114*(23), 234504.

Delacote, G. M., Fillard, J. P., & Marco, F. (1964). *Solid State Communications. 2,* 373.

DeLongchamp, D. M., Klinea, R. J., & Herzing, A. (2012). Nanoscale structure measurements for polymer-fullerene photovoltaics. *Energy & Environmental Science, 5,* 5980.

Dimitrakopoulos, C. D., & Malenfant, P. R. L. (2002). Organic thin film transistors for large area electronics. *Advanced Materials, 14*(2), 99.

Dou, L., Gao, J., Richard, E., You, J., Chen, C.-C., Cha, K. C., He, Y., Li, G., & Yang, Y. (2012). Systematic Investigation of Benzodithiophene- and Diketopyrrolopyrrole-Based Low-Bandgap Polymers Designed for Single Junction and Tandem Polymer Solar Cells. *Journal of the American Chemical Society, 134*(24), 10071-10079.

Duche, D., Torchio, P., Escoubas, L., Monestier, F., Simon, J. J., Flory, F., & Mathian, G. (2009). Improving light absorption in organic solar cells by plasmonic contribution. *Solar Energy Materials and Solar Cells, 93*(8), 1377-1382.

El-Nahass, M., Abd-El-Rahman, K., & Darwish, A. (2005). Fourier-transform infrared and UV-vis spectroscopes of nickel phthalocyanine thin films. *Materials Chemistry and Physics, 92*(1), 185-189.

El-Nahass, M., & Yaghmour, S. (2008). Effect of annealing temperature on the optical properties of thermally evaporated tin phthalocyanine thin films. *Applied Surface Science, 255*(5), 1631-1636.

Etzold, F., Howard, I. A., Mauer, R., Meister, M., Kim, T.-D., Lee, K.-S., Baek, N. S., & Laquai, F. (2011). Ultrafast Exciton Dissociation Followed by Nongeminate Charge Recombination in PCDTBT:PCBM Photovoltaic Blends. *Journal of the American Chemical Society, 133*(24), 9469-9479.

Fritts, C. E. (1883). On a New Form of Selenium Photocell. *American Journal of Science, 26*, 465.

Gao, F., & Inganas, O. (2014). Charge generation in polymer-fullerene bulk-heterojunction solar cells. *Physical Chemistry Chemical Physics, 16*(38), 20291-20304.

Garreau, S., Louarn, G., Buisson, J., Froyer, G., & Lefrant, S. (1999). In situ spectroelectrochemical Raman studies of poly (3, 4-ethylenedioxythiophene)(PEDT). *Macromolecules, 32*(20), 6807-6812.

Geacintov, N., Pope, M., & Kallmann, H. J. (1966). *Journal of Chemical Physics, 45*, 2639-2649.

Gélinas, S., Rao, A., Kumar, A., Smith, S. L., Chin, A. W., Clark, J., van der Poll, T. S., Bazan, G. C., & Friend, R. H. (2014). Ultrafast Long-Range Charge Separation in Organic Semiconductor Photovoltaic Diodes. *Science, 343*(6170), 512-516.

Gevorgyan, S. A., Jørgensen, M., & Krebs, F. C. (2008). A setup for studying stability and degradation of polymer solar cells. *Solar Energy Materials and Solar Cells, 92*(7), 736-745.

Gregg, B. A., Fox, M. A., & Bard, A. K. (1990). Photovoltaic Effect In Symmetrical Cells of a Liquid Crystal Porphyrin. *Journal of Physical Chemistry, 94*, 1586-1598.

Gupta, D., Bag, M., & Narayan, K. S. (2008). Correlating reduced fill factor in polymer solar cells to contact effects. *Applied Physics Letters, 92*(9), 093301.

Gusain, A., Saxena, V., Veerender, P., Jha, P., Koiry, S. P., Chauhan, A. K., Aswal, D. K., & Gupta, S. K. (2013). Investigation on the effects of thermal annealing on PCDTBT:PCBM bulk-heterojunction polymer solar cells. *AIP Conference Proceedings, 1512*(1), 776-777.

Guvenc, A. B., Ozkan, C., & Ozkan, M. (2012). Early-Effect like Behavior in Space Charge Regions of Organic Bulk-Heterojunction Photodiodes: Cambridge Univ Press.

He, Z., Zhong, C., Su, S., Xu, M., Wu, H., & Cao, Y. (2012). Enhanced power-conversion efficiency in polymer solar cells using an inverted device structure. *Nature Photonics, 6*(9), 591-595.

Helgesen, M., Søndergaard, R., & Krebs, F. C. (2010). Advanced materials and processes for polymer solar cell devices. *Journal of Materials Chemistry, 20*(1), 36-60.

Heller, C., Leising, G., Godon, C., Lefrant, S., Fischer, W., & Stelzer, F. (1995). Raman excitation profiles of conjugated segments in solution. *Physical Review B, 51*(13), 8107.

Hiramoto, M., Fukusumi, H., & Yokoyama, M. (1991). *Applied Physics Letters, 58*, 1062.

Hoegl, H. (1965). On Photoelectric Effects in Polymers and Their Sensitization by Dopants. *The Journal of Physical Chemistry, 69*(3), 755-766.

Honda, S., Nogami, T., Ohkita, H., Benten, H., & Ito, S. (2009). Improvement of the light-harvesting efficiency in polymer/fullerene bulk heterojunction solar cells by interfacial dye modification. *ACS Applied Materials & Interfaces, 1*, 804-810.

Honda, S., Yokoya, S., Ohkita, H., Benten, H., & Ito, S. (2011). Light-Harvesting Mechanism in Polymer/Fullerene/Dye Ternary Blends Studied by Transient Absorption Spectroscopy. *The Journal of Physical Chemistry C, 15*(22), 11306–11317.

Hoppe, H., & Sariciftci, N. S. (2004). Organic solar cells: An overview. *Journal of Materials Research, 19*(7), 1924-1945.

Hummelen, J. C., Knight, B. W., LePeq, F., Wudl, F., Yao, J., & Wilkins, C. L. (1995). Preparation and Characterization of Fulleroid and Methanofullerene Derivatives. *The Journal of Organic Chemistry, 60*(3), 532-538.

Ichikawa, M., Takeuchi, T., Jeon, H. G., Jin, Y., Lee, S., & Kim, K. S. (2012). Organic photodiode with high infrared light sensitivity based on tin phthalocyanine/C_{60} bulk heterojunction and optical interference effect. *Japanese Journal Applied Physics, 51*, 034103.

Jiang, J., Bao, M., Rintoul, L., & Arnold, D. P. (2006). Vibrational spectroscopy of phthalocyanine and naphthalocyanine in sandwich-type (na) phthalocyaninato and porphyrinato rare earth complexes. *Coordination Chemistry Reviews, 250*(3-4), 424-448.

Jin, H., Tuomikoski, M., Hiltunen, J., Kopola, P., Maaninen, A., & Pino, F. (2009). Polymer−Electrode Interfacial Effect on Photovoltaic Performances in Poly(3-hexylthiophene):Phenyl-C61-butyric Acid Methyl Ester Based Solar Cells. *The Journal of Physical Chemistry C, 113*(38), 16807-16810.

Jørgensen, M., Norrman, K., & Krebs, F. C. (2008). Stability/degradation of polymer solar cells. *Solar Energy Materials and Solar Cells, 92*(7), 686-714.

Kaake, L., Barbara, P. F., & Zhu, X.-Y. (2010). Intrinsic charge trapping in organic and polymeric semiconductors: a physical chemistry perspective. *The Journal of Physical Chemistry Letters, 1*(3), 628-635.

Kallmann, H., & Pope, M. (1959). Photovoltaic Effect in Organic Crystals. *The Journal of Chemical Physics, 30*, 585.

Katz, H. E., Johnson, J., Lovinger, A. J., & Li, W. (2000). Naphthalenetetracarboxylic diimide-based n-channel transistor semiconductors: structural variation and thiol-enhanced gold contacts. *Journal of the American Chemical Society, 122*(32), 7787-7792.

Kawano, K., Pacios, R., Poplavskyy, D., Nelson, J., Bradley, D. D. C., & Durrant, J. R. (2006). Degradation of organic solar cells due to air exposure. *Solar Energy Materials and Solar Cells, 90*(20), 3520-3530.

Kearns, D., & Calvin, M. (1958). Photovoltaic Effect and Photoconductivity in Laminated Organic Systems. *The Journal of Chemical Physics, 29*(4), 950.

Kepler, R. G. (1960). Charge Carrier Production and Mobility in Anthracene Crystals. *Physical Review, 119*(4), 1226-1229.

Khan, S. M., Sayyad, M. H., & Karimov, K. S. (2010). Investigation of temperature-dependent electrical properties of p-VOPc/n-si heterojunction under dark conditions. *Ionics*, 1-7.

Kim, J. Y., Lee, K., Coates, N. E., Moses, D., Nguyen, T.-Q., Dante, M., & Heeger, A. J. (2007). Efficient Tandem Polymer Solar Cells Fabricated by All-Solution Processing. *Science, 317*(5835), 222-225.

Kim, Y., Cook, S., Tuladhar, S. M., Choulis, S. A., Nelson, J., Durrant, J. R., Bradley, D. D. C., Giles, M., McCulloch, I., Ha, C.-S., & Ree, M. (2006). A strong regioregularity effect in self-organizing conjugated polymer films and high-efficiency polythiophene:fullerene solar cells. *Nature Materials, 5*(3), 197-203.

Koenigsberger, J., & Steubing, W. (1910). *Annalen der Physik, 32*, 179.

Kraus, M., Haug, S., Brütting, W., & Opitz, A. (2011). Achievement of balanced electron and hole mobility in copper-phthalocyanine field-effect transistors by using a crystalline aliphatic passivation layer. *Organic Electronics, 12*(5), 731-735.

Krebs, F. C., Gevorgyan, S. A., & Alstrup, J. (2009). A roll-to-roll process to flexible polymer solar cells: model studies, manufacture and operational stability studies. *Journal of Materials Chemistry, 19*(30), 5442-5451.

Krebs, F. C., Tromholt, T., & Jorgensen, M. (2010). Upscaling of polymer solar cell fabrication using full roll-to-roll processing. *Nanoscale, 2*(6), 873-886.

Kulkarni, A. P., Noone, K. M., Munechika, K., Guyer, S. R., & Ginger, D. S. (2010). Plasmon-enhanced charge carrier generation in organic photovoltaic films using silver nanoprisms. *Nano letters, 10*(4), 1501-1505.

Lenes, M., Shelton, S. W., Sieval, A. B., Kronholm, D. F., Hummelen, J. C. K., & Blom, P. W. M. (2009). Electron Trapping in Higher Adduct Fullerene-Based Solar Cells. *Advanced Functional Materials, 19*(18), 3002-3007.

Leznoff, C. C., & Lever, A. B. P. (1996). *Phthalocyanines: Properties and Applications* VCH, New York

Li, G., Shrotriya, V., Huang, J., Yao, Y., Moriarty, T., Emery, K., & Yang, Y. (2005). High-efficiency solution processable polymer photovoltaic cells by self-organization of polymer blends. *Nature Materials, 4*(11), 864-868.

Li, H., Duan, L., Zhang, D., Dong, G., Qiao, J., Wang, L., & Qiu, Y. (2014). Relationship between Mobilities from Time-of-Flight and Dark-Injection Space-Charge-Limited Current Measurements for Organic Semiconductors: A Monte Carlo Study. *The Journal of Physical Chemistry C, 118*(12), 6052-6058.

Li, W., Furlan, A., Hendriks, K. H., Wienk, M. M., & Janssen, R. A. J. (2013). Efficient Tandem and Triple-Junction Polymer Solar Cells. *Journal of the American Chemical Society, 135*(15), 5529-5532.

Li, W., Hendriks, K. H., Roelofs, W. S. C., Kim, Y., Wienk, M. M., & Janssen, R. A. J. (2013). Efficient Small Bandgap Polymer Solar Cells with High Fill Factors for 300 nm Thick Films. *Advanced Materials, 25*(23), 3182-3186.

Li, Z., Wong, H. C., Huang, Z., Zhong, H., Tan, C. H., Tsoi, W. C., Kim, J. S., Durrant, J. R., & Cabral, J. T. (2013). Performance enhancement of fullerene-based solar cells by light processing. *Nature Communications, 4*, 2227.

Liang, Y., Feng, D., Wu, Y., Tsai, S.-T., Li, G., Ray, C., & Yu, L. (2009). Highly Efficient Solar Cell Polymers Developed via Fine-Tuning of Structural and Electronic Properties. *Journal of the American Chemical Society, 131*(22), 7792-7799.

Liang, Y., Xu, Z., Xia, J., Tsai, S.-T., Wu, Y., Li, G., Ray, C., & Yu, L. (2010). For the Bright Future—Bulk Heterojunction Polymer Solar Cells with Power Conversion Efficiency of 7.4%. *Advanced Materials*, *22*(20), E135-E138.

Lilliedal, M. R., Medford, A. J., Madsen, M. V., Norrman, K., & Krebs, F. C. (2010). The effect of post-processing treatments on inflection points in current–voltage curves of roll-to-roll processed polymer photovoltaics. *Solar Energy Materials and Solar Cells, 94*(12), 2018-2031.

Lilliu, S., Böberl, M., Sramek, M., Tedde, S. F., Macdonald, J. E., & Hayden, O. (2011). Inkjet-printed organic photodiodes. *Thin Solid Films, 520*, 610-615.

Lo, M. F., Ng, T. W., Lai, S. L., Fung, M. K., Lee, S. T., & Lee, C. S. (2011). Stability enhancement in organic photovoltaic device by using polymerized fluorocarbon anode buffer layer. *Applied Physics Letters, 99*(3), 033302.

Louarn, G., Trznadel, M., Buisson, J., Laska, J., Pron, A., Lapkowski, M., & Lefrant, S. (1996). Raman spectroscopic studies of regioregular poly (3-alkylthiophenes). *The Journal of Physical Chemistry, 100*(30), 12532-12539.

Ma, W., Yang, C., Gong, X., Lee, K., & Heeger, A. J. (2005). Thermally Stable, Efficient Polymer Solar Cells with Nanoscale Control of the Interpenetrating Network Morphology. *Advanced Functional Materials, 15*(10), 1617-1622.

Machui, F., Langner, S., Zhu, X., Abbott, S., & Brabec, C. J. (2012). Determination of the P3HT:PCBM solubility parameters via a binary solvent gradient method: Impact of solubility on the photovoltaic performance. *Solar Energy Materials and Solar Cells, 100*, 138-146.

MacNeill, C. M., Peterson, E. D., Noftle, R. E., Carroll, D. L., & Coffin, R. C. (2011). A cyclopentadithiophene/thienopyrroledione-based donor-acceptor copolymer for organic solar cells. *Synthetic Metals*.

Manaka, T., Liu, F., Weis, M., & Iwamoto, M. (2008). Diffusionlike electric-field migration in the channel of organic field-effect transistors. *Physical Review B, 78*(12), 121302.

Manceau, M., Bundgaard, E., Carle, J. E., Hagemann, O., Helgesen, M., Sondergaard, R., Jorgensen, M., & Krebs, F. C. (2011). Photochemical stability of [small pi]-conjugated polymers for polymer solar cells: a rule of thumb. [10.1039/C0JM03105D]. *Journal of Materials Chemistry, 21*(12), 4132-4141.

Mark, P., & Helfrich, W. (1962). Space-Charge-Limited Currents in Organic Crystals. *Journal of Applied Physics, 33*(1), 205-215.

Matsuura, T., & Shimoyama, Y. (2002). Growth kinetics of self-assembled monolayers of thiophene and terthiophene on Au (111): An infrared spectroscopic study. *The European Physical Journal E: Soft Matter and Biological Physics, 7*(3), 233-240.

Maxwell, J. C. (1954). *A Treatise on Electricity and Magnetism Unabridged*: Dover.

Menke, S. M., & Holmes, R. J. (2014). Exciton diffusion in organic photovoltaic cells. *Energy & Environmental Science, 7*(2), 499-512.

Mette, H., & Pick, H. (1953). *Zeitschrift für Physik, 134*, 566.

Moon, J. S., Jo, J., & Heeger, A. J. (2012). Nanomorphology of PCDTBT:PC70BM Bulk Heterojunction Solar Cells. *Advanced Energy Materials, 2*(3), 304-308.

Motaung, D. E., Malgas, G. F., & Arendse, C. J. (2010). Correlation between the morphology and photo-physical properties of P3HT: fullerene blends. *Journal of Materials Science*, *45*(12), 3276-3283.

Motaung, D. E., Malgas, G. F., Arendse, C. J., Mavundla, S. E., & Knoesen, D. (2009). Structural and photo-physical properties of spin-coated poly(3-hexylthiophene) thin films. *Materials Chemistry and Physics, 116*(1), 279-283.

Natale, C. D., Macagnano, A., Repole, G., Saggio, G., D'Amico, A., Paolesse, R., & Boschi, T. (1998). The exploitation of metalloporphyrins as chemically interactive material in chemical sensors. *Materials Science and Engineering: C, 5*, 209-215.

Nogueira, A. F., Montanari, I., Nelson, J., Durrant, J. R., Winder, C., Sariciftci, N. S., & Brabec, C. (2003). Charge recombination in conjugated polymer/fullerene blended films studied by transient absorption spectroscopy. *The Journal of Physical Chemistry B, 107*(7), 1567-1573.

Norde, H. (1979). A modified forward I-V plot for Schottky diodes with high series resistance. *Journal of Applied Physics, 50*(7), 5052-5053.

Norrman, K., Gevorgyan, S. A., & Krebs, F. C. (2009). Water-Induced Degradation of Polymer Solar Cells Studied by H218O Labeling. *ACS Applied Materials & Interfaces, 1*(1), 102-112.

Norrman, K., Madsen, M. V., Gevorgyan, S. A., & Krebs, F. C. (2010). Degradation Patterns in Water and Oxygen of an Inverted Polymer Solar Cell. *Journal of the American Chemical Society, 132*(47), 16883-16892.

Ohshima, Y., Lim, E., Manaka, T., Iwamoto, M., & Sirringhaus, H. (2011). Observation of electron behavior in ambipolar polymer-based light-emitting transistor by optical second harmonic generation. *Journal of Applied Physics, 110*(1), 013715-013715-013716.

Opitz, A., Horlet, M., Kiwull, M., Wagner, J., Kraus, M., & Brütting, W. (2012). Bipolar charge transport in organic field-effect transistors: Enabling high mobilities and transport of photo-generated charge carriers by a molecular passivation layer. *Organic Electronics, 1614-1622*.

Ozaki, M., Peebles, D., Weinberger, B., Heeger, A., & MacDiarmid, A. (1980). Semiconductor properties of polyacetylene p-(CH) x: n-CdS heterojunctions. *Journal of Applied Physics, 51*(8), 4252-4256.

Padinger, F., Rittberger, R. S., & Sariciftci, N. S. (2003). Effects of postproduction treatment on plastic solar cells. *Advanced Functional Materials, 13*(1), 85-88.

Pal, S. K., Kesti, T., Maiti, M., Zhang, F., Inganäs, O., Hellström, S., Andersson, M. R., Oswald, F., Langa, F., Österman, T., Pascher, T., Yartsev, A., & Sundström, V. (2010). Geminate Charge Recombination in Polymer/Fullerene Bulk Heterojunction Films and Implications for Solar Cell Function. *Journal of the American Chemical Society, 132*(35), 12440-12451.

Park, S.-H., Ogino, K., & Sato, H. (2000). Synthesis and characterization of a main-chain polymer for single component photorefractive materials. *Synthetic Metals, 113,* 135-143.

Park, S. H., Roy, A., Beaupré, S., Cho, S., Coates, N., Moon, J. S., Moses, D., Leclerc, M., Lee, K., & Heeger, A. J. (2009). Bulk heterojunction solar cells with internal quantum efficiency approaching 100%. *Nature Photonics, 3*(5), 297-302.

Parthasarathy, B. (2005). *Fabrication and Characterization of CuPc Based Organic Solar Cells,* Master Theses, University of Kentucky.

Peet, J., Kim, J. Y., Coates, N. E., Ma, W. L., Moses, D., Heeger, A. J., & Bazan, G. C. (2007). Efficiency enhancement in low-bandgap polymer solar cells by processing with alkane dithiols. *Nature Materials, 6*(7), 497-500.

Peeters, E., Hal, P. A. v., Knol, J., Brabec, C. J., Sarciftci, N. S., Hummelen, J. C., & Janssen, R. A. J. (2000). *Physical Chemistry B., 104,* 10174.

Peumans, P., & Forrest, S. R. (2004). Separation of geminate charge-pairs at donor–acceptor interfaces in disordered solids. *Chemical Physics Letters, 398*(1–3), 27-31.

Peumans, P., Yakimov, A., & Forrest, S. R. (2003). Small molecular weight organic thin-film photodetectors and solar cells. *Journal of Applied Physics, 93*(7), 3693-3723.

Pierret, R. F. (1996). *Semiconductor Device Fundamentals*: Wesley Reading.

Pochettino, A. (1906). *Accademia dei Lincei Rendiconti, 15,* 355.

Rajaputra, S., Vallurupalli, S., & Singh, V. P. (2007). Copper phthalocyanine based Schottky diode solar cells. Journal of Materials Science: Materials in Electronics, *18*(11), 1147-1150.

Reese, M. O., White, M. S., Rumbles, G., Ginley, D. S., & Shaheen, S. E. (2008). Optimal negative electrodes for poly (3-hexylthiophene):[6, 6]-phenyl C61-butyric acid methyl ester bulk heterojunction photovoltaic devices. *Applied Physics Letters, 92*(5), 053307-053307-053303.

Rhoderick, E. H. (1978). *Metal-Semiconductor Contacts*: Oxford University Press.

Rivaton, A., Chambon, S., Manceau, M., Gardette, J.-L., Lemaître, N., & Guillerez, S. (2010). Light-induced degradation of the active layer of polymer-based solar cells. *Polymer Degradation and Stability, 95*(3), 278-284.

Roes, A. L., Alsema, E. A., Blok, K., & Patel, M. K. (2009). Ex-ante Environmental and Economic Evaluation of Polymer Photovoltaics. *Progress in Photovoltaics: Research and Applications, 17*, 372-393.

Roesch, R., Eberhardt, K.-R., Engmann, S., Gobsch, G., & Hoppe, H. (2013). Polymer solar cells with enhanced lifetime by improved electrode stability and sealing. *Solar Energy Materials and Solar Cells, 117*(0), 59-66.

Rosenthal, I. (1991). Phthalocyanines as photodynamic sensitizers. *Photochemistry and Photobiology, 53*(6), 859.

Ruderer, M. A., Hinterstocker, M., & Müller-Buschbaum, P. (2011). Structure in ternary blend systems for organic photovoltaics. *Synthetic Metals, 161*, 2001-2005.

Rushby, A. J., Claire, M. W., Osborn, H., & Watson, A. J. (2013). Habitable Zone Lifetimes of Exoplanets around Main Sequence Stars. *Astrobiology, 13*(9), 833-849.

Sariciftci, N. S., Smilowitz, L., Heeger, A. J., & Wudl, F. (1992). Photoinduced electron transfer from a conducting polymer to buckminsterfullerene. *Science, 258*, 1474-1476.

Sayhan, I., Bauersfeld, M. L., Woellenstein, J., & Becker, T. (2008). Dye and polymer based light sensor for tag integration. *Microsystem Technologies, 14*, 659-664.

Sayyad, M. H., Z. Ahmad, K. S. Karimov, M. Yaseen, M. Ali. (2009). Photo-organic field effect transistor based on a metalloporphyrin *Journal of Physics D: Applied Physics*, *42* 105112

Schäfer, S., Petersen, A., Wagner, T. A., Kniprath, R., Lingenfelser, D., Zen, A., Kirchartz, T., Zimmermann, B., Würfel, U., Feng, X., & Mayer, T. (2011). Influence of the indium tin oxide/organic interface on open-circuit voltage, recombination, and cell degradation in organic small-molecule solar cells. *Physical Review B, 83*(16), 165311.

Schilinsky, P., Waldauf, C., & Brabec, C. J. (2002). Recombination and loss analysis in polythiophene based bulk heterojunction photodetectors. *Applied Physics Letters, 81*(20), 3885-3887.

Schilinsky, P., Waldauf, C., Hauch, J., & Brabec, C. J. (2004). Simulation of light intensity dependent current characteristics of polymer solar cells. *Journal of Applied Physics, 95*(5), 2816-2819.

Schindler, W., Wollgarten, M., & Fostiropoulos, K. (2012). Revealing nanoscale phase separation in small-molecule photovoltaic blends by plasmonic contrast in the TEM. *Organic Electronics, 13*(6), 1100-1104.

Schmidt-Mende, L., Fechtenkötter, A., Müllen, K., Moons, E., Friend, R. H., & MacKenzie, J. D. (2001). Self-Organized Discotic Liquid Crystals for High-Efficiency Organic Photovoltaics. *Science, 293*(5532), 1119-1122.

Scott, J. C., & Malliaras, G. G. (1999). Charge injection and recombination at the metal-organic interface. *Chemical Physics Letters, 299*(2), 115-119.

Seok, J., Shin, T. J., Park, S., Cho, C., Lee, J.-Y., Yeol Ryu, D., Kim, M. H., & Kim, K. (2015). Efficient Organic Photovoltaics Utilizing Nanoscale Heterojunctions in Sequentially Deposited Polymer/fullerene Bilayer. *Scientific Reports, 5,* 10.1038/srep08373.

Shaheen, S. E., Brabec, C. J., & Sariciftci, N. S. (2001). 2.5% efficient organic plastic solar cells. *Applied Physics Letters, 78*(6), 841-843.

Shen, L., Zhu, G., Guo, W., Tao, C., Zhang, X., Liu, C., Chen, W., Ruan, S., & Zhong, Z. (2008). Performance improvement of TiO2/P3HT solar cells using CuPc as a sensitizer. *Applied Physics Letters, 92*(7), 073307-073307-073303.

Singh, T. B., Meghdadi, F., Günes, S., Marjanovic, N., Horowitz, G., Lang, P., Bauer, S., & Sariciftci, N. S. (2005). High-Performance Ambipolar Pentacene Organic Field-Effect Transistors on Poly (vinyl alcohol) Organic Gate Dielectric. *Advanced Materials, 17*(19), 2315-2320.

Smith, W. (1873). Effect of Light on Selenium during the passage of an Electric Current. *Nature*, 303.

Song, Q. L., Li, F. Y., Yang, H., Wu, H. R., Wang, X. Z., Zhou, W., Zhao, J. M., Ding, X. M., Huang, C. H., & Hou, X. Y. (2005). Small-molecule organic solar cells with improved stability. *Chemical Physics Letters, 416*(1–3), 42-46.

Spanggaard, H., & Krebs, F. C. (2004). A brief history of the development of organic and polymeric photovoltaics. *Solar Energy Materials and Solar Cells, 83*(2), 125-146.

Sun, X., Zhou, Y., Wu, W., Liu, Y., Tian, W., Yu, G., Qiu, W., Chen, S., & Zhu, D. (2006). X-shaped oligothiophenes as a new class of electron donors for bulk-heterojunction solar cells. *The Journal of Physical Chemistry B, 110*(15), 7702-7707.

Sze, S. (1981). *Physics of semiconductor devices* (2nd ed.): Wiley-Blackwell.

Taguchi, D., Inoue, S., Zhang, L., Li, J., Weis, M., Manaka, T., & Iwamoto, M. (2010). Analysis of Organic Light-Emitting Diode As a Maxwell− Wagner Effect Element by Time-Resolved Optical Second Harmonic Generation Measurement. *The Journal of Physical Chemistry Letters, 1*(5), 803-807.

Taguchi, D., Masada, H., Manaka, T., Iwamoto, M., Nishiura, T., Iizuka, T., & Takemori, T. (2012). Probing a two-step channel formation process in injection-type pentacene field-effect transistors by time-resolved electric-field-induced optical second-harmonic generation measurement. *Organic Electronics, 13*(12), 2801-2806.

Taguchi, D., Shino, T., Chen, X., Zhang, L., Li, J., Weis, M., Manaka, T., & Iwamoto, M. (2011). Analyzing photovoltaic effect of double-layer organic solar cells as a Maxwell-Wagner effect system by optical electric-field-induced second-harmonic generation measurement. *Journal of Applied Physics, 110*(10), 103717.

Tanase, C., Meijer, E. J., Blom, P. W. M., & de Leeuw, D. M. (2003). Unification of the Hole Transport in Polymeric Field-Effect Transistors and Light-Emitting Diodes. *Physical Review Letters, 91*(21), 216601.

Tang, C. W. (1986). Two-layer organic photovoltaic cell. *Applied Physics Letters, 48*(2), 183-185.

Thompson, B. C., Kim, Y. G., & Reynolds, J. R. (2005). Spectral broadening in MEH-PPV: PCBM-based photovoltaic devices via blending with a narrow band gap cyanovinylene-dioxythiophene polymer. *Macromolecules, 38*(13), 5359-5362.

Tress, W., Petrich, A., Hummert, M., Hein, M., Leo, K., & Riede, M. (2011). Imbalanced mobilities causing S-shaped IV curves in planar heterojunction organic solar cells. *Applied Physics Letters, 98*(6), 063301.

Tsumura, A., Koezuka, H., & Ando, T. (1988). Polythiophene field-effect transistor: Its characteristics and operation mechanism. *Synthetic Metals, 25*(1), 11-23.

Wagenpfahl, A., Rauh, D., Binder, M., Deibel, C., & Dyakonov, V. (2010). S-shaped current-voltage characteristics of organic solar devices. *Physical Review B, 82*(11), 115306.

Wagner, K. (1914). Erklärung der dielektrischen Nachwirkungsvorgänge auf Grund Maxwellscher Vorstellungen. *Archiv für Elektrotechnik, 2*(9), 371-387.

Wakim, S., Beaupre, S., Blouin, N., Aich, B.-R., Rodman, S., Gaudiana, R., Tao, Y., & Leclerc, M. (2009). Highly efficient organic solar cells based on a poly(2,7-carbazole) derivative. *Journal of Materials Chemistry, 19*(30), 5351-5358.

Wang, D. H., Kim, J. K., Seo, J. H., Park, O. O., & Park, J. H. (2012). Stability comparison: A PCDTBT/PC71BM bulk-heterojunction versus a P3HT/PC71BM bulk-heterojunction. *Solar Energy Materials and Solar Cells, 101*(0), 249-255.

Wang, T., Pearson, A. J., Dunbar, A. D. F., Staniec, P. A., Watters, D. C., Yi, H., Ryan, A. J., Jones, R. A. L., Iraqi, A., & Lidzey, D. G. (2012). Correlating Structure with Function in Thermally Annealed PCDTBT:PC70BM Photovoltaic Blends. *Advanced Functional Materials, 22*(7), 1399-1408.

Wang, Y., Wei, W., Liu, X., & Gu, Y. (2012). Research progress on polymer heterojunction solar cells. *Solar Energy Materials and Solar Cells, 98*(0), 129-145.

Weis, M., Lin, J., Manaka, T., & Iwamoto, M. (2010). The charge transport in organic field-effect transistor as an interface charge propagation: The Maxwell-Wagner effect model and transmission line approximation. *Japanese Journal of Applied Physics, 49*(7), 1603.

Woo, S., Hyun Kim, W., Kim, H., Yi, Y., Lyu, H.-K., & Kim, Y. (2014). 8.9% Single-Stack Inverted Polymer Solar Cells with Electron-Rich Polymer Nanolayer-Modified Inorganic Electron-Collecting Buffer Layers. *Advanced Energy Materials, 4*(7), 10.1002/aenm.201301692.

Wu, Q., Bhattacharya, M., Moore, L. M. J., & Morgan, S. E. (2014). Air processed P3HT:PCBM photovoltaic cells: Morphology correlation to annealing, degradation, and recovery. *Journal of Polymer Science Part B: Polymer Physics*, 1511–1520.

Yakimov, A., & Forrest, S. R. (2002). High photovoltage multiple-heterojunction organic solar cells incorporating interfacial metallic nanoclusters. *Applied Physics Letters, 80*(9), 1667-1669.

Yakuphanoglu, F. (2007). Photovoltaic properties of hybrid organic/inorganic semiconductor photodiode. *Synthetic Metals, 157*(21), 859-862.

Yakuphanoglu, F. (2008). Photovoltaic properties of the organic–inorganic photodiode based on polymer and fullerene blend for optical sensors. *Sensors and Actuators A: Physical, 141,* 383-389.

Yang, X., & Uddin, A. (2014). Effect of thermal annealing on P3HT:PCBM bulk-heterojunction organic solar cells: A critical review. *Renewable and Sustainable Energy Reviews, 30,* 324-336.

You, J., Dou, L., Yoshimura, K., Kato, T., Ohya, K., Moriarty, T., Emery, K., Chen, C.-C., Gao, J., Li, G., & Yang, Y. (2013). A polymer tandem solar cell with 10.6% power conversion efficiency.. *Nature Communications, 4*, 1446.

Yu, G., Gao, J., Hummelen, J. C., Wudl, F., & Heeger, A. J. (1995). Polymer Photovoltaic Cells: Enhanced Efficiencies via a Network of Internal Donor-Acceptor Heterojunctions. *Science, 270,* 1789-1791.

Yu, G., & Heeger, A. J. (1995). Charge separation and photovoltaic conversion in polymer composites with internal donor/acceptor heterojunctions. *Journal of Applied Physics, 78*(7), 4510-4515.

Yu, G., Pakbaz, K., & Heeger, A. J. (1994). *Applied Physics Letters, 64,* 3422.

Zhang, L., Taguchi, D., Li, J., Manaka, T., & Iwamoto, M. (2010). Probing of interfacial charging and discharging in double-layer devices with a polyimide blocking layer by time-resolved optical second harmonic generation. *Journal of Applied Physics, 108*(9), 093707.

Zhang, L., Taguchi, D., Manaka, T., & Iwamoto, M. (2011). Bulk-trap modulated Maxwell-Wagner type interfacial carrier relaxation process in a fullerene/polyimide double-layer device investigated by time-resolved second harmonic generation. *Journal of Applied Physics, 110*(3), 033715.

Zhang, M., Gu, Y., Guo, X., Liu, F., Zhang, S., Huo, L., Russell, T. P., & Hou, J. (2013). Efficient Polymer Solar Cells Based on Benzothiadiazole and Alkylphenyl Substituted Benzodithiophene with a Power Conversion Efficiency over 8%. *Advanced Materials, 25*(35), 4944-4949.

Zhang, X., Zhang, Y., & Jiang, J. (2004). Towards clarifying the N ・ M vibrational nature of metallo-phthalocyanines: Infrared spectrum of phthalocyanine magnesium complex: density functional calculations. *Spectrochimica Acta Part A: Molecular and Biomolecular Spectroscopy, 60*(10), 2195-2200.

Zhao, L., Zhao, S., Xu, Z., Gong, W., Yang, Q., Fan, X., & Xu, X. (2014). Influence of morphology of PCDTBT:PC71BM on the performance of solar cells. *Applied Physics A, 114*(4), 1361-1368.

Ziminov, A., Ramsh, S., Terukov, E., Trapeznikova, I., Shamanin, V., & Yurre, T. (2006). Correlation dependences in infrared spectra of metal phthalocyanines. *Semiconductors, 40*(10), 1131-1136.

LIST OF PUBLICATIONS

A. Research papers

1) Shahino Mah Abdullah, Zubair Ahmad, Khaulah Sulaiman, The Impact of Thermal Annealing to the Efficiency and Stability of Organic Solar Cells based PCDTBT:PC$_{71}$BM, Procedia - Social and Behavioral Sciences, Vol. 195, (2015) 2135-2142
2) Zubair Ahmad, Shahino Mah Abdullah, Dai Taguchi, Khaulah Sulaiman, Mitsumasa Iwamoto, A way for studying the impact of PEDOT:PSS interface layer on carrier transport in PCDTBT:PC$_{71}$BM bulk hetero junction solar cells by electric field induced optical second harmonic generation measurement, Journal of Applied Physics, Vol. 117 (2015) 163101.
3) Fakhra Aziz, Zubair Ahmad, Shahino Mah Abdullah, Khaulah Sulaiman and Muhammad Hasssan Sayyad, Photovoltaic Effect In Single-Junction Organic Solar Cell Fabricated Using Vanadyl Phthalocyanine Soluble Derivative, Pigment and Resin Technology, Vol. 44 (2015) Issue 1, 26-32.
4) Zubair Ahmad, Shahino Mah Abdullah, Dai Taguchi, Khaulah Sulaiman, Takaaki Manaka and Mitsumasa Iwamoto, Investigation of Carrier Transit Motion in PCDTBT by Optical SHG Technique, Laser Physics, Vol. 24 (2014) 105701.
5) Shahino Mah Abdullah, Zubair Ahmad, and Khaulah Sulaiman, A Solution-Based Temperature Sensor Using Organic Compound CuTsPc, Sensors, Vol. 14 (2014) 9878-9888.
6) Zubair Ahmad, Shahino Mah Abdullah, Qayyum Zafar and Khaulah Sulaiman, Investigation of charge transport in organic polymer donor/acceptor photovoltaic materials, Journal of Modern Optics, Vol. 61, No. 21, (2014), 1730–1734.
7) Khairus Syifa Hamdan, Shahino Mah Abdullah, Khaulah Sulaiman, and Rozalina Zakaria, Effects of silver nanoparticles towards the efficiency of organic solar cell, Applied Physics A:Materials Science & Processing, Vol. 115, Issue 1 (2014), 63-68.
8) Zubair Ahmad, Shahino Mah Abdullah, Khaulah Sulaiman, Bulk heterojunction photodiode: To detect the whole visible spectrum, Measurement, Vol. 46, Issue 7 (2013), 2073-2079.

9) Khaulah Sulaiman, Zubair Ahmad, Muhamad Saipul Fakir, Fadilah Abd Wahab, Shahino Mah Abdullah, and Zurianti Abd. Rahman, Organic Semiconductors: Applications in Solar Photovoltaic and Sensor Devices, Material Science Forum Vol. 737 (2013), 126-132.
10) Shahino Mah Abdullah, Zubair Ahmad, Fakhra Aziz, and Khaulah Sulaiman, Investigation of VOPcPhO as an acceptor material for bulk heterojunction solar cells, Organic Electronics, Vol. 13, Issue 11 (2012), 2532-2537.
11) Zubair Ahmad, Shahino Mah Abdullah, and Khaulah Sulaiman, Temperature-sensitive chemical cell based on Nickel (II) phthalocyanine-tetrasulfonic acid tetrasodium salt, Sensors and Actuators A: Physical, Vol. 179 (2012), 146-150.

Papers to be submitted

12) Shahino Mah Abdullah, Zubair Ahmad, and Khaulah Sulaiman, Extraction of Electrical Parameter of VOPcPhO/P3HT bulk heterojuction diode
13) Shahino Mah Abdullah, Zubair Ahmad, Khaulah Sulaiman, Mitsumasa Iwamoto, Dai Taguchi, The effect of thermal annealing to the stability of solar cells based on PCDTBT:$PC_{71}BM$
14) Saqib Rafique, Shahino Mah Abdullah, Waleed E. Mahoud, A. A. Al-Ghamdi, and Khaulah Sulaiman, Stability enhancement of PCDTBT:$PC_{71}BM$ solar cells by incorporation of V_2O_5 nanoparticles in PEDOT:PSS layer
15) Saqib Rafique, Shahino Mah Abdullah, Waleed E. Mahoud, A. A. Al-Ghamdi, Khaulah Sulaiman, The effect of fabrication environment to the stability of PCDTBT:$PC_{71}BM$
16) Shahino Mah Abdullah, Zubair Ahmad, and Khaulah Sulaiman, Electrolytic Nanofluid of CuTsPc-TiO_2 for Temperature Sensing Application
17) Mansoor Ani Najeeb, Shahino Mah Abdullah, Fakhra Aziz, Zubair Ahmad, and Khaulah Sulaiman, Effect of ZnSe quantum dots-PEDOT:PSS nano-composite on the photovoltaic properties of the organic solar cells
18) Mansoor Ani Najeeb, Shahino Mah Abdullah, Fakhra Aziz, Zubair Ahmad, and Khaulah Sulaiman, The Enhancement of P3HT:PCBM Organic Solar Cells by Incorporation of CdSe Quantum Dots in PEDOT:PSS Layer
19) Mansoor Ani Najeeb, Shahino Mah Abdullah, Zubair Ahmad, Khaulah Sulaiman, The enhancement of response current and sensitivity of light sensor based on P3HT:PCBM by incorporation of CdSe quantum dots in PEDOT:PSS layer

20) Mansoor Ani Najeeb, Shahino Mah Abdullah, Zubair Ahmad, Khaulah Sulaiman, Effect of temperature on the efficiency of PCPDTBT:PCBM based solar cell

21) Mansoor Ani Najeeb, Shahino Mah Abdullah, Zubair Ahmad, Khaulah Sulaiman, Investigation of ZnO nanostructures as electrode in organic solar cell

22) Khairus Syifa Hamdan, Shahino Mah Abdullah, Khaulah Sulaiman, and Rozalina Zakaria, Effects of silver nanoparticles towards the stability of organic solar cell based on PCDTBT:$PC_{71}BM$ blend

23) Mansoor Ani Najeeb, Shahino Mah Abdullah, and Khaulah Sulaiman, Dual-gate electric-double-layer field effect transistor for detection of prostate cancer

24) Shahino Mah Abdullah, and Khaulah Sulaiman, Fabrication of ITO-free organic solar cells by solution processable silver nanowires

B. Book

1) Shahino Mah Abdullah, and Khaulah Sulaiman, Application of Metal-Phthalocyanines in Sensor and Solar Cells, LAP Lambert Academic Publishing, Saarbrücken, Germany, (ISBN:978-3-659-57066-7), 8th July 2014.

C. Seminar

1) PhD conversion seminar, *"Application of Metal-Phthalocyanines in Physical Sensors and Solar Cells"*, Auditorium Fizik, Block C, Department of Physics, Faculty of Science, University of Malaya, Malaysia, 25th October 2013.

2) Posgraduate seminar, *"Investigation of Charge Carriers Behaviour in Organic Sensors and Solar Cell"*, Auditorium Fizik, Block C, Department of Physics, Faculty of Science, University of Malaya, Malaysia, 16th October 2014.

3) Postgraduate candidature defence, *"The study of charge transport behavior in solution processable organic devices"*, Seminar Room B, Block C, Department of Physics, Faculty of Science, University of Malaya, Malaysia, 30thOctober 2014.

4) Collaboration seminar, *"Organic Solar Cells: Fabrication and Characterizations in Low Dimensional Materials Research Centre"*, King Faisal Convention Centre, King Abdul-Aziz University, Jeddah, Saudi Arabia, 4thDecember 2014.

5) Viva-voce (presentation for PhD evaluation), "*The Study of Charge Transport Behaviour in Organic Devices: Light Sensor & Solar Cells*", Meeting room, Dean Office, Faculty of Science, University of Malaya, Malaysia, 3rd November 2015.

CONFERENCES AND SCIENTIFIC TRAINING

A. Conferences

1) Nanotechnology Applications in Energy and Environment (NAEE 2012), 20th – 21st September 2012, Institut Teknologi Bandung, Bandung, Indonesia (Poster).
2) The 3rd ISESCO International Workshop and Conference On Nanotechnology 2012 (IWCN 2012), 5th – 7th December 2012, Universiti Kebangsaan Malaysia, Selangor, Malaysia (Participant).
3) The 4th International Conference on Solid State Science and Technology (ICSSST 2012), 18th – 20th December 2012, Holiday Inn, Malacca, Malaysia (Committee).
4) The 4th International Conference on Functional Materials & Devices 2013 (ICFMD 2013), 8th – 11thApril 2013, Rainbow Paradise Hotel, Penang, Malaysia
5) University of Malaya Researchers' Conference (UMRC 2013), 19th – 20th November 2013, University of Malaya, Kuala Lumpur, Malaysia (Poster).
6) World Conference on Technology, Innovation and Entrepreneurship(WOCTINE 2015), 28th – 30th May 2015, WOW Convention Center, Istanbul, Turkey (Poster).

B. Training

1) Research training, “Evaluation of Organic Thin Film by Electrical and Optical Methods”, 2nd June – 2nd July 2013, Tokyo Institute of Technology, Tokyo, Japan.
2) Summer course, “Summer School on Organic Photovoltaic”, 1st – 4th September 2014, Strasbourg, France (Organized by Rhin-Solar and funded by European Union).

C. Awards

1) International Exposition of Research and Innovation in Education 2013 (Edu-InERI2013), 20th – 22nd Sep 2013, Universiti Pendidikan Sultan Idris, Malaysia
   Presented title: *“From Organic Semiconductor to Multifunctional Sensors: Towards Green Technology”*
   i. Gold Medal (Researcher Category)
   ii. Best Awards (Best-of-the-best award among the gold medal recipients)